Proc. 10th ERCOFTAC (SIG-15)/IAHR/QNET-CFD Workshop on Refined Turbulence Modelling

Remi Manceau, Jean-Paul Bonnet, Michael Leschziner, Florian Menter

Proceedings of the

10th joint ERCOFTAC (SIG-15)/IAHR/QNET-CFD Workshop

on Refined Turbulence Modelling

October 10-11, 2002

Laboratoire d'études aérodynamiques

UMR 6609 CNRS/Université de Poitiers/ENSMA, France

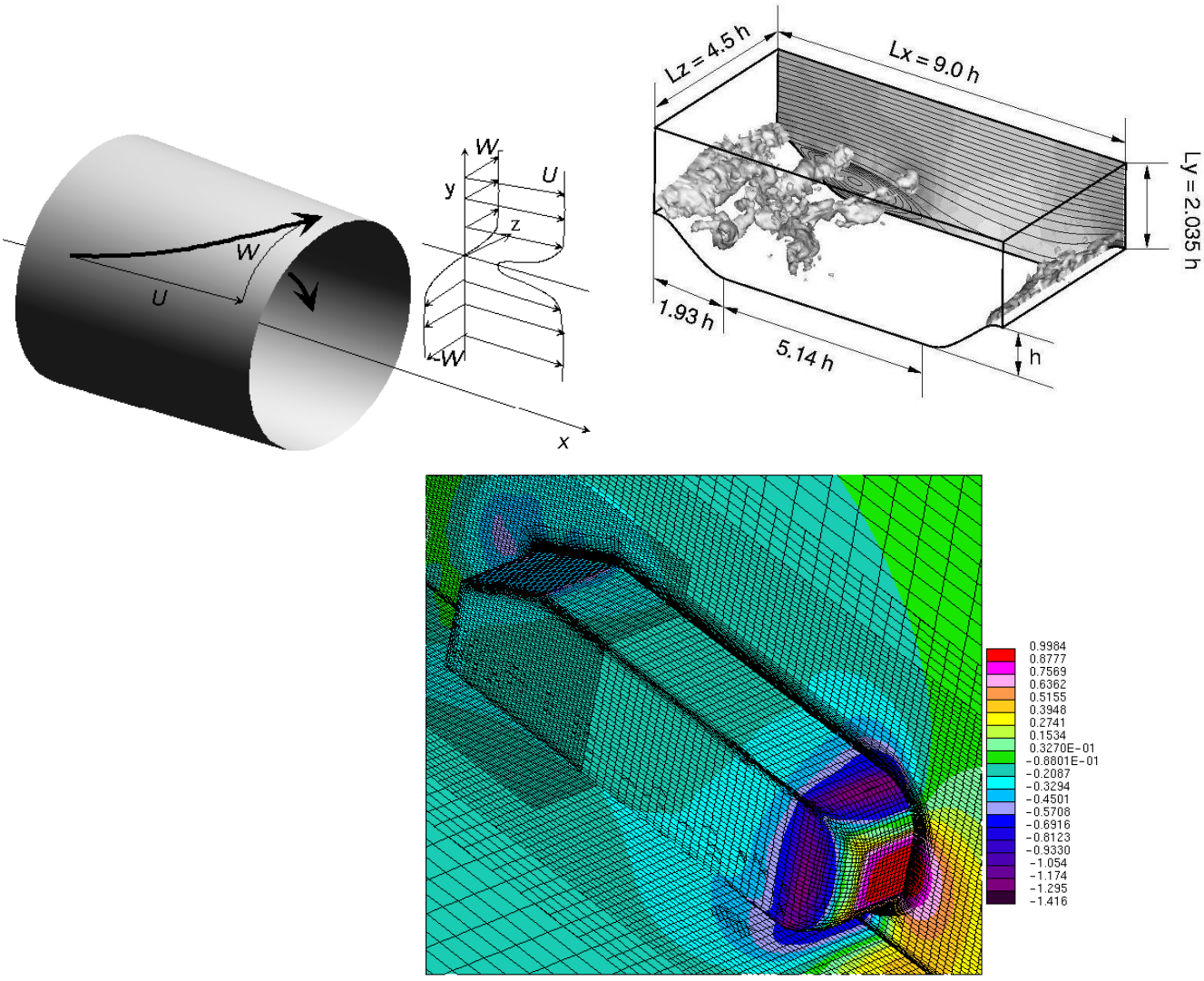

Editors : R. Manceau, J.-P. Bonnet, M. A. Leschziner, F. Menter

10th joint ERCOFTAC (SIG-15)-IAHR-QNET/CFD Workshop on Refined Turbulence Modelling

October 10–11, 2002

Laboratoire d'Études Aérodynamiques
University of Poitiers, France

Under the auspices of ERCOFTAC, Special Interest Group on Turbulence Modelling (SIG 15).

Standing Committee:

Chairman: Prof. Hanjalić, Delft University of Technology, the Netherlands
Co-chairman: Prof. Laurence, UMIST, UK, and Électricité de France
Prof. H. Andersson: University of Science and Technology, Trondheim, Norway
Prof. Karlsson: Chalmers University of Technology and Vattenfall Utveckeling, Sweden
Prof. Launder: UMIST, UK
Prof. Leschziner: Imperial College of London, UK
Prof. Rodi: University of Karlsruhe, Germany

Local Organization: Laboratoire d'Études Aérodynamiques
UMR 6609, CNRS/University of Poitiers/ENSMA, France
Dr. Manceau
Dr. Bonnet
Ms. Ecale

Editorial board for the proceedings:
Dr. Manceau, Dr. Bonnet: Laboratoire d'Études Aérodynamiques, UMR 6609, CNRS/University of Poitiers/ENSMA, France
Prof. M. A. Leschziner: Imperial College of London, UK
Dr. F. Menter: Ansys-CFX, Germany

Sponsoring Organizations:

Laboratoire d'Études Aérodynamiques
UFR Sciences Fondamentales et Appliquées
Université de Poitiers
CNRS
AEA Technology France/CFX
CD Adapco France

The CFX Solver:

- Most Advanced Coupled Solver
- Scalable Algebraic Multigrid Technology
- Accurate and Robust Second Order Bounded Scheme
- Superb Parallel Efficiency
- Most Advanced Turbulence Models
- Scalable Wall Functions

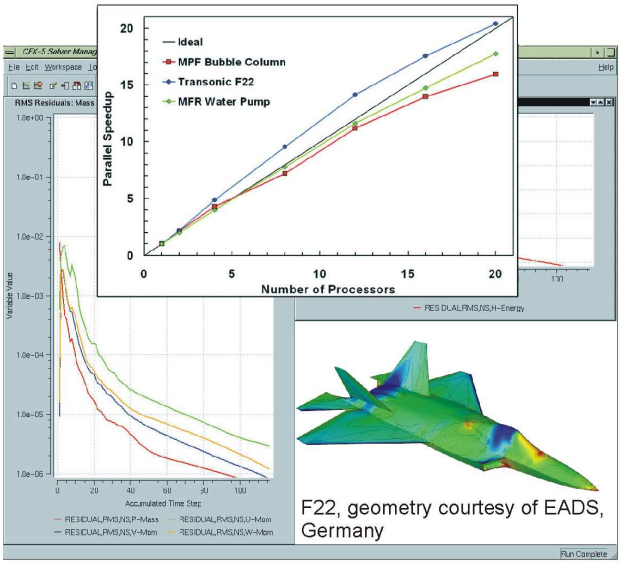

F22, geometry courtesy of EADS, Germany

Test Case: Diffuser Flow with Separation

k-ε Turbulence Model

SST Turbulence Model

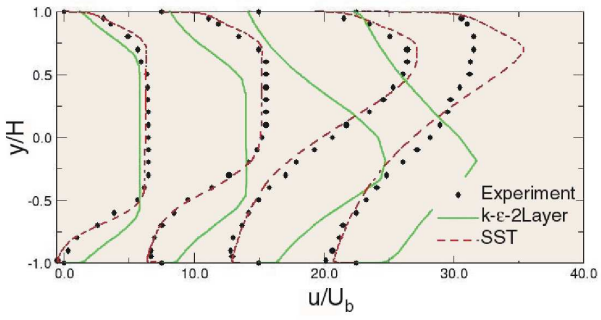

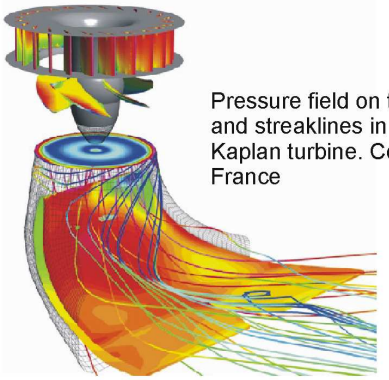

Pressure field on the runner blades and streaklines in the draft tube of the Kaplan turbine. Courtesy of EDF-CIH, France

CFX

www.cfx.aeat.com

Introduction

Computational Fluid Dynamics (CFD) has developed to a key technology which plays an important role in design, development and optimization in engineering practice. Although increasing computer capacities enable a broader use of highly resolved computational schemes such as Direct Numerical Simulation (DNS) and Large Eddy Simulation (LES), the statistical turbulence modelling used in the framework of the Reynolds Averaged Navier-Stokes (RANS) approach represents the current industrial standard. The ERCOFTAC-IAHR Workshops on Refined Turbulence Modelling (SIG-15) aim to bring together scientists, researchers, users and developers from industry and from the academic field.

Following the previous workshops, the test cases chosen for the workshop to be held in Poitiers are all very challenging cases, involving complex underlying mechanisms of primary significance for industrial applications. Two of the test cases, i.e., the flow over a periodic 2D hill and the flow around the Ahmed body (simplified car body), were already selected for the preceding workshop held in Darmstadt, Germany: the complexity of the underlying mechanisms and the challenge they represent for turbulence models have led to the renewal of these test cases.

The QNET-CFD network is associated to this ERCOFTAC-IAHR workshop because the case 9.4 (Flow around a simplified car body) is one of the 53 test cases under consideration in this network, in its Thematic Area 1 (External Aerodynamics), Application Challenge 5 (Ahmed body). This network is aimed at providing European industries with a knowledge base of high quality application challenges and best practice guidelines. Therefore, the second day of the workshop is going to be completely dedicated to the Ahmed body test case, in order to analyse in detail the features of the flow and the performances of the models.

Test cases

The workshop focuses on three test cases involving complex features: boundary layer separation on a smooth wall, recirculation, reattachment, boundary layer recovery, wake/mixing layer interaction, three-dimensionality, massively separated wake, etc.

- Case 10.1: Contra-rotating jets (wake/mixing layer interaction)
- Case 9.2: Periodic flow over a 2-D hill
- Case 9.4: Flow around a simplified car body (Ahmed body)

After the workshop, the participants were given the opportunity to update their results or to submit new computations: new results were submitted during more than one year after the workshop. Therefore, the present proceedings does not contain exactly the same results as the draft proceedings distributed during the workshop. Moreover, it has been enriched by reports written by R. Manceau, M. A. Leschziner and F. Menter about the three test cases. Despite the cautiousness in avoiding omissions and mistakes, the local organizers apology for any missing or misplaced results.

-

Programme

October 9:

18.00-20.00 Registration and proceedings handout

October 10:

8.00– 9.00 Registration and proceedings handout

9.00– 9.05 Welcome (J.-P. Bonnet, head of the LEA)

9.05– 9.15 Opening (SIG-15 chairman: Prof. Hanjalic)

Case 10.1: Contra-rotating jets (wake/mixing layer interaction)

Chairman: Dr. Bonnet

9.15–9.45 Presentation of the reference experiments (Dr. Delville)

9.45– 10.45 Presentation of the computations by the participants

Merci, De Langhe, Lodefier, Dick (Ghent University)

Deng, Visonneau (Ecole Centrale de Nantes)

Pellerin, Fournier, Goossens (LIMSI–CNRS)

Manceau (Université de Poitiers/CNRS/ENSMA)

Coffee Break

11.15– 11.45 Comparison of the results (Dr. Manceau)

11.45– 12.00 General discussion

Lunch

Case 9.2: Periodic flow over a 2-D hill

Chairman: Prof. Launder

14.00–14.30 Presentation of the reference LES (Prof. Leschziner)

14.30–16.00 Presentation of the computations by the participants

Jakirlić, Šarić, Djugum (TU Darmstadt)

Deng, Visonneau (Ecole centrale Nantes)

Merci, De Langhe, Lodefier, Dick (Ghent University)

Salo, Hellsten (Helsinki UT)

Rumsey (NASA Langley)

Kolkka, Ahlstedt (Tampere UT)

Uribe, Laurence (UMIST)

Wang, Jang, Leschziner (Imperial College)

Coffee break

16.30–17.30 Comparison of the results (Prof. Leschziner)
17.30–17.45 General discussion

19.30 *Departure of the bus*
20.00 *Dinner*

October 11:

Case 9.4: Flow around a simplified car body (Ahmed body)

Chairman: Prof. Hanjalic

9.00– 9.30 Presentation of the relevance to industry and
of the structure visualizations performed at the LEA (Dr. Spohn)
9.30–10.00 Presentation of the reference experiments (Dr. Lienhart)
10.00–11.00 Presentation of the computations by the participants
Hinterberger, Garcia-Villaba, Rodi (University of Karlsruhe)
Leonard (NUMECA Int.)
Hadžiabdić, Hanjalić, Khier, Liu, Oulhous (TU Delft)
Craft, Gant, Iacovides, Launder, Robinson (UMIST)
Kuntz, Menter, Durand (CFX Germany)

Coffee break

11.30–12.15 Comparison of the results (25° case) (Dr. Menter)
12.15–12.30 General discussion

Lunch

14.00–14.30 Comparison of the results (35° case) (Dr. Menter)
14.30–15.00 General discussion
15.00–16.00 Plans for the future workshops
Chairman: Prof. Hanjalic
16.00 Closing of the workshop

List of Participants

TITLE	FIRST NAME	LAST NAME	INSTITUTION	CITY	COUNTRY
Dr.	Jean-Paul	Bonnet	Université de Poitiers/CNRS/ENSMA	Poitiers	France
	Sabrina	Carpy	Université de Poitiers/CNRS/ENSMA	Poitiers	France
	Laurent	Collonge	Fluent France	Montigny le Bretonneux	France
Dr.	Joël	Delville	Université de Poitiers/CNRS/ENSMA	Poitiers	France
Dr.	Ganbo	Deng	Ecole centrale de Nantes	Nantes	France
Prof.	Erik	Dick	Université de Gand	Gand	Belgium
Dr.	Philippe	Druault	Université Paris VI/CNRS	Orsay	France
	Guillaume	Fournier	LIMSI	Orsay	France
	Simon	Gant	UMIST	Manchester	UK
	Muhamed	Hadžiabdić	Delft University of Technology	Delft	The Netherlands
Prof.	Kemal	Hanjalić	Delft University of Technology	Delft	The Netherlands
	Antti	Hellsten	Helsinki University of Technology	Espoo	Finland
Dr.	Vincent	Herbert	PSA Peugeot-Citroën	Velizy	France
Dipl. Ing.	Christof	Hinterberger	University of Karlsruhe	Karlsruhe	Germany
Dr.	Suad	Jakirlić	Darmstadt University of Technology	Darmstadt	Germany
Prof.	Gunnar	Johansson	Chalmers University of Technology	Goteborg	Sweden
	Jonna	Kolkka	Tampere University of Technology	Tampere	Finland
	Siniša	Krajnović	Chalmers University of Technology	Goteborg	Sweden
Prof.	Brian	Launder	UMIST	Manchester	UK
Prof.	Dominique	Laurence	EDF/UMIST	Chatou/Manchester	France/UK
Ir.	Benoît	Leonard	NUMECA	Bruxelles	Belgium
Prof.	Michael	Leschziner	Imperial College	Londres	UK
Dr.	Hermann	Lienhart	Erlangen University	Erlangen	Germany
Dr. Ing.	Petr	Louda	Institut of Thermomechanics	Prague	Czech Republic
Dr.	Rémi	Manceau	Université de Poitiers/CNRS/ENSMA	Poitiers	France
Dr.	Florian	Menter	CFX	Otterfing	Germany
Dr.	Stéphanie	Pellerin	LIMSI	Orsay	France
Dr.	Pierre	Perrier	Dassault	Saint-Cloud	France
	Daniel	Pierrat	CETIM	Nantes	France
	Christopher	Rumsey	NASA Langley	Hampton, VA	USA
	Sanjin	Šarić	Darmstadt University of Technology	Darmstadt	Germany
Dr.	Andreas	Spohn	Université de Poitiers	Poitiers	France

-

Report on the 10th joint ERCOFTAC (SIG-15)/IAHR/QNET-CFD Workshop on Refined Turbulence Modelling

Poitiers, october 10-11, 2002

Rémi Manceau
Laboratoire d'études aérodynamiques
CNRS UMR 6609, Université de Poitiers
86 962 Futuroscope Chasseneuil cedex
France

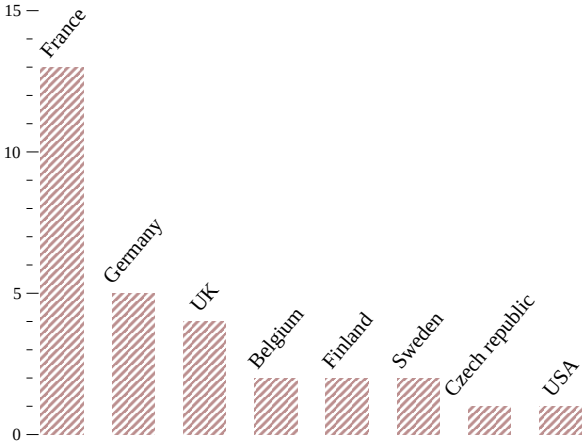

Figure 1: Repartition of the participants

1 Introduction

Computational Fluid Dynamics (CFD) has developed to a key technology which plays an important role in analysis, design, development and optimization in engineering practice. Although increasing computer capacities enable a broader use of highly resolved computational schemes such as Direct Numerical Simulation (DNS) and Large Eddy Simulation (LES), the statistical turbulence modelling used in the framework of the Reynolds Averaged Navier-Stokes (RANS) approach represents the current industrial standard. The ERCOFTAC-IAHR Workshops on Refined Turbulence Modelling (SIG-15) aim to bring together scientists, researchers, users and developers from industry and from the academic field.

The QNET-CFD network was associated to this ERCOFTAC/IAHR workshop because the case 9.4 (Flow around a simplified car body) is one of the 53 test cases under consideration in this network, in its Thematic Area 1 (External Aerodynamics), Application Challenge 5 (Ahmed body). This network is aimed at providing European industries with a knowledge base of high quality application challenges and best practice guidelines. Therefore, the second day of the workshop was completely dedicated to the Ahmed body test case, in order to analyse in detail the features of the flow and the performances of the models.

2 Participants

The workshop attracted 32 participants from 9 countries, distributed as shown in figure 1.

Most of them came from European universities or research institutes (24), 7 from European industries and 1 from NASA.

They represented 24 different institutions. 15 of them submitted results.

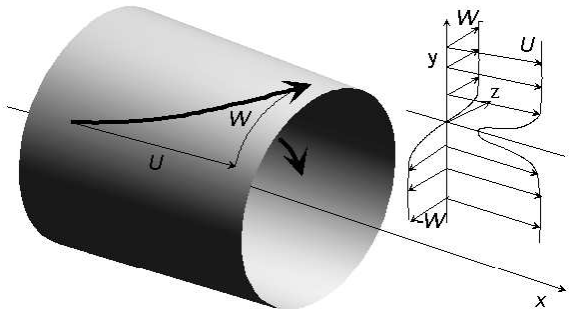

Figure 2: Sketch of the wake/mixing layer interaction test case

3 Test cases

This series of workshops of the Special Interest Group on Refined Turbulence Modelling (SIG-15) aim at evaluating the comparative performances of turbulence models in the prediction of very challenging test cases, involving complex underlying mechanisms of primary significance for industrial applications.

Two of the test cases, i.e., the flow over a periodic 2D hill and the flow around the Ahmed body (simplified car body), were already selected for the preceding workshop held in Darmstadt, Germany [2]: the complexity of the underlying mechanisms and the challenge they represent for turbulence models have led to the renewal of these test cases.

3.1 Case 10.1: Wake/mixing layer interaction (contra-rotating jets)

The flow is generated by two coaxial jets with opposite rotation. An azimuthal mixing layer develops, and an interaction between the wake of the inner nozzle and the azimuthal mixing layer takes place, as shown in figure 2.

A transition from a wake to a mixing layer behaviour occurs as the flow develops is x-direction. In particular, the Reynolds stress tensor experiences a drastic change in its structure.

Detailed experiments performed at the LEA [1] at $Re = 212,000$ were made available for this workshop. The database contains profiles of the mean velocities, Reynolds stresses (6 components) and budgets at 15 location downstream of the nozzle.

3.2 Case 9.2: Periodic flow over a 2-D hill

This case is a statistically 2D turbulent flow in a channel with a wall consisting of a periodic series of hills, as shown in figure 3. Separation occurs on the leeward face of the hill due to adverse pressure gradient and reattaches on the flat part, before the next hill.

The main difficulty of the case is to predict the location where separation and reattachment occur, as well as the high level of turbulent stresses in the shear region.

Detailed statistics of the flow were available from a highly resolved LES [4].

3.3 Case 9.4: Flow around a simplified car body (Ahmed body)

The Ahmed body is a simplified car, shown in figure 4, defined by the car industry in order to focus on a particular aspect of the flow: the complex wake structure at the origin of the drag crisis experienced by ground vehicles when the angle of the hatchback approaches 25 degrees.

Detailed experiments were provided by Lienhart, Stoots and Becker, 2000.

4 Programme

4.1 October 10

Morning: case 10.1 (chairman: Dr. Bonnet)

The first talk was given by Dr. Delville (LEA, university of Poitiers/CNRS) who presented the test case, its underlying physics and the experiments performed at the LEA.

The 4 teams that performed computations of the case presented their numerical methods and turbulence models. 12 different computations had been submitted, using 7 different RANS models and 1 LES model.

Dr. Manceau (LEA, university of Poitiers/CNRS) then presented cross-plots of the results submitted by the participants and tried to analyse the relative merits and weaknesses of the different turbulence models.

Finally, an open discussion allowed commenting and completing this analysis.

Afternoon: case 9.2 (chairman: Pr. Launder)

First, Pr. Leschziner (Imperial College) presented the test case and the highly resolved LES performed by Imperial College.

8 teams then presented the computations they had submitted for this case, i.e., 38 different computations using 23 different turbulence models.

Pr. Leschziner gave a synthesis of the comparative performances of the numerous turbulence models.

An open discussion closed the first workshop day.

4.2 October 11

Case 9.4 (chairman: Pr. Hanjalić)

The first talk was given by Dr. Spohn (LEA, university of Poitiers/CNRS), who presented visualisation performed at the LEA at a low Reynolds number in order to better understand the flow structures.

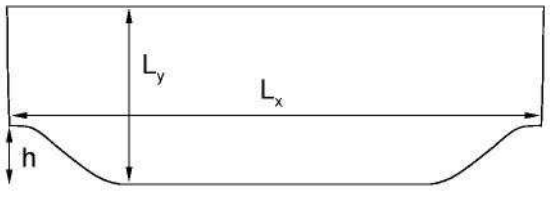

Figure 3: Geometry of the case 9.2

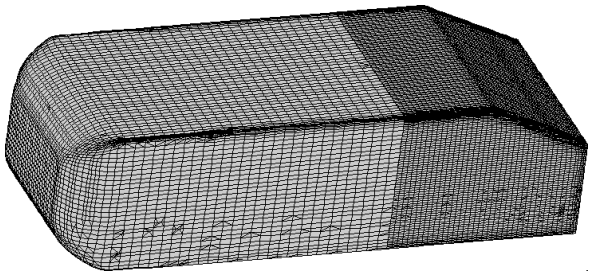

Figure 4: Geometry of the case 9.4

The second talk was given by Dr Lienhart (Erlangen University), who presented the flow conditions and the experiments performed at Erlangen.

The 5 teams that had submitted results for this case then gave an overview of their numerical methods. 10 computations were presented for the 25 degree case and 11 for the 35 degree case, using 11 different RANS models and 1 LES model.

Dr. Menter (CFX) then synthesized the computational results for both the 25 and 35 degree test cases.

5 Conclusions

So many comments were made about the relative performances of the models in the reproduction of the different physical mechanisms involved in the 3 test cases that it is not possible to go into details in the frame of this report. However, some aspects were particularly interesting and deserve some comments.

Wake/Mixing layer interaction. It was clear that linear eddy-viscosity models are not suited to this case in which the turbulence production mechanisms of the different components are absolutely not the same. However, even for nonlinear and Reynolds stress models, which are able to reproduce these subtle production mechanisms, the transition from a wake to a mixing layer behaviour, which is clearly seen in the experimental budgets, is not obtained correctly.

Periodic flow over a 2-D hill. Pr. Leschziner particularly emphasized the large scale unsteadiness of the flow at the origin of large variations of the instantaneous locations of the separation and reattachment points: this feature, observed in the highly resolved LES computation, makes the case very challenging for statistical models. Reynolds-averaged computations do not resolve this low frequency unsteadiness and the turbulence models do not predict its mean effect, which is probably far from standard turbulence agitation.

Flow around a simplified car body (Ahmed body). While the low-drag configuration (35 degrees) is correctly predicted by different turbulence models, the complex 3D structure of the wake of the body for the high-drag case is only reproduced by LES. Conclusions must be drawn with caution for this very complex flow, but it seems like either some fundamental physical mechanism is missed by RANS models or large scale unsteadiness plays again a crucial role in the sustainment of the complex 3D wake.

6 Proceedings

Detailed descriptions of the test cases, the numerical methods used by the participants and the results can be found in the proceedings of the workshop:

R. Manceau, J.-P. Bonnet, M. A. Leschziner, F. Menter, editors. *Proc. 10th ERCOFTAC (SIG-15)/IAHR/QNET-CFD Workshop on Refined Turbulence Modelling*. Laboratoire d'études aérodynamiques, UMR CNRS 6609, Université de Poitiers, France, October 10–11, 2002.

Links to the databases used for the workshop can be found on the workshop web site:

http://labo.univ-poitiers.fr/informations-lea/Workshop-Ercoftac-2002/Index.html

7 Acknowledgement

Beside ERCOFTAC and IAHR, the workshop was supported by the CNRS, the university of Poitiers, CD-Adapco and CFX.

Bibliography

[1] S. Béharelle, J. Delville, and J.-P. Bonnet. On the three-dimensional evolution of a wake subjected to cross-shear. In *Proc. 11th Symp. Turb. Shear Flows, Grenoble, France*, 1997.

[2] S. Jakirlić, R. Jester-Zürker, and C. Tropea, editors. *Proc. 9th ERCOFTAC/IAHR/COST Workshop on Refined Turbulence Modelling*. Darmstadt University of Technology, Germany, October 4–5, 2001.

[3] R. Manceau, J.-P. Bonnet, M. A. Leschziner, and F. Menter, editors. *Proc. 10th ERCOFTAC (SIG-15)/IAHR/QNET-CFD Workshop on Refined Turbulence Modelling*. Laboratoire d'études aérodynamiques, UMR CNRS 6609, Université de Poitiers, France, October 10–11, 2002.

[4] L. Temmerman and M. A. Leschziner. Large eddy simulation of separated flow in a streamwise periodic channel constriction. *Int. Symp. Turb. Shear Flow Phenomena, Stockholm, Sweden*, 2001.

-

Main conclusions of the workshop

R. Manceau, M. A. Leschziner, F. Menter

Comparisons of the relative performances of the different turbulence models used by the participants were presented during the workshop. The three following articles are summaries of the main remarks that were made during the workshop by the participants chosen by the committee of the 15th Special Interest Group to analyse the cross-plots:

- Case 10.1: Contra-rotating jets (wake/mixing layer interaction)
  Rémi Manceau (Université de Poitiers/CNRS/ENSMA, France)
- Case 9.2: Periodic flow over a 2-D hill
  Michael Leschziner (Imperial College, London, UK)
- Case 9.4: Flow around a simplified car body (Ahmed body)
  Florian Menter (CFX, Otterfing, Germany)

The complete set of crossplots can be found on the CD-Rom that contains:

- A color PDF version of the present report;
- All the crossplots for the case 10.1:
  - Wake width and mixing layer vorticity thickness;
  - Profiles of U, W, and all the Reynolds stresses, at 15 downstream locations;
  - Budgets of the turbulent kinetic energy equation at 15 downstream locations.
- All the crossplots for the case 9.2:
  - Streamlines;
  - Profiles of U, V, k, $\overline{uv}$, $\overline{u^2}$, $\overline{v^2}$, and the length scale l at 10 locations;
  - Budgets of the turbulent kinetic energy equation at 10 locations.
- All the crossplots for the case 9.4 (25 deg and 35 deg):
  - Vector plots and turbulent energy contours in the symmetry plane;
  - Velocity and Reynolds stress profiles in the symmetry plane over the slant part;
  - Vector plots and turbulent energy contours in constant-x plane (upstream of the base and in the wake);
  - Contours of pressure coefficients on the slant part and the base.

-

Case 10.1

Results and comments

Contra-rotating jets (wake/mixing layer interaction)
Analysis of the results

Rémi Manceau
Laboratoire d'études aérodynamiques
UMR 6609, CNRS/Université de Poitiers/ENSMA, France

A brief description of the test case is given in the report published in *ERCOFTAC Bulletin* (see a few pages before the present report). For a more detailled description, see the CD-Rom or the web-site
http://labo.univ-poitiers.fr/informations-lea/Workshop-Ercoftac-2002/Index.html

Contributions

10 series of results were submitted, from 4 different research teams: École centrale de Nantes (France), Ghent University (Belgium), LIMSI (CNRS, France), and LEA (Université de Poitiers/CNRS/ENSMA, France). The list of contributions is given in table 1. The turbulence models used by the contributors are of 4 types:

- Linear eddy-viscosity models: EC–Nantes/k–ω–BSL, EC–Nantes/k–ω–SRSST, Ghent–U/Low–Re–k–ε–Yang–Shih, LEA/k–ε.
- A nonlinear eddy-viscosity model: Ghent–U/cubic–k–ε.
- Reynolds stress models: EC–Nantes/RSM–IP, EC–Nantes/RSM–SSG.
- Large-eddy simulation: LIMSI/LES.

For the sake of concision, the results are crossplotted in two groups:

- Eddy-viscosity models
- Reynolds stress models and Large-eddy simulation

Moreover, Ghent University and LEA both studied the influence of the use or not of the inlet condition $V_{\text{in}} = 0$, which are presented in separate crossplots.
Details on the models used by the participants can be found from page after the present report.
The complete set of results is given on the CD-Rom.

Results

Some definitions

The wake is visible in plots of U as a function of y, and the mixing layer in plots of the azimuthal component W as a function of y. The downstream evolutions of their spreading rates can be investigated separately.

- Width of the wake: A self-similar plane wake satisfies the following relation:

$$U(x,y) = U_\infty - U_s(x)\,\exp\left(-\frac{1}{2}\kappa\frac{y^2}{b(x)^2}\right) \tag{1}$$

  where $U_s(x)$ is the maximum of the velocity deficit. $\kappa = 1$ can be used [**?**]. $b(x)$ is thus the half-width of the wake. Since

$$\frac{U_\infty - U(x,\pm b(x))}{U_s(x)} = \exp\left(-\frac{1}{2}\right) \simeq 0.607$$

  the width of the wake, $2b$, is thus evaluated by $y_2 - y_1$, where y_1 and y_2 are the 2 locations where this function takes the value $\exp(-1/2)$.

- Vorticity thickness of the mixing layer: A self-similar mixing layer satisfies the relation:

$$W(x,y) = \frac{1}{2}\,\Delta W\,\mathrm{erf}\left(\sqrt{\pi}\frac{y}{\delta_\omega}\right) \tag{2}$$

  where ΔW is the mean velocity difference. Using this definition, δ_ω can be simply evaluated by:

$$\delta_\omega = \frac{\Delta W}{\left(\dfrac{\partial W}{\partial y}\right)_{\max}}$$

The downstream evolutions of these quantities are plotted in Figs. 1 and 2.
The width of the wake, $2b$, scales with $\sqrt{x}$ in a standard self-similar wake. In the present case, $2b$ seems to behave as $\sqrt{x}$ before $x/r_0 \simeq 2$ (but the wake does not reach a real self-similar state). After $x/r_0 \simeq 2$, the spreading of the flow is driven by the mixing layer, and the behaviour of $2b$ experiences a transition to a "mixing-layer type", with

$$2b \propto x$$

Concerning δ_ω, after a short region of establishment, before $x/r_0 \simeq 3$, it seems to grow linearly in the downstream direction: $\delta_\omega \propto x$.

Predictions of $2b$ and δ_ω

- Only models based on ω are able to reproduce correctly the spreading of the wake (before $x/r_0 \simeq 2$) and of the mixing layer (Figs. 1 and 2). This is quite surprising since both the BSL and the SST models are supposed to be equivalent to k–ε models in free flows.

- Note that the strong underestimation of δ_ω by the EC–Nantes/k–ω–SRSST, Ghent–U/Low–Re–k–ε–Yang–Shih and EC–Nantes/RSM–SSG are not due to a true underestimation of the spreading, but to the prediction of steep gradients of W close to the outer boundary of the mixing layer (Figs. 7 and 9). The max of $\partial W/\partial y$ used

Authors	Institution	Identifier
Béharelle, Delville, Bonnet	LEA, University of Poitiers	Experiments
Deng, Visonneau	Ecole centrale Nantes	EC–Nantes/k–ω–BSL
Deng, Visonneau	Ecole centrale Nantes	EC–Nantes/k–ω–SRSST
Deng, Visonneau	Ecole centrale Nantes	EC–Nantes/RSM–IP
Deng, Visonneau	Ecole centrale Nantes	EC–Nantes/RSM–SSG
Merci, De Langhe, Lodefier, Dick	Ghent University	Ghent–U/Low–Re–k–ε–Yang–Shih
Merci, De Langhe, Lodefier, Dick	Ghent University	Ghent–U/cubic–k–ε
Merci, De Langhe, Lodefier, Dick	Ghent University	Ghent–U/cubic–k–ε–$V_{\text{in}} = 0$
Pellerin, Fournier, Goossens	LIMSI–CNRS	LIMSI/LES
Manceau	LEA, University of Poitiers	LEA/k–ε
Manceau	LEA, University of Poitiers	LEA/k–ε–$V_{\text{in}} = 0$

Table 1: List of contributions for the case10.1.

in the definition of δ_ω is reached in this region: δ_ω does not represent correctly the width of the mixing layer.

- None of the models is able to capture the transition of the wake width to a behaviour in x: although the Yang-Shih low-Re model reproduces the correct evolution of $2b$, this is only fortuitous, since it is seen in Figs. 3 and 4, as well as Figs. 7 and 8 that this model actually gives the poorest predictions.

Near-wake region

- In the near-wake region, i.e., before $x/r_0 \simeq 2$, the mean flow can be considered a superposition of a wake and a mixing layer, as a first approximation. The shapes of all the components of the Reynolds stress can thus be explained by simple mechanisms. The figure below explains almost everything: the shapes of the different components of the production tensor are guessed, simply by using Eqs. (1) and (2) as basic shapes for the mean velocities and assuming that $\overline{v^2}$ is roughly Gaussian (which can be seen in experiments). Derivatives in the x–direction are neglected.

$$P_{ij} = \left(\quad \right)$$

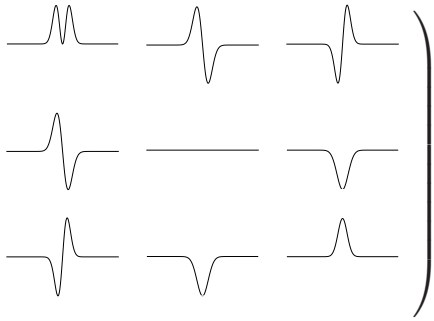

The shapes on the Reynolds stresses (Figs. 3 and 4) are basically the same as those of their respective production components: redistribution of energy from $\overline{w^2}$ to $\overline{v^2}$ explains why $\overline{v^2}$ is not zero, and the conjugate influence of diffusion and redistribution from $\overline{w^2}$ explains why the double peak of $\overline{u^2}$ is smoothed. Moreover, profiles are slightly asymmetric, which is inherited from the boundary layers along the nozzle wall.

- Reynolds stress models and LES are able to predict these shapes correctly (Figs. 5 and 6), because the production mechanisms are solved exactly rather than modelled. However, it is clear that the amplitudes are not accurately obtained for all the components, in particular with LES. The SSG model performs slightly better than the IP model.

- Linear eddy-viscosity models are, by construction, unable to reproduce correctly the Reynolds stress tensor (Figs. 3 and 4). This is explained by the use of the Boussinesq hypothesis:

$$\overline{u_i u_j} = -2\nu_t S_{ij} + \frac{2}{3} k \delta_{ij}$$

  Assuming that ν_t is basically Gaussian (this is confirmed by the results), and that k has the same shape as its production rate P_k, the following shapes are obtained:

$\overline{u_i u_j} =$ 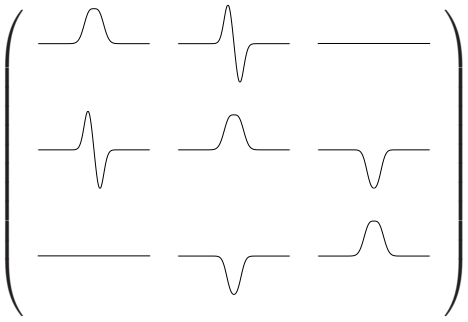

  Therefore, linear eddy-viscosity models predict completely wrong Reynolds stresses (Figs. 3 and 4):

  - $\overline{u^2} = \overline{v^2} = \overline{w^2}$ is predicted.
  - Only $\overline{uv}$ and $\overline{vw}$, which can be directly related to the two mean shear components $\partial U/\partial y$ and $\partial W/\partial y$ by a mixing length argument, are correctly reproduced.
  - The double peak of $\overline{u^2}$ is totally missed, because k is driven by the *total* production P_k, which is dominated by P_{33}.
  - $\overline{uw}$ is close to zero (only non-zero values of $\partial W/\partial x$ prevent $\overline{uw}$ from being exactly zero). This is the most striking drawback of the Boussinesq hypothesis. This component is indeed produced by the wake/mixing layer interaction:

$$P_{13} = -\overline{uv}\frac{\partial W}{\partial y} - \overline{vw}\frac{\partial U}{\partial y}$$

    ($\overline{uv}$ is produced by $\partial U/\partial y$ and $\overline{vw}$ by $\partial W/\partial y$). This problem is fixed by the use of a nonlinear constitutive equation, as shown by the results of the Ghent–U/cubic–k–ε, which gives excellent predictions of all the Reynolds stresses in this region (even better that second moment closures).

- Finally, it can be noted that all the models used predict a much too sharp turbulent/non-turbulent interface (all the Reynolds stress components): this is a common drawback of virtually all one-point closures.

Far-wake region

- Further downstream, all the models but LES strongly underpredict the width of the wake (Figs. 1 and 2, and Figs. 7–10): the flow in this region is driven by large-scale

coherent structures generated by the mixing layer, which is missed by steady-state computations.

- As a consequence, the amplitude of the Reynolds stress component linked to the wake profile, $\overline{uv}$, is strongly overestimated.
- The mean velocity profiles are also shifted towards positive y's, which is missed by all the computations but those of Ghent University.
- Since the turbulence is now mainly driven by the mixing layer, linear eddy-viscosity models are able to predict the correct shapes of the Reynolds stresses $\overline{u^2}$, $\overline{v^2}$ and $\overline{w^2}$, although they are all equal to $2/3\ k$.
- The cubic k–ε model yields different levels of normal stresses, but underestimates the total turbulent energy, contrary to linear models.
- Reynolds stress models also slightly underestimate the turbulent kinetic energy, and in particular the component $\overline{v^2}$ (Fig. 10). The IP model globally gives better predictions than the SSG model in this region.

Budget of turbulent kinetic energy

Figs. 11 and 12 show the budget of k at two different locations.

- At $x/r_0 = 4.17$, the budget is clearly the budget of a standard mixing layer: diffusion exhibits a single, negative peak at the centre and two positive peaks at the edge of the mixing layer; convection is negative, and nearly zero at the centre.
- On the contrary, at $x/r_0 = 1.25$, the budget is influenced by the wake: diffusion displays a double negative peak, and convection is positive on the centreline. However, production is dominated by P_{33}, i.e., by the mixing layer.
- It is clear from Figs. 11 and 12 that the models fail to predict this transition from a wake-type to a mixing-layer-type budget. In particular, for all the models, including LES, convection remains positive at the centreline. The double negative peak of diffusion disappears much too slowly.
- The cubic k–ε model gives quite a good budget in the wake region (Fig. 11), but predicts a spurious drop of production at the centre, which survives all along the domain.

Influence of the inlet condition for V

Ghent University and LEA have investigated the influence of enforcing $V_{\text{in}} = 0$ instead of the profile from the experiments.

- The influence on the spreading of the wake and the mixing layer is significant (Fig. 13): the use of $V_{\text{in}} = 0$ artificially increases both spreading rates.
- In the near-wake region, the inlet condition has a strong influence on U (Fig. 14): actually, the discrepancies due to the inlet condition is much more significant than those due to the choice of the model.

- The Reynolds stresses are also strongly influenced by the inlet condition for the cubic k–ε model, while for the linear k–ε model, the influence is much weaker (Fig. 15).
- The modification in the inlet condition is felt throughout the domain (Figs. 16 and 17), in particular as concerns the profile of U. The influence on the turbulent energy level is still of the order of 8%.
- In general, the predictions are improved by using inlet conditions from the experiments. Note that the results by Ghent University and LEA presented in previous crossplots are those obtained with the experimental V profiles.

Conclusions

- This test case is very challenging for turbulence models, because of the interaction of two different flow types, oriented in orthogonal directions. It appears that the transition from a wake-dominated to a mixing-layer-dominated flow is particularly difficult to predict.
- Linear eddy-viscosity models are by construction unable to reproduce the underlying mechanisms. Firstly, they predict equal levels of normal stresses ($\overline{u^2} = \overline{v^2} = \overline{w^2}$), while these components are driven by completely different production mechanisms. Secondly, they predict $\overline{uw} \simeq 0$: this component is actually produced by the interaction between the wake and the mixing layer, which is totally missed by linear eddy-viscosity models.
- The cubic k–ε model used by Ghent University yields much more realistic Reynolds stresses in the wake-dominated region. However, the analysis of the turbulent energy budgets shows that the transition to a mixing-layer-type behaviour is missed, or at least much delayed.
- Reynolds stress models give quite satisfactory results in the near-wake region, but fail in some respects in the far-wake region: they underestimate the turbulent energy and the wake width.
- The LES computation is a preliminary computation, and is not sufficient to draw conclusions about the LES capabilities in this configuration.
- Although the inlet V velocity is very weak, it has a significant influence on the results, even far downstream: the use of $V_{\text{in}} = 0$ must be avoided.

References

S. Béharelle. *Influence du cisaillement transversal sur le développement d'une couche cisaillée libre turbulente incompressible.* PhD thesis, université de Poitiers, 1999.

Contra-rotating jets: WAKE WIDTH AND MIXING LAYER VORTICITY THICKNESS

Eddy-viscosity models

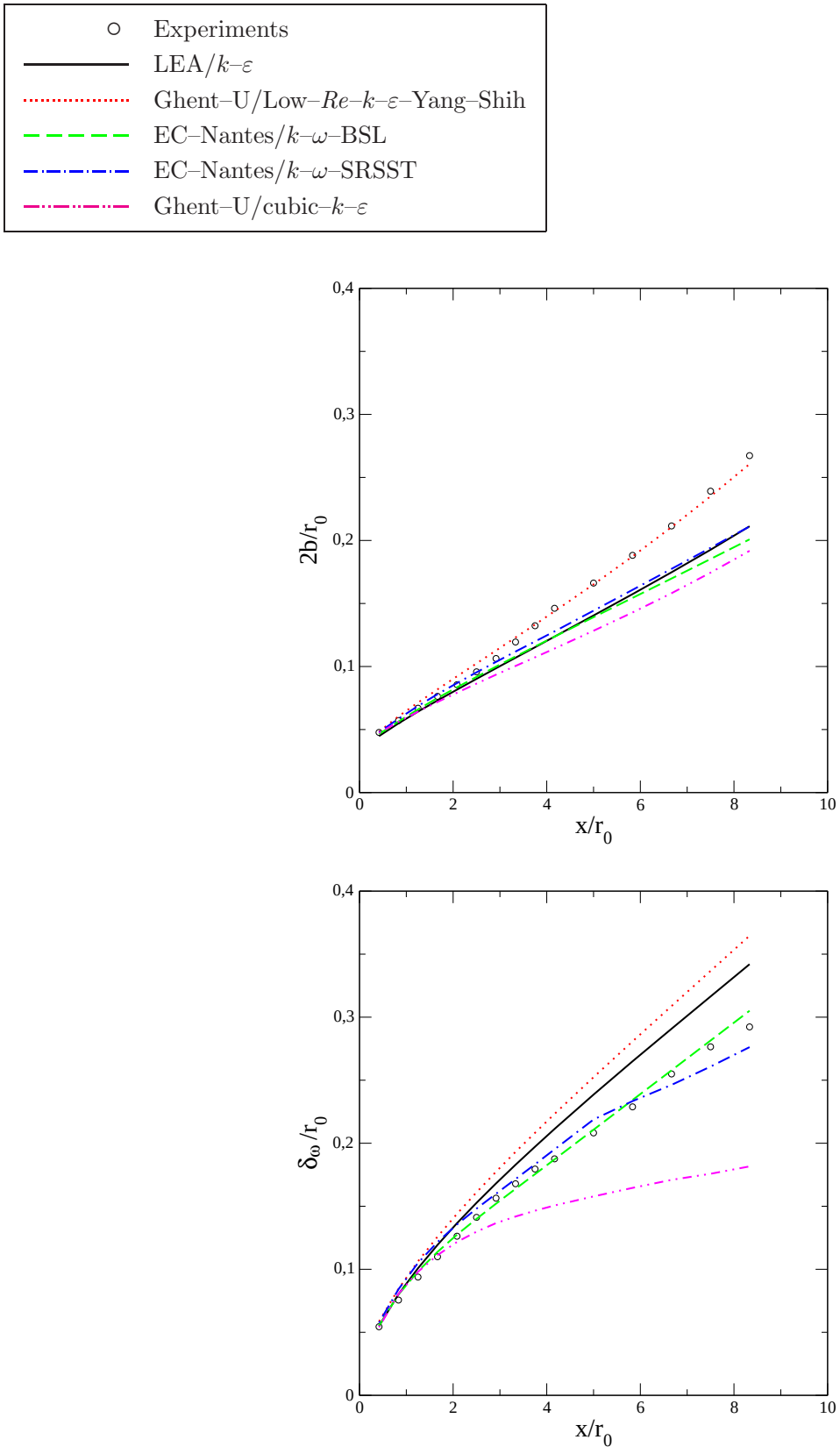

Figure 1: Eddy-viscosity models. Downstream evolution of $2b$ and δ_ω.

Contra-rotating jets: WAKE WIDTH AND MIXING LAYER VORTICITY THICKNESS

Reynolds stress models
Large Eddy Simulation

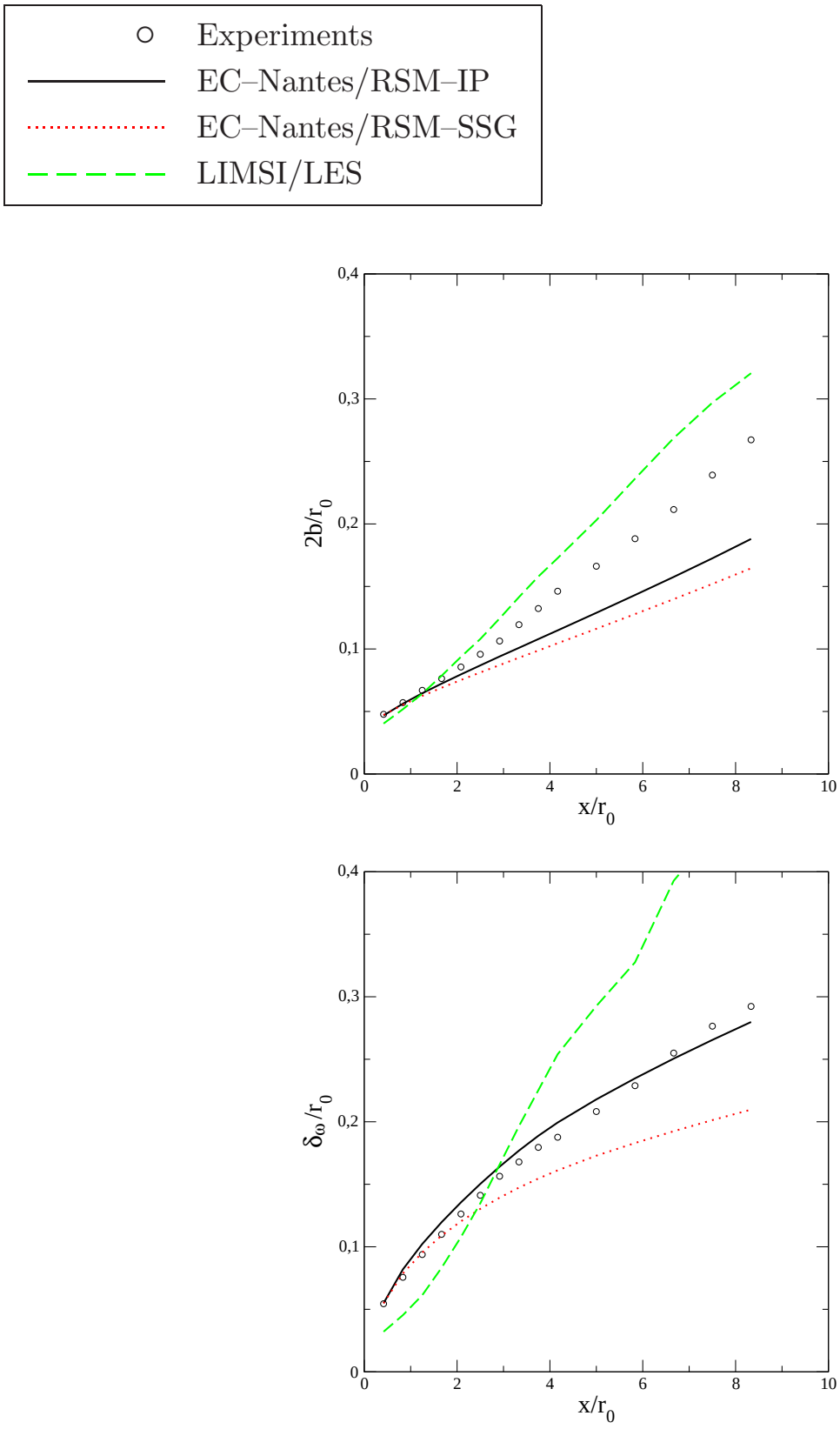

Figure 2: Reynolds stress models and LES. Downstream evolution of $2b$ and δ_ω.

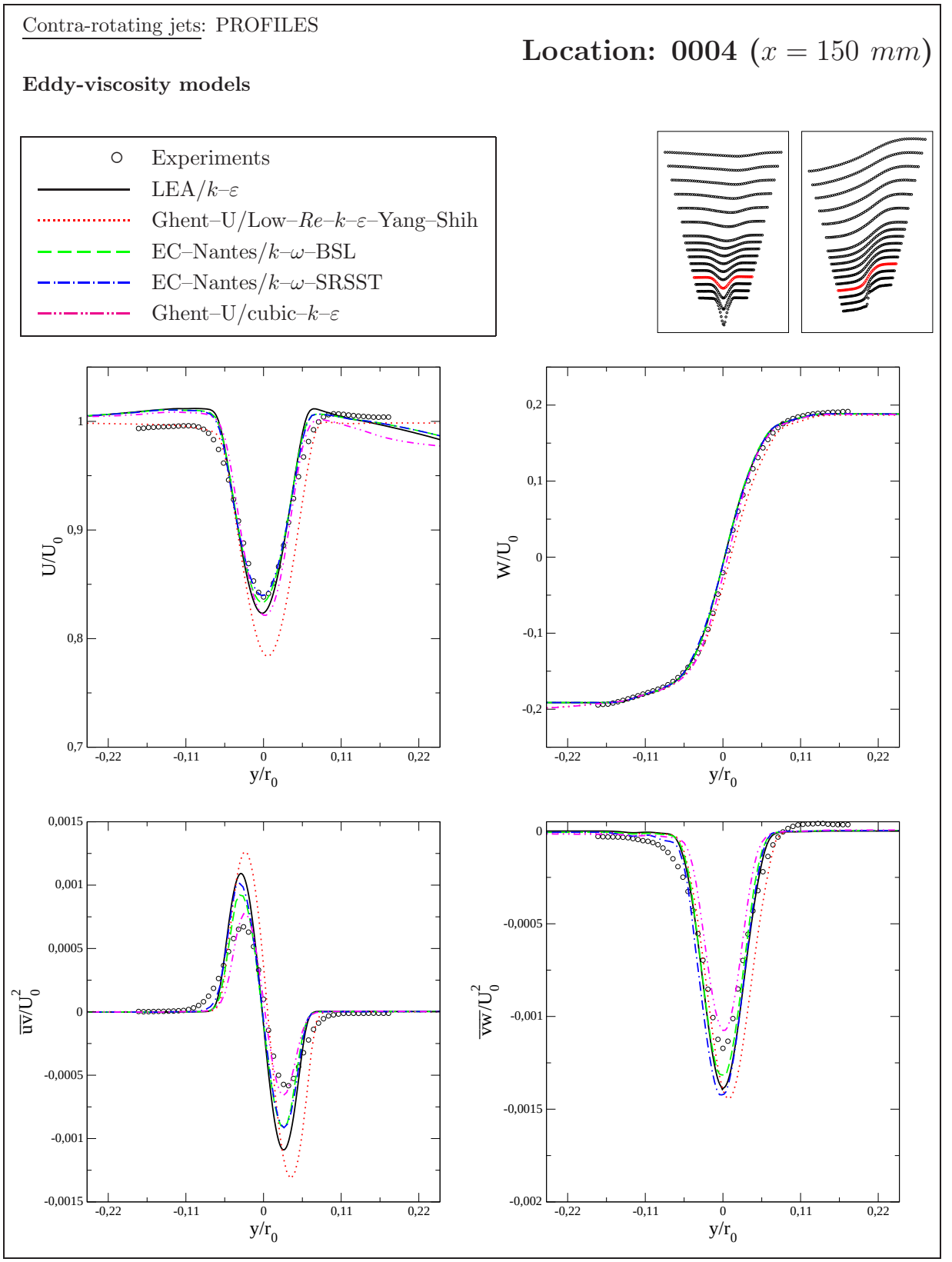

Figure 3: Eddy-viscosity models. Profiles at $x/r_0 = 1.25$.

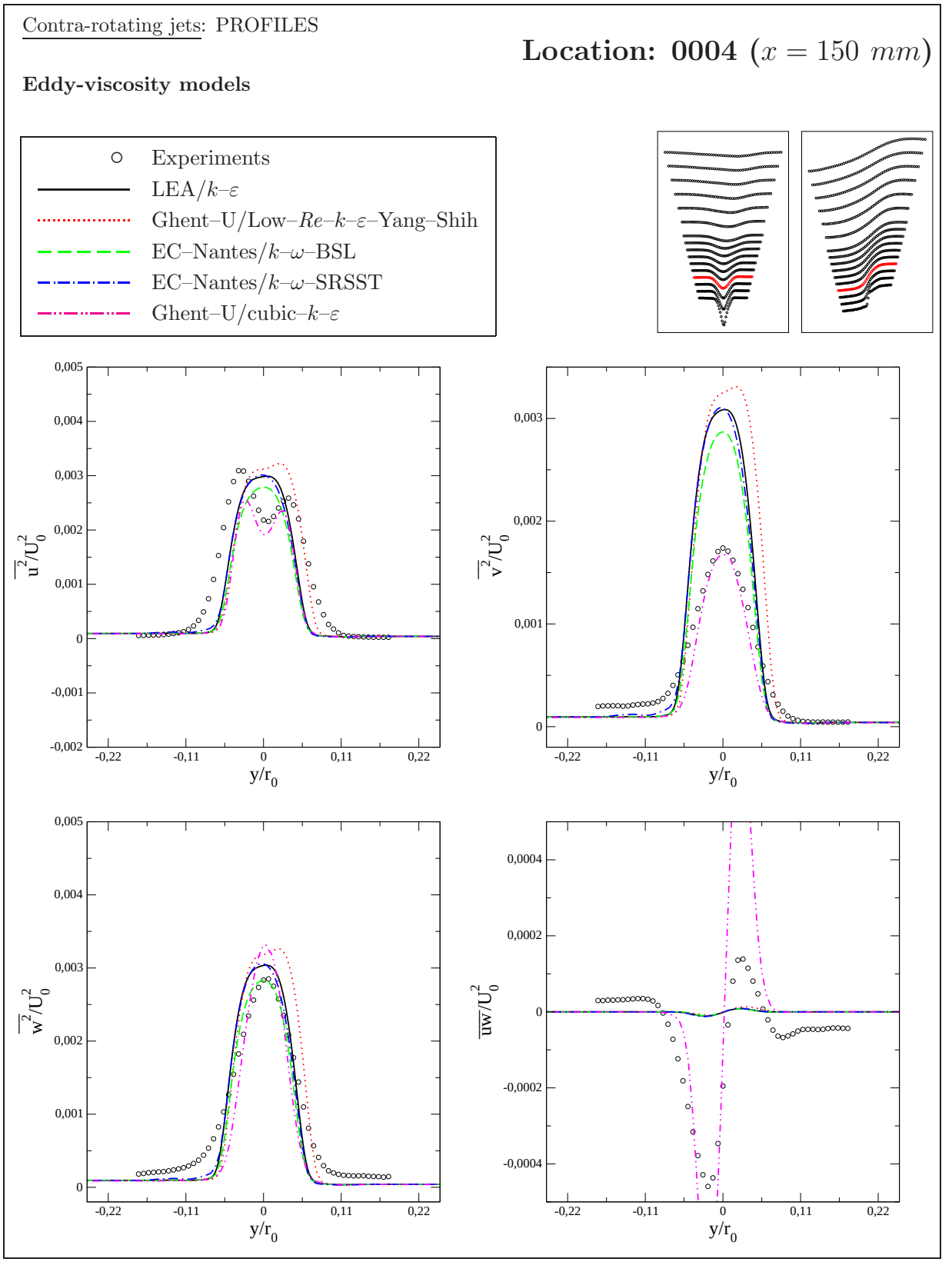

Figure 4: Eddy-viscosity models. Profiles at $x/r_0 = 1.25$ (continued).

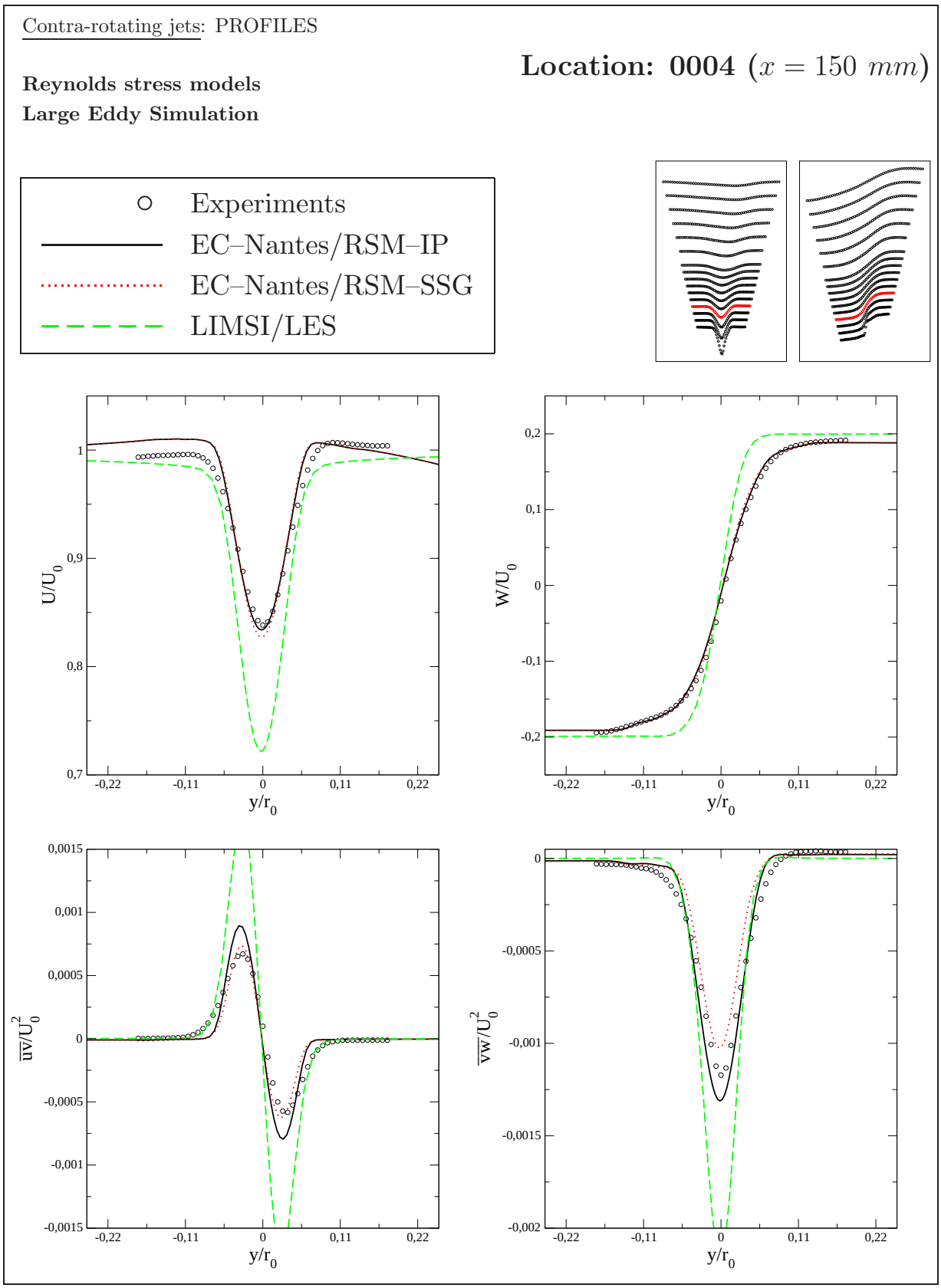

Figure 5: Reynolds stress models and LES. Profiles at $x/r_0 = 1.25$.

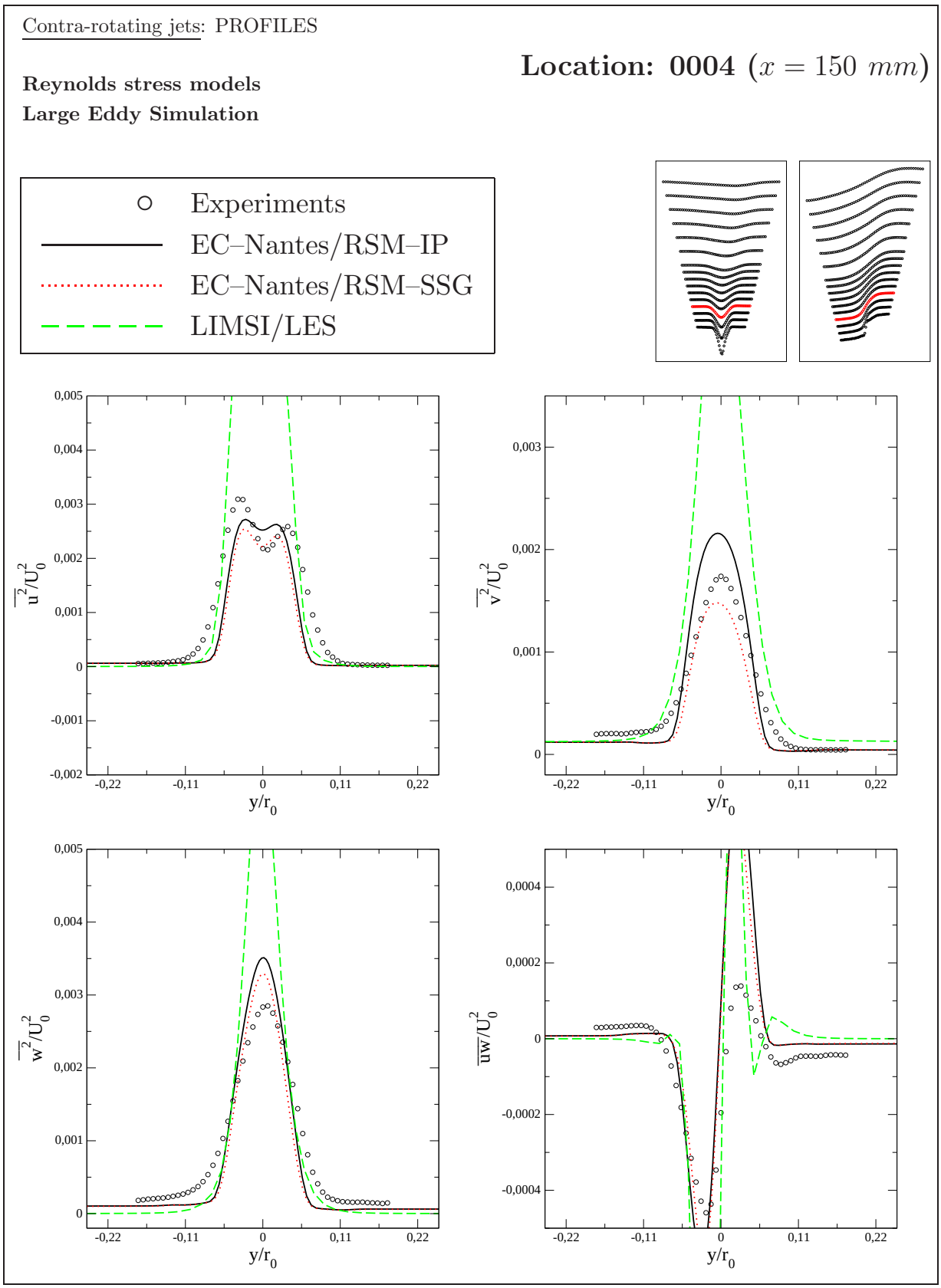

Figure 6: Reynolds stress models and LES. Profiles at $x/r_0 = 1.25$ (continued).

Contra-rotating jets: PROFILES

Location: 0013 ($x = 700\ mm$)

Eddy-viscosity models

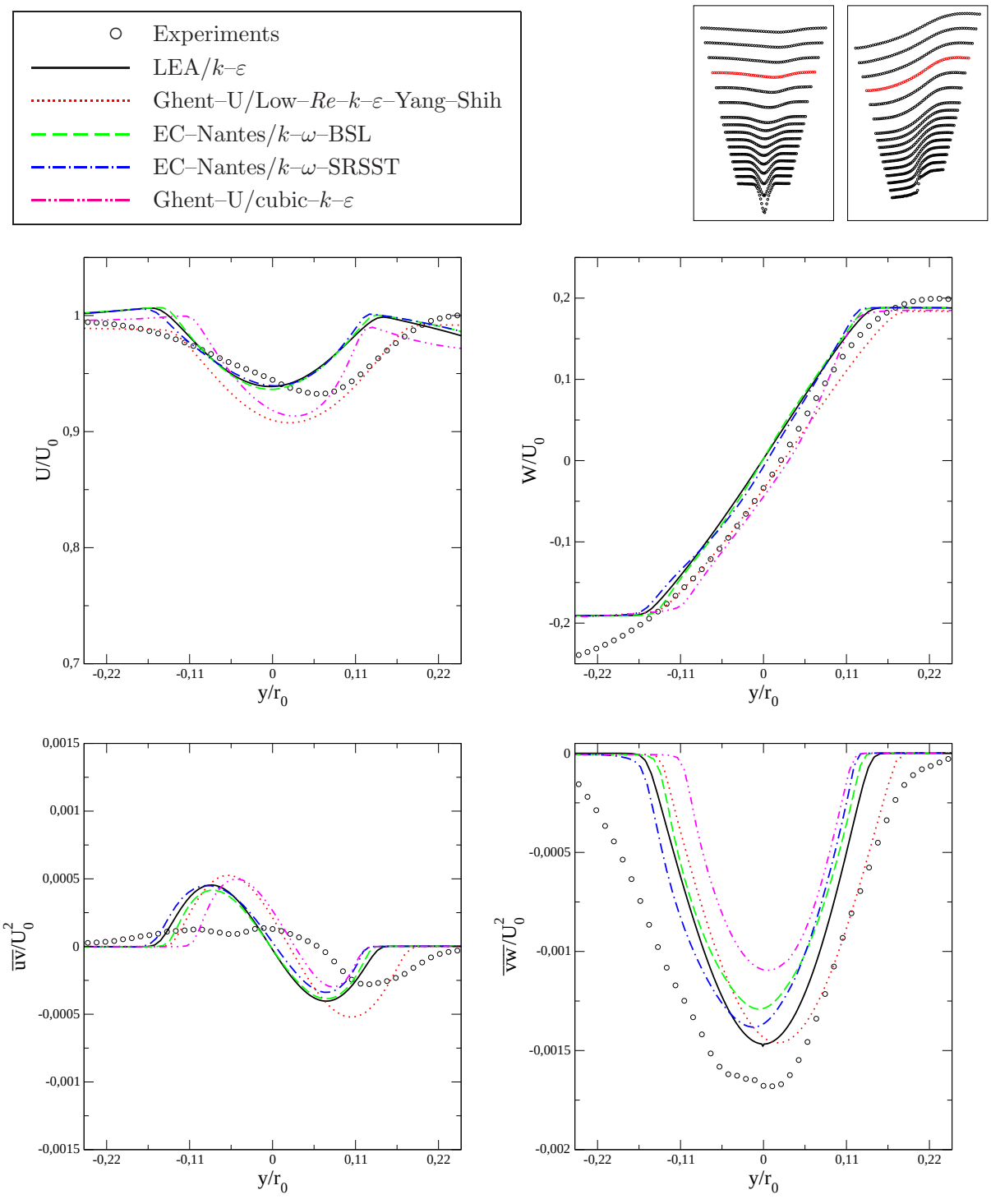

Figure 7: Eddy-viscosity models. Profiles at $x/r_0 = 5.83$.

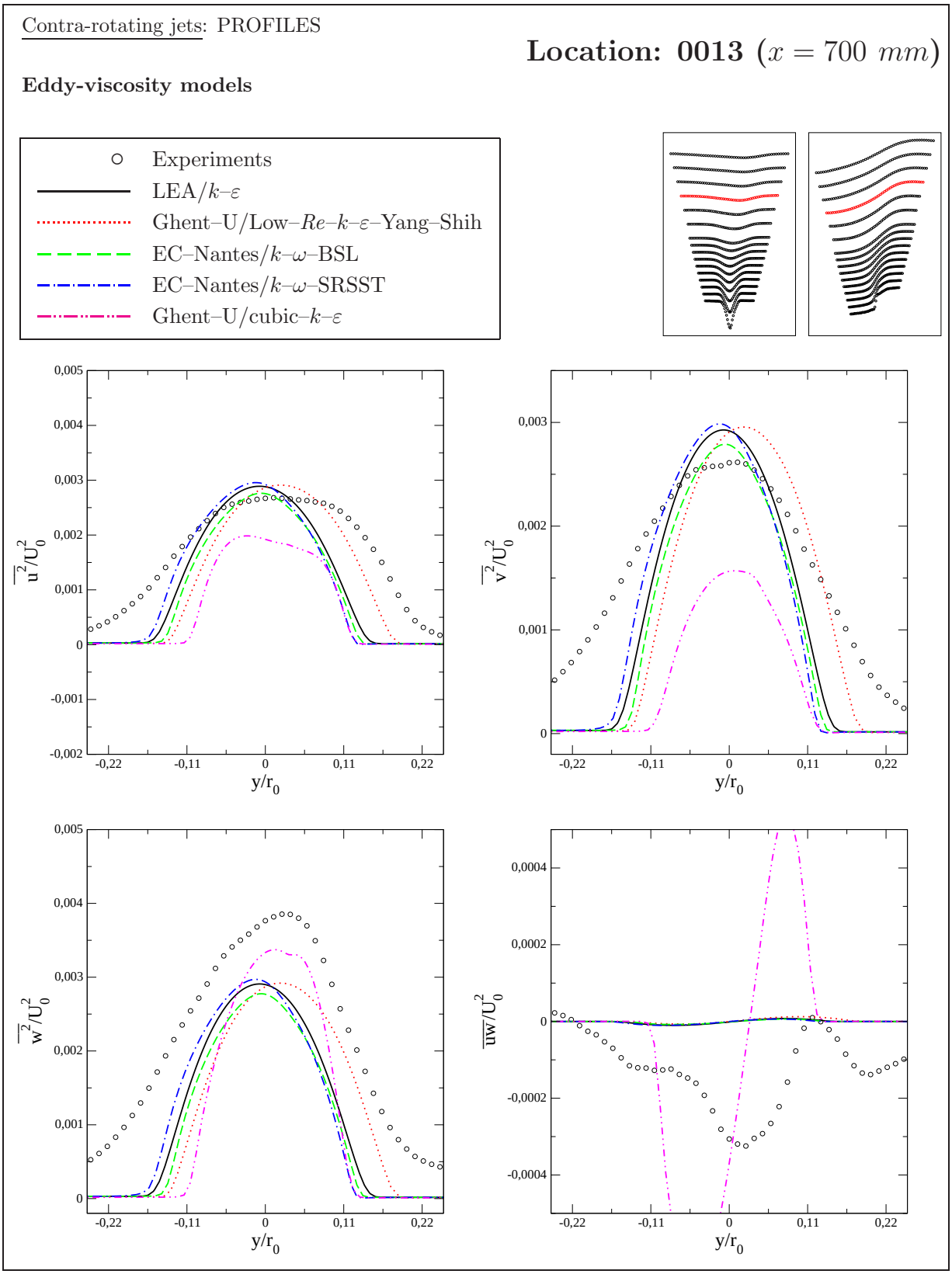

Figure 8: Eddy-viscosity models. Profiles at $x/r_0 = 5.83$ (continued).

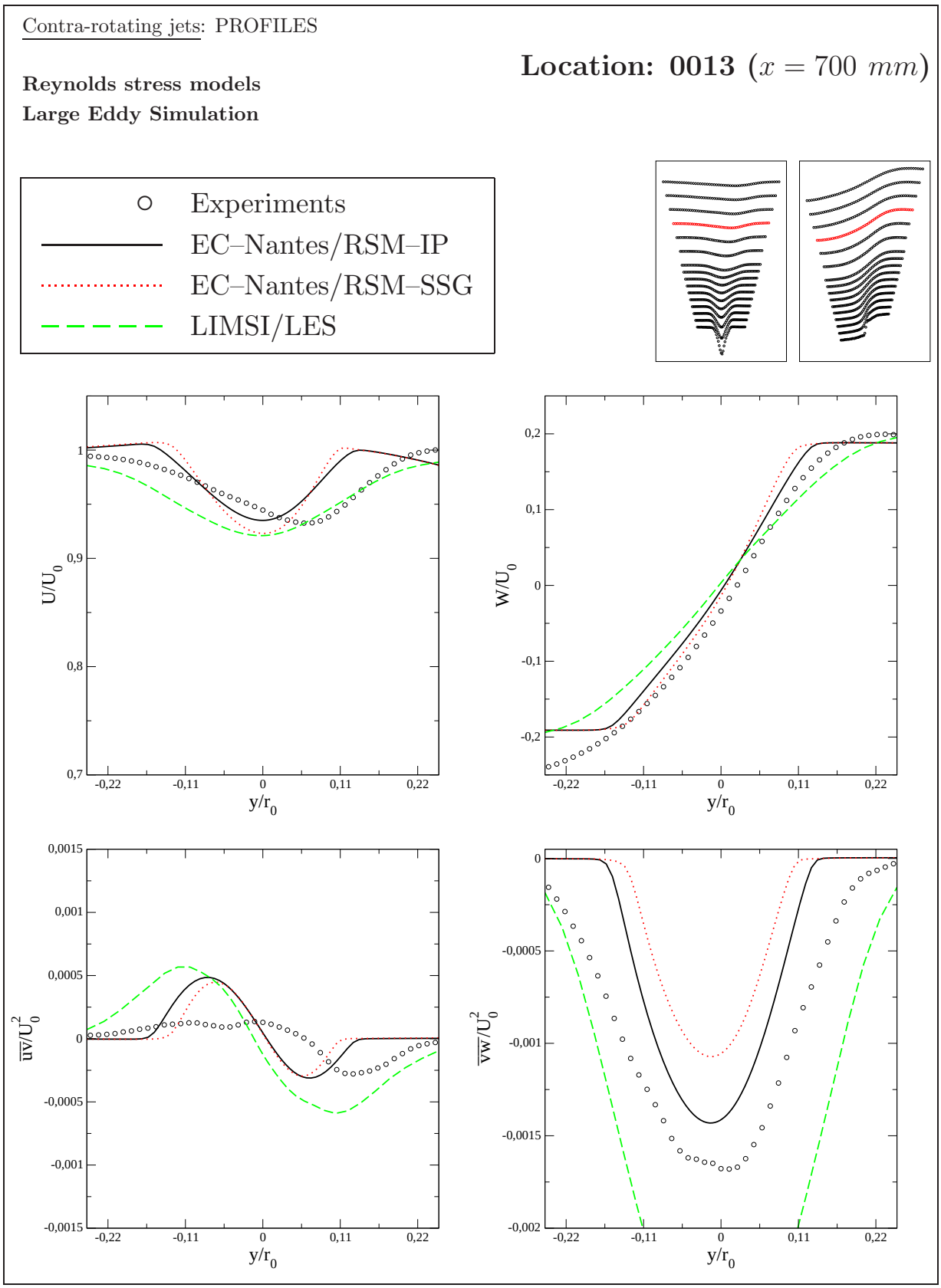

Figure 9: Reynolds stress models and LES. Profiles at $x/r_0 = 5.83$.

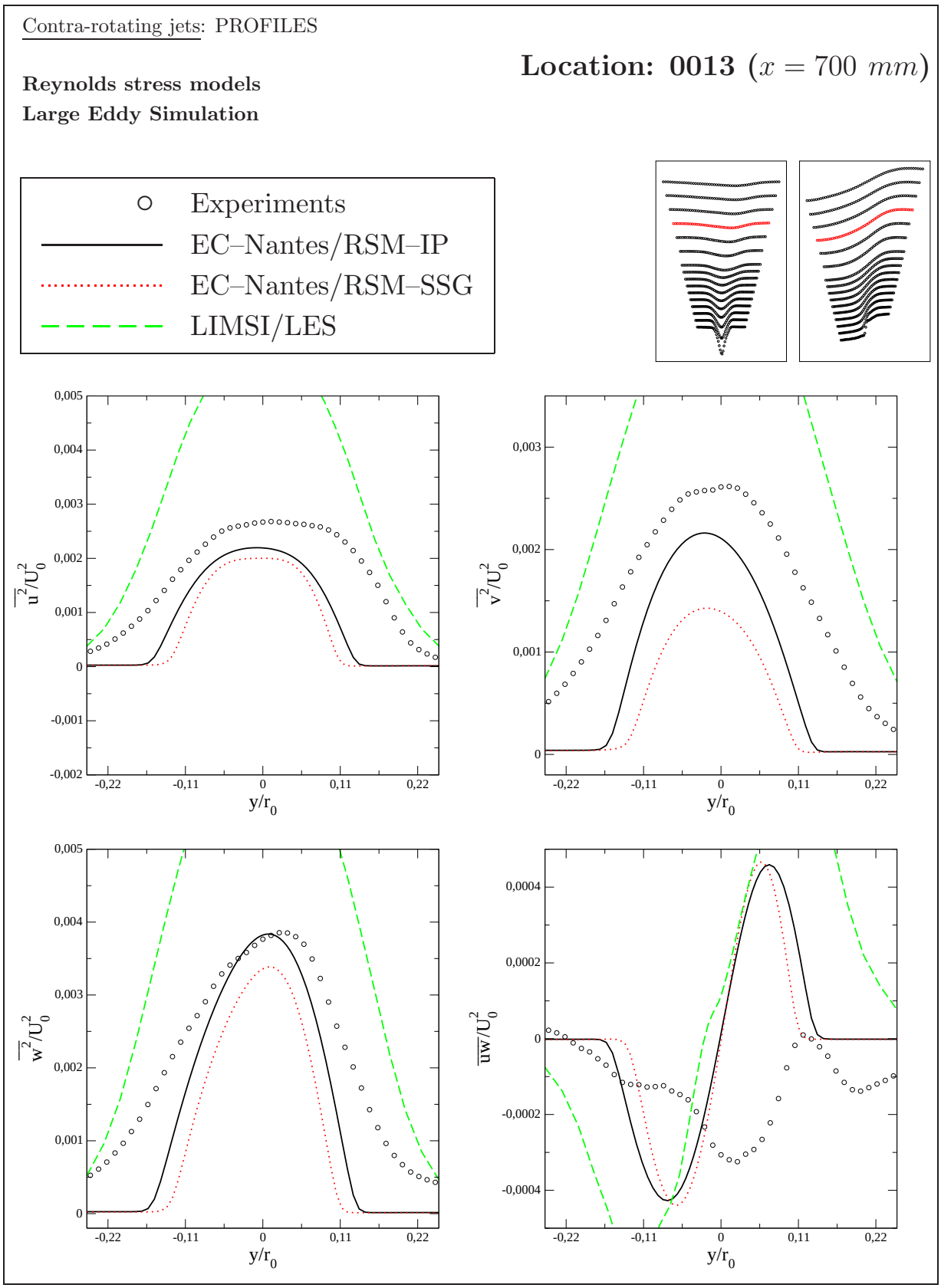

Figure 10: Reynolds stress models and LES. Profiles at $x/r_0 = 5.83$ (continued).

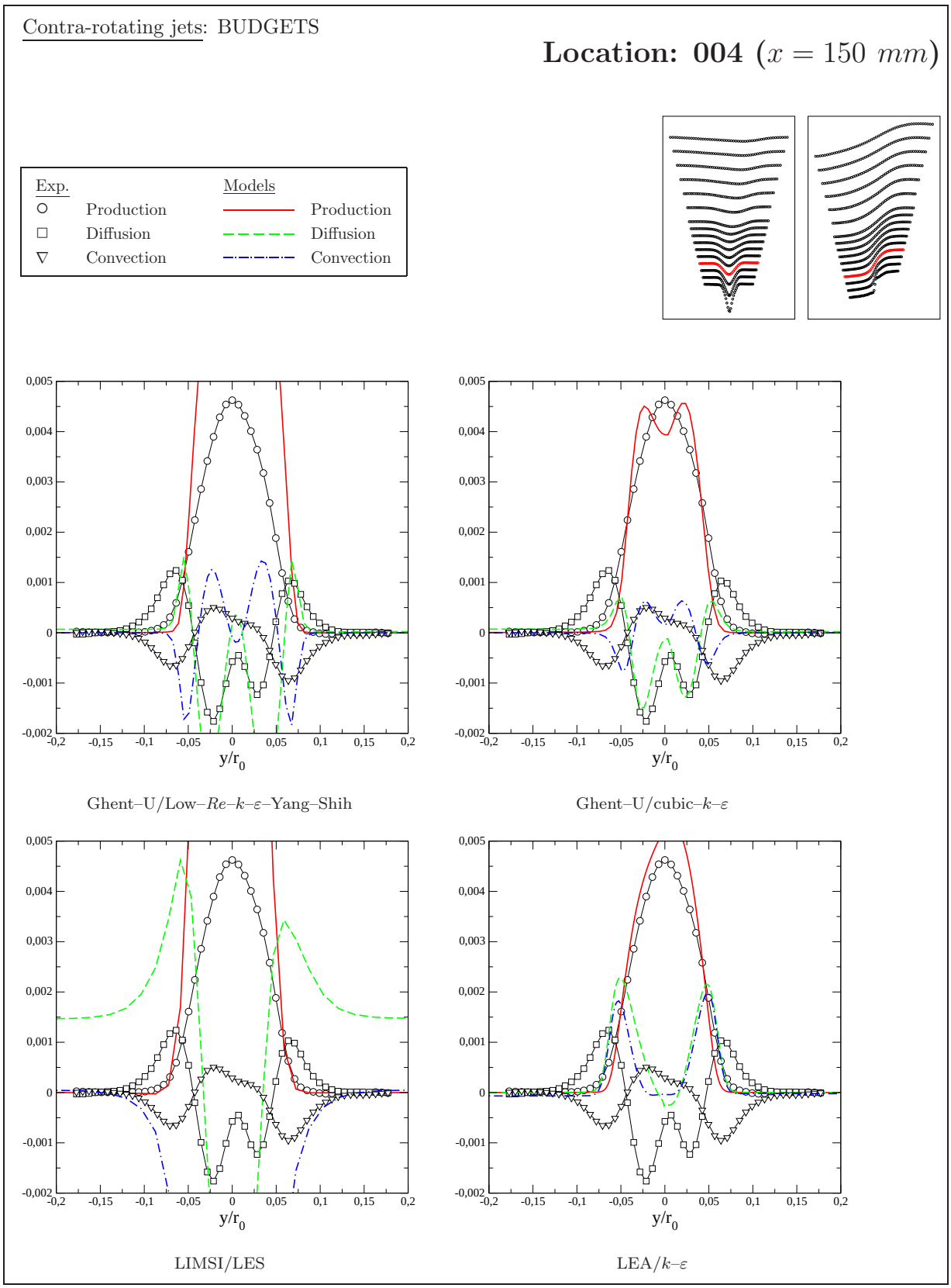

Figure 11: Budget of k (except dissipation) at $x/r_0 = 1.25$.

Contra-rotating jets: BUDGETS

Location: 011 ($x = 500\ mm$)

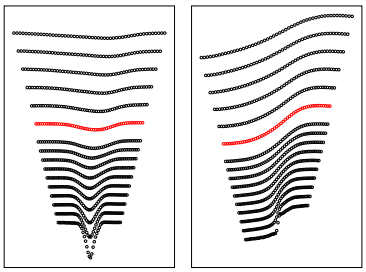

Exp.		Models	
○	Production	———	Production
□	Diffusion	– – –	Diffusion
▽	Convection	–·–·–	Convection

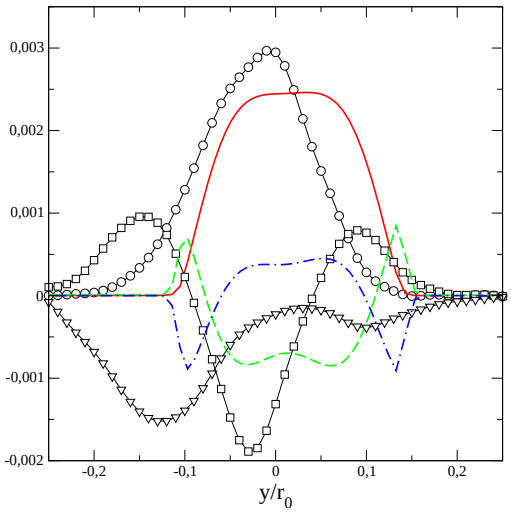

Ghent–U/Low–Re–k–ε–Yang–Shih

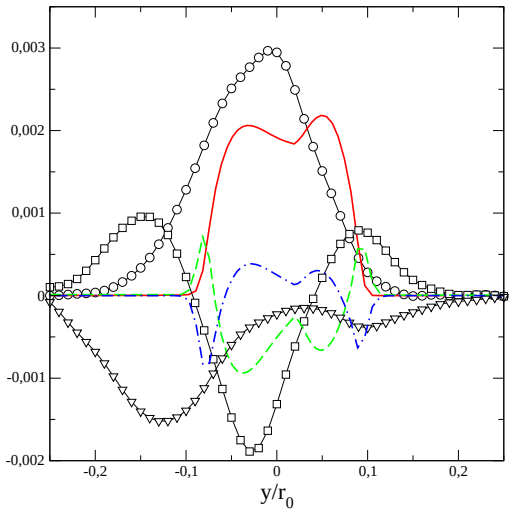

Ghent–U/cubic–k–ε

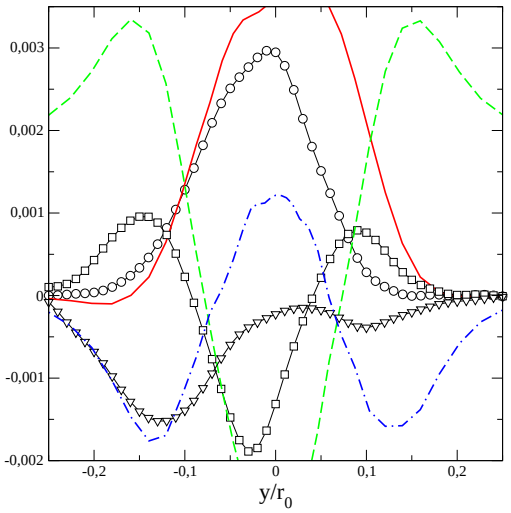

LIMSI/LES

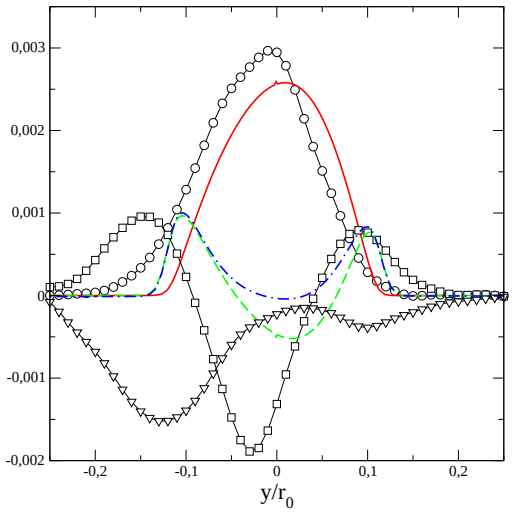

LEA/k–ε

Figure 12: Budget of k (except dissipation) at $x/r_0 = 4.17$.

Contra-rotating jets: WAKE WIDTH AND MIXING LAYER VORTICITY THICKNESS

Analysis of the influence of the inlet condition for V Ghent U. and LEA

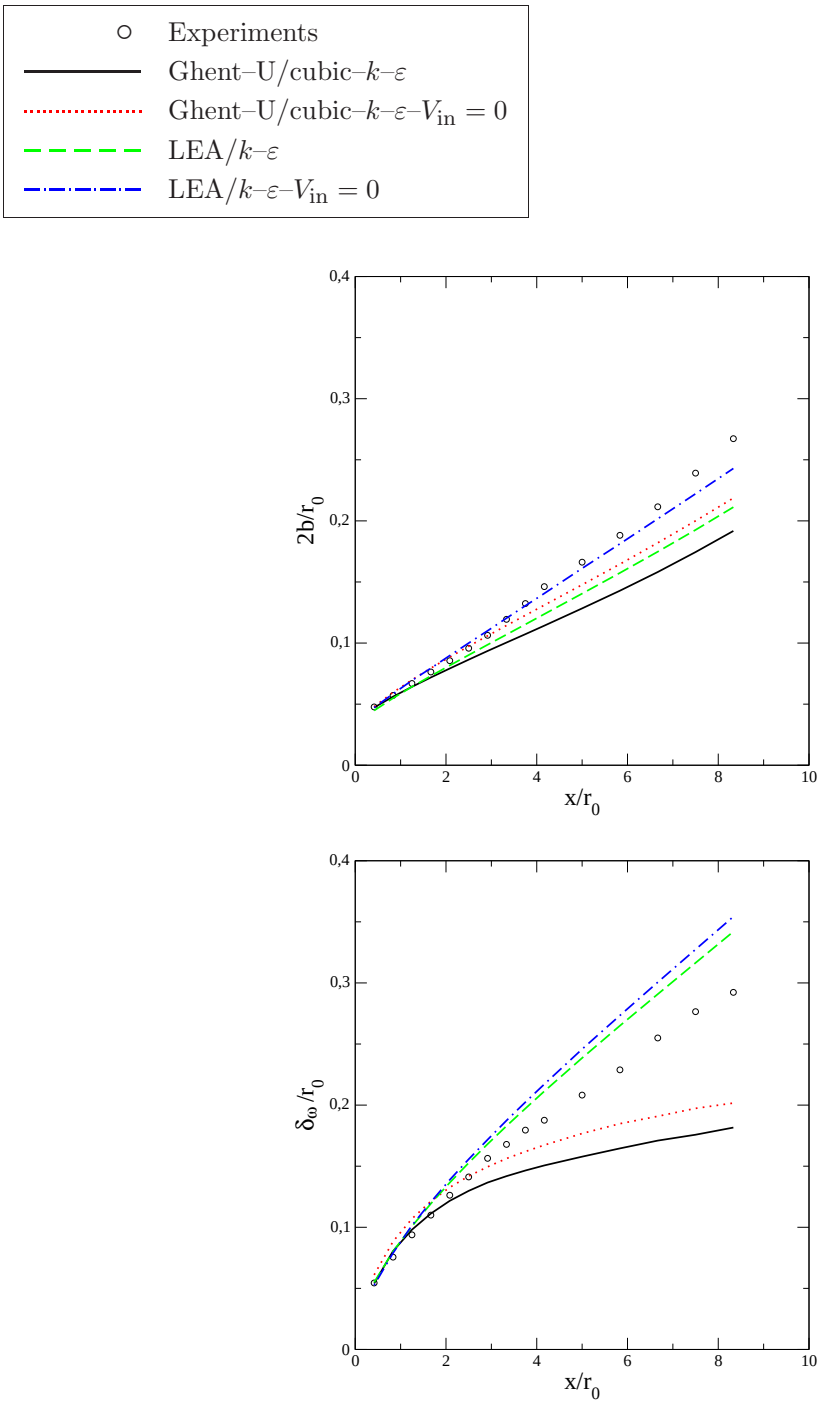

Figure 13: Influence of the inlet condition for V. Downstream evolution of $2b$ and δ_ω.

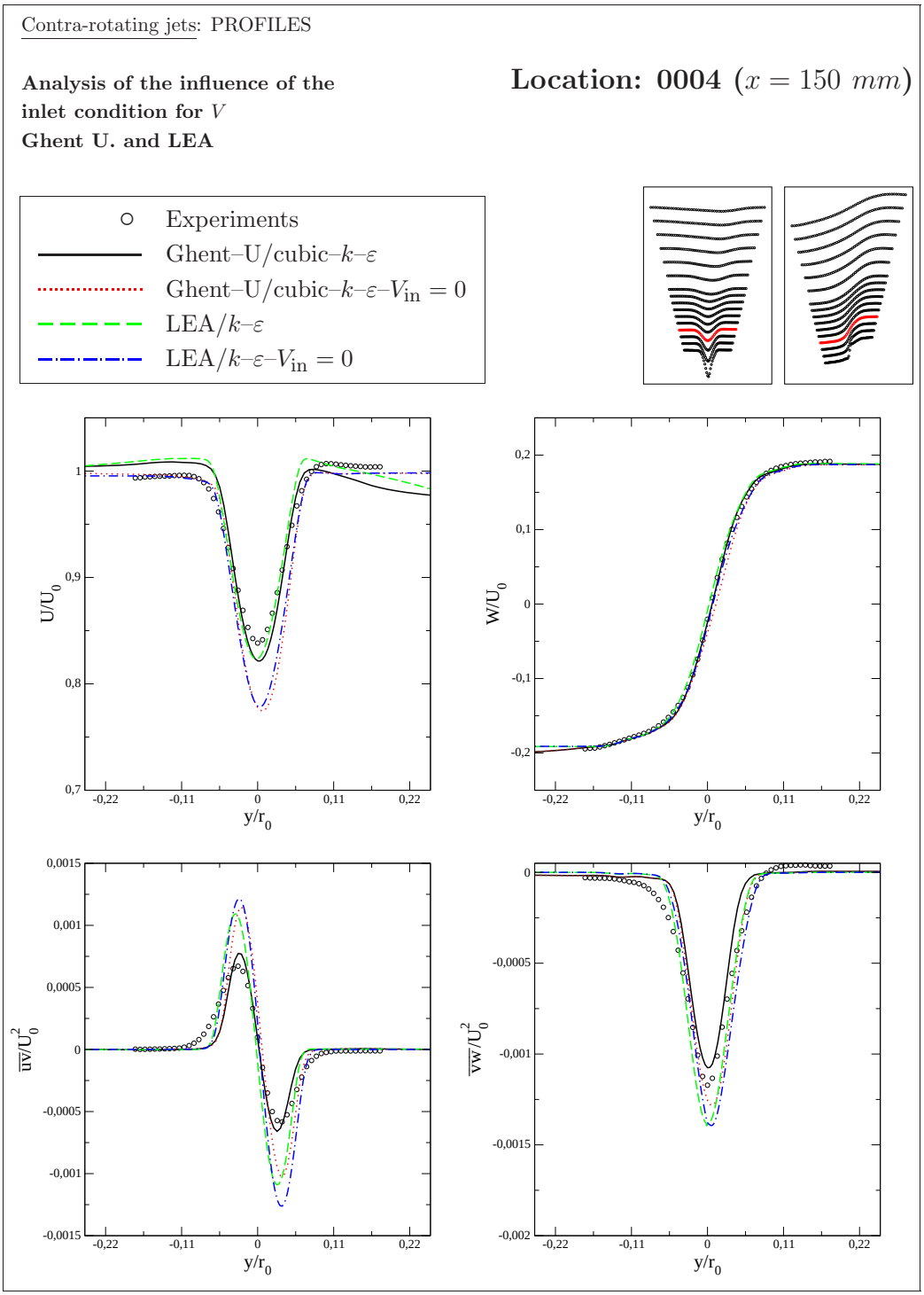

Figure 14: Influence of the inlet condition for V. Profiles at $x/r_0 = 1.25$.

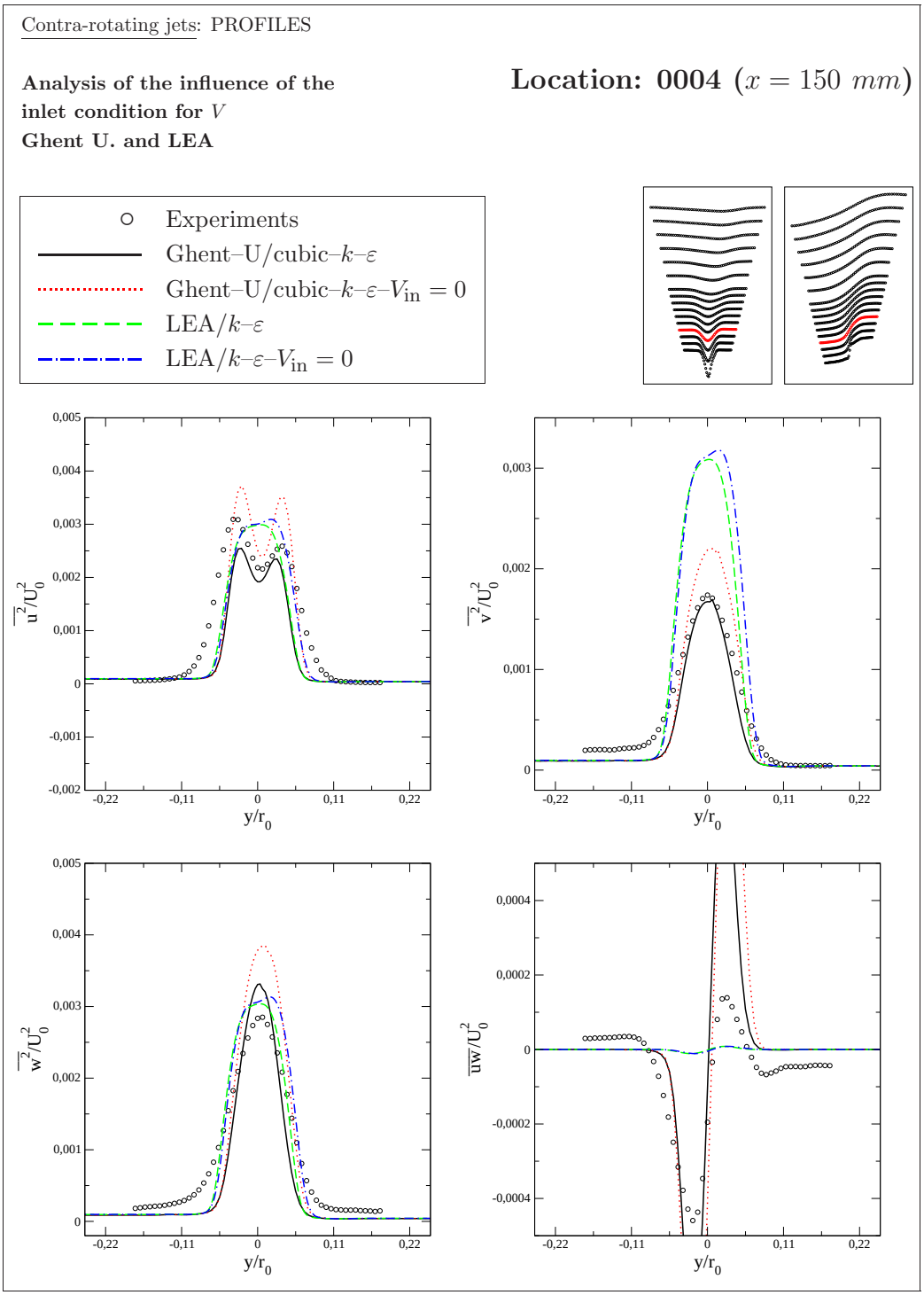

Figure 15: Influence of the inlet condition for V. Profiles at $x/r_0 = 1.25$ (continued).

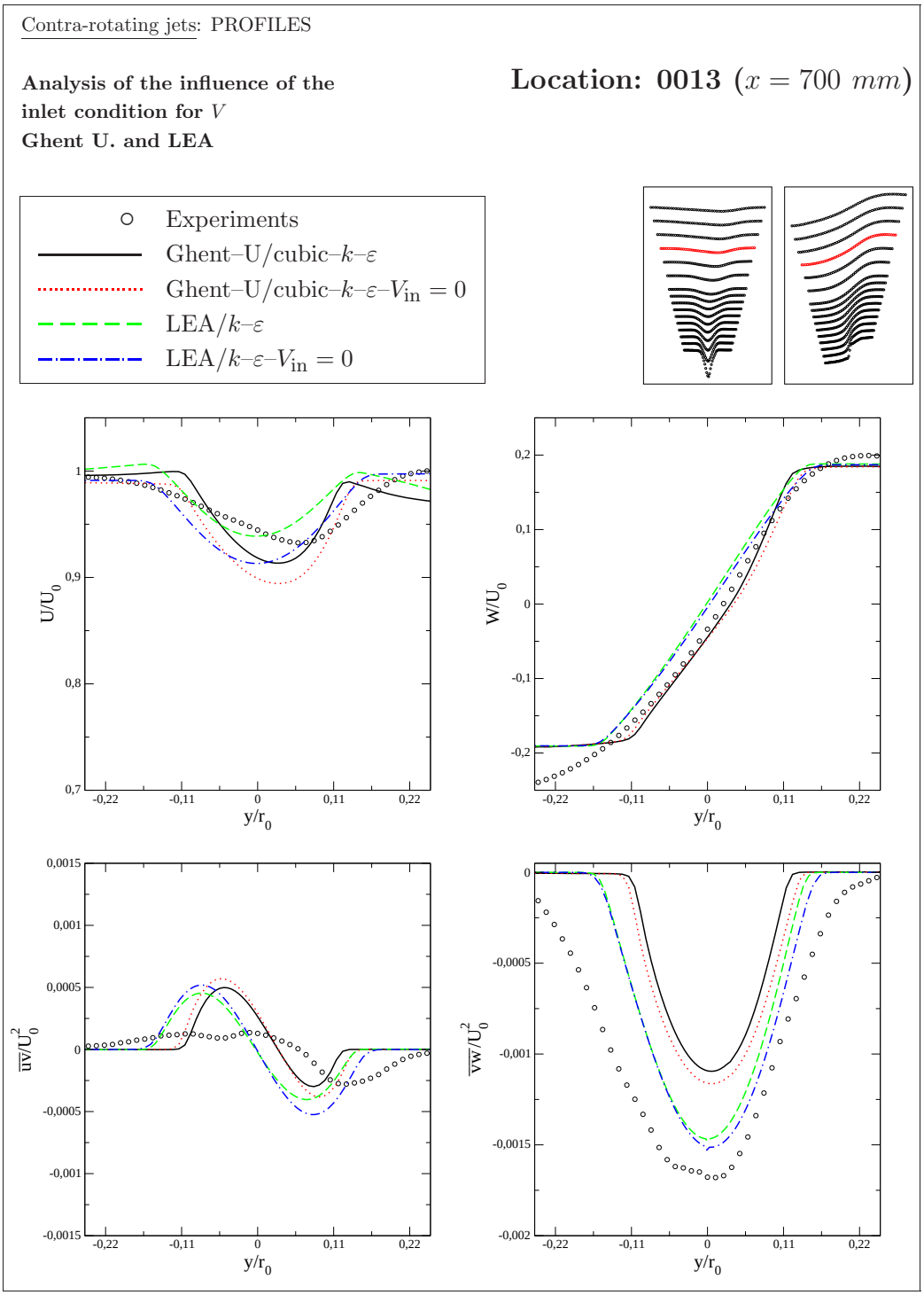

Figure 16: Influence of the inlet condition for V. Profiles at $x/r_0 = 5.83$.

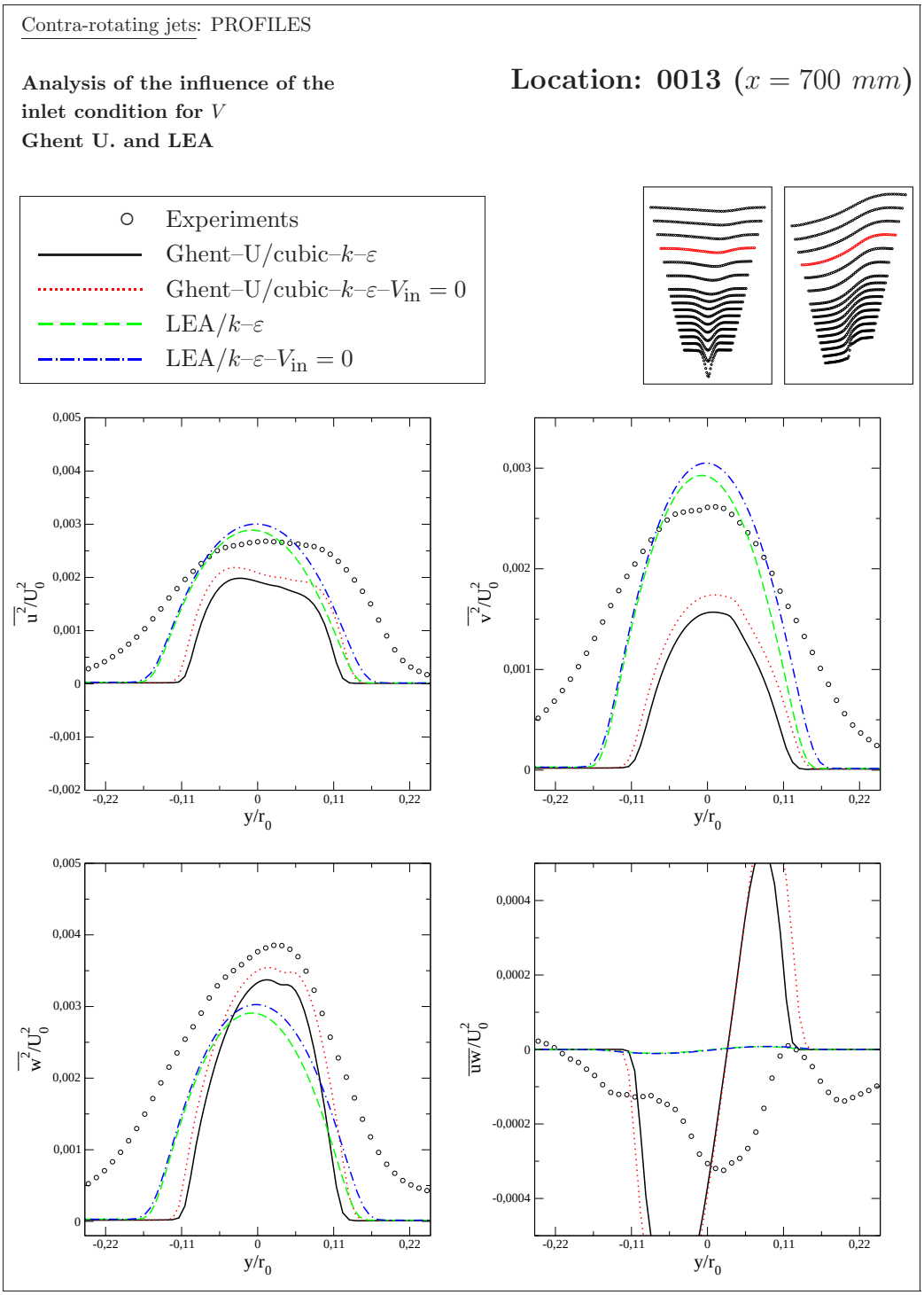

Figure 17: Influence of the inlet condition for V. Profiles at $x/r_0 = 5.83$ (continued).

Case 10.1

Articles written by the participants

Contribution to test case 10.1

G.B. Deng & M. Visonneau
Laboratoire de Mécanique des Fluides, Ecole Centrale de Nantes
1 Rue de la Noë, B.P. 92101, 44321 Nantes Cedex 3, France
E-Mail: Ganbo.Deng@ec-nantes.fr

Introduction

One of the principal goal of the present test case is to study the influence of rotation on the mixing layer. It is well known that the conventional linear eddy-viscosity models are unable to take adequately into account the effect of rotation. Considerable efforts have been devoted during the past three decades to develop more advanced models. Reynolds stress models, cubic nonlinear models and rotation sensitive linear eddy-viscosity closures are among the most representative. The main object of the present work is to compare the performance of Reynolds stress model and rotation sensitive linear eddy-viscosity model for the present configuration.

Turbulence models

The first turbulence model selected for the present study is a rotation sensitive linear eddy-viscosity model based on the k-ω SST model proposed by Menter [1]. It contains a rotation and curvature correction proposed by Hellsten [2] which is further retuned by the authors for swirling flow [3]. It is based on the Richardson number defined by

$$R_i = max\left[max\left(2, \frac{|\Omega_{ij}|}{|S_{ij}|}\right)\left(max(2, \frac{|\Omega_{ij}|}{|S_{ij}|}) - 1\right), -\frac{0.8}{C_{sr}}\right]$$

The destruction term in the ω equation $\beta\rho\omega^2$ is multiplied by the swirling correction function computed by

$$F_{sr} = \frac{1}{1 + C_{sr}R_i}$$

Where $C_{sr} = 2.75$, $|S_{ij}| = \sqrt{2S_{ij}S_{ij}}$, and $|\Omega_{ij}| = \sqrt{2\Omega_{ij}\Omega_{ij}}$, S_{ij} and Ω_{ij} being the strain-rate and the vorticity tensor. The second revision concerns the eddy-viscosity limiter in the SST model. Hellsten [2] discovered that the limiter in the SST model is not rotational invariant, hence unsuitable for rotating flow computation. The revision proposed by Hellsten has been found to be unable to give satisfactory prediction for swirling flow by the authors [3]. In our implementation, the following eddy-viscosity limiter is proposed :

$$\nu_t = min\left(\frac{k}{\omega}, \frac{0.31k}{max(2|S_{12}|, 2|S_{13}|, 2|S_{23}|)}\right)$$

$$\nu_t = min\left(\nu_t, \frac{\frac{2}{3}k}{2S_{ii}}\right)$$

if $S_{ii} > 0$ (with no summation on i). The second limiter that does not exist in the original SST model ensures the positiveness of the normal stress. The first eddy-viscosity limiter should be activated only on wall boundary layer. No mechanism has been designed in the present implementation to prevent the activation of the eddy-viscosity limiter in the free shear layer. It should be employed with caution. In the following, the SST model with the above mentionned revision will be referred as SRSST model.

The second selected turbulence model is a Reynolds stress model. Two different pressure-strain models have been used, namely the IP [4] and the SSG models [5]. Details concerning the Reynolds stress models can be found in the references and will not be repeated here. Finally, Menter's k-ω BSL model [1] is chosen as reference model. In the present configuration, the BSL model should give the same result as the standard k-ϵ model.

Results and discussions

Geometry and flow characteristics are described in the test case instruction for the workshop (http://labo.univ-poitiers.fr/informations-lea/Workshop-Ercoftac-2002) and will not be repeated here. All computations have been performed with the ISIS code developed by our team. It is a finite volume unstructured code for incompressible fluids. Viscous flux is evaluated with second order central difference scheme. Inviscid flux is computed with 50% second order upwind interpolation and 50% second order downwind interpolation. For rotationally symmetric configurations, computation is performed in a 3D domain with one control volume in the circumferential direction where rotationally symmetric condition is applied. Results submitted to the workshop were obtained on a 151x110x2 grid. Grid independency is ensured by a 251x169x2 fine grid solution.

As requested by the workshop, symmetry conditions are applied on both boundaries in the radial direction. Such boundary conditions are not physical in an axisymmetric configuration. With the ISIS code, this treatment results in an oscillation of the V velocity component near the boundaries and a decrease of U velocity component approaching the upper boundary as shown in figure 1. Such behavior may have an impact on the accuracy of the numerical computation. Figures 2 to 4 compare the axial velocity profiles for different turbulence models. All tested turbulence models give similar solution. The SRSST model performs slightly better than other models. Results obtained by the RSM-IP model are very similar to that obtained with the BSL model. The SSG model presents no advantage compared with the IP model. Discrepancies observed between the computation and the measurement are quite important. The center of the wake shifts up in the measurement while it stays almost at the same position in the computation. The wake spreads much faster in the measurement than in the computation.

Conclusions

Two coaxial jets with opposite rotation have been computed with four different turbulence models. Models with different sensitivity to rotation give similar prediction, which suggests that the effect of rotation is small. On the other hand, considerable discrepancy is observed between the measurement and the computation. Even uncertainty concerning boundary condition exists in the computation, such discrepancies are more likely due to physical phenomena, such as the interaction between laminar and turbulent flow, which are difficult to simulate with statistical models.

References

[1] F. Menter, "Zonal two-equations $k-\omega$ turbulence models for aerodynamic flows.," *AIAA Paper*, vol. 93-2906, 1993.

[2] A. Hellsten, "Some improvements in Menter's k-ω SST turbulence model," in *29th AIAA Fluid Dynamics Conference*, AIAA-98-2554, 1998.

[3] G. Deng and M. Visonneau, "Implantation et validation du modèlek-ω dans n3s-natur," tech. rep., Rapport de Contrat ECN, 2002.

[4] M. Gibson and B. Launder, "Ground effects on pressure fluctuations in the atmospheric boundary layer," *J. Fluid Mech.*, vol. 86, pp. 491–511, 1978.

[5] C. Speziale, S. Sarkar, and T. Gatski, "Modeling the pressure-strain correlation of turbulence: An invariant dynamical systems approach," *Journal of Fluid Mechanics*, vol. 227, pp. 245–272, 1991.

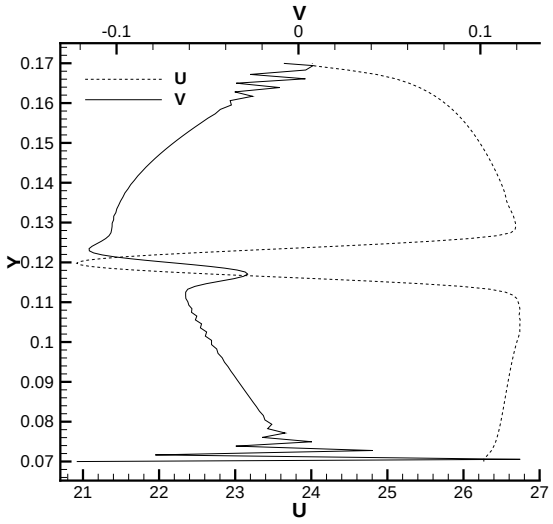

Figure 1: Effect of boundary condition.

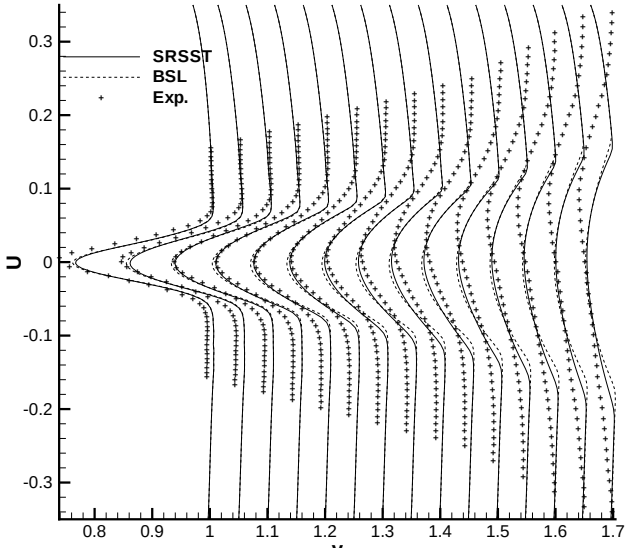

Figure 2: Comparison between BSL model and SRSST model.

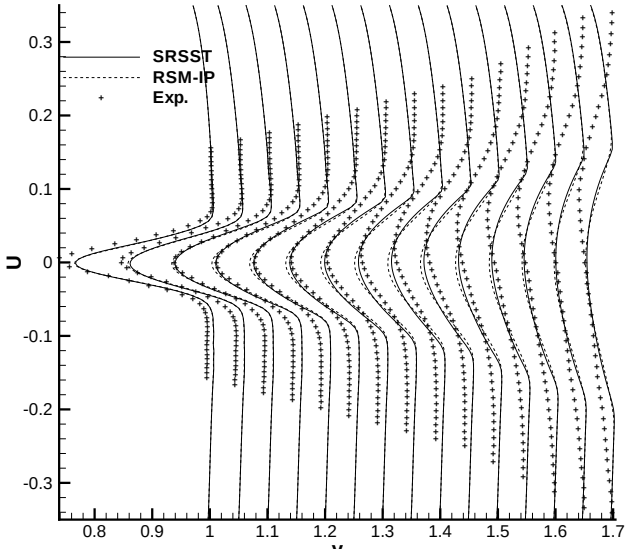

Figure 3: Comparison between RSM-IP model and SRSST model.

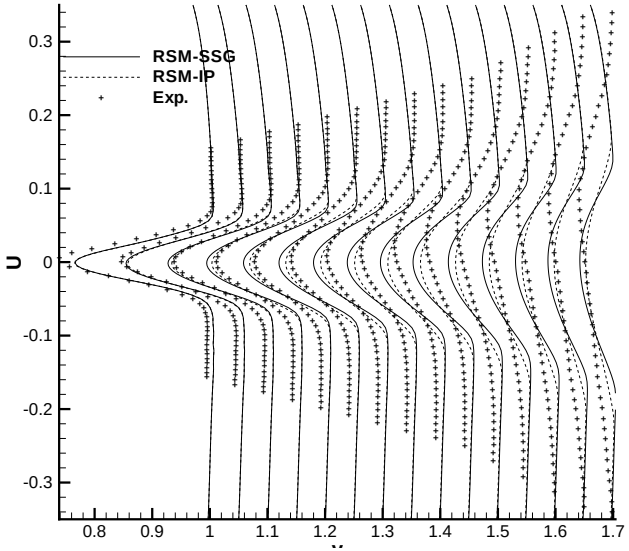

Figure 4: Comparison between RSM-IP model and RSM-SSG model.

Case 10.1: Description of the Cubic Low-Reynolds $k-\varepsilon$ Model, the Grid and the Method

B. Merci[1], C. De Langhe, K. Lodefier and E. Dick

Ghent University - Dept. of Flow, Heat and Combustion Mechs.
Tel.: +/32/9/264.33.14, Fax: +/32/9/264.35.86, E-mail: Bart.Merci@rug.ac.be
[1] Postdoctoral Fellow of the Fund for Scientific Research - Flanders (Belgium) (FWO-Vlaanderen).

1 Model Description

The model, which is completely described in [1], consists of a new constitutive law for the Reynolds stresses and an improved ε transport equation.

1.1 Constitutive Law

The anisotropy tensor $\overline{\mathbf{a}}$, defined as

$$\overline{a}_{ij} = \frac{\overline{v_i' v_j'}}{\overline{k}} - \frac{2}{3}\delta_{ij} \ , \tag{1}$$

with δ_{ij} the Kronecker delta, is expressed in terms of the dimensionless strain rate tensor ($\mathbf{S}\tau_t$) and vorticity tensor ($\mathbf{\Omega}\tau_t$), where τ_t is the turbulence time scale (defined in eq. (4)).

The tensors $\mathbf{S}$ and $\mathbf{\Omega}$ are:

$$S_{ij} = \frac{1}{2}(\frac{\partial v_i}{\partial x_j} + \frac{\partial v_j}{\partial x_i}) - \frac{1}{3}\delta_{ij}\frac{\partial v_k}{\partial x_k} \tag{2}$$

and

$$\Omega_{ij} = \frac{1}{2}(\frac{\partial v_i}{\partial x_j} - \frac{\partial v_j}{\partial x_i}) \ . \tag{3}$$

The turbulence time scale τ_t is defined as:

$$\tau_t = \frac{k}{\varepsilon} + \sqrt{\frac{\mu}{\rho\varepsilon}} \ . \tag{4}$$

Two following tensor invariants are used:

$$S = \sqrt{2 S_{ij} S_{ij}} \ , \ \Omega = \sqrt{2\Omega_{ij}\Omega_{ij}} \ , \ \eta = \tau_t (S^2 + \Omega^2)^{1/2} \ . \tag{5}$$

The constitutive law is given by:

$$\begin{aligned} a_{ij} = & - 2c_\mu f_\mu \tau_t S_{ij} \\ & + q_1 \tau_t^2 (S_{ik}S_{kj} - \frac{1}{3}\delta_{ij} S_{lm} S_{ml}) \\ & + (q_2 + q_1/6)\tau_t^2 (\Omega_{ik}S_{kj} - S_{ik}\Omega_{kj}) \\ & + \tau_t^3 (c_1 S_{mn} S_{nm} + c_2 \Omega_{mn}\Omega_{nm}) S_{ij} \\ & + c_3 \tau_t^3 (\Omega_{ik}S_{kl}S_{lj} - S_{ik}S_{kl}\Omega_{lj}) \ . \end{aligned} \tag{6}$$

The expression for c_μ is:

$$c_\mu = \frac{1}{A_1 + A_s \eta} \ , \tag{7}$$

with

$$A_1 = 4 \ , \ A_s = \sqrt{3} cos\phi \tag{8}$$

$$\phi = \frac{1}{3} arccos(\sqrt{6}W) \ , \ W = 2^{1.5}\frac{S_{ij}S_{jk}S_{ki}}{S^3} \ . \tag{9}$$

The damping function f_μ is defined as:

$$f_\mu = 1. - exp(-6\ 10^{-2}\sqrt{R_y} - 2\ 10^{-4} R_y^{1.5} - 2\ 10^{-8} R_y^4) \ , \tag{10}$$

with $R_y = \frac{\rho\sqrt{k}y}{\mu}$, y being the normal distance from the nearest solid boundary.

The coefficients q_1 and q_2 are:

$$\begin{cases} q_1 = (7 + 2.1\eta + 4.2\ 10^{-3}\eta^3)^{-1} \\ q_2 = (10 + 3.6\eta + 1\ 10^{-2}\eta^3)^{-1} \end{cases} \tag{11}$$

The coefficients c_i are:

$$\begin{cases} S \geq \Omega : c_1 = c_2 = -min(40 c_\mu^4 ; 0.15) \\ S < \Omega : c_1 = c_2 = -min(min(600 c_\mu^4 ; 0.15); 4 f_\mu c_\mu / (\Omega^2\tau_t^2 - S^2\tau_t^2)) \end{cases} \tag{12}$$

and

$$c_3 = -2c_1 \ . \tag{13}$$

1.2 Dissipation rate equation

The transport equation for k is standard:

$$\frac{\partial}{\partial t}(\rho k) + \frac{\partial}{\partial x_j}(\rho k v_j) = \tau_{ij}^T \frac{\partial v_j}{\partial x_i} - \rho\varepsilon + \frac{\partial}{\partial x_j}[(\mu + \frac{\mu_t}{\sigma_k})\frac{\partial k}{\partial x_j}] \ , \tag{14}$$

with the eddy viscosity $\mu_t - \rho c_\mu f_\mu k \tau_t$. The transport equation for the dissipation rate is original[1]. It is a combination of the equation in [2] and the one in [3]:

$$\frac{\partial}{\partial t}(\rho\varepsilon) + \frac{\partial}{\partial x_j}(\rho\varepsilon v_j) = (1 - f_{R_y}) c_{\varepsilon 1} \frac{\tau_{ij}^T \frac{\partial v_j}{\partial x_i}}{\tau_t} + f_{R_y} C_1 S \rho\varepsilon - c_{\varepsilon 2} f_2 \rho\varepsilon \frac{1}{\tau_t} + \frac{\partial}{\partial x_j}[(\mu + \frac{\mu_t}{\sigma_\varepsilon})\frac{\partial\varepsilon}{\partial x_j}] + E \ . \tag{15}$$

The blending function f_{R_y} goes from zero to one as R_y goes from 1000 to 2000:

$$f_{R_y} = \frac{1}{2} + \frac{1}{2} sin(\frac{\pi}{2} min[max(\frac{R_y}{500} - 3; -1); 1]) \ . \tag{16}$$

Due to the blending, good results are obtained for free shear flows (in particular, the plane jet - round jet anomaly is resolved), as well as for wall-dominated flows. The model parameters are as follows:

$$c_{\varepsilon 1} = 1.44 \ , \ C_1 = max(0.43; \frac{Sk/\varepsilon}{5 + Sk/\varepsilon}) \ , \tag{17}$$

$$c_{\varepsilon 2} = max(1.83 + \frac{0.075\Omega\tau_t}{1 + S^2\tau_t^2}; C_2 f_{R_y}) \ ; C_2 = 1.9 \tag{18}$$

$$f_2 = 1 - 0.22 exp(-\frac{Re_T^2}{36}) \ , \ Re_t = \frac{\rho k \tau_t}{\mu} \ , \ \sigma_\varepsilon = 1.2 \ . \tag{19}$$

The source term E has been determined from the standard $k-\omega$ model:

$$E = -1.8(1 - f_\mu)(\mu + \frac{\mu_t}{\sigma_\varepsilon})\frac{\partial k}{\partial x_i}\frac{\partial \tau_t^{-1}}{\partial x_i} \ . \tag{20}$$

2 Grid Description

The structured computational grid consists of 101×81 grid nodes. Stretching is applied in both directions, with grid refinement in the mixing layer and towards the inlet of the computational domain.

3 Method Description

A finite volume method is used. The scheme is a second-order AUSM-like discretization, with a dissipation term in the mass equation for stability reasons, as described in [4] and [5]. The method contains preconditioning and multistage (pseudo-)time stepping towards the steady state solution, with four stages.

The boundary conditions are as described on the web. At the inlet boundary, all quantities are imposed, except for static pressure, which is extrapolated from the flow field. At the outlet boundary, static pressure is imposed and zero axial derivatives are used for all other quantities.

An important remark, however, is that it was found that the influence of the radial velocity component at the inlet is not small, although this velocity component itself is small. Therefore, results have been submitted with inlet V = 0 and with inlet V as in the first data profile.

References

[1] Merci, B. and Dick, E., 'Predictive Capabilities of an Improved Cubic $k-\varepsilon$ Model for Inert Steady Flows', *Flow, Turbulence and Combustion* (in press).

[2] Merci, B., De Langhe, C., Vierendeels, J. and Dick, E., 'A Quasi-Realizable Cubic Low-Reynolds Eddy-Viscosity Turbulence Model with a New Dissipation Rate Equation', *Flow, Turbulence and Combustion*, 66(2):133–157, 2001.

[3] Shih, T.H., Liou, W.W., Shabbir, A., Yang, Z. and Zhu, J., 'A New $k-\varepsilon$ Eddy Viscosity Model for High Reynolds Number Turbulent Flows', *Computers and Fluids*, 24(3):227–238, 1995.

[4] Vierendeels, J., Merci, B. and Dick, E., 'A Blended AUSM+ Method for All Speeds and All Grid Aspect Ratios', *AIAA Journal*, 39(12):2278–2282, 2001.

[5] Merci, B., Steelant, J., Vierendeels, J., Riemslagh, K. and Dick, E., 'Computational Treatment of Source Terms in Two-Equation Turbulence Models', *AIAA Journal*, 38(11):2085–2093, 2000.

Description of the computations of the case 10.1

S. Pellerin, G. Fournier, T. Goossens
LIMSI-CNRS, UPR 3251, BP 133, 91403 Orsay Cedex, France

Numerical method

Equations and formulation

The incompressible Navier-Stokes equations, using a velocity-vorticity formulation are solved by a finite differences method. The flow considered corresponds to high Reynolds numbers and the Large Eddy Simulation is then chosen. In LES, only the largest eddies are solved and the smallest ones are modeled. Any variable ϕ is splitted into two parts, $\phi = \overline{\phi} + \phi'$ where $\overline{\phi}$ is the resolved or filtered part, and ϕ' the subgrid part, not calculated, but which effects will be taken into account using a subgrid model. The filtered Navier-Stokes equations are given by:

$$\frac{\partial \overline{\omega}}{\partial t} - \nabla \times (\overline{v} \times \overline{\omega}) = -\frac{1}{\mathcal{R}_e} \nabla \times \nabla \times \overline{\omega} + \nabla \times \tau \tag{1}$$

$$\overline{\omega} = \nabla \times \overline{v} \qquad \nabla . \overline{v} = 0 \qquad \tau = \overline{v \times \omega} - \overline{v} \times \overline{\omega} \tag{2}$$

where $\overline{v}$ and $\overline{\omega}$ correspond to the filtered variables. The vector τ represents the subgrid scale contributions and has to be modeled. The vorticity transfer decomposition of Taylor (1932) is used to link the subgrid vector τ to the local filtered vorticity $\overline{\omega}$ as:

$$\tau = -\frac{\nu_t}{\mathcal{R}_e} \nabla \times \overline{\omega} \tag{3}$$

where ν_t is the eddy viscosity.

Subgrid model

The eddy viscosity is modeled using the mixed scale subgrid model (Ta Phuoc, 1994), jointly developed at LIMSI and ONERA. This model balances the macroscopic effects (using the filtered vorticity) and the microscopic ones (using the subgrid kinetic energy k') and is given by:

$$\nu_t = \left((C_S \Delta)^2 \|\overline{\omega}\| \right)^{\alpha} \left(C_B \Delta \sqrt{|k'|} \right)^{1-\alpha} \tag{4}$$

where Δ represents the cutoff length scale related to the grid cell volume.

Discretization and resolution

A staggered M.A.C. grid is used for the spatial discretization. The space derivatives are discretized with second order centered schemes in order to minimize the numerical diffusion. The temporal derivative is evaluated using a second order backward Euler scheme. For stability reasons, the diffusive term is treated implicitly. The convective term is linearized by a second order Adams-Bashforth extrapolation.
The transport equation of the vorticity components can then be solved simultaneously by a coupled algorithm. Moreover, the velocity components are considered as solutions of a Cauchy-Riemann problem, solved using a fractional step method (Lardat, Bertagnolio and Daube, 1997). The velocity $\overline{v}$ and filtered pressure fields can then be solved. The LES code used is vectorized and runs on a NEC-SX5 (IDRIS, Orsay).

Geometry and Grid

We modeled the case of two coaxial jets and more precisely the vicinity of the separating wall position. The domain considered is 3D cartesian and a plane approximation is used for the azimuthal direction. Uniform meshes are chosen for propagation (x) and azimuthal (z) directions. The (y) grid for the radial direction is refined close to the jets interface.
The grid used is $701(x) \times 71(y) \times 84(z)$ i.e. 4.2 million points. The dimensions of the domain are 1050 mm for the propagation direction (x) and 180 mm for the radial direction (y) (from -90 mm to 90 mm, with $y = 0$ located at the interface position). For the azimuthal direction, the length of the domain does not correspond to the entire circumference, but to 1/6 of it, i.e. 60 degrees, for grid size considerations.

Boundary Conditions

The upstream condition corresponds to mean velocities, according to experimental values. A white noise perturbation is superimposed on this condition in order to obtain a correct development of the flow (Pellerin, Dulieu, Tenaud and Ta Phuoc, 2001).
At the outlet surface, a convective transport hypothesis is applied (viscous effects neglected). The vorticity tangential components are calculated using an extrapolation along the characteristics. The outlet propagation velocity $\overline{v_x}$ is deduced from vorticity, taking into account the mass flux conservation over this surface. In the inhomogeneous direction (y), a slip condition is imposed at the lower and upper surfaces. A periodicity condition is used for the spanwise direction (z).

Differences with the experimental configuration

The plane approximation has been used before for computations of an incompressible turbulent 3D mixing layer. For the same experiment in LEA, numerical and experimental results are then in very good agreement (PELLERIN *et al.*, 2001). We have supposed here that this approximation can still be used. For grid size reasons, the z size of the domain is smaller than the total circumference of $2\pi r_0$ inducing probably an influence of the periodic conditions and reducing the rotation effect. An additional term may also be included in the cartesian equations to take into account the rotation, taking care of the velocity-vorticity formulation.
Moreover, the mean profile imposed numerically at the inlet of the domain is computed from experimental values which are the external velocity, the displacement thickness and the form factor. We don't have these values for the azimuthal profile $< w >$ and consequently we impose a profile rather different of the experimental one.
In addition, the numerical solution is certainly under-resolved and next simulations will use finer grids. Note that the numerical results presented in this workshop correspond to a first attempt. Thus, this study is still in progress.

References

(1) Ta Phuoc L., 1994 Modèles de sous-maille appliqués aux écoulements instationnaires et décollés, *Journée Thématique DRET*, Paris, France.

(2) Lardat R., Bertagnolio F. et Daube O., 1997 La formulation vitesse-tourbillon en maillage décalé : une méthode de projection, *C.R.Ac.Sc.*, 324, II b, pp. 747-753.

(3) Pellerin S., Dulieu A., Ta Phuoc L. and Tenaud C., 2001 Incompressible 3-D mixing layer using LES: Influences of subgrid scale models and of upstream perturbations, Proceedings of the ISCFD'99, ZARM Bremen (Germany) Sept. 5-10, 1999. In Special Number 2001 of Computational Fluid Dynamics Journal, ISSN 0918-6654.

Contra-rotating jets: wake/mixing layer interaction.

Computational method

Rémi Manceau
Laboratoire d'études aérodynamique
UMR CNRS 6609, Université de Poitiers, France

Introduction

These computations are not performed in order to test new models or formulations specific to this case, but rather to provide a reference set of results. This allows the knowledge of how the standard k–ε model behaves in this case, which serves a basis for comparisons. A grid convergence test is performed to eliminate this source of error.

Model

The model used is the standard k–ε model as provided by Star–CD.

Numerical schemes

The commercial package Star–CD is used. The discretization is second order accurate, with centered convection.

Grids

Three different grids are used: $n_y \times n_x = 100 \times 30$, 150×45, 200×60.

Inlet conditions

As a preliminary study shows, the choice $V = 0$ or $V \neq 0$ at the inlet has only a slight influence on U profiles. However, the experimental profile is used since it yields a slightly better solution.

Case 9.2

Results and comments

Test Case 9.2: The Flow in a Channel with periodic 'hills' on one wall
M.A. Leschziner, Imperial College London

1. The test flow and its features

This test configuration, shown in Figs. 1 and 2, presents a number of predictive challenges that arise from a combination of a separation from a curved surface, massive recirculation, streamwise periodicity and a high level of acceleration upstream of the separated region. The geometry is a nominally infinite sequence of periodic 2-d 'hills' on one side of a channel. The flow is at Re=21900, based on mean velocity and channel height. Extensive data for spanwise-homogeneous and streamwise-periodic flow conditions are available for this case from two highly-resolved LES computations (for a single periodic segment, Fig. 1) performed independently by Temmerman and Leschziner at IC-London and Froehlich et al. at the University of Karlsruhe (Temmerman et al. (2003), Froehlich et al. (2004)) on the same mesh containing almost 5 million nodes. These simulations are analysed exhaustively in Froehlich et al (2005). Accuracy and resolution checks included an examination of spectra, the minimum resolved scale vs. the Kolmogorov scale, the contribution of subgrid-scale transport and the level of de-correlation in both streamwise and spanwise directions. The data may thus be taken to be of high quality and level of reliability.

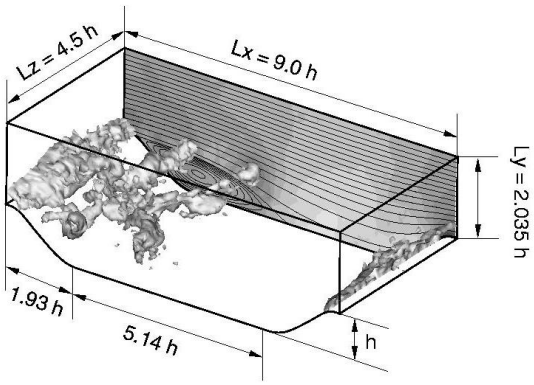

Fig. 1: Periodic channel segment for which the LES data were generated

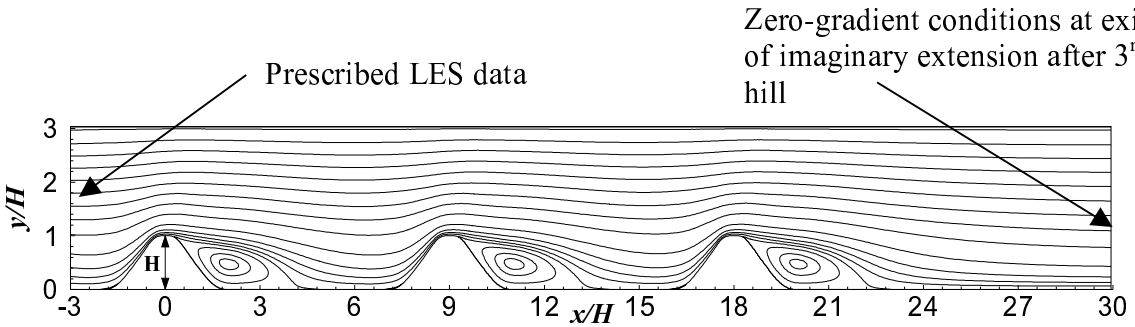

Fig.2: Geometry for which RANS computations were performed (this 3-hill configuration was only computed by Chen et al. - see Table 1. All other contributors computed a two-hill geometry).

In terms of flow physics, one particular case-specific difficulty for any RANS model arises from the fact that the separation process is highly time- and space-dependent, occurring over a large proportion of the surface on the leeward hill side. Indeed, there is no 'separation line' as such at any one instant. Rather, the simulation shows a complex collection of patches of forward and reverse flow over the surface around the mean separation line. Thus, the region in which the time-averaged flow is attached is, in fact, one in which large vortices are shed intermittently and which does not, therefore, comply with any of the concepts applicable to a boundary-layer flow. This highly dynamic region, in which turbulence is strongly 'non-local' and in which the turbulence level tends to be very high – much higher than in a statistically attached near-wall layer, is extremely difficult if not impossible to describe within any existing RANS-modelling framework. This is an influential issue for the overall character of the flow, for the simulations reveal that even slight changes in the time-averaged location of the separation line result in substantial changes in the reattachment behaviour (the ratio being around 1:7) and thus in gross-flow features. In fact, the RANS solutions discussed herein also indicate this sensitivity, albeit less distinctly.

Within a statistical framework, a RANS model is first required to represent the response of turbulence to the strong acceleration and curvature in the boundary layer upstream of the hill crest and the following deceleration leading up to separation. In the region immediately

upstream of the separation line, the model has then needs to capture the high level of turbulence associated with intermittent separation. There follows a detached, curved shear layer in which turbulence/curvature interaction and its effects on turbulence anisotropy are expected to influential. The ability of a model to represent these processes influences materially the predicted reattachment characteristics. This region is dominated by the impingement of large, energetic eddies on the wall, and the impingement region is characterised by a high level of redistribution of energy among its components effected by strong pressure fluctuations. The simulation shows intermittent forward and reverse motion over almost the entire horizontal region between the two hill surfaces. Post reattachment (in the mean), there is a partial flow recovery in which the model is required to represent, on the one hand, the inviscid interaction between the outer shear layer and the wall, and on the other hand, the viscous interaction of this layer with the boundary layer developing from the mean reattachment point. Finally, the time-averaged attached flow undergoes a strong overall acceleration towards the next hill crest, preceded, however, by local deceleration and incipient separation of the boundary layer close to the windward foot of the hill. In this region, strong normal straining occurs, and the correct representation of its effects on the turbulence state is yet another challenge for any model. Hence, although this is a statistically two-dimensional flow in a relatively simple geometry, it is highly challenging in physical terms, and it represents searching test case for turbulence models.

An interesting supplementary question in relation to the present flow is whether streamwise periodicity is an important aspect in judging alternative turbulence closures. Periodicity is often claimed to be unrepresentative of real predictive situations and assumed to pose added challenges through the fact that errors in the inner-domain solution are fed back to the inlet plane, thus progressively amplifying the departure of the model solution from reality and obscuring model capabilities. The extent to which this issue affects conclusions on closure performance and their applicability to cases in which the inlet flow is specified as a boundary condition can be (and has been) addressed by performing computations for a sequence of 3 hills hills, with LES conditions applied to the inflow plane, as well as for a single segment, with imposed periodicity conditions. The former practice allows the rate of approach to the periodic state to be studied and the ‘anchoring’ influence of the specified inlet conditions to be identified in terms of its importance to the assessment of turbulence models. Because this

study was at the margins of the workshop activity, its results are not included in the main part of this report or discussed. However, the results are contained in Appendix 2 and are also reported in Wang et al. (2004). They demonstrate that streamwise periodicity is not a critical issue in assessing models. If a model performs reasonable well for the periodic segment, periodicity is very quickly established when a solution evolves from prescribed upstream conditions. If, on the other hand, a model performs poorly in the periodic segment, periodicity takes longer to establish itself, but agreement can be worse in the evolutionary phase than in the periodic state. Thus, the conclusion emerging is that judging turbulence-model performance by reference to a periodic flow is appropriate and fair.

2. The Contributors and their Approaches

A total of 36 computational solutions were contributed by eight groups – see Table 1. However, not all arose from the application of different models or model variations. For example, Rumsey (NASA) provides solutions for a sequence of four grids to demonstrate the sensitivity of some flow properties to grid density (see section 3.2). Next, Wang et al (IC-London) provide results for the flow in the first (default) valley as well as in the second valley of the 3-segment (hill) domain. Finally, Kolkka and Ahlstedt (UT-Tampere) report computations for the same set of model on both structured and unstructured grids. Detailed statements provided by the contributors are contained in Appendix 1.

Models adopted fall into five groups:

- The one-equation Spalart-Allmaras model (1992).
- Variants of the linear eddy-viscosity (LEVM) k-ε model, the major ones being the standard k-ε model, either with wall functions or in combination with a near-wall-layer model in which a lower-order (1-equation or algebraic) model is applied (referred to as "two-layer model") and the low-Re form of Launder and Sharma (1974).
- Variants of the linear EVM k-ω form, the major ones being the basic form of Wilcox (1988), the Menter (1994) BSL and SST implementations, which blend the ω-equation near the wall with the ε-equation (reformulated in terms of ω) in the inner region, and these

same two versions in combination with wall functions, as well as variants that include a curvature (and swirl) correction by Deng & Visonneau (2002) .

- The "code-friendly" version of the V2F model of Lien and Durbin (1996)).
- Non-linear eddy-viscosity (NLEVM) and explicit algebraic Reynolds-stress (EASM) models, including the models by Apsley and Leschziner (1998), Merci and Dick (2004), Wallin and Johansson (2000) and Abe et al (2003).
- Reynolds-stress-transport models (RSM), including the versions of Speziale et al. (1991) and the Gibson and Launder model (1973), both implemented either in combination with wall functions, or with a low-Re extension of Chen et al. (2000), or with a low-Re sublayer model within a two-layer strategy.

Table 1: Summary of contributions

Contributors	Codes	Models	Numerics	Grids	Run identifier
TU-Darmstadt: S. Sarić, A.Djugum, S. Jakirlić,	FLUENT SWIFT (AVL) FAN-2D (in-house FAN-3D (in-house	*Standard* k-ε + WF (FLUENT, FAN-3D) Launder-Sharma low-Re k-ε (FAN2D) Two-layer k-ε (FAN2D) Spalart-Allmaras ν_t (FLUENT, FAN3-D)	LUDS TVD CDS+LUDS CDS+LUDS	518x95 500x60 354x60 – WF 518x95 – low-Re	Darmst/Std-k-ε+WF Darmst/LS-k-ε Darmst/2L-k-ε Darmst/SA
EC-Nantes: G.B Deng, M. Visonneau	N3S-NATUR	*Standard* k-ε+WF, Launder-Sharma low-Re k-ε Wilcox 88 k-ω +/-*WF* Menter BSL & SST +/- WF Low-Re RSM Gibson-Launder (IP) Low-Re RSM Speziale et al		221x121	Nantes/k-ω-BSL+WF Nantes/k-ω-BSL Nantes/low-Re-RSM-IP Nantes/low-Re-RSM-SSG
U-Ghent: B. Merci, C. De Langhe, K. Lodefier, E. Dick		Cubic NLEVM (Authors)	AUSM-like 2nd order	181x73	Ghent/cubic-k-ε
UT-Helsinki: K. Salo, A. Hellsten	FINFLO	Wallin-Johansson EASM Curvature-Modified EASM+Menter BSL RSM Speziale et al+BSL	Roe+MUSCL	384x128	Helsinki/EASM-WJ-k-ω Helsinki/EASM-CCWJ-k-ω Helsinki/RSM-SSG+BSL
NASA: C.L. Rumsey	CFL3D	Spalart-Allmaras ν_t Menter SST EASM-k-ε and k-ω Ramsey-Gatski	Roe (2nd order) for momentum, UDS for k,ε	Max 737x193	NASA/EASM-k-ε NASA/EASM-k-ε-medium NASA/EASM-k-ε-coarse NASA/EASM-k-ε-v.coarse NASA/EASM-k-ω NASA/k-ω-SST NASA/SA
UT-Tempere J. Kolkka, H. Ahlstedt	FLUENT	*Standard* k-ε+2-layer Shih et al Realizable k-ε +2-layer Gibson-Launder RSM-	LUDS	73530-Struct. 86371-Unstruct.	Tampere/2-layer-k-ε Tampere/2-layer-real-k-ε Tampere/2-layer-RSM-IP Tampere/k-ω-SST Tampere/2-

		IP+2-layer			layer-*k*-ε-unstrct Tampere/2-layer-real-*k*-ε-unstruct Tampere/2-layer-RSM-IP-unstruct Tampere/2-layer-*k*-ω-SST-unstruct
U-Manchester: J.C. Uribe, D. Laurence	STURNE	Lien-Durbin V2F (Code friendly)	CDS for momentum UDS for *k*,ε	282x150	UMIST/V2F-codeFriendly
IC-London: C. Wang, Y.J. Jang, M. Leschziner	STREAM	Launder-Sharma low-Re *k*-ε Apsley-Leschziner Cubic NLEVM *k*-ε Abe et al EASM k-ω Wallin-Johansson EASM Speziale et al RSM+ Chen low-Re extension	QUICK+TVD	721x91	IC/LS-*k*-ε IC/quad-*k*-ω-AJL IC/cubic-*k*-ε-AL IC/EASM-WJ IC/RSM-SSG+low-Re IC/LS-*k*-ε-valley2 IC/quad-*k*-ω-AJL-valley2 IC/cubic-*k*-ε-AL-valley2 IC/EASM-WJ-valley2 IC/RSM-SSG+low-Re-valley2

3. Contributed Results

3.1 General comments

As is usually the case with relatively loosely coordinated validation exercises, efforts to interpret the capabilities of turbulence models are, here too, inhibited by the multitude of modelling variations implemented, often within one and the same model category, by the variety of grids and codes used and by uncertainties about the validity and consistency of the implementation practices. This problem is aggravated by the well-documented, generally high level of sensitivity of turbulent-flow solutions to even minor variations in model fragments and numerical constants, especially in the length-scale equation and in the near-wall model. Thus, for example, a single model, applicably in its basic form to high-Re conditions and then modified to operate in combination with wall functions, or within a two-layer strategy, or with a low-Re extension of the basic model, can give an entirely different solution to that of the basic form for a flow which is strongly affected by near-wall processes, as is the present flow. In particular, slight changes in the predicted separation point can results in major differences further downstream, as pointed out in Section 1. Thus, the presentation and discussion to follow can only identify trends of model categories, and there a number of open questions will remain at the end in relation to particular models or variations.

3.2 **Grid-dependence tests**

An assumption that has to be made when comparing results from different contributors is that all have undertaken grid-dependence tests before generating their 'definitive' results with a demonstrably adequate grid. Even if this is so, a difficulty is that numerical accuracy depends not simply on the grid density, but also the numerical scheme and the turbulence model employed. Moreover, adequate grid density is not merely identified by the total number of nodes, but also the cell distribution, grid-aspect ratio, expansion rate (especially at walls) and, generally, its 'adequacy' in resolving, locally, all important scales. Within this extensive 'parameter space', grid-independence is difficult to achieve in all circumstances, and its verification can be a challenging exercise in itself. It is important, however, to be able to gain some insight into what grid characteristics are at least adequate in so far as they secure sufficiently low numerical errors to allow some degree of confidence to be placed on reported model dependence. Given that all numerical scheme used here are nominally second-order accurate (or better), such insight can be gained from results reported by NASA for the EASM-k-ε model and U-Tampere for the k-ε model as well k-ω SST and RSM models .

NASA has provides results for a sequence of 4 grids: 92x24, 184x48, 368x96 and 737x193, the third, designated "medium" being representative of the grid most contributors have used. The solution at x/h=2.0, shown in Fig. 3.2.1 in the form of profiles for mean-flow and turbulence quantities, should suffice to convey the main message. The distributions shown in the figure are representative of the behaviour in other sections. As seen, grid dependence persists up to the finest grid used. However, viewed against the differences between results for different models, to emerge later, grid dependence is practically negligible beyond the "medium" grid. Thus, if this is representative of other contributions, and if the models are correctly implemented, it may be assumed that the solutions reported represent, essentially, the predictive capabilities of the models. One important uncertainty that needs to reiterated, however, arises from the grid resolution adopted at walls. There is no information, beyond the total umber of nodes and, in some cases, plots of the grids, allowing an assessment of whether this resolution is appropriate to the models used.

A different type of grid-dependence test is reported by UT-Tampere who used the FLUENT code with both structured and unstructured grids, the latter refined locally at the lower wall. Both grids, while very different in terms of density distribution, contain around 80000 nodes. This translates to roughly 400x200 or 500x160 cells, which is a density approaching the finest examined by NASA, and is thus considerably finer than the mesh most contributors have used. All of U-Tampere's computations have been undertaken with two versions of the k-ε model as well k-ω SST and RSM models. Representative results, again at x/h=2.0, are given in Fig. 3.2.2 and 3.2.3. As seen, agreement between corresponding structured-grid and unstructured-grid solutions for the k-ε-models is close, except for minor wiggles in the relatively low V-velocity component. Similarly close agreement is obtained for the RSM. However, in the case of the SST model, the differences are not insignificant, perhaps because of the sensitivity of the BSL blending practice to grid parameters, especially in the outer region where the unstructured is quite coarse, and this demonstrates starkly that numerical accuracy can depend sensitively on the nature of the turbulence model used to examine grid independence.

3.3 Overall flow features

The most important global feature of the present flow is the recirculation region in the leeward side of the hill . Its size and shape are dictated by the ability of a model to return the correct separation point, by the level of mixing in the separated shear layer and by the representation of the interaction of the shear layer with the wall as the flow reattaches.

Plots of streamfunction fields for 6 model categories are given in Figs. 3.3.1-3.3.6. The separation and reattachment points given by the LES are x/h=0.2 and 4.7, respectively – that is, reattachment occurs close to the mid-segment point. Although the 'reattachment angle' (the angle of the separation streamline) is quite acute (around 20^o), a reasonable way of assessing the size/shape of the recirculation region is to extrapolate the separation streamline in the region y/h=0.2-0.5 as it approaches reattachment. This extrapolation gives, for the LES, an intersection at around x/h=4.5, i.e. close to the actual reattachment point.

Fig. 3.3.1 shows six solutions for variants of the linear k-ε model. The three plots provided by TU-Darmstadt demonstrate starkly the strong sensitivity of the solution to the near-wall treatment: while all three model versions predict late separation and premature reattachment, the two-layer implementation results in a recirculation zone twice the size of that using wall functions. UT-Tampere's plots do not, unfortunately, include the separation streamline, but the impression is that both two-layer formulations give a recirculation zone which is close to, if not more extensive than, the LES result. Because the two-layer implementation controls (limits) the length scale at the wall, it is perhaps expected to lead to a larger recirculation zone. However, the same may be said about the wall-function variant, for the length scale is, here too, limited to the equilibrium level. Thus, the origin of the major predictive differences is unclear at this stage, but may emerge from a detailed examinations of the property profiles to follow.

Fig. 3.3.2 contains four solutions obtained with various forms of the blended k-ω/k-ε model, with the blending achieved with Menter's BSL practice. Two implementations also include Menter SST (shear-stress-transport) limiter. Evidently, use of the k-ω model in the near-wall region leads to an earlier separation and to a major elongation of the recirculation zone, relative to the k-ε-model (at least in its basic form). Interestingly, EC-Nantes's results suggest the effect of wall functions to be opposite to that observed in Fig. 3.3.1. Introducing the SST limiter is seen to cause a further major elongation of the recirculation zone, well beyond the LES result. This is in broad conformity with other studies of separated flows in which the SST model has been found to predict premature separation and, to a lesser extent, delayed reattachment.

Results arising from non-linear eddy-viscosity and explicit algebraic stress models are given in Fig. 3.3.3 and 3.3.4. U-Ghent's model gives a slightly excessive recirculation length and a broadly correct shape, while NASA's k-ε implementation returns a rather poor result, with the recirculation region too thin and too short. The latter behaviour is contrary to the general observation, not only from the present workshop results, that models of this type tend to predict excessive recirculation in this geometry. The k-ω-model solutions, in Fig. 3.3.2, are consistent with this observation. While use of the ω-equation on its own appears to increase the recirculation zone relative to k-ε variants, its combination with non-linear stress/strain relations

evidently results in excessive recirculation. Jang et al (2002) also show that other forms, even those using the ε-equation tend to over-estimate the recirculation region, in agreement with U-Ghent's result and contrary to NASA's prediction.

Fig. 3.3.5 shows two results derived from the Spalart-Allmaras model. Here, there is gratifyingly close agreement between the predictions of TU-Darmstadt and NASA: both show grossly excessive recirculation, with marginal or no reattachment at all on the plane between hills. This model gives the poorest performance among all models investigated herein, certainly in terms of global mean-flow features.

Results for full Reynolds-stress models are finally given in Fig. 3.3.6. Excluding UT-Tampere's results, all others show the stress models (all used in conjunction with variants of the ε-equation) to give excessive recirculation. Moreover, most display the well-known tendency for reattachment to be corrupted by the doubling up of the separation streamline at reattachment, the origin of which is unclear, but occasionally attributed to the defects in the length-scale equation that are alleviated by the use of a Yap-type length-scale-reducing term.

In summary, the following conclusions arise from the above:

(i) Linear k-ε variants tend to predict late separation, early reattachment and an excessively short recirculation region, but the extent of these deficiencies depends greatly on near-wall modelling.

(ii) Linear k-ω models, applied in the near-wall region, give a significant elongation of the recirculation zone, an observation also pointing to the extremely high sensitivity of the solution to near-wall modelling.

(iii) The SST strategy tends to unduly depress the turbulence activity, leading to a gross exaggeration of recirculation. The Spalart-Allmaras model perform even worse and appears to be inapplicable for modelling internal separation (and probably any separated flow).

(iv) Non-linear eddy-viscosity and related models tend to result in excessively long recirculation zones, especially when used in conjunction with the ω-equation. This suggests that the 'effectiveness' of the ω-equation in the context of an isotropic-

viscosity scheme rests on a compensation of defects arising from the isotropic eddy-viscosity assumption. Thus, Once these defects are removed, in one way or another, the ω-equation becomes inappropriate.

(v) Reynolds-stress models tend to predict excessive separation, even with forms of the ε-equation, and give the wrong reattachment behaviour, at least when not combined with length-scale limiters in the ε-equation. However, such a correction is likely to result in a further elongation of the recirculation zone.

3.4 Velocity and turbulence profiles

3.4.1 *Introductory comments*

Profiles of streamwise and cross-flow velocity components, turbulence energy and shear stress are available at ten positions: x/h=0.05, 0.5, 1.0, 2.0, 3.0, 4.0, 5.0, 6.0, 7.0 and 8.0. However, the present discussion will be restricted to a subset of results, deemed to convey the most important features at 'representative' positions. A complete set is provided in Appendix 2. Attention will focus on conditions on x/h=0.05, 2.0, 6.0 and 8.0, held to be representative of processes associated with separation, recirculation, post-reattachment recovery and re-accerleration, respectively. Results for these four locations are given in Figs. 3.4.2.1-3.4.2.6, 3.4.3.1-3.4.3.6, 3.4.3.1-3.4.3.6, and 3.4.4.1-3.4.4.6, respectively, and these are discussed in related sections below. For each section, there are six figures, each relating to a particular (broad) model category. In each figure, a side-by-side presentation of mean-flow and turbulence quantities is adopted. This is judged to be the most useful practice, as there is evidently a strong causal relationship between the mean flow and the turbulence state.

3.4.2 *The separation location: x/h=0.05*

The location x/h=0.05 is just upstream of the separation region. The flow at this position is heavily marked by its complex history further upstream: the separation, reattachment and strong acceleration on the upstream hill side. The LES solution for the streamwise velocity exhibits a distinctive peak close to the wall and a significant upward motion, both associated

with the upstream hill side and the strong acceleration along it. There is also a strong peak of turbulence energy and a negative shear stress across almost the entire flow, despite a negative shear strain, the latter pointing to counter-gradient diffusion and the important role of stress transport.

Figs. 3.4.2.1-3.4.2.6 demonstrate that no eddy-viscosity model or EASM is able to give even a close approximation of the conditions predicted by the LES. Most models miss the velocity peak altogether, predicting a thick boundary layer with a high level of turbulence energy above the LES near-wall peak. While the linear k-ε solutions fall within a fairly narrow band, there are some major variations within other categories. In the linear k-ω category, NASA's and UT-Tampere's SST solutions differ drastically. The former shows a much lower level of turbulence in the boundary layer then all other models, and this favours the resolution of the near-wall velocity peak, a feature reflecting the type of free-vortex condition encountered in highly curved flow at a relatively low level of turbulent mixing. It cannot be said that any of the NLEVMs and EASMs perform better than simpler models at this station. A worrying observation is that three implementations (NASA, IC-London and U-Manchester) of what appears to be one and the same form of the Wallin-Johansson EASM give substantially different results, with the NASA profiles lying between the other two. Given the broad band of results of different implementations, it is not really possible to propose a general conclusion on the predictive capabilities of non-linear eddy-viscosity models as a category, at least not at this position.

The streamfunction contours discussed earlier showed the Spalart Allmaras model to perform poorly. The profiles in Fig. 3.4.2.5 serve to amplify this. Close agreement is here observed between TU-Darmstadt's and NASA's results, and NASA's k-profile, in particular, shows an entirely wrong behaviour of the turbulence energy, the level being at a small fraction of what it should be. U-Manchester's result for the v2F model, also included in Fig. 3.4.2.5, shows the model to perform no better than models discussed so far.

The results for the RSMs are especially interesting in view of the supposition, expressed earlier, that stress transport plays a crucial role in the structure of the flow upstream of x/h=0.05, as a consequence of the strong acceleration in this region. Indeed, the results shown

in Fig. 3.4.2.6 contain features that clearly supports this supposition. This is the only model category that clearly resolves the near-wall velocity peak, gives an approximately correct level of turbulence energy and returns the correct trends in the shear stress. The RSM-IP implementation of EC-Nantes gives an excellent agreement with the LES data, while IC-London's low-Re SSG implementation actually over-estimates the velocity peak and gives a reasonable shear-stress profile and close agreement in respect of k. Thus, while agreement between model predictions and LES is by no means even close to perfect, the results provide very clear pointers to the importance of stress transport. The fact that the curvature-modified variant of the Wallin-Johansson model does not procure better agreement than the basic form of the model (Fig. 3.4.2.4) serves to indicate that curvature is not the major element in recovering the transport of the anisotropy and shear stress ignored in the derivation of EASM. It is rather streamwise advection which appear to be the important mechanism. This subject will be revisited in more detail in Section 3.5.

The anisotropy of the turbulence field can only be resolved credibly by NLEVMs, EASMs and RSMs . In view of the large errors in the representation of the mean-flow, turbulence energy and shear stress by the first two groups of models, all that can be said in relation to anisotropy, in the light of the results in Figs. 3.4.2.3 and 3.4.2.4, is that most predict, qualitatively, the separation between a larger streamwise and a lower cross-flow stress that would be expected in a conventional shear flow. However, the RSM shows a close-to-isotropic state away from the highly anisotropic layer very close the wall. Generally, the Reynolds-stress transport models tend to perform much better, although there are significant variations among the solutions for the cross-flow stress. In particular, TU-Tampere's v^2-profile appears to be wrong. Significantly, IC-London's low-Re implementation captures the high u^2-peak near the wall. Two other versions show signs of doing likewise, but the predicted peaks are much too low.

The large majority of models give a poor representation of the length scale, although it is judicious to point to the challenges of extracting this quantity reliably from the LES, especially near the lower wall, because of the extreme conditions. All models underestimate the length scale, some by up to 50%, and v2F model even by about 80%. There are no obvious advantages accruing in this respect from using the ω-equation relative to the ε-equation. All models predict especially poorly the steep rise in the length scale close to the lower wall, and

this is linked closely to equally poor predictions of other properties in this region. Unfortunately, too few contributors have reported length-scale distributions for RSM implementations to make related comments with any degree of confidence. The single distribution reported by UT-Helsinki in Fig. 3.4.2.6 indicates that this model also under-estimates the length scale by a fair margin.

In summary, the following conclusion appear appropriate:

(i) The flow at x/h=0.05 is extremely challenging and poorly represented by all but the RSM category. In particular, the near-wall velocity and energy peaks are missed, and the models predict a much too thick boundary layer with an excessively high level of turbulence energy and entirely wrong variations of the shear stress.

(ii) RSMs give a much better, though far from perfect, representation at this position, and this must be assumed to reflect the importance of stress transport in the strongly accelerating upstream region.

3.4.3 *The recirculation zone: x/h=2.0*

This position is roughly mid-way along the recirculation zone, and it may be assumed to represent the conditions over a significant proportion of this zone. The flow may be thought of as consisting of an outer shear layer, emanating from the upstream separation line, which interacts with a lower reverse-flow layer, which is itself a combination of post-reattachment fluid from the separated shear layer and a boundary layer nominally originating at the impingement line.

Model predictions are compared with the LES in Figs. 3.4.3.1-3.4.3.6. Results emerging from linear k-ε models are given in Fig. 3.4.3.1. Most model implementations predict insufficient shear strain, or a too rapid erosion of the shear layer, and this is consistent with the premature reattachment observed by reference to the streamfunction plots (Figs. 3.3.1-3.3.6). The two-layer formulations return a pronounced near-wall peak in the reverse-velocity profile, possibly indicative of an 'incompatibility' between the two turbulence states across the interface. The fact that all models predict much too low turbulence energy and shear stress in the shear layer suggests that the insufficient shear strain is not due to excessive mixing, but reflects serious

defects in the flow upstream of the separated shear layer, especially such arising from late separation and early reattachment. These defects have been identified and discussed already. Thus, the low level of shear stress appears to be a result of the low strain rate and hence low turbulence-production rate, which are effected by other processes.

There are large differences among the k-ω/BSL/SST solutions, shown in Fig. 3.4.3.2. However, a general trend is for steeper velocity gradients to be predicted in the shear layer, which is consistent with earlier separation and later reattachment. Excluding the anomalous NASA result, the higher shear strain is accompanied by higher turbulence energy and shear stress, strengthening the argument about the causal relationship between strain and stress noted in the previous paragraph. However, here again, the shear stress is too low, indicating that upstream defects of the type noted above play an important role.

Results for NLEVMs and EASMs are given in Figs. 3.4.3.3 and 3.4.3.4. Unfortunately, the profiles differ greatly from one to another, and it is difficult, therefore, to identify features specific to this model category. One general trend that emerges, however, is that the shear strain in the shear layer is excessive, one exception being the solution predicted with U-Ghent's model. This is especially prominent in the solutions derived from the non-linear k-ω models. It is recalled that these models also give excessively long recirculation zones. If, as suggested above, the strain 'drives' the stress, an excessively high strain should also result in a high level of shear-stress. While the shear stress tends, indeed, to be higher than that predicted especially by the linear k-ε models, it is perplexing to observe that all models continue to predict far too low shear-stress levels, despite the high shear strain. The only model that shows the expected trend is the IC/Quad-k-ω model. This gives the highest shear stress and turbulence energy and also a broadly correct shear strain in the outer shear layer. As the upstream state predicted by any of these models at x/h=0.05 is no better than that returned by the linear variants, it seems that the causal relationship between strain and stress, suggested above, does not in fact hold here: there are clear indications that a low stress goes hand-in-hand with excessive strain – that is, the stress may be perceived as driving the strain, rather than the reverse. Evidently, shear-induced generation is not high enough (as will be shown later by reference to budgets), perhaps because the highly energetic, large-scale dynamics in

the shear layer is not captured, so that there is a wrong relationship between stress and strain. Here then, insufficient stress, and the insufficient mixing in the shear layer that goes with it, results in the observed marked elongation in the recirculation zone. Why this causal relationship does not hold in the case of the linear k-ε is not clear, but the reason may simply lie in the significant downstream shift in the separation point and hence the necessarily much smaller recirculation zone.

Results for the Spalart-Allmaras and v2F model are given in Fig. 3.4.3.5. The performance of the latter model is unremarkable: it is similar to the linear k-ε models. The former model gives roughly the correct strain, but a much too low shear stress. At this low level, mixing across the shear layer is too weak, and this then leads to a grossly excessive recirculation length.

The performance of the Reynolds-stress models is conveyed in Fig. 3.4.3.6. Except the IC-London's low-Re SSG implementation, the profiles lie within fairly narrow bands. The IC-London result differs from the others mainly in respect of the lower location of the thinner recirculatioin zone and thus the lower location of the shear layer. In common with the NLEVMs and the EASMs, the RSMs predict excessive shear strain going hand-in-hand with low shear stress and low turbulence energy. Thus, here too, there seems to be insufficient shear-produced turbulence generation, or an excessive reduction by the pressure-strain model (which is, however, not a process resolved taken into account in NLEVMs).

The question may be raised as to whether this commonality in defects betrays the existence of non-turbulent (periodic) motions, the effect of which on the mean flow are ill-described by RANS models. If such periodic motions *are* present then no RANS model would be expected to resolve this flow properly. However, an analysis of the LES data by Froehlich et al. (2005) does not reveal a distinct periodic component, beyond that associated with the structural vortical features (emanating from a Kelvin-Helmholtz instability) found in any separated shear layer. The distinct possibility of the large-scale dynamics not being captured remains, however.

As regards the prediction of normal-stress anisotropy, all that can be said in relation to the NLEVMs and EASMs is that they predict qualitatively correctly the significant excess of u^2

relative to v^2. Virtually all models give an insufficient level of transverse stress, and this is compatible with the correspondingly low shear stress already noted. There is an especially poor representation returned by all models in the reverse-flow region and the lower part of the outer shear layer. The RSMs tend to perform better, but this performance varies greatly from model to model, and there is also a general tendency for the stresses, again especially the transverse stress, to be substantially too low.

The length-scale distributions for most models for which data have been provided show far too low levels near the lower wall, consistent with low turbulence activity, and excessive values towards the upper wall. Most models give at least a broadly correct length-scale gradient on both the upper and lower walls. The v2F model predicts an especially poor length-scale distribution (assuming the data have been correctly conveyed), the predicted level being of order 25% of the LES value.

The above observations may be summarised as follows:

(i) Most models display significant predictive defects at this location.

(ii) All models predict too low (many far too low) turbulence activity in the shear layer. This applies to all stresses and also to the turbulence energy.

(iii) In the case of linear k-ε models, the low shear stress goes hand-in-hand with low strain.

(iv) In contrast, in the case of anisotropy-resolving models, the low shear stress is accompanied by excessive strain.

(v) Based on (iii) and (iv), it is suggested that most models, if not all, misrepresent the link between shear stress and shear strain by the action of production. Observation (iii) which might be taken to contradict this suggestion, may be explained simply by the fact that the k-ε model predict late separation and hence a short recirculation region.

(vi) It is possible that the defects observed, apart from being linked to defects upstream, are due to an inability of all RANS models to represent realistically the effects of the dynamics of large-scale motions in the shear layer.

3.4.4 *The recovery region: x/h=6.0*

This position is roughly midway between the nominal reattachment point and the foot of the next hill along which the flow re-accelerates. The predicted conditions at this position, shown in Figs. 3.4.4.1-3.4.4.6, obviously depend greatly upon the corresponding reattachment location. Unfortunately, this obscures the answer to the question of whether the flow recovers from reattachment at the correct rate, unless the predicted reattachment point happens to agree with the LES result.

It is recalled that linear k-ε models tend to predict premature reattachment, although the location depends greatly on the near-wall approximation. It is not surprising, therefore to observe in Fig. 3.4.4.1 that the predicted recovery is generally more advanced than the LES state. The exception is one of UT-Tampere's solutions (with a realisable variant), which also gives an especially long recirculation region. Generally, the profiles agree reasonably well with the LES data, although the turbulence level is, yet again, too low, suggesting that the recovery is too slow. This is brought out especially well by UT-Tampere's solution, which, despite an excessive strain rate, gives an insufficient level of turbulence energy (the shear stress is unfortunately not available).

The profiles predicted by the linear k-ω models, shown in Fig. 3.4.4.2, feature significant scatter, as they do at other stations. The models themselves are virtually identical (there should be little difference between the BSL and the SST implementations), and there should be close agreement among the solutions. As the models generally predict an excessively long recirculation region, the resulting wakes at this station are more pronounced. In fact, the NASA profile even features a thin reverse-flow region, suggesting reattachment at about x/h=6.5, i.e. far too late. The trends in the shear-stress and turbulence-energy profiles are broadly correct. The predicted maxima of the turbulence profiles are higher than the LES result, and this is consistent with the excessive shear strain predicted around y/h=1. The NASA result does not conform to this linkage, and this suggests an error in the implementation. The shear stress appears to be generally too low, which then gives rise to a serious delay in reattachment.

Profile predicted by NLEVMs are shown in Figs. 3.4.4.3 and 3.4.4.4. Most velocity profiles reflect the delayed reattachment predicted by the models, except for NASA's EASM implementation. This model gives slightly premature reattachment, and this defect, coupled with the exceptionally low level of turbulence energy and shear stress within this model category and hence slow recovery rate, is the reason for the relatively close agreement in respect of the velocity. All other models give an excessively intense wake, i.e. insufficient recovery, two containing thin reverse-flow regions, consistent with much too late reattachment. Despite the excessive strain, the turbulence energy and shear stress are broadly at the correct level, if not slightly too low. Hence, here again, there is the suggestion of an insufficiently strong linkage between strain and turbulence production - although it has to be said that this suggestion assumes that stress-transport effects play an insignificant role. As regards anisotropy, all models return, qualitatively correctly, the excess of u^2 over v^2, although the actual levels may not agree well with the LES result. This last comment applies, in particular, to NASA's implementation, which also gives too low levels of shear stress and turbulence energy. All contributed length-scale distributions agree broadly with the LES data, but as is evident from Figs. 3.4.4.3 and 3.4.4.4, the gradient of the length scale, especially close to the bottom wall, is seriously under-estimated, suggesting that the near-wall flow does not adhere well to a conventional boundary layer and is not, therefore, represented well by length-scale equations calibrated by reference to equilibrium constraints.

Results for the Spalart-Allmaras and v2F models are shown in Fig. 3.4.4.5. The former has already been shown to give a seriously erroneous solution for this flow, and will not be considered further as a closure appropriate to the present complex conditions. The v2F model shows a behaviour which is, again, close to the conventional linear k-ε model. Thus, because of premature reattachment, low shear stress and turbulence energy – and hence relatively slow recovery – agreement in respect of velocity is good at the present location. However, as for the position x/h=2.0, the length scale is, here too, much too low, perhaps due to wrong data being conveyed by U-Manchester.

The Reynolds-stress models provide a generally disappointing representation at this location, as seen in Fig. 3.4.4.6. As most models predict a excessively thick separation line, delayed reattachment and wrong reattachment behaviour (at a much too large angle between the

separation line and the wall), the wake above the thin near-wall layer developing after reattachment tends to be too intense, giving very high shear straining above y/h=0.5. As is the case with NLEVMs and EASMs, the shear stress and turbulence components are roughly in line with, or lower than, the LES data. Thus, here again, there is the problem of incompatibility between the high strain rates and the apparently insufficient level of production. Also in common with the former category of models, the RSMs give roughly the correct level of anisotropy, but the actual magnitude of the normal stresses tends to be too low.

The above observations can be summarised by the following comments:

(i) It is difficult to judge the performance of the models on the basis of the behaviour at this position, because the flow is dictated by upstream features, especially the size of the recirculation zone.

(ii) Because of early reattachment and insufficient turbulence activity in the recovery region, which inhibit recovery, linear k-ε models (excluding two-layer implementations) give broadly correct velocity profiles. But this is fortuitous. Indeed, any of the models that predicts premature reattachment also gives fairly good agreement in respect of velocity at this location.

(iii) A general problem with all models appears to be that the turbulence level in the wake is lower than is commensurate with the shear strain. Most models return excessive shear strain, reflecting delayed reattachment, but also because recovery is inhibited by insufficient turbulence activity in the wake.

(iv) Reynolds-stress model do poorly at this location, principally in respect of the mean flow, because most predict an inappropriate reattachment behaviour, in addition to an excessively long recirculation zone. This cause the wake to be too pronounced, a defect aggravated by insufficient turbulent mixing, which would otherwise aid recovery.

(v) The v2F model gives a behaviour fairly similar to that of a standard k-ε model.

3.4.5 *The acceleration region: x/h=8.0*

The conditions in this region are especially challenging. The highly inhomogeneous flow, still recovering from separation, is subjected to strong curvature and acceleration. Close to the wall, at the foot of the hill, slightly upstream of this section, the flow is locally strongly decelerated to the point of being incipiently separated. The analysis of the LES data reveals

that the spanwise normal stress rises rapidly as the near-wall flow progresses up the hill slope. Consistently, the stress budgets show an extraordinarily intensive transfer of energy from the streamwise stress to the spanwise stress via the pressure-velocity correlation. An supplementary analysis of structural features suggests that this is due to intense impingement (splatting) of large and energetic upstream eddies onto the windward slope. Thus, this is a process which, one would assume, can only be resolved, if at all, by second-moment closure.

Model predictions are shown in Figs. 3.4.5.1-3.4.56. The k-ε solutions in Fig. 3.4.5.1 are remarkable in so far as they are closely bunched together and show a broadly satisfactory behaviour of the velocity. To a major extent, this is due to the fact that the velocity profile upstream of the hill is broadly correct, albeit for the wrong reasons. The mean-flow evolution of the flow from the foot of the hill to the present position is governed, principally, by inviscid processes associated with the strong acceleration. Also to a large extent, the turbulence field simply responds to the deformation, but hardly influences the mean-flow behaviour. While the turbulence energy is broadly correct, except in the near-wall region where the actual flow is close to separation and thus highly turbulent, the shear stress is much too high, presumably because of the rigid stress-strain linkage provided by the eddy-viscosity concept. As the turbulence energy upstream is too low, the agreement seen in Fig. 3.4.5.1 suggests an excessively rapid rise in k, probably due to a combination of (inappropriate) normal-strain-induced generation and the failure to account for stress transport.

The response of the turbulence field to the strong straining predicted by linear k-ω models is shown in Fig. 3.4.5.2. With the NASA solution set aside, because of defects highlighted earlier, the other models are seen to return seriously excessive turbulence levels, partly because the upstream levels are considerably higher than those predicted by k-ε models. This upstream elevation is due, in turn, to the substantial downstream shift of the reattachment point predicted by the k-ω models and thus the higher straining in the region upstream of the location considered. Thus, the defects associated with the wrong response to normal straining and the absence of transport result here in a serious worsening of the predictions relative to those arising from the k-ε models. The predicted length scale is also excessive over most of the flow (as well as having the wrong shape), reflecting the rapid increase in k relative to dissipation.

Here again, one major defect is that the slope of the length scale near the wall is seriously underestimated in the strongly non-equilibrium conditions.

The NLEVMs and EASMs perform little better thatn the linear k-ω formulations. It is recalled that both classes of model share a number of common features: late reattachment, high shear strain and a broadly correct turbulence level upstream of the present position. All these again conspire to result in excessive turbulence energy and shear stress, for reasons similar to those pertaining to the linear models. One difference is, however, that the rise in turbulence energy is (or should be) reduced by the action of terms designed to procure the correct response of the stresses to strain, either by limiting the coefficient C_μ multiplying the linear term, or by means of 'high-strain' correction terms, or, indeed, in the case of EASMs, by retaining the correct link between strain and production inherent in second-moment closure. This is probably why the rise in turbulence energy predicted by most models in the present category is much more modest, and this also explains the lower level of the length scale, although its variation is still seriously erroneous.

The v2F model gives, as shown in Fig. 3.4.5.4 among the best results at this section. But here too, as in other respects, this is due to features that are analogous to those of the k-ε models. One advantage the model shows, however, is a more benign response of the shear stress to the strong straining, perhaps because of realisability-procuring measures. As before, the length-scale value reported by U-Manchester is only a fraction of what it should be.

In view of earlier comments on the likely importance of stress transport, the RSMs would be expected to perform relatively well at this location. While this is not, in fact, the case, there are some encouraging features and expected symptoms in the results shown in Fig. 3.4.5.6. It must be noted, here again, that the upstream state is highly influential. This state is characterised by excessive shear strain, wrong wake structure and broadly correct turbulence energy and shear stress. As seen in Fig. 3.4.5.6, the strong straining does not lead to the rapid growth in turbulence energy observed in earlier solutions. This is due to a combination of a correct stress-strain linkage, procured by the (exact) production terms, and the fact that stress transport is accounted for. The shear stress is still too high, however, although the excess is generally

lower than that returned by other models. All these are positive signs, and these are further enhanced by the broadly correct anisotropy levels produced by most models.

The following summarises the above observations:

(i) At this location, the mean flow is governed, principally, by inviscid processes associated with the strong acceleration. The performance of the models is reflected mainly by the response of the turbulence fields to the straining.

(ii) None of the model can be said to give a satisfactory representation of the flow at this position.

(iii) Linear eddy-viscosity models display defects that may be taken to reflect the incorrect link between stress and strain and the absence of stress transport.

(iv) NLEVMs and EASMs do not fare much better, but their solution give evidence of either the effect of terms designed to limit an excessively strong response of the stresses to high rates of straining, or, in the case of EASMs, the effects of the stress-strain linkage inherent in the underlying second-moment equations.

(v) The solutions arising from the Reynolds-stress models also give evidence of the influence of stress transport, which has the consequence of preventing the rapid rise of the turbulence energy and shear stress seen in solutions of other models. These models also give a credible representation of the anisotropy.

3.5 **Assessment of stress convection and related curvature correction in EASM**

One important assumption underlying the derivation of explicit algebraic stress models is that the convection of stress anisotropy and the diffusion of the stresses are both zero – i.e.:

$$\left(\frac{Da_{ij}}{Dt} - d_{ij} \right) = 0 \; ; \quad a_{ij} = \frac{\overline{u_i u_j}}{k} - \frac{2}{3}\delta_{ij}$$

The convective part, when expressed in Cartesian coordinates (as it normally is in most codes), can be very influential when the flow is highly curved and/or when it is subjected to strong normal straining. Evidence of this has been provided earlier in the discussion of the flow conditions at x/h=8. If curvature is the dominant process, while normal straining in the (local) streamwise direction is relatively weak, it is possible to derive, by appropriate coordinate transformation of the anisotropy gradient, an algebraic correction to the baseline algebraic

stress formulation, which accounts, approximately, for the curvature-induced contribution. This has been done formally by Wallin et al. (2003). It can be shown that

$$\frac{Da_{ij}}{Dt} \approx \left(a_{ik}\varepsilon_{kjm}\omega_m^{(r)} - \varepsilon_{ikm}\omega_m^{(r)}a_{kj} \right)$$

where $\omega^{(r)}$ is a curvature-related vorticity. In practice, the implementation of the correction can be effected by modifying the vorticity tensor as follows:

$$\mathbf{\Omega} \leftarrow \mathbf{\Omega} - c\mathbf{\Omega}^{(r)}$$

where the r.h.s. correction can be expressed as a function of the strain tensor and its (Oldroyd) derivatives only.

The effectiveness of this correction in the present flow – or, rather, the importance of the curvature contribution to the advective process – has been investigated by UT-Helsinki through two sets of comparison:

- The Wallin-Johansson EASM model was used with and without curvature corrections;
- The model without the correction was compared to the underlying full second-moment closure from which the model was derived.

Results for the EASM with and without the correction have already been presented and discussion in previous sections (Figs. 3.4.2.4, 3.4.3.4, 3.4.4.4 and 3.4.5.4), and these indicate that the contribution of the correction is very small. Thus, the profiles with and without the correction are close.

The strongest effects of stress transport would be expected within the recirculation region and above the windward side of the hill. Thus, a comparison of solutions for the EASM and the underlying RSM is given in Figs. 3.5.1 and 3.5.2 only for the locations x/h=2.0 and 8.0, respectively. At the former location, the contribution of stress transport is relatively weak, although substantially larger than that suggested by the curvature correction. The effect is most pronounced in the curved shear layer, but the curvature correction does not capture the

process. At x/h=8.0, the effect is larger, unsurprisingly, because of the combination of strong acceleration and curvature. Here, inclusion of the transport terms results in a marked suppression of turbulence energy and shear stress, reflecting mainly streamwise acceleration. Again, the curvature modification does not capture the process and is not, in the present flow, an effective means of recovering the terms ignored in the derivation of the algebraic model.

3.6 Budgets

Turbulence-energy budgets have been contributed in respect of many of the models featuring in this workshop, and a complete set is given in the Appendix 3. A searching analysis of the budgets is hindered by the fact that most models provide a rather poor representation of the mean-flow and turbulence fields. Thus, the budgets reflect not simply the ability of a model to represent any one process contributing to the budget, but is distorted, possibly seriously, by defects in the predicted primary fields.

Another problem is that most of the budgets, here presented in terms of outer scales, are dominated, over most of the flow away from the wall, by two processes: production and dissipation. Many of the interesting (and influential) processes take place very close to the wall, however, and these come to the fore only if the near-wall budgets are plotted in terms of wall (inner) scaling. Such data are not available.

In view of the above constraints, it seems most sensible to consider a few representative budgets for selected stations, in an effort to identify some general trends specific to different model categories. To this end, attention is focused on Figs. 3.6.1-3.6.3, relating to x/h=2.0, 6.0 and 8.0, respectively. In each figure, nine budgets (except convection) for nine 'representative' models are given. The term 'representative' is used very loosely, for earlier considerations show that model variants within any one category can give materially different results and, indeed, even qualitatively different behaviour.

Fig. 3.6.1 gives compares budgets for the section x/h=2.0. It is recalled that this position is roughly mid-way along the recirculation zone and may be assumed to represent the conditions over a significant proportion of this zone. The flow may be thought of as consisting of an outer

shear layer, emanating from the upstream separation line, which interacts with a lower reverse-flow layer, extending to y/h=0.7, which is itself a combination of post-reattachment fluid from the separated shear layer and a boundary layer nominally originating at the impingement line. Not surprisingly, the budget is dominated by production and dissipation in the outer shear layer. Most budgets show the production to be too low, consistent with a generally too low level of turbulence energy and shear stress in the shear layer predicted by many models, despite the excessive shear strain rate. Among the worst results are that from the v2F model, U-Ghent's cubic k-ε model and the EASM-k-ω model. The first, in particular, returns far too low levels for all processes. The RSMs give higher generation rates, but this is partly a reflection of seriously excessive shear-strain in the shear layer, which naturally enhances production. Most models give a qualitatively valid representation of dissipation, but this is not surprising in view of the close linkage between production and dissipation, both in reality and the models. However, only three models give anywhere nearly the correct variation of the high dissipation rate within the recirculation region. More generally, most models tend to underestimate the dissipation rate, but by a smaller margin than production, pointing to the flow being far from equilibrium conditions. The LES shows the excess in production over dissipation to be balanced mainly by diffusion, which is almost as influential as dissipation. None of the models gives anywhere near the correct variation of diffusion. UT-Helsinki's low-Re RSM comes close, but that model evidently gives a wrong turbulence production and dissipation profile, due to the shear layer being too thin and too highly sheared, and the excessive peak of the former is compensated by increased diffusion, as well as increased dissipation.

One overall conclusion emerging from the budgets at this station is that, consistent with insufficient shear stress and turbulence energy in the shear layer, production is generally much too low, pointing to some important large-scale dynamics being missed by the models.

The budgets for the section x/h=6.0 are shown in Fig. 3.6.2. It is recalled that the flow at this position undergoes (according to the LES) recovery, following reattachment at x/h=4.7. However, a number of models predict a substantial forward shift in the reattachment point, with some residual backflow still present at this position. As in the previous location, the budgets are dominated by production and dissipation, but diffusion is also highly influential.

Here, most models give a qualitatively correct representation of the budget contributions. Two notable exceptions are, again, the U-Manchester's v2F model and UT-Helsinki's low-Re RSM, the latter implying a far too weak recovery and the persistence of high shear, possibly because of a serious defect with the representation of diffusive transport in the outer part of the outer shear layer. As noted in earlier parts of the discussion, most models predict excessive strain, also at x/h=6. However, the maximum production rate is broadly correct, or slightly too high. Hence, in this region, the persistence of the excessive shear rate appears to be due to upstream effects, and the suggestion has already been made that the origin of the problem is that large-scale dynamics are missed in early parts of the evolution of the separated shear layer.

Finally, the budgets at x/h=8. are shown in Fig. 3.6.3. Here, some dramatic differences arise between the LES and most model predictions, reinforcing the extreme challenges posed by the severe straining in this area. The LES budget shows that in the production around its peak to be balanced by dissipation and (negative) turbulent diffusion. The steep rise in diffusion towards the wall reflects the contribution by pressure fluctuations ("pressure diffusion") which is agglomerated with diffusion by velocity fluctuations. However, closer to the wall, around y/h=0.8, production and diffusion are balanced mainly by (negative) advection (which is, unfortunately, not included in Fig. 3.6.3) and, to a lesser extent, dissipation. Thus, at this station, the usual link between (positive) production and dissipation does not apply. Indeed, very close to the wall (not visible in Fig. 3.6.3), production is negative! Moreover, advection is very influential. As seen from Fig. 3.6.3, most models predict excessive production, due to the severe straining. EASMs and RSMs tend to limit this excess by virtue of maintaining the correct linkage between normal straining and stresses. The SST model, on the other hand, does so by means of a limiter. The v2F model seems to perform well here, but it is recalled that it gave far too low rates of production further upstream, so the picture it projects here is misleading. U-Ghent's NLEVM seriously exaggerates the production, suggesting the absence of a correction that limits the response of the stresses to the linear strain term. Finally, the linear k-ω also performs poorly, again because of the excessive response of the stresses and turbulence energy to normal straining. Most models seriously over-estimate the dissipation rate and also seriously misrepresent diffusion, although some qualitative trends are returned broadly correctly.

In summary, the predicted budgets are mostly at serious variance with the LES data, especially at x/h=8.0. However, the models based on second-moment closure (including EASMs) at least give a reasonable level of production. Dissipation is generally excessive, and diffusion is poorly modelled.

References

Abe, K., Jang, Y.-J. and Leschziner, M.A.(2003): An investigation of wall-anisotropy expressions and length-scale equations for non-linear eddy-viscosity models, *Int. J Heat and Fluid Flow* 24, 181-198.

Apsley, D.D. and Leschziner, M.A.(1998): A new low-Reynolds-number nonlinear two-equation turbulence model for complex flows, *Int. J. Heat and Fluid Flow* 19, 209-222.

Chen, H.C., Jang, Y.J. and Han, J.C. (2000): Computation of heat transfer in rotating two-pass square channels by a second-moment closure model, *Int. J. Heat and Mass Transfer* 43, 1603-1616.

Deng, G. and Visonneau, M. (2002): Implementation et validation du modele k-ω dans n3s-natur, Rapport de Contrat ECN.

Froehlich, J., Mellen, C., Rodi, W., Temmerman, L. and Leschziner, M.A. (2004), Highly resolved large eddy simulation of separated flow in a channel with streamwise periodic constrictions, *Journal Fluid Mech*. (in press).

Gatski, T.B. and Speziale, C.G. (1993): On explicit algebraic stress models for complex turbulent flows, *J. Fluid Mech.* 254, 59-78.

Jang, Y.J., Leschziner, M.A., Abe, K. and Temmerman, L. (2002): Investigation of anisotropy-resolving turbulence models by reference to highly-resolved LES data for separated flows. *Flow, Turbulence and Combustion* 69, 161-203.

Launder, B.E., Reece, G.J. and Rodi, W. (1975): Progress in the development of Reynolds-stress turbulence closure, *J. Fluid Mech.* 68, 537-566.

Launder, B.E. and Sharma, B.I. (1974): Application of the energy-dissipation model of turbulence to the calculation of flow near a spinning disc, *Letters in Heat and Mass Transfer* 1, 131-138.

Lien, F.S., Durbin, P.A. (1996): Non-linear k-ε-v^2 modelling with application to high lift. Center for Turbulence Research, Proc. of the Summer Program, 5-26.

Menter, F. R. (1994): Two equation eddy viscosity turbulence models for engineering applications, *J. AIAA* 32, 1598-1605.

Merci, B. and Dick, E. (2004): Predictive capabilities of an improved cubic k-ε model for inert steady flows, *Flow, Turbulence and Combustion* (in press).

Spalart P.R. and Allmaras, S.R. (1992): A one-equation turbulence model for aerodynamic flows. *AIAA Paper 92-0439*.

Speziale, C.G, Sarkar, S. and Gatski, T.B. (1991) Modelling the pressure –strain correlation of turbulence: An invariant dynamical systems approach. *Journal of Fluid Mech*. 227 , 245-272.

Temmerman, L., Leschziner, M.A., Mellen, C., and Frohlich, J. (2003): Investigation of wall-function approximations and subgrid-scale models in large eddy simulation of separated flow in a channel with streamwise periodic constrictions. *Int. J. Heat and Fluid Flow* 24, 157-180.

Wallin, S., Hellsten, A., Schatz, M., Rung, T., Peshkin, D., Johansson, A.V. (2003): Streamline curvature corrected algebraic Reynolds stress turbulence modelling, *Proceedings of the 3rd Int. Symposium on Turbulence and Shear Flow Phenomena*, I, 45-50, Sendai, Japan.

Wallin, S. and Johansson, A.V. (2000): An explicit algebraic Reynolds stress model for incompressible and compressible turbulent flows, *J. Fluid Mech*. 403, 89-132.

Wang, C., Jang, Y.J. and Leschziner, M.A. (2004): Modelling two- and three-dimensional separation from curved surfaces with anisotropy-resolving turbulence closures, *Int. J Heat and Fluid Flow* 25, 499-512.

Wilcox, D.C., (1988): Reassessment of the scale-determining equation for advanced turbulence models. *J. AIAA* 26, 1299-1310.

EASM–k–ε model:
Grid sensitivity analysis (NASA)

Location: 004 ($x/h = 2.00$)

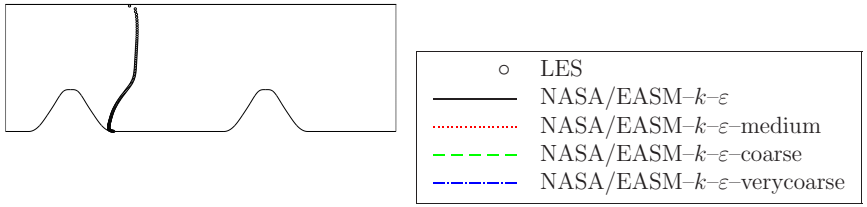

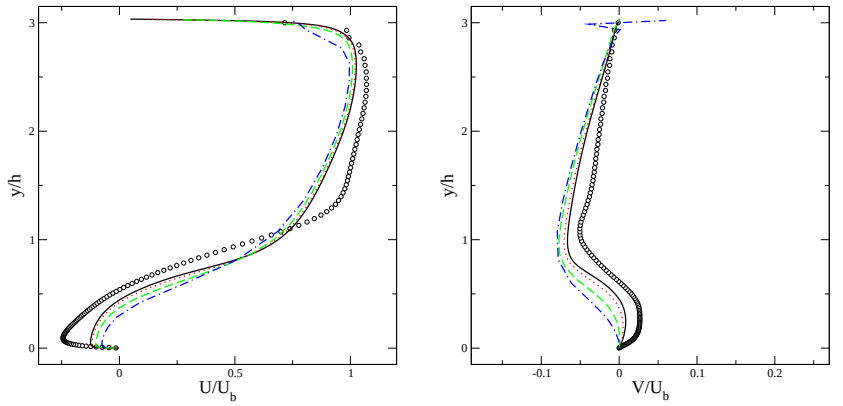

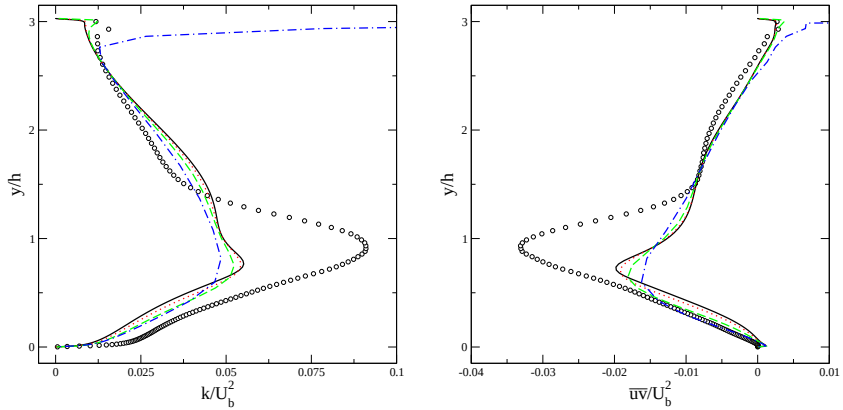

Figure 3.2.1

EASM–k–ε model:
Grid sensitivity analysis (NASA)

Location: 004 ($x/h = 2.00$)

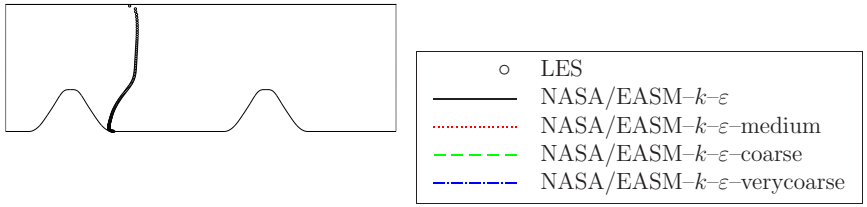

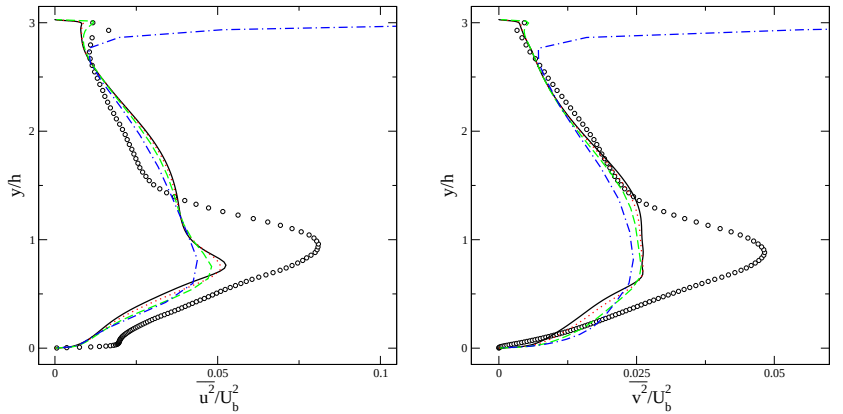

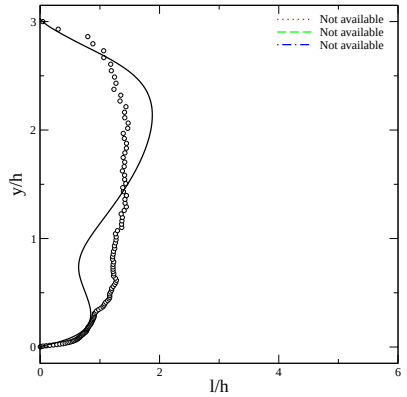

Comparison between results obtained on structured and unstructured meshes (Tampere UT)
Part 1

Location: 004 ($x/h = 2.00$)

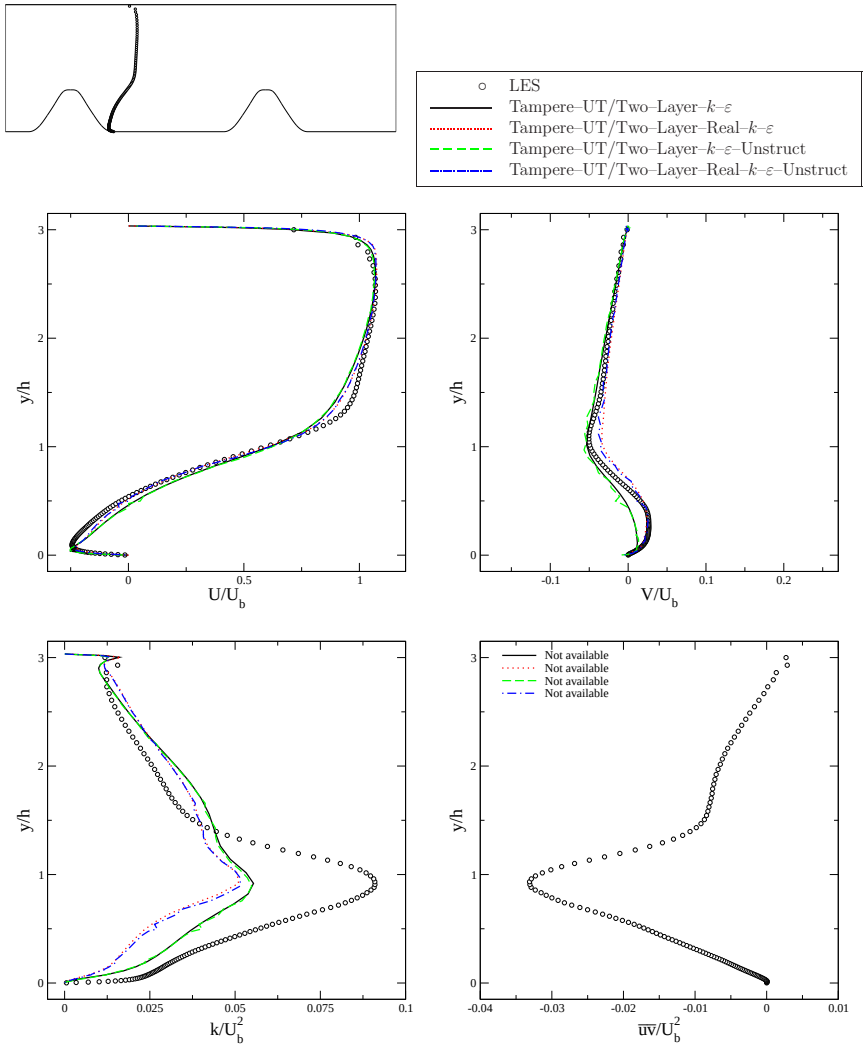

Figure 3.2.2

Comparison between results obtained on structured and unstructured meshes (Tampere UT)
Part 1

Location: 004 ($x/h = 2.00$)

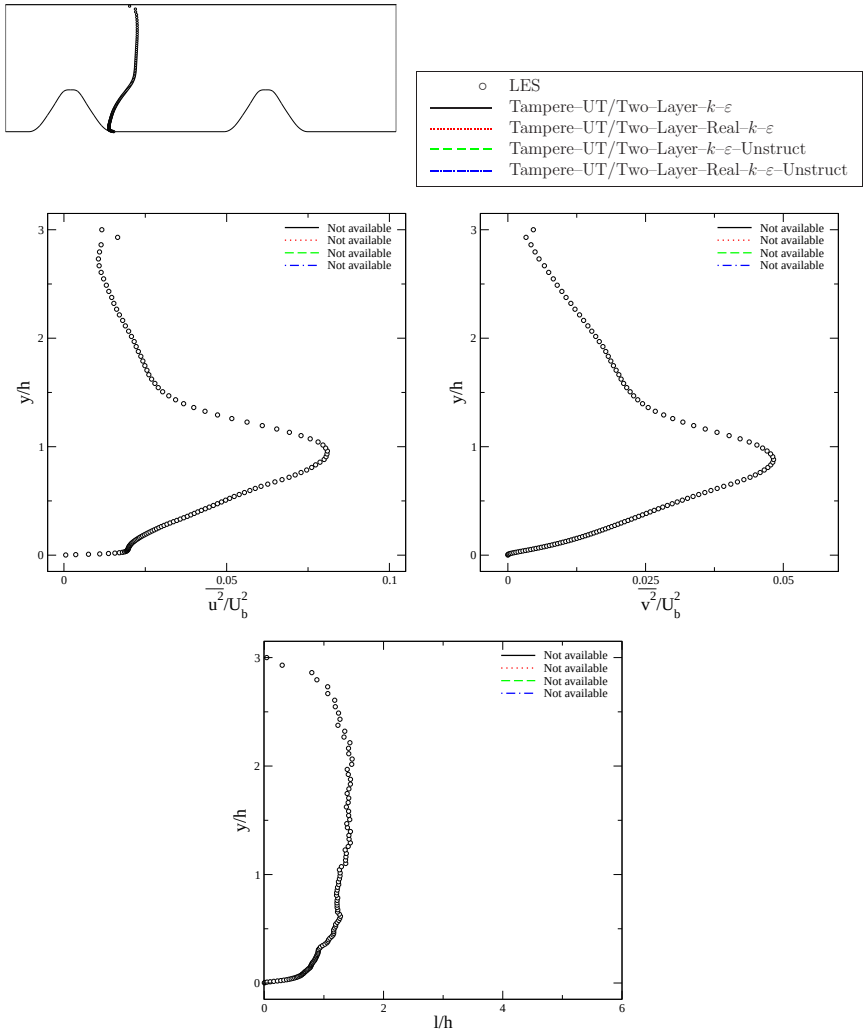

Comparison between results obtained on structured and unstructured meshes (Tampere UT)
Part 2

Location: 004 ($x/h = 2.00$)

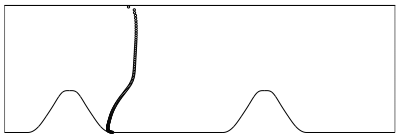

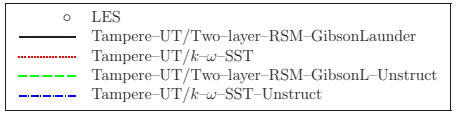

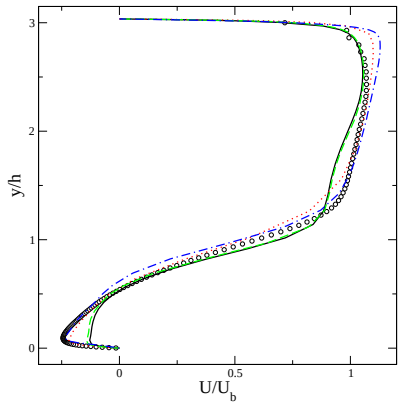

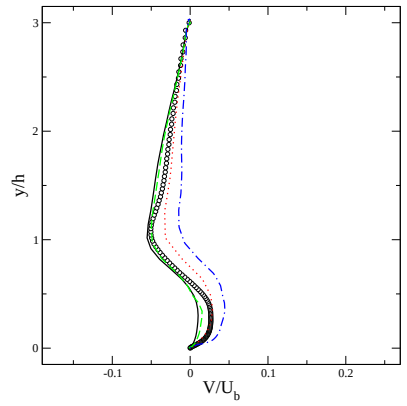

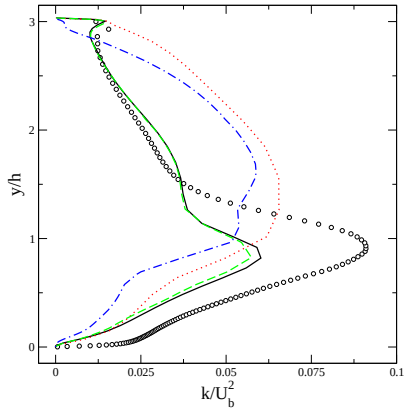

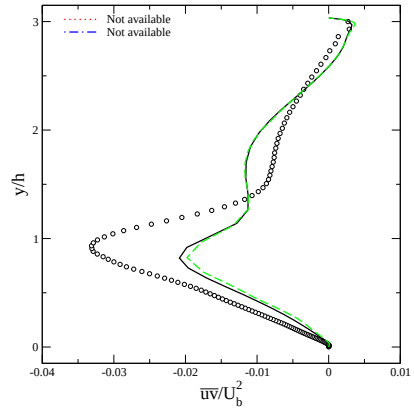

Figure 3.2.3

Comparison between results obtained on structured and unstructured meshes (Tampere UT)
Part 2

Location: 004 ($x/h = 2.00$)

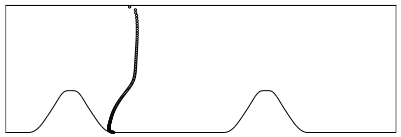

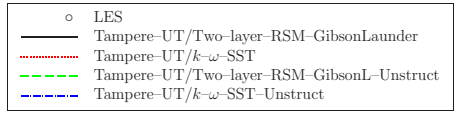

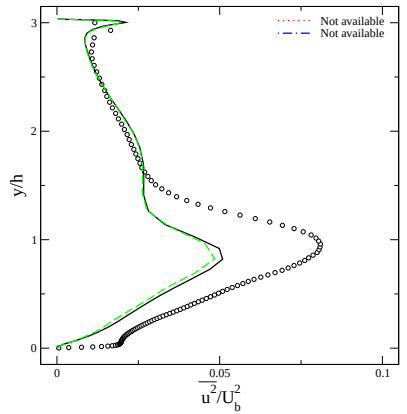

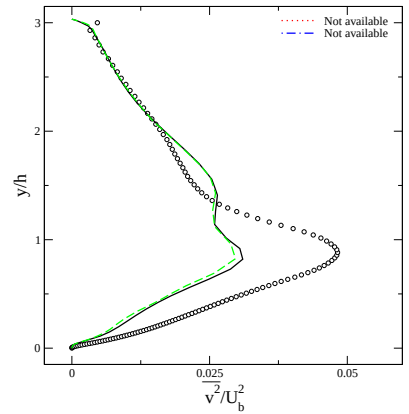

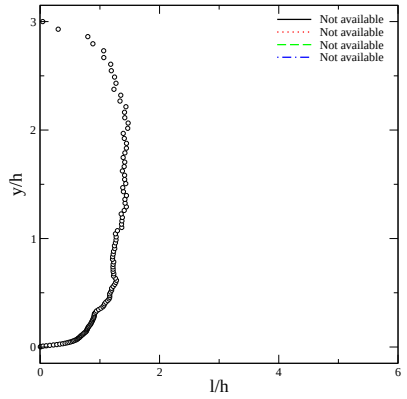

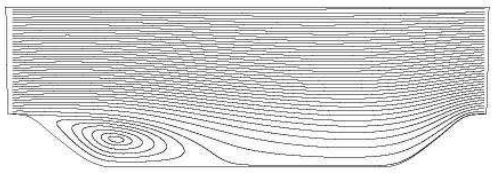

LES

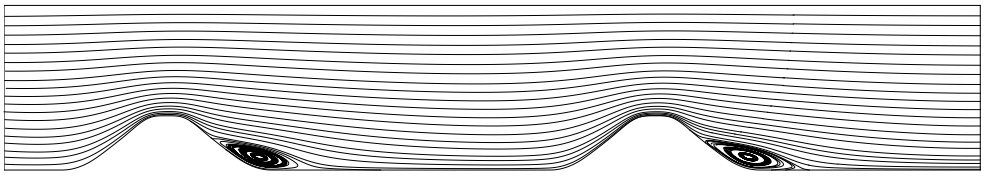

TU–Darmstadt/Standard–k–ε+WF

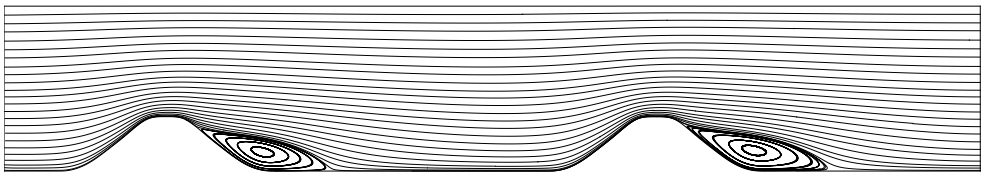

TU–Darmstadt/Launder–Sharma–k–ε

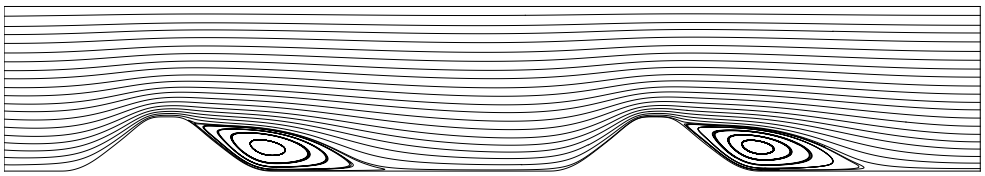

TU–Darmstadt/Two–Layer–k–ε

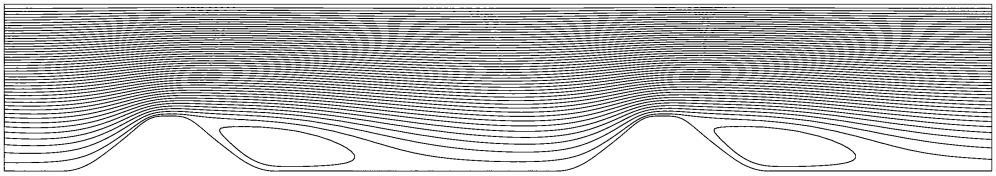

Tampere–UT/Two–Layer–k–ε

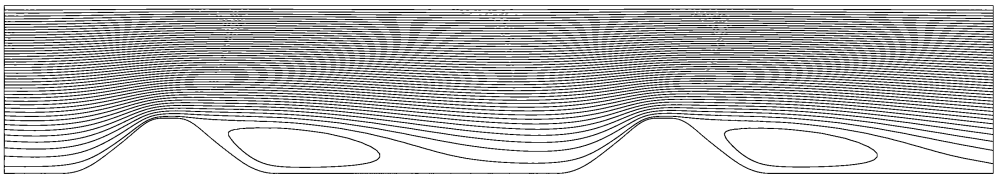

Tampere–UT/Two–Layer–Real–k–ε

Figure 3.3.1

Linear k–ω models

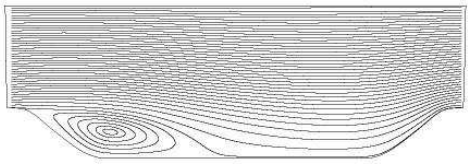

LES

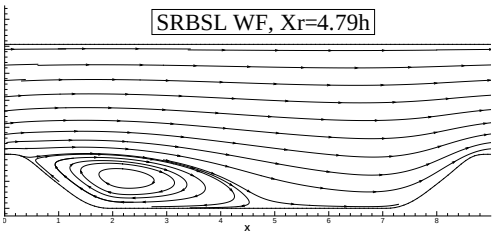

EC–Nantes/k–ω–BSL+WF

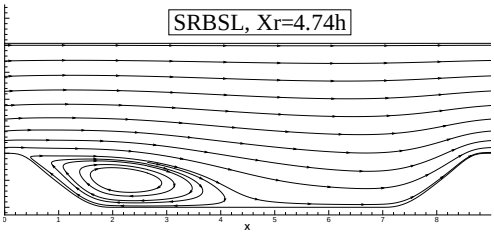

EC–Nantes/k–ω–BSL

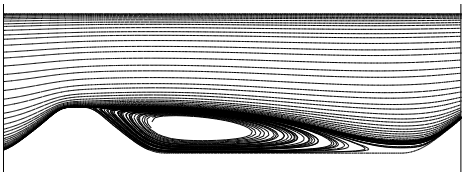

NASA/k–ω–SST

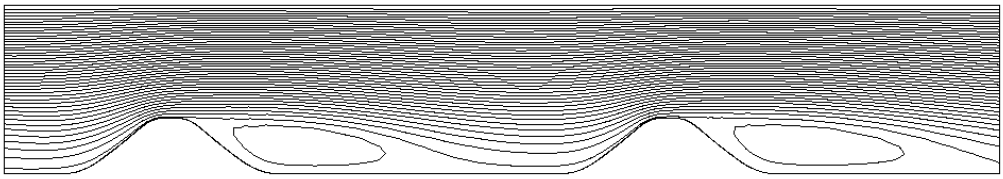

Tampere–UT/k–ω–SST

Figure 3.3.2

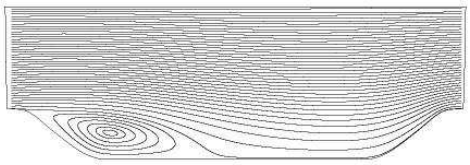

LES

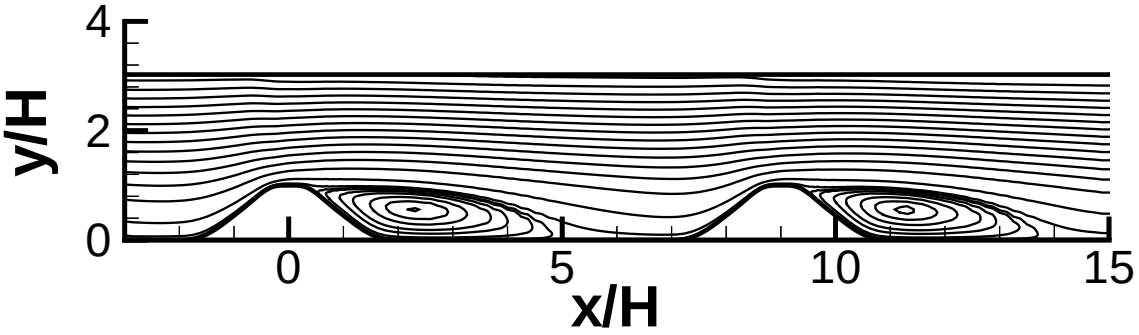

Ghent–U/cubic–k–ε

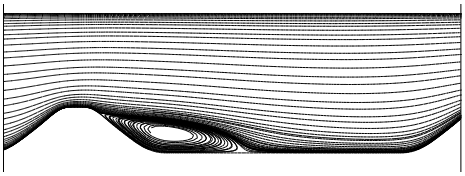

NASA/EASM–k–ε

Figure 3.3.3

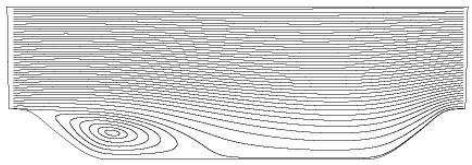

LES

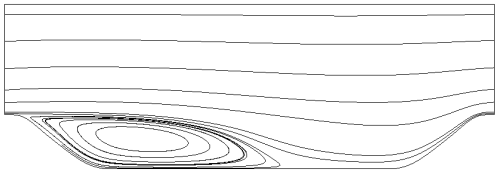

Helsinki–UT/EARSM–WallinJ–k–ω

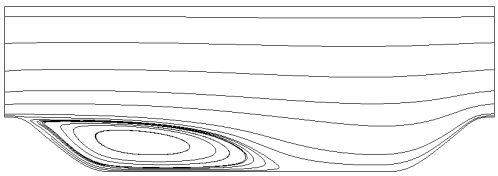

Helsinki–UT/EARSM–CCWallinJ–k–ω

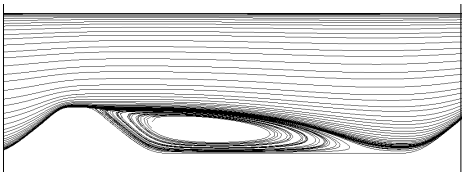

NASA/EASM–k–ω

Figure 3.3.4

Other eddy-viscosity models:
Spalart-Allmaras model
$\overline{v^2}$–f model

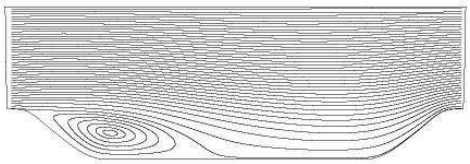

LES

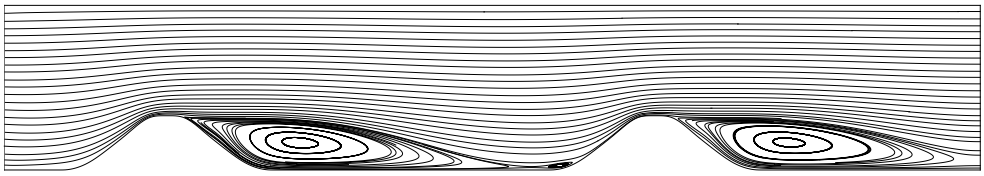

TU–Darmstadt/Spalart–Allmaras

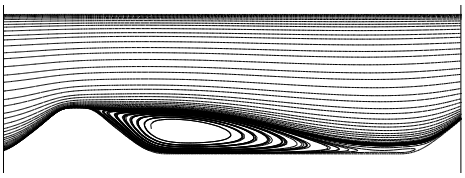

NASA/Spalart–Allmaras

Figure 3.3.5

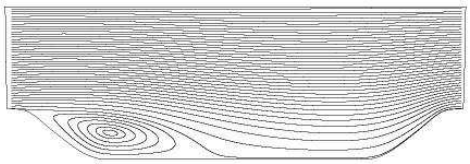

LES

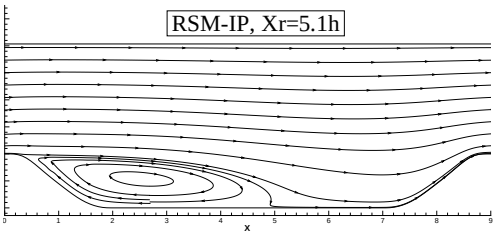

EC–Nantes/Low–*Re*–RSM–IP

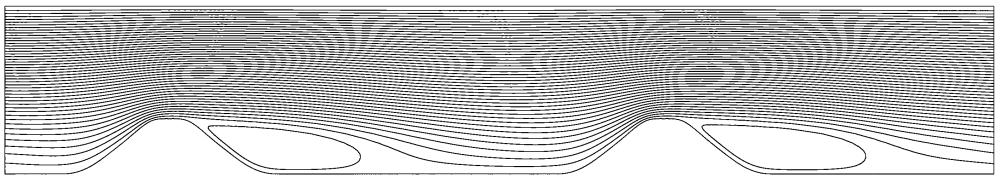

Tampere–UT/Two–layer–RSM–GibsonLaunder

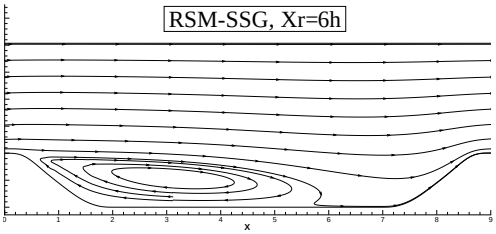

EC–Nantes/Low–*Re*–RSM–SSG

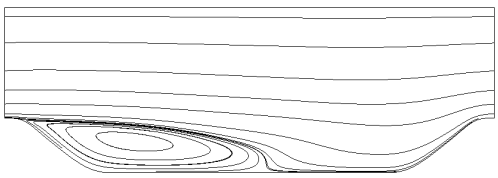

Helsinki–UT/Low–*Re*–RSM

Figure 3.3.6

Flow over a 2–D hill: PROFILES

Linear and quasilinear k–ε models

Location: 001 ($x/h = 0.05$)

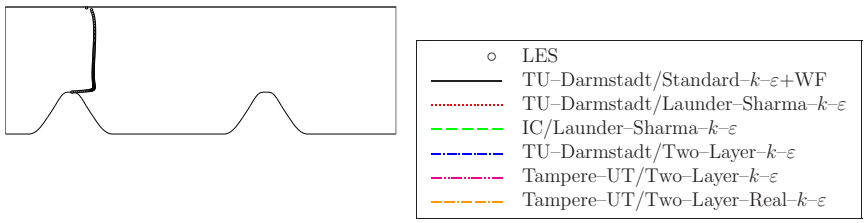

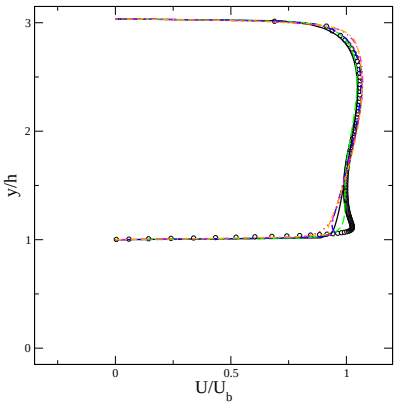

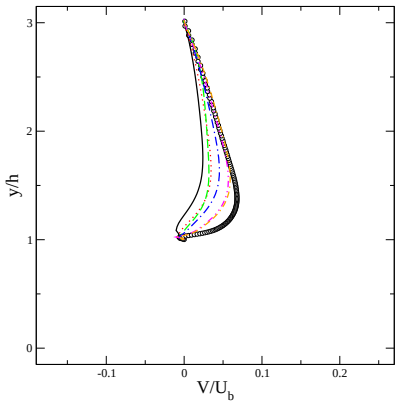

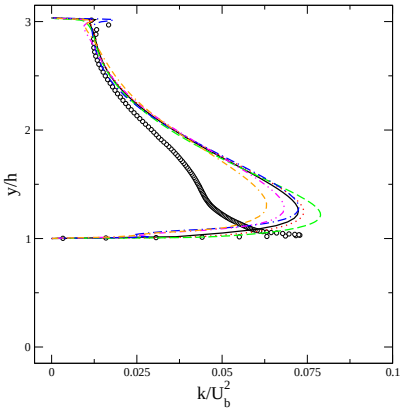

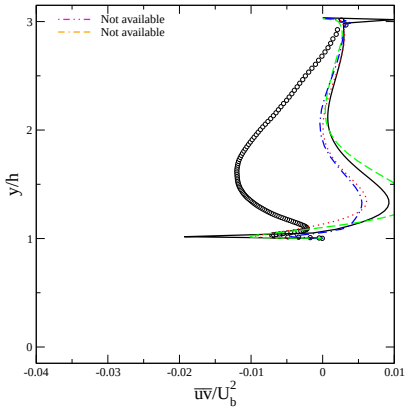

Figure 3.4.2.1

Flow over a 2–D hill: PROFILES

Linear and quasilinear k–ε models

Location: 001 ($x/h = 0.05$)

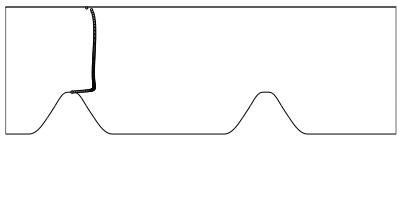

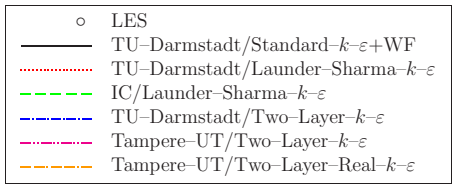

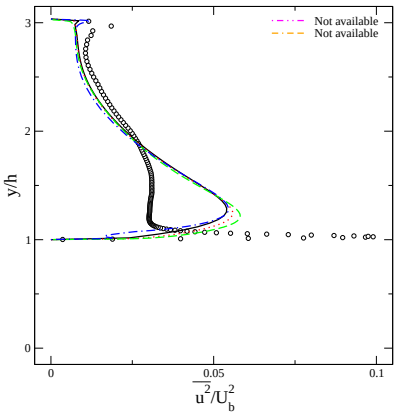

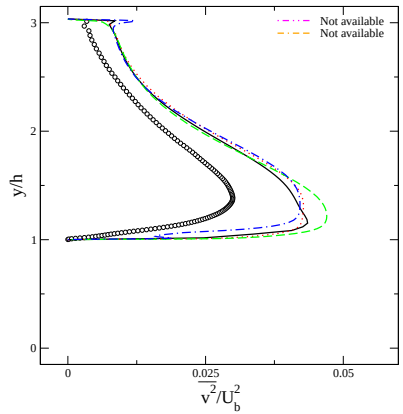

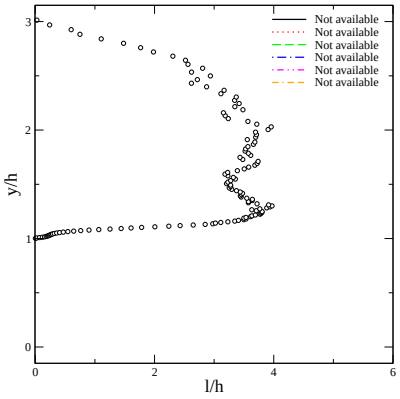

Flow over a 2–D hill: PROFILES

Linear k–ω models

Location: 001 ($x/h = 0.05$)

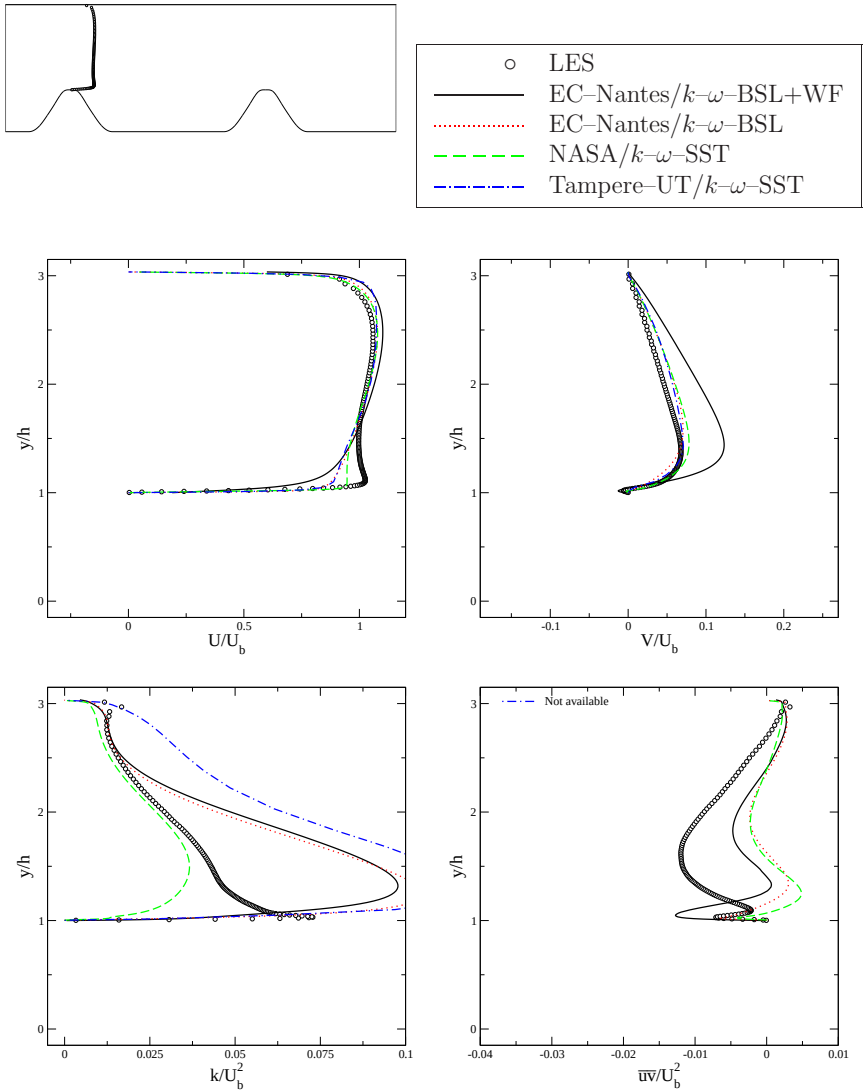

Figure 3.4.2.2

Flow over a 2–D hill: PROFILES

Linear k–ω models

Location: 001 ($x/h = 0.05$)

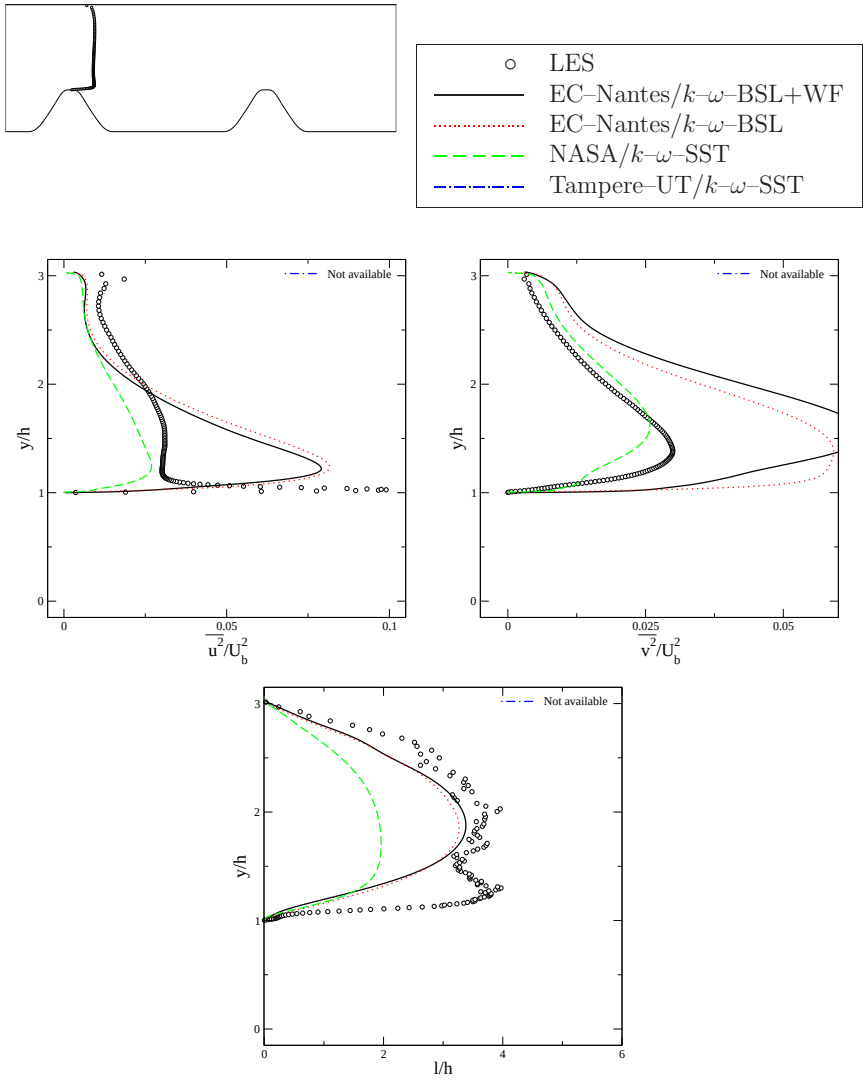

Flow over a 2–D hill: PROFILES

Nonlinear k–ε models

Location: 001 ($x/h = 0.05$)

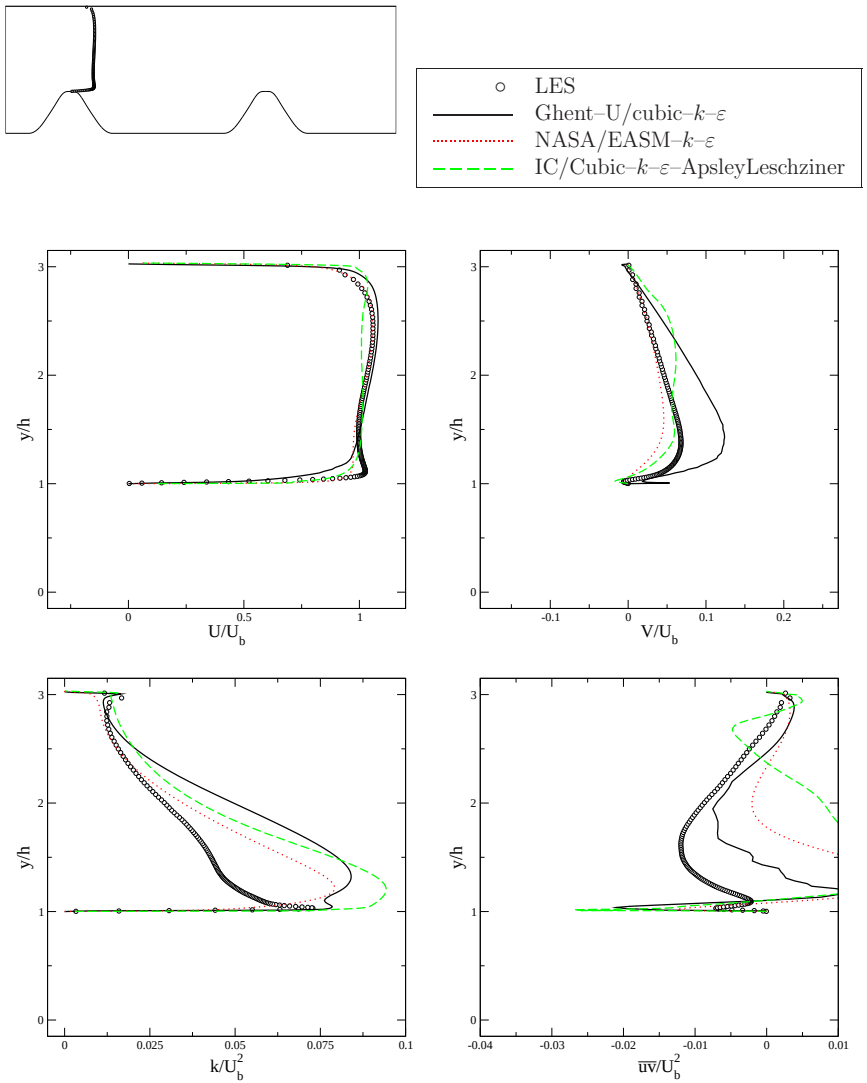

Figure 3.4.2.3

Flow over a 2–D hill: PROFILES

Nonlinear k–ε models

Location: 001 ($x/h = 0.05$)

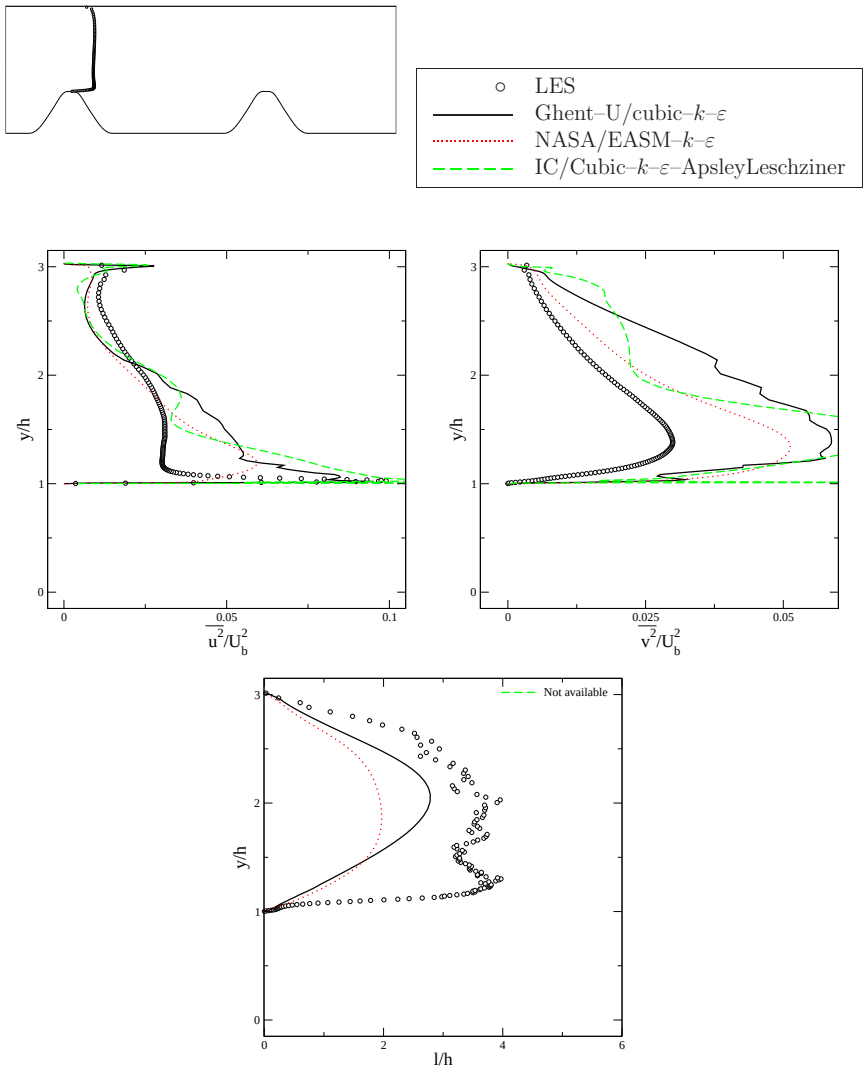

Flow over a 2–D hill: PROFILES

Nonlinear k–ω models

Location: 001 ($x/h = 0.05$)

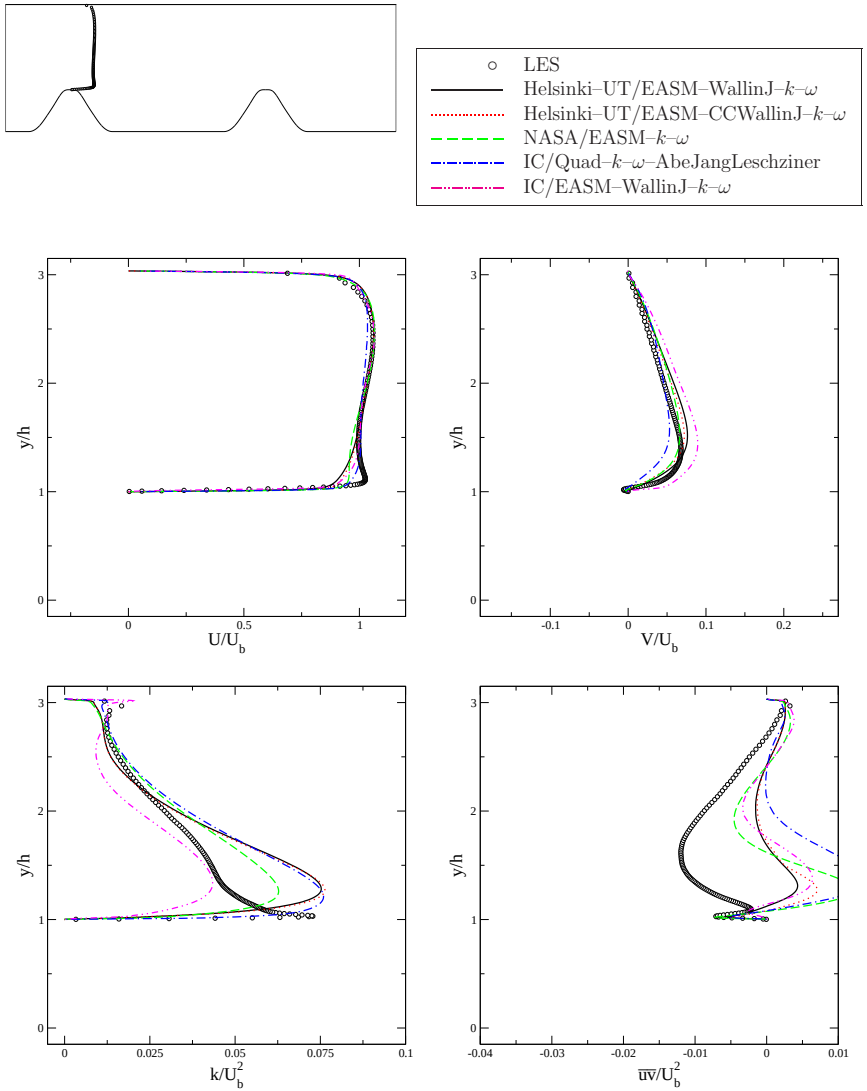

Figure 3.4.2.4

Flow over a 2–D hill: PROFILES

Nonlinear k–ω models

Location: 001 ($x/h = 0.05$)

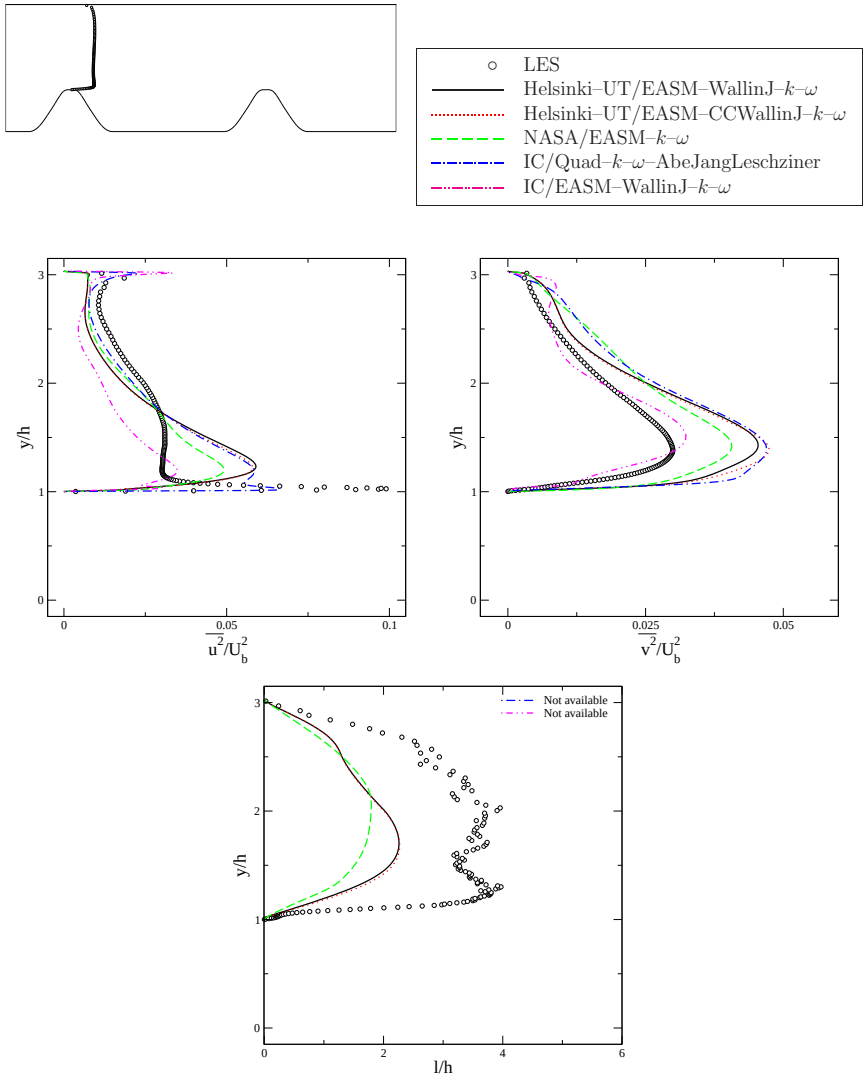

Other eddy-viscosity models:
Spalart-Allmaras model
$\overline{v^2}$–f model

Location: 001 ($x/h = 0.05$)

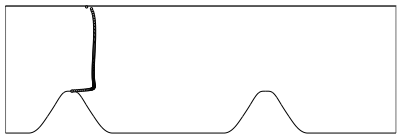

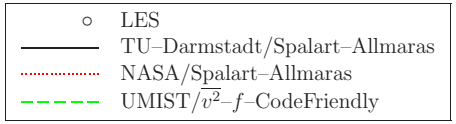

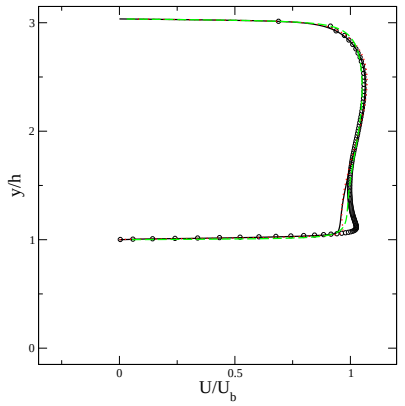

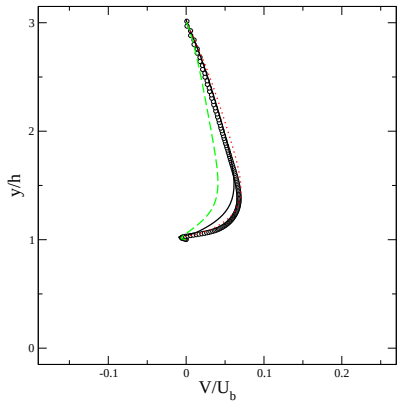

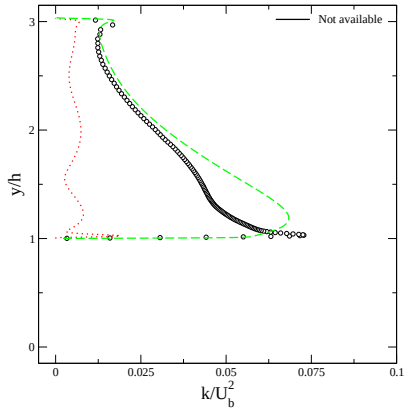

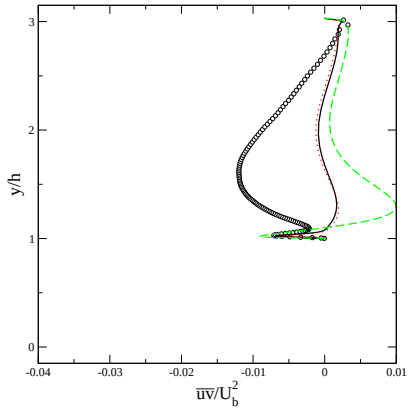

Figure 3.4.2.5

Other eddy-viscosity models:
Spalart-Allmaras model
$\overline{v^2}$–f model

Location: 001 ($x/h = 0.05$)

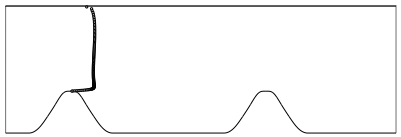

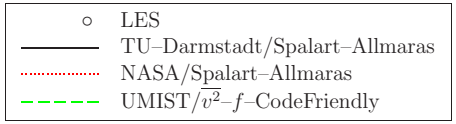

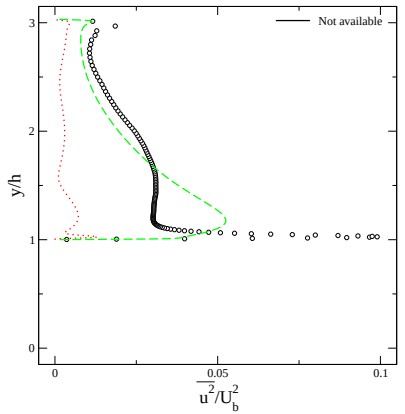

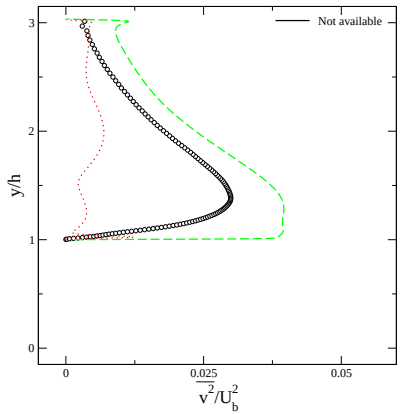

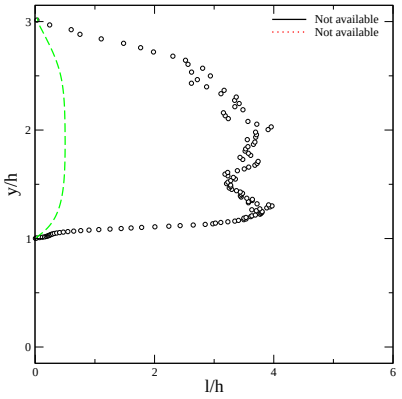

Flow over a 2–D hill: PROFILES

Reynolds stress models

Location: 001 ($x/h = 0.05$)

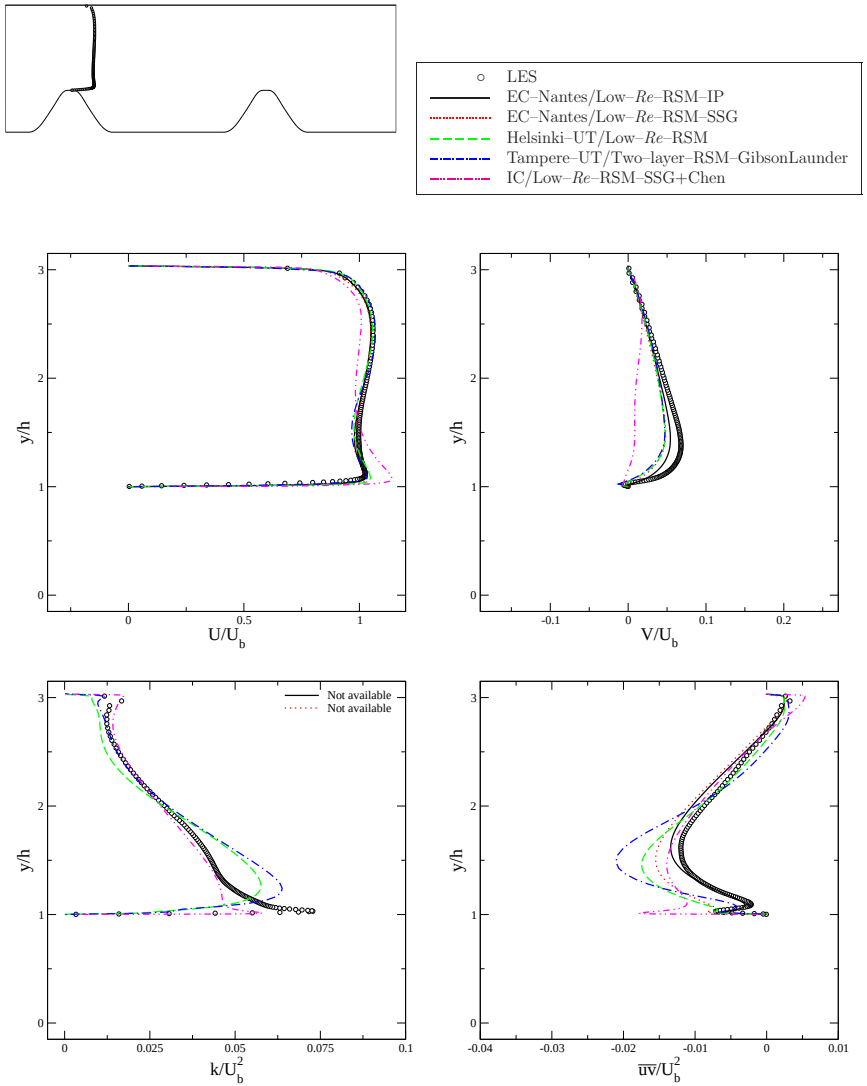

Figure 3.4.2.6

Flow over a 2–D hill: PROFILES

Reynolds stress models

Location: 001 ($x/h = 0.05$)

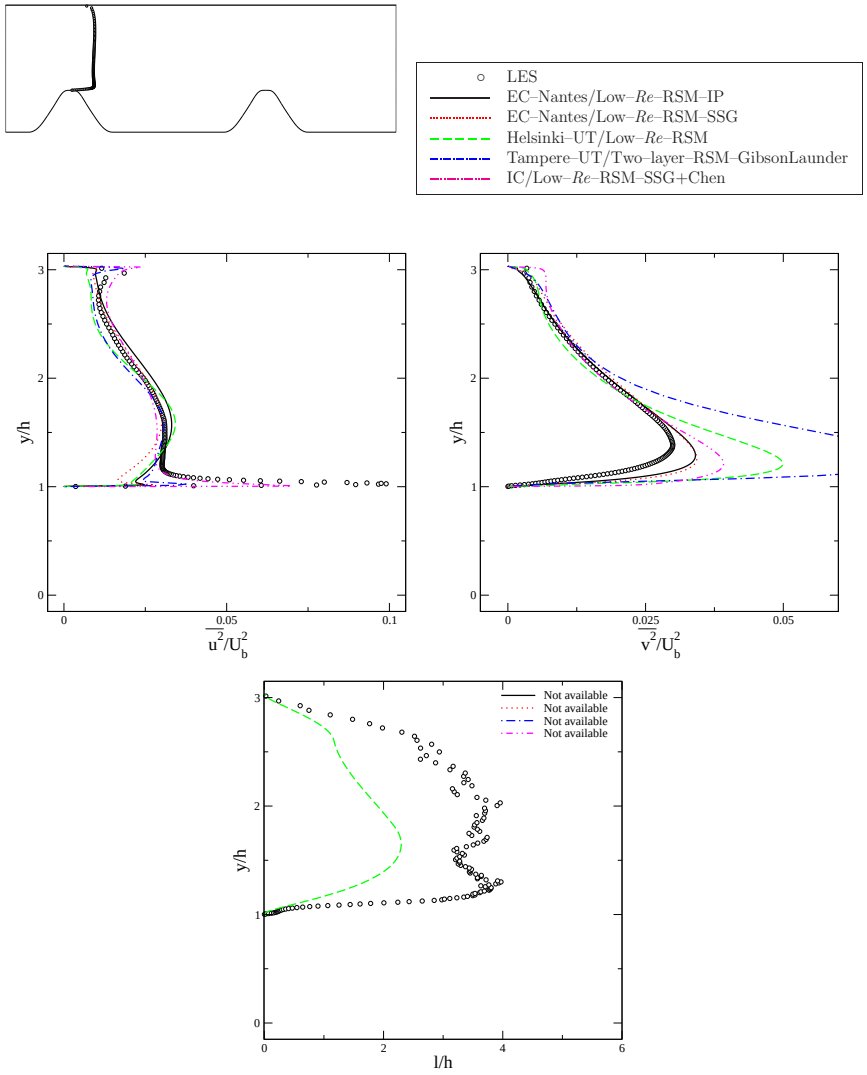

Flow over a 2–D hill: PROFILES

Linear and quasilinear k–ε models

Location: 004 ($x/h = 2.00$)

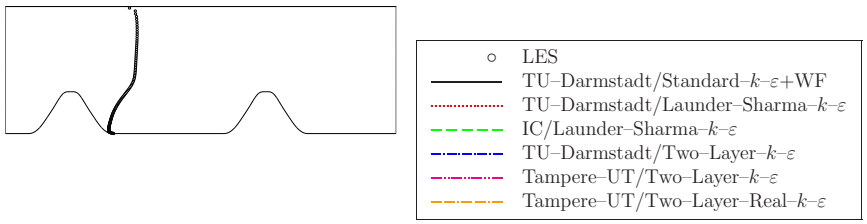

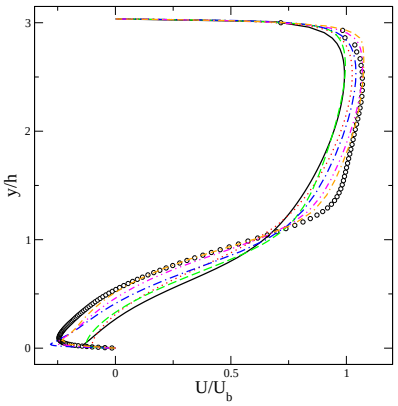

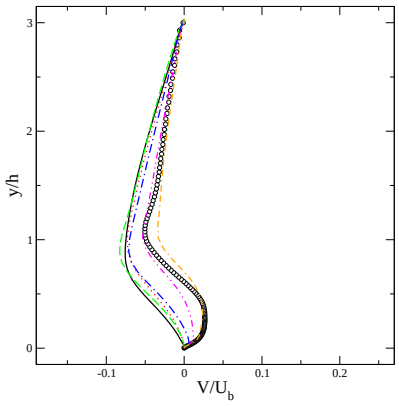

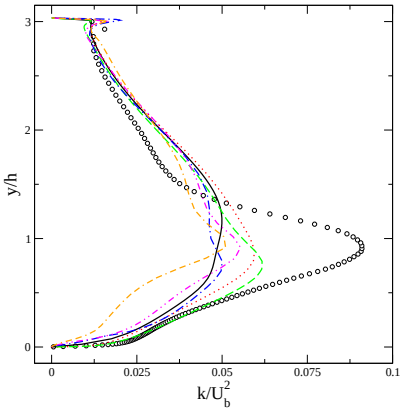

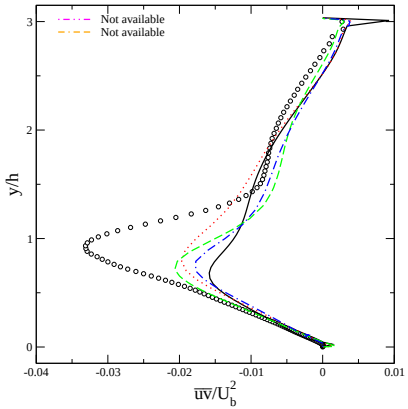

Figure 3.4.3.1

Flow over a 2–D hill: PROFILES

Linear and quasilinear k–ε models

Location: 004 ($x/h = 2.00$)

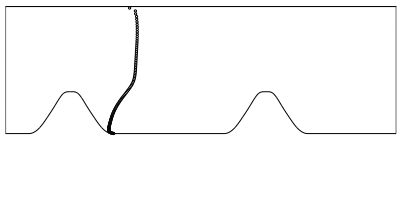

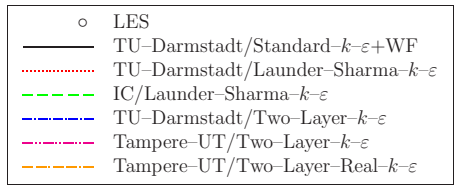

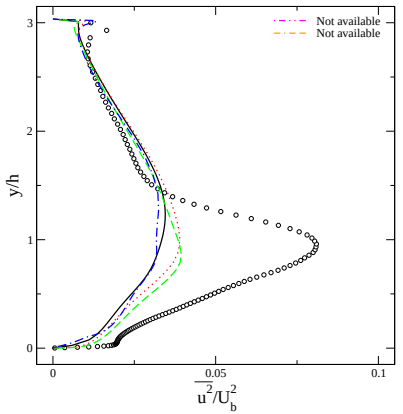

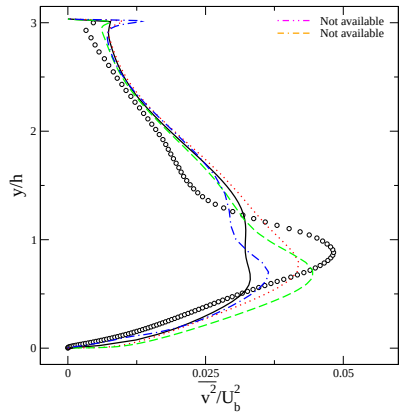

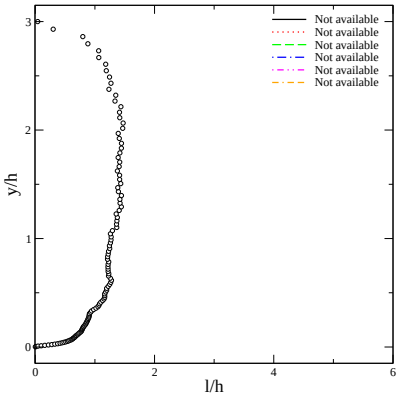

Flow over a 2–D hill: PROFILES

Linear k–ω models

Location: 004 ($x/h = 2.00$)

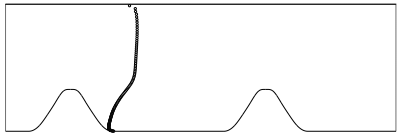

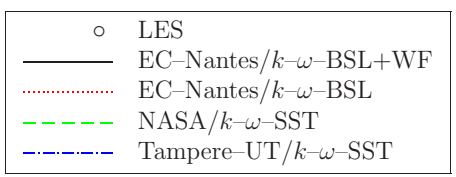

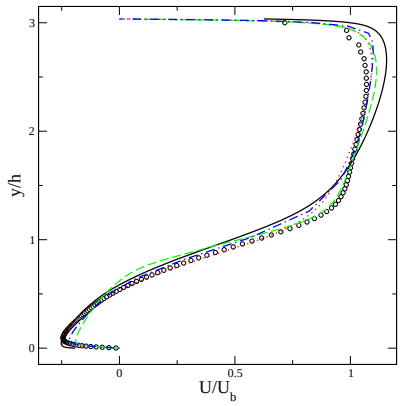

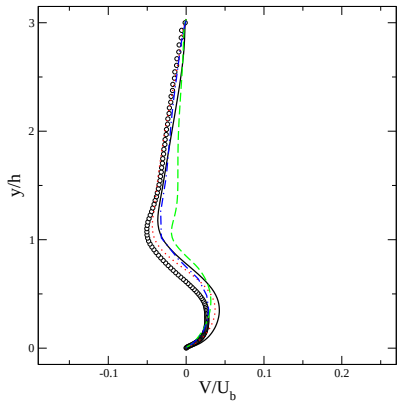

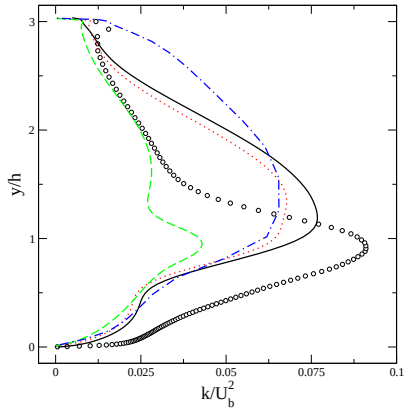

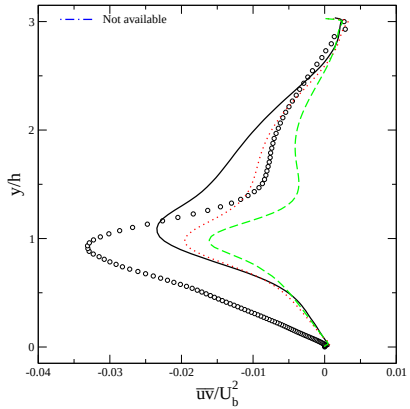

Figure 3.4.3.2

Flow over a 2–D hill: PROFILES

Linear k–ω models

Location: 004 ($x/h = 2.00$)

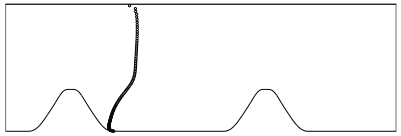

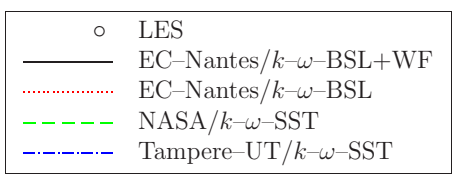

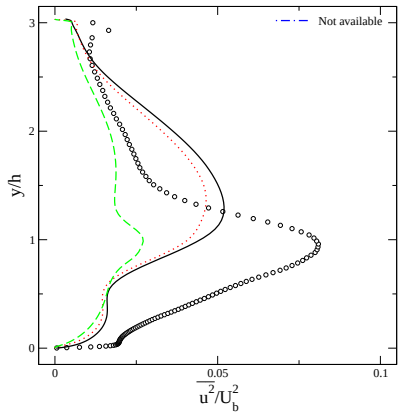

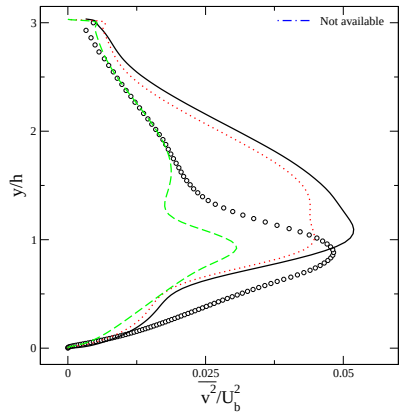

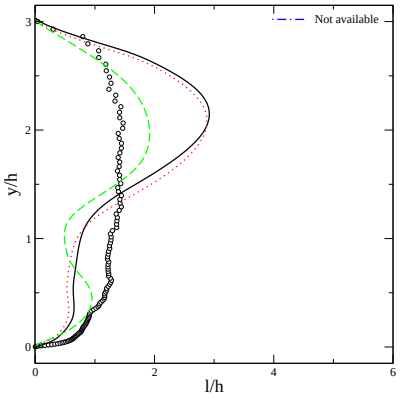

Flow over a 2–D hill: PROFILES

Nonlinear k–ε models

Location: 004 ($x/h = 2.00$)

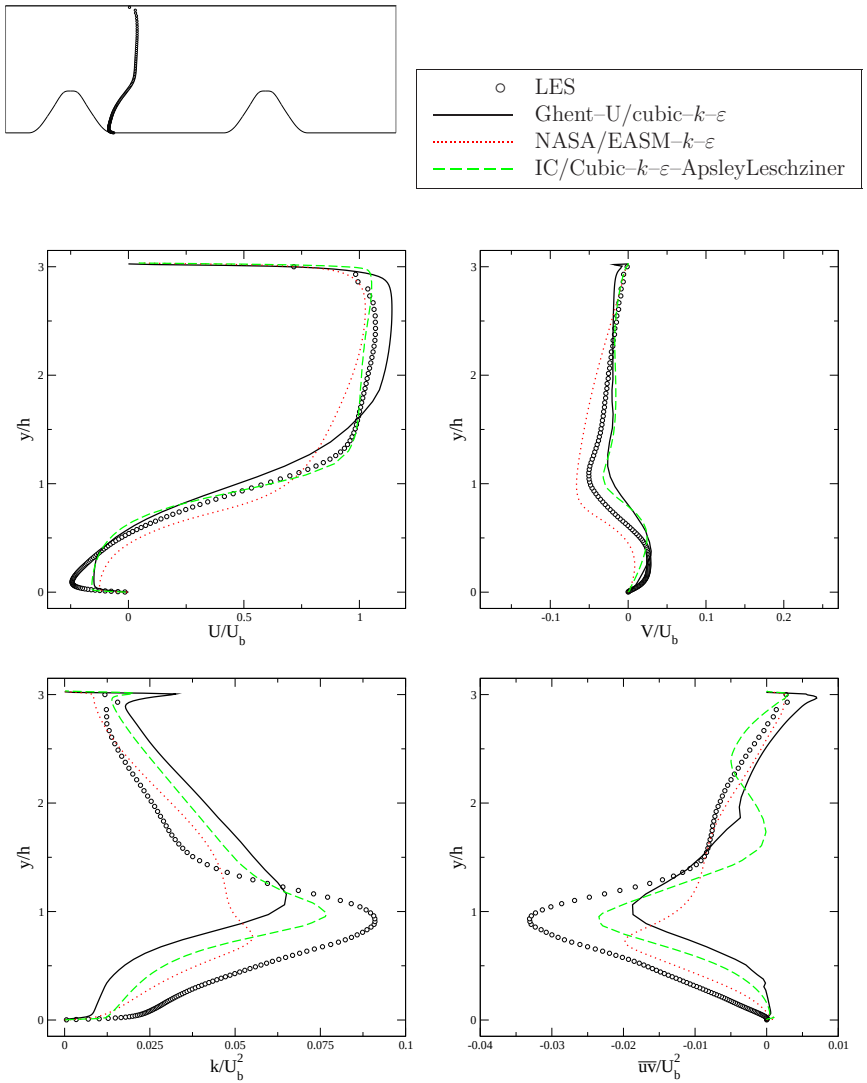

Figure 3.4.3.3

Flow over a 2–D hill: PROFILES

Nonlinear k–ε models

Location: 004 ($x/h = 2.00$)

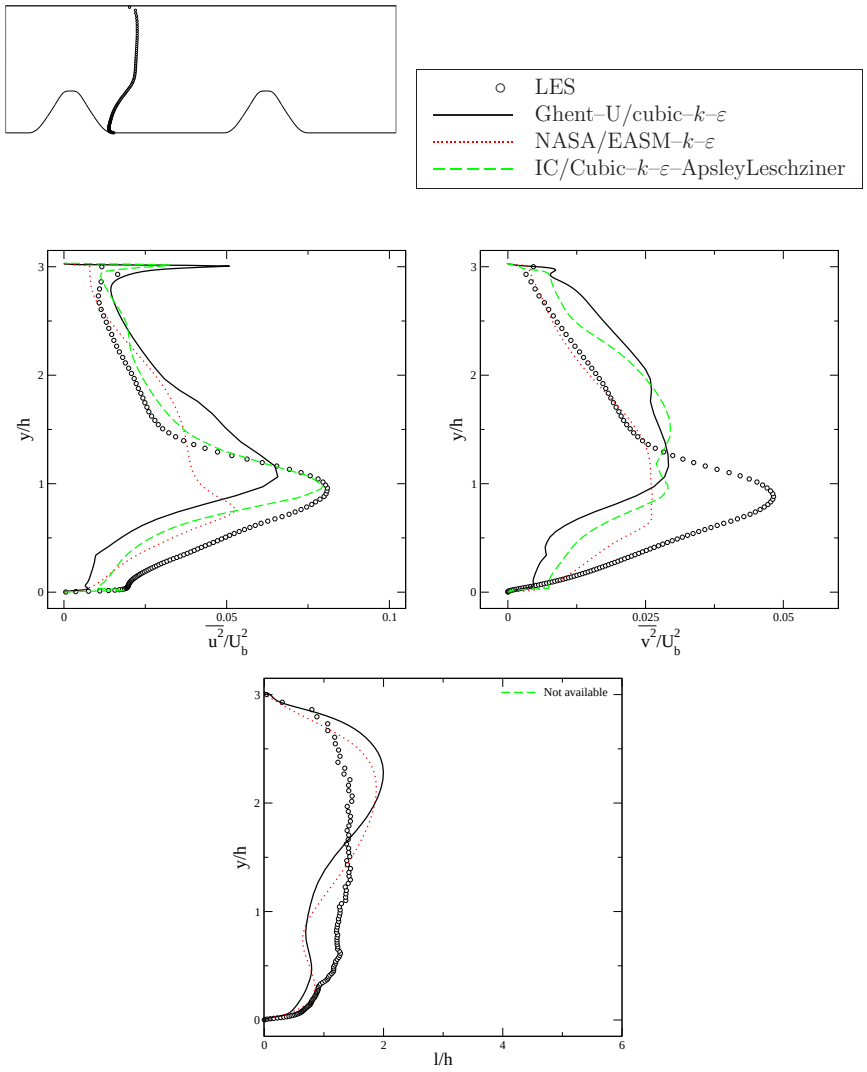

Flow over a 2–D hill: PROFILES

Nonlinear k–ω models

Location: 004 ($x/h = 2.00$)

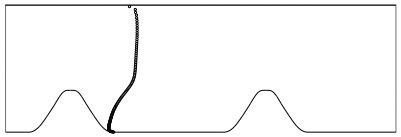

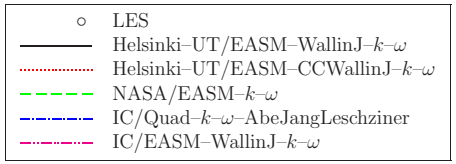

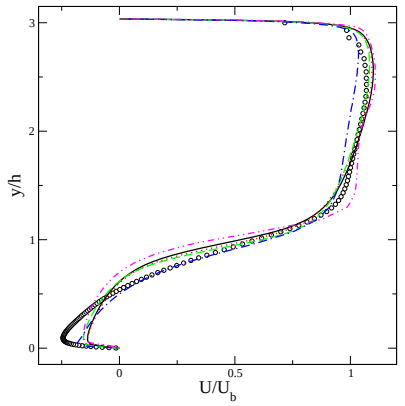

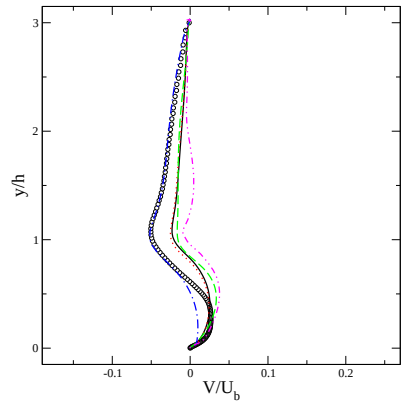

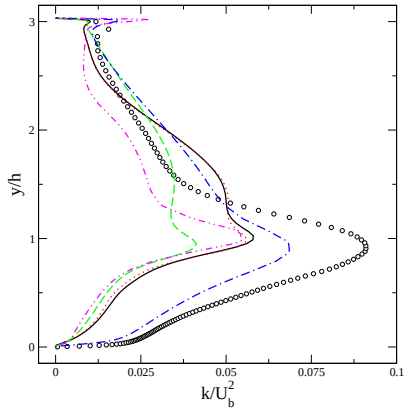

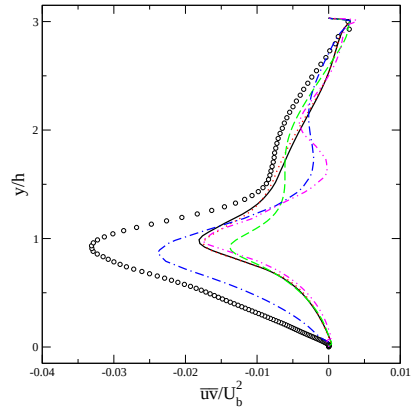

Figure 3.4.3.4

Flow over a 2–D hill: PROFILES

Nonlinear k–ω models

Location: 004 ($x/h = 2.00$)

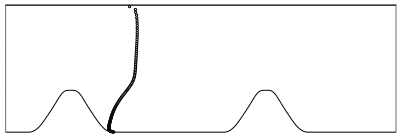

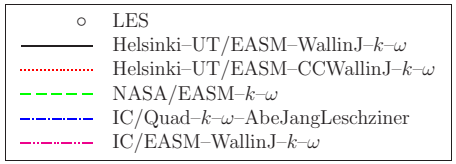

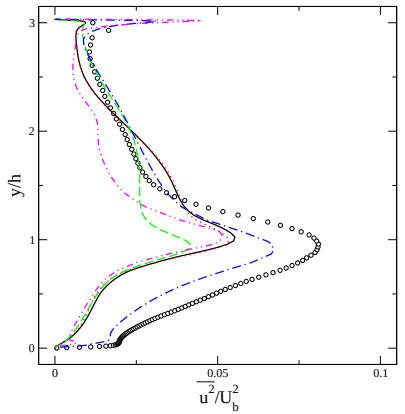

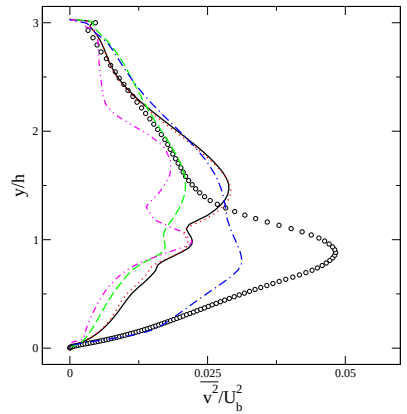

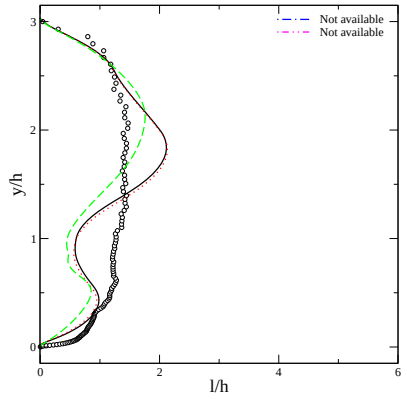

Other eddy-viscosity models:
Spalart-Allmaras model
$\overline{v^2}$–f model

Location: 004 ($x/h = 2.00$)

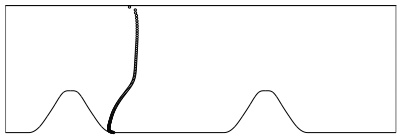

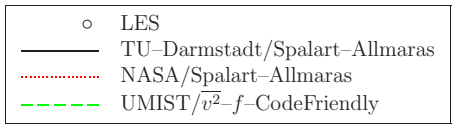

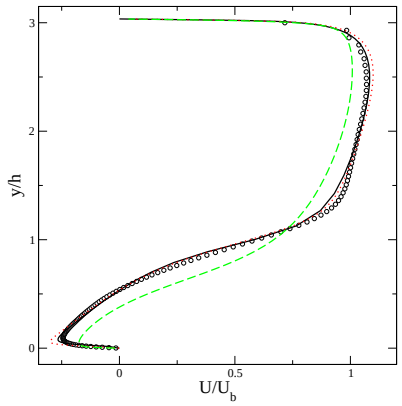

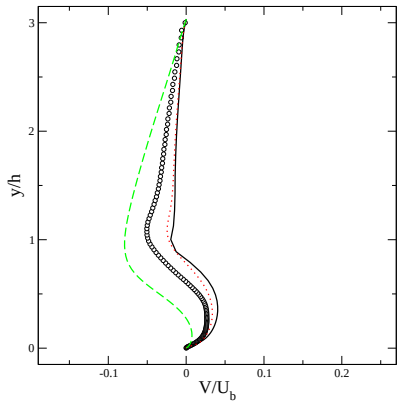

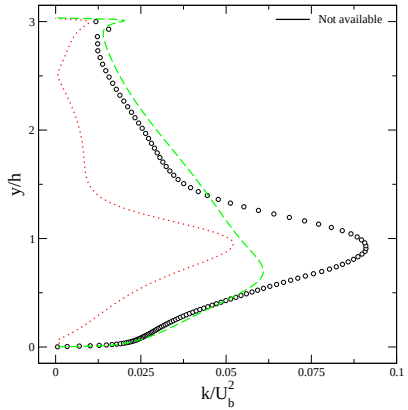

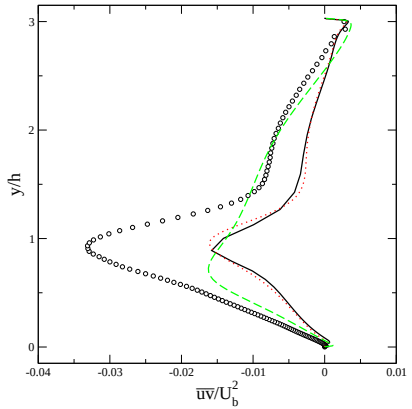

Figure 3.4.3.5

Other eddy-viscosity models:
Spalart-Allmaras model
$\overline{v^2}$–f model

Location: 004 ($x/h = 2.00$)

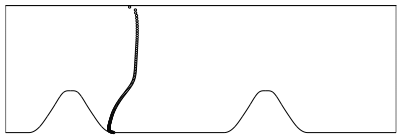

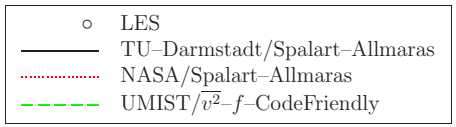

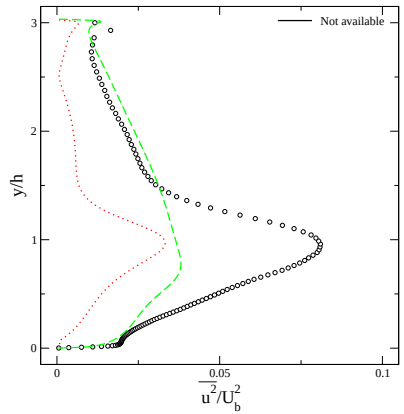

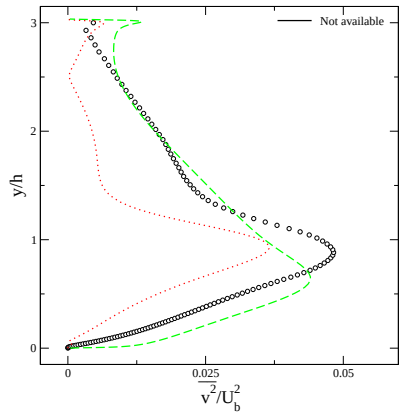

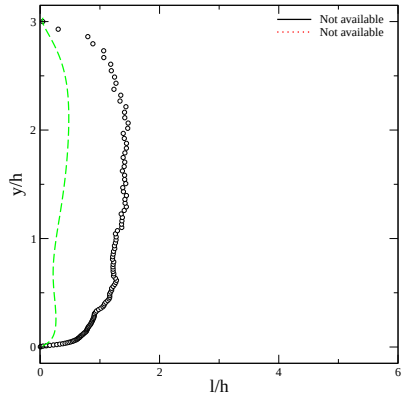

Flow over a 2–D hill: PROFILES

Reynolds stress models

Location: 004 ($x/h = 2.00$)

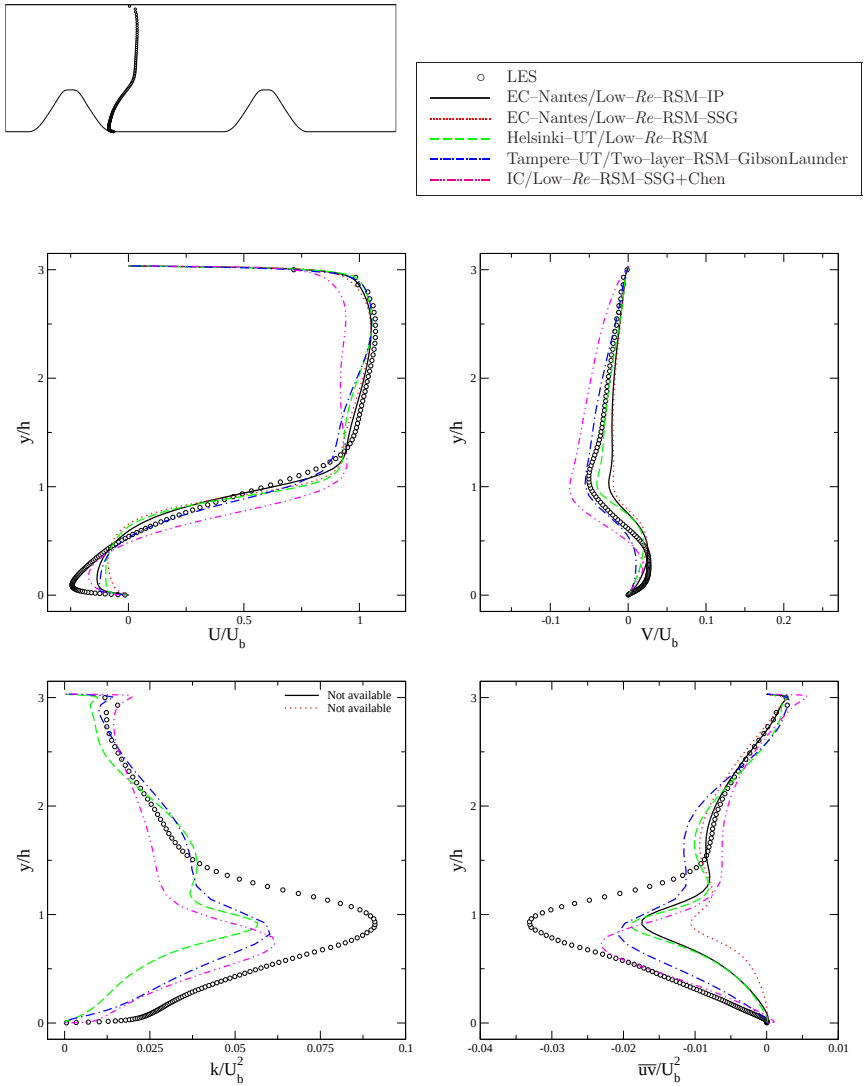

Figure 3.4.3.6

Flow over a 2–D hill: PROFILES

Reynolds stress models

Location: 004 ($x/h = 2.00$)

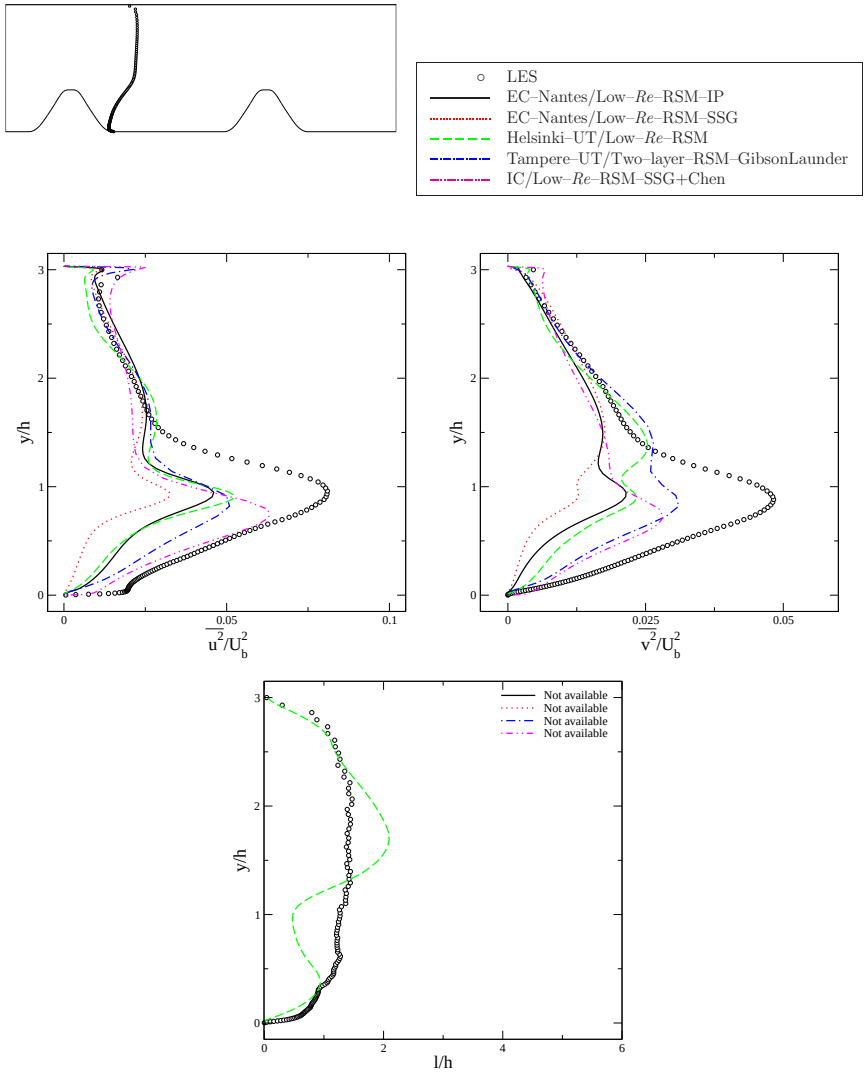

Flow over a 2–D hill: PROFILES

Linear and quasilinear k–ε models

Location: 008 ($x/h = 6.00$)

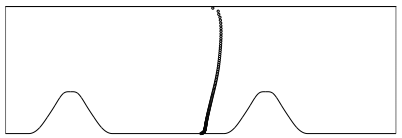

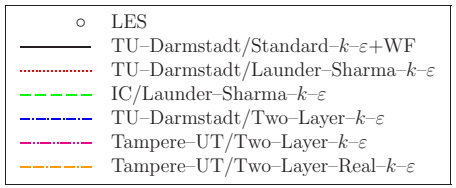

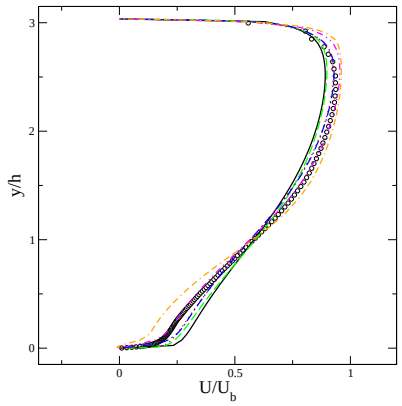

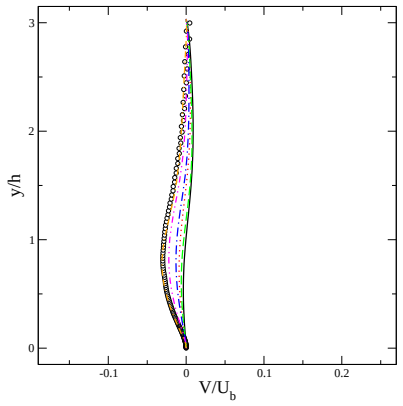

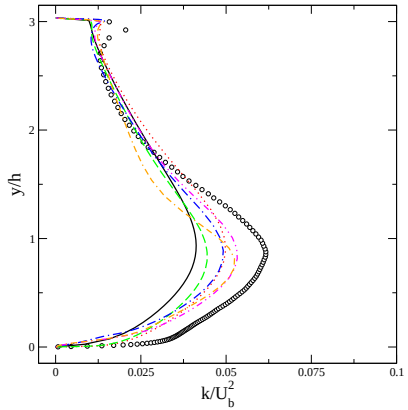

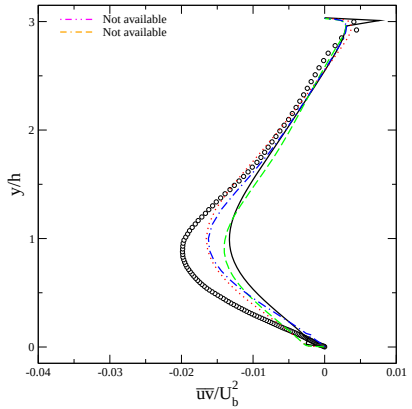

Figure 3.4.4.1

Flow over a 2–D hill: PROFILES

Linear and quasilinear k–ε models

Location: 008 ($x/h = 6.00$)

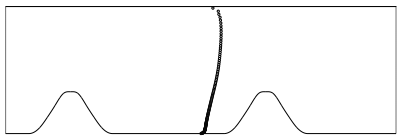

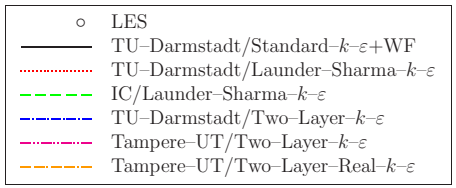

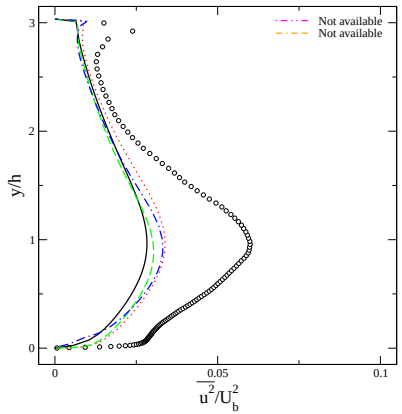

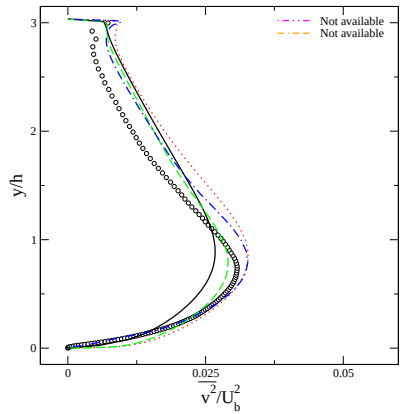

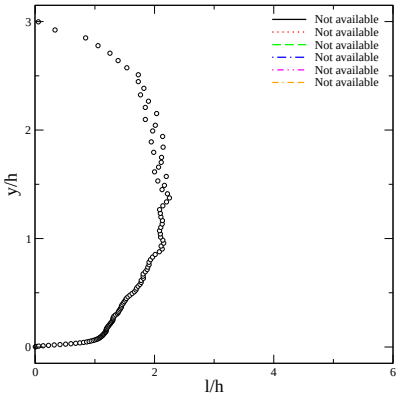

Flow over a 2–D hill: PROFILES

Linear k–ω models

Location: 008 ($x/h = 6.00$)

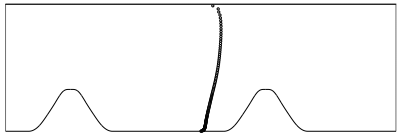

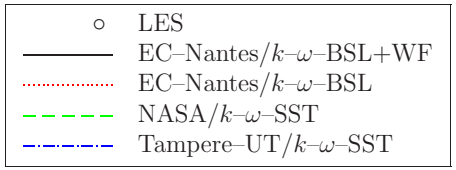

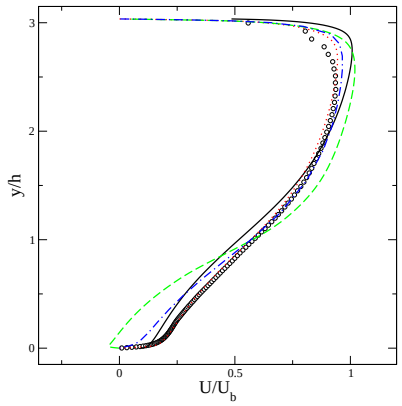

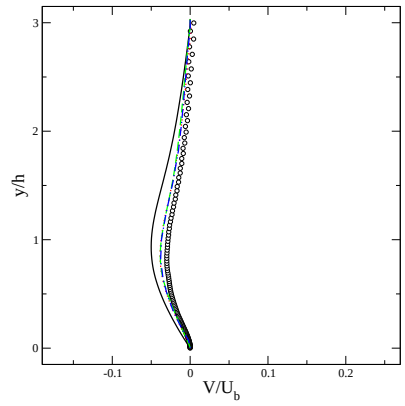

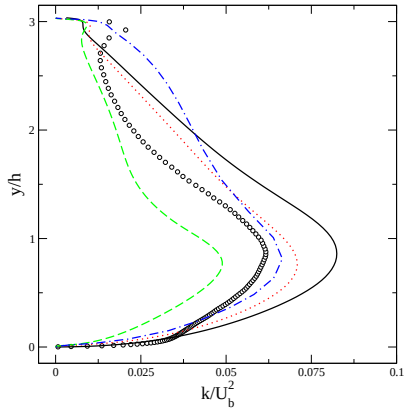

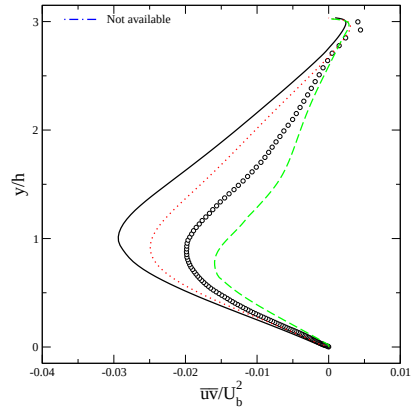

Figure 3.4.4.2

Flow over a 2–D hill: PROFILES

Linear k–ω models

Location: 008 ($x/h = 6.00$)

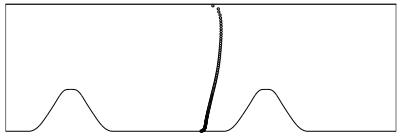

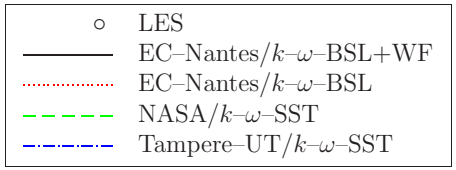

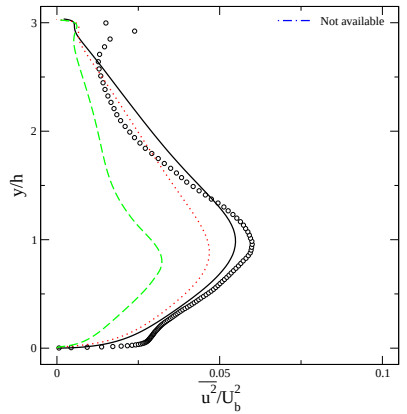

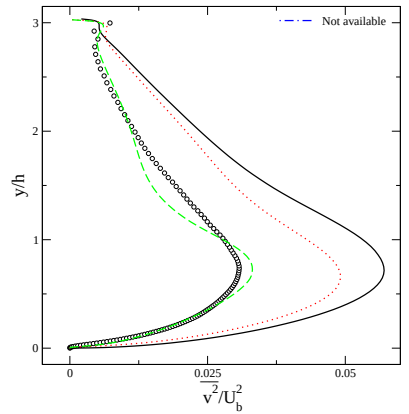

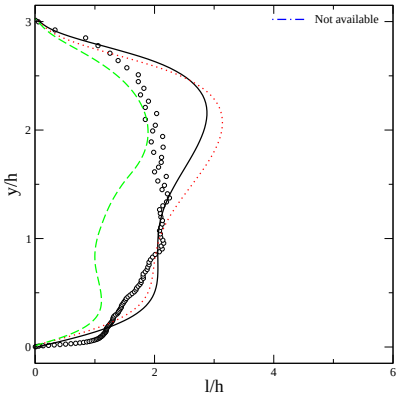

Nonlinear k–ε models

Location: 008 ($x/h = 6.00$)

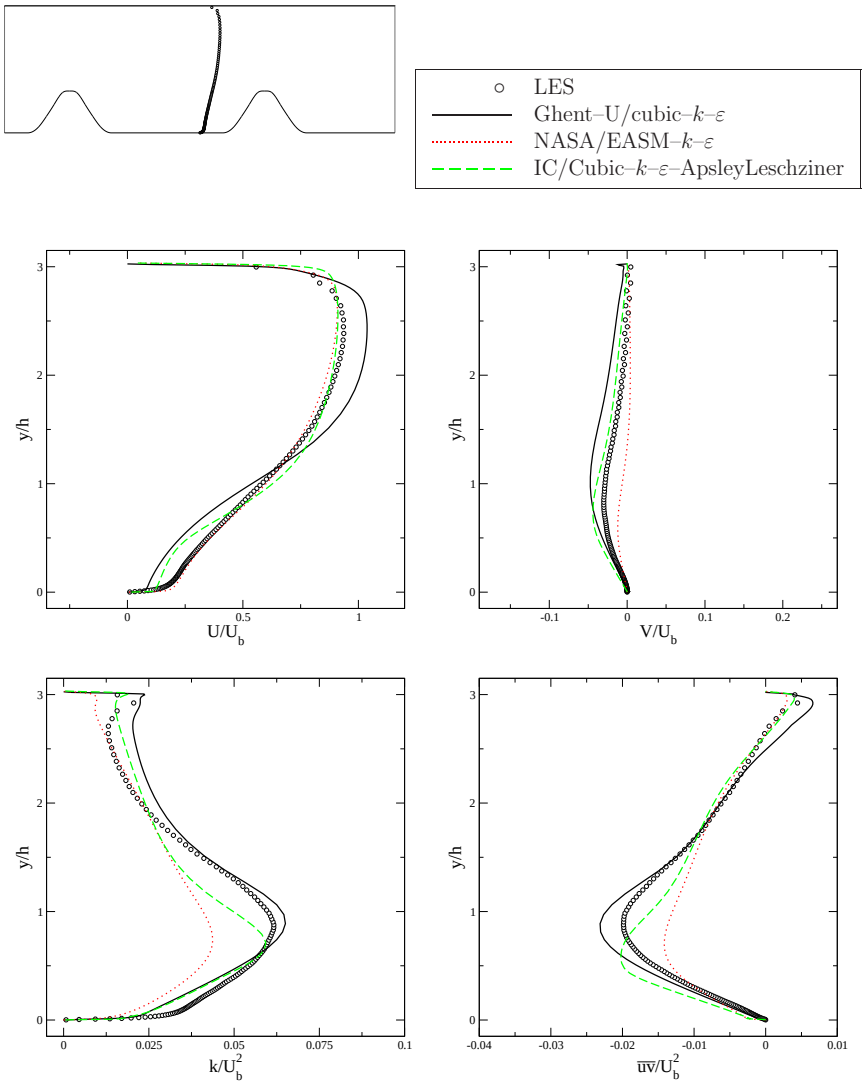

Figure 3.4.4.3

Nonlinear k–ε models

Location: 008 ($x/h = 6.00$)

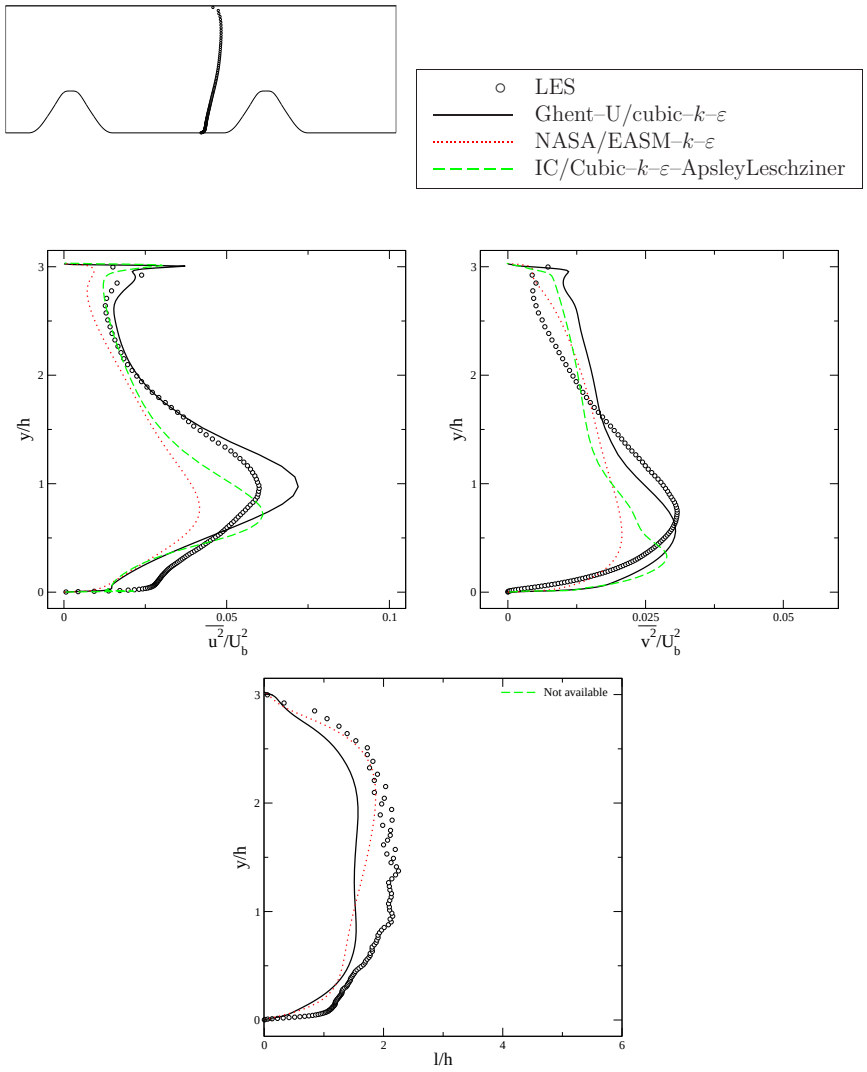

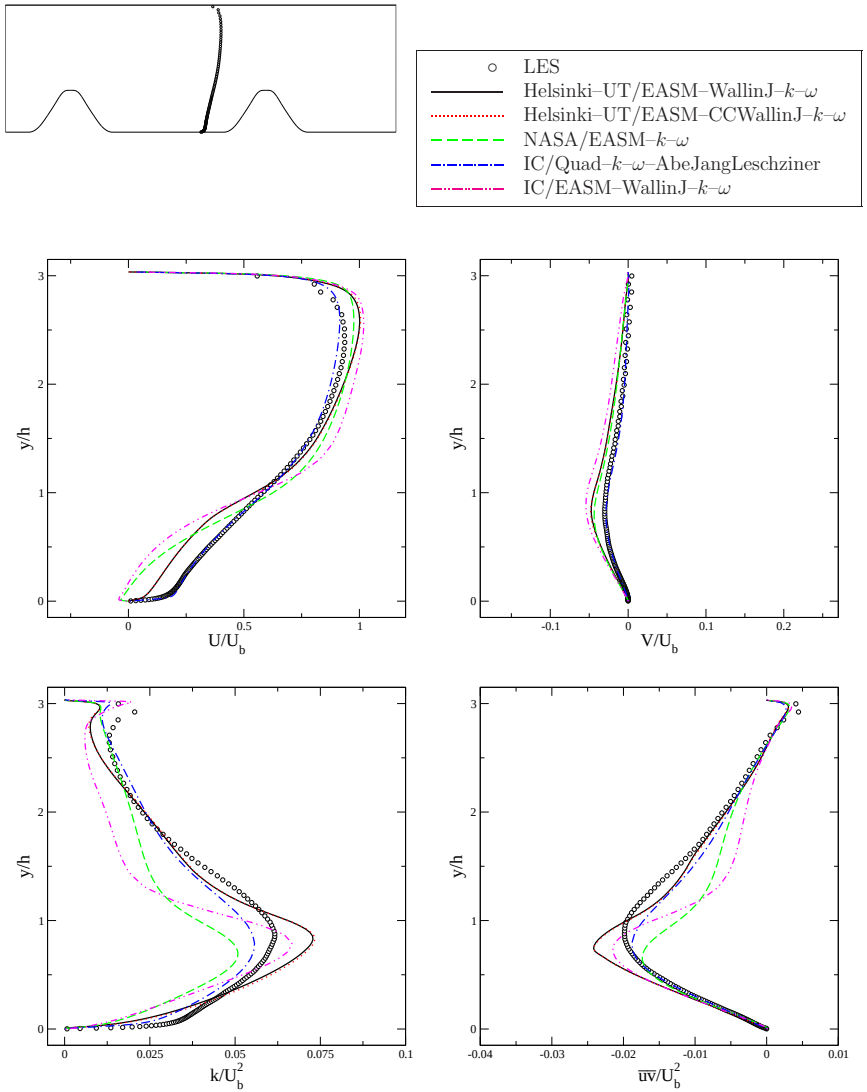

Figure 3.4.4.4

Flow over a 2–D hill: PROFILES

Nonlinear k–ω models

Location: 008 ($x/h = 6.00$)

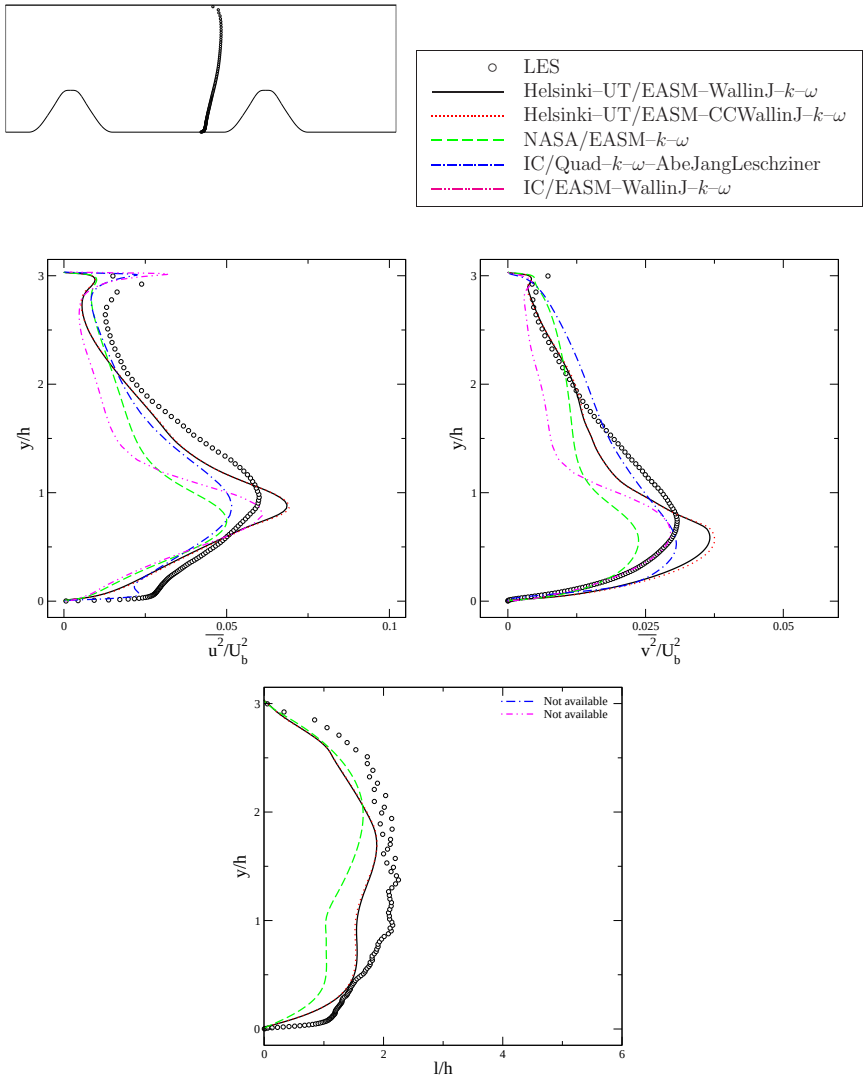

Other eddy-viscosity models:
Spalart-Allmaras model
$\overline{v^2}$–f model

Location: 008 ($x/h = 6.00$)

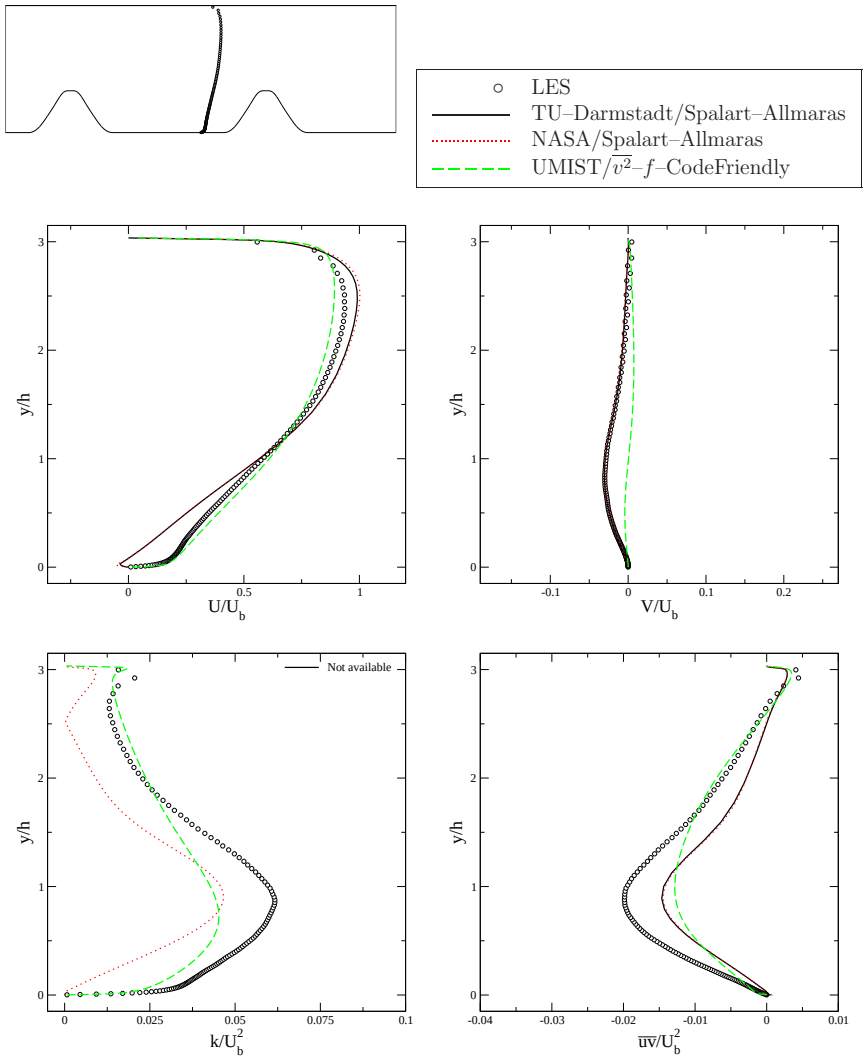

Figure 3.4.4.5

Other eddy-viscosity models:
Spalart-Allmaras model
$\overline{v^2}$–f model

Location: 008 ($x/h = 6.00$)

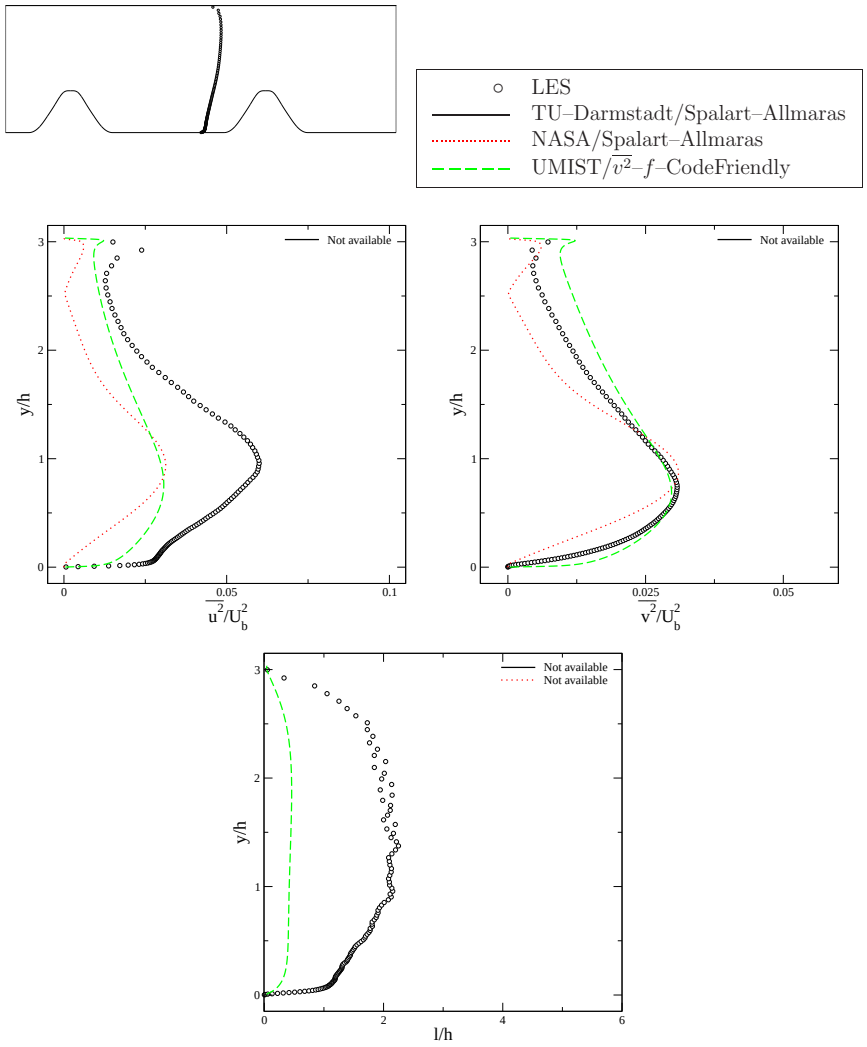

Flow over a 2–D hill: PROFILES

Reynolds stress models

Location: 008 ($x/h = 6.00$)

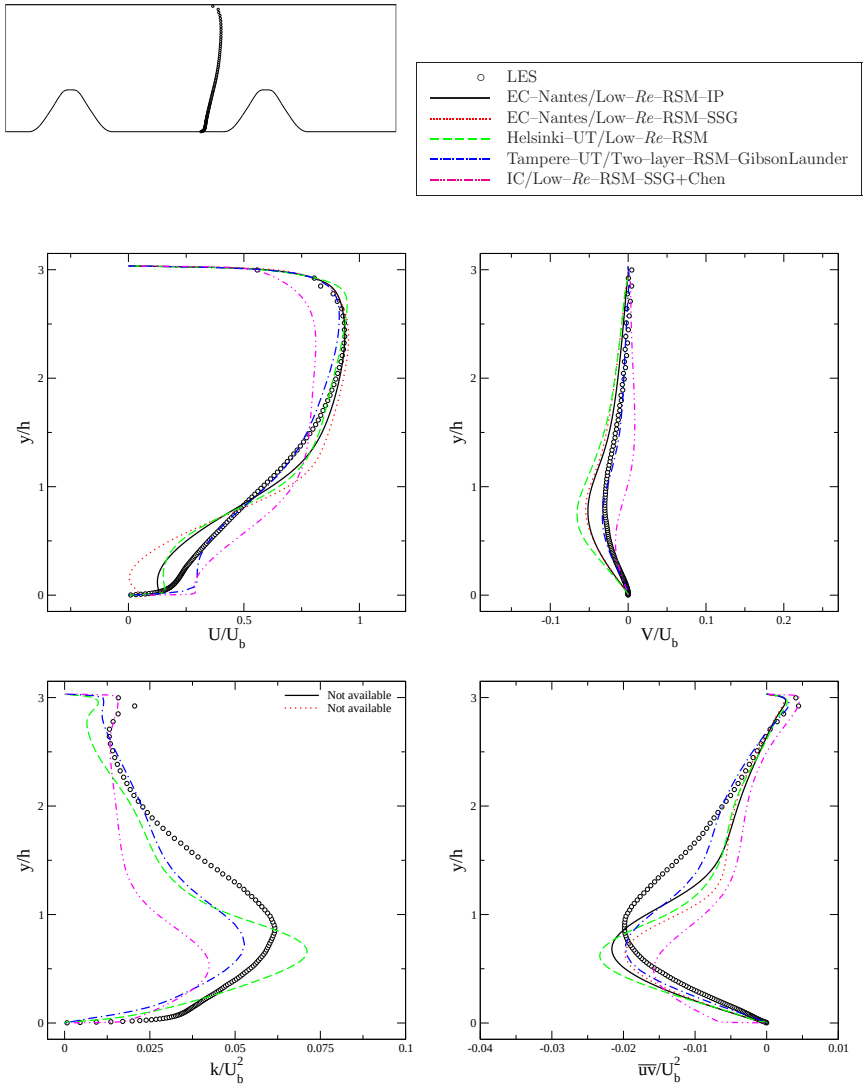

Figure 3.4.4.6

Flow over a 2–D hill: PROFILES

Reynolds stress models

Location: 008 ($x/h = 6.00$)

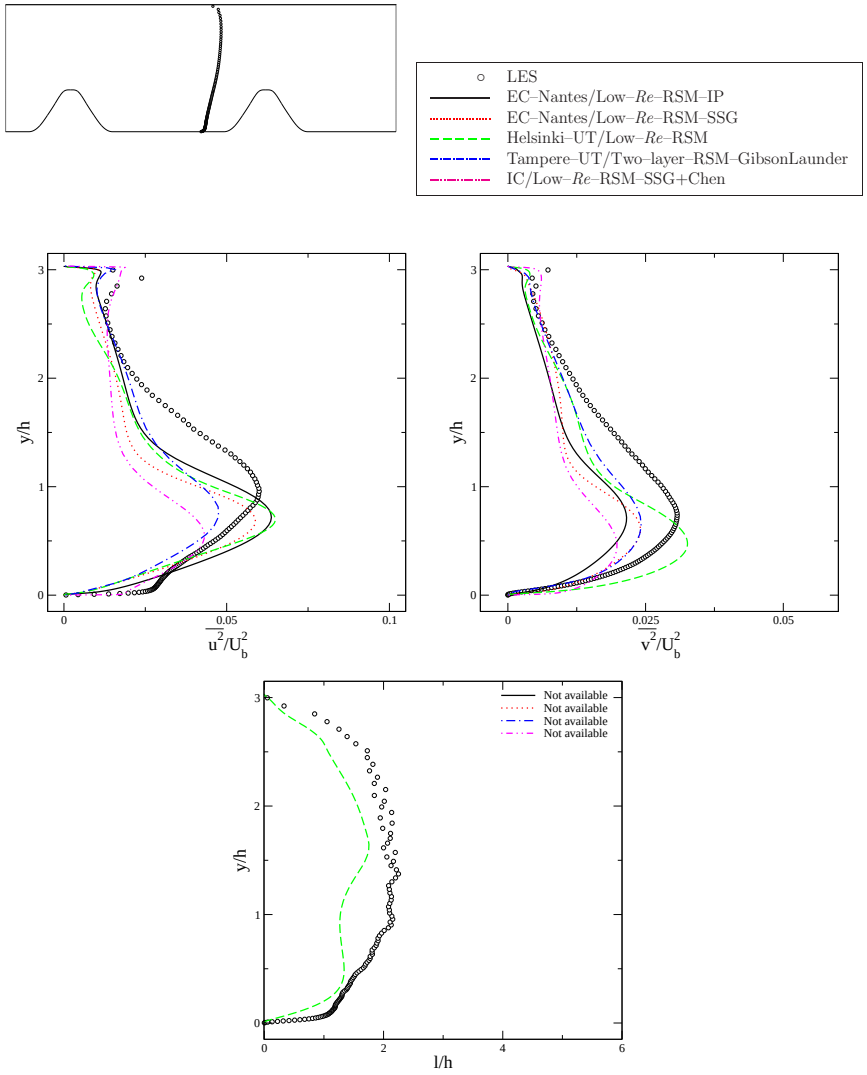

Flow over a 2–D hill: PROFILES

Linear and quasilinear k–ε models

Location: 010 ($x/h = 8.00$)

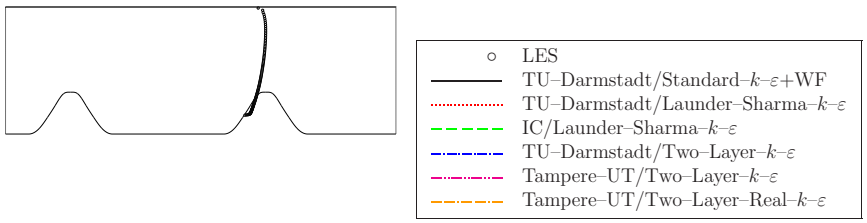

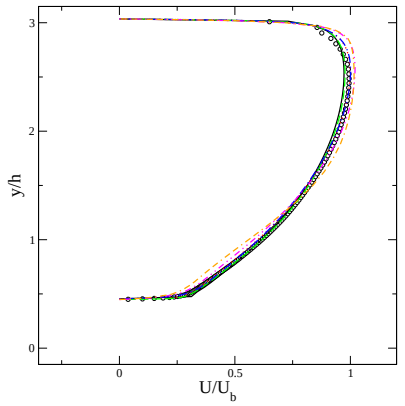

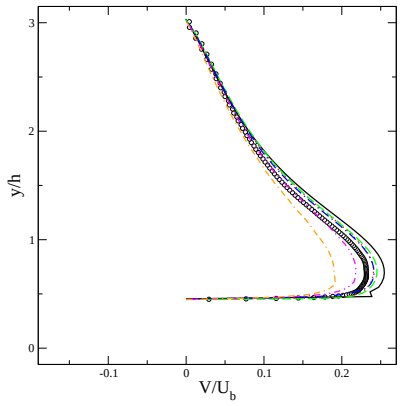

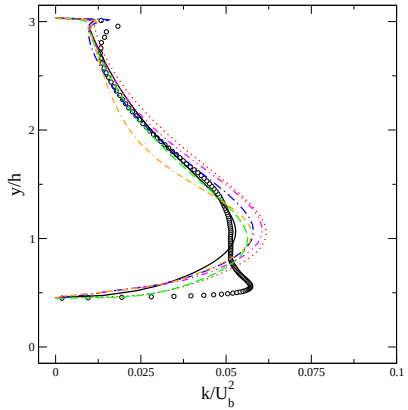

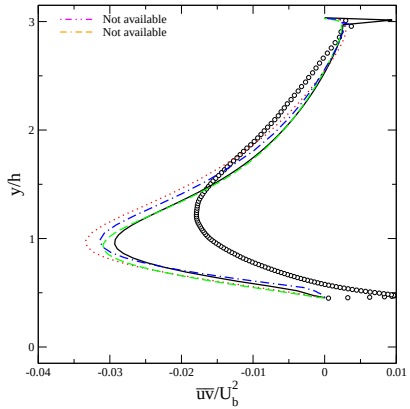

Figure 3.4.5.1

Flow over a 2–D hill: PROFILES

Linear and quasilinear k–ε models

Location: 010 ($x/h = 8.00$)

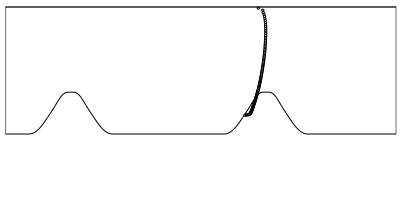

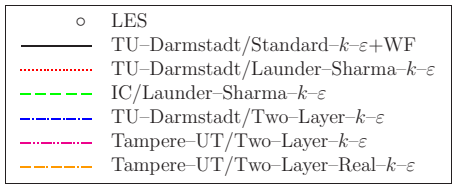

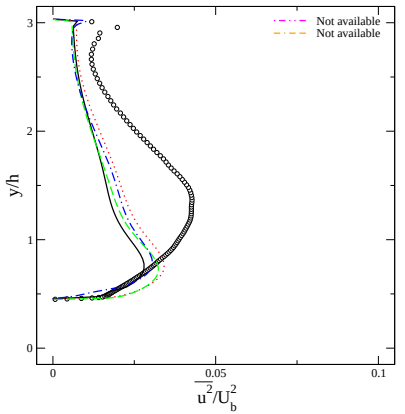

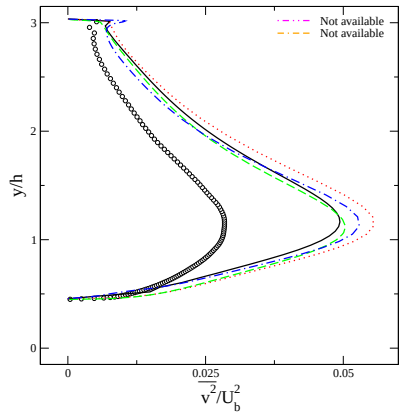

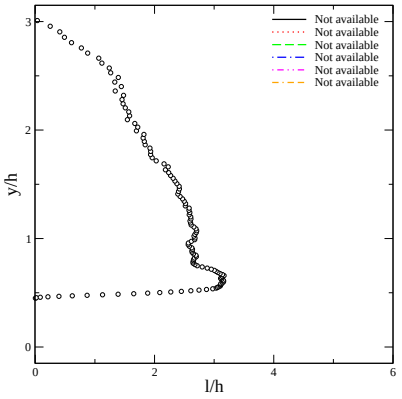

Flow over a 2–D hill: PROFILES

Linear k–ω models

Location: 010 ($x/h = 8.00$)

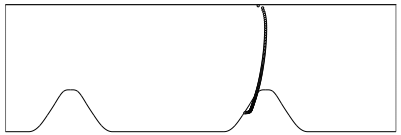

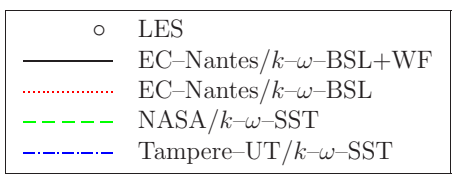

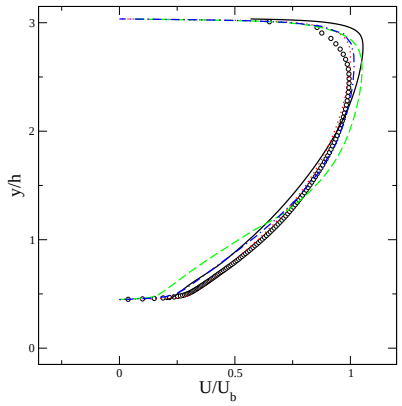

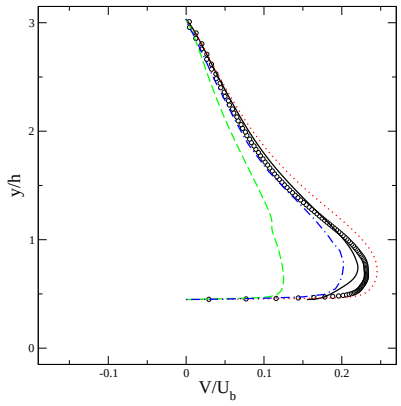

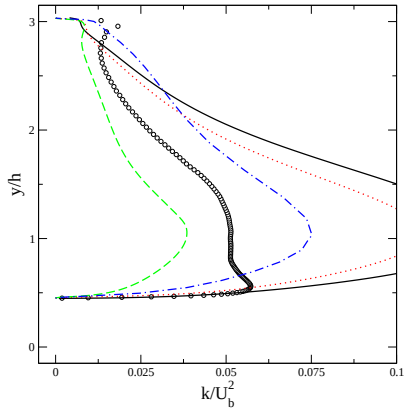

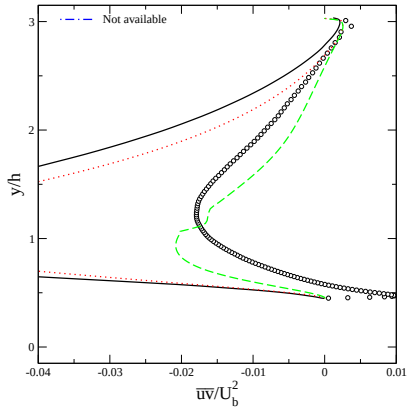

Figure 3.4.5.2

Flow over a 2–D hill: PROFILES

Linear k–ω models

Location: 010 ($x/h = 8.00$)

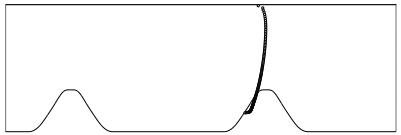

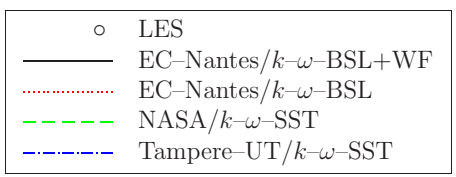

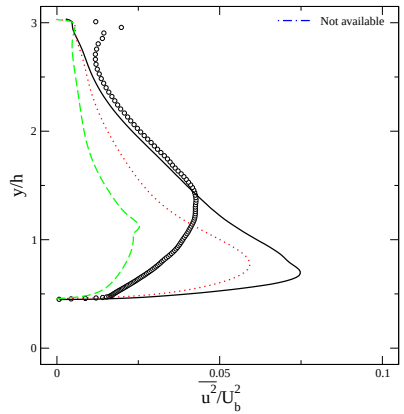

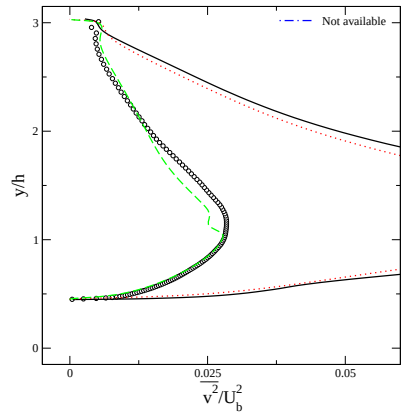

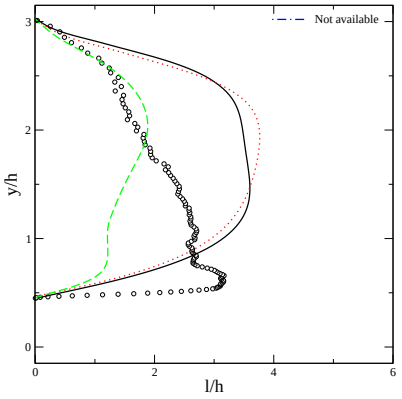

Flow over a 2–D hill: PROFILES

Nonlinear k–ε models

Location: 010 ($x/h = 8.00$)

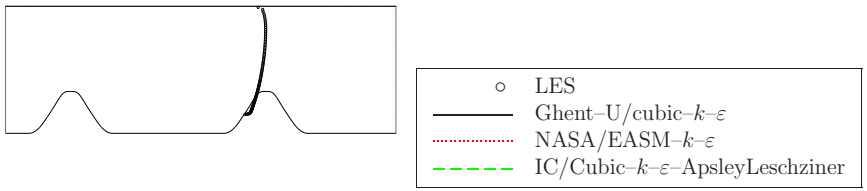

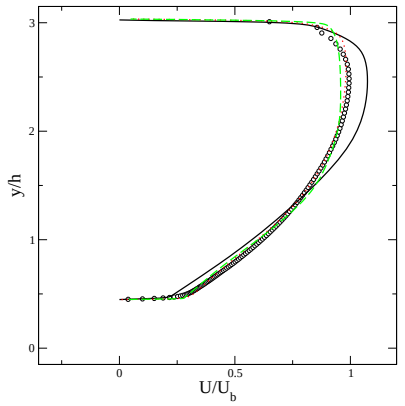

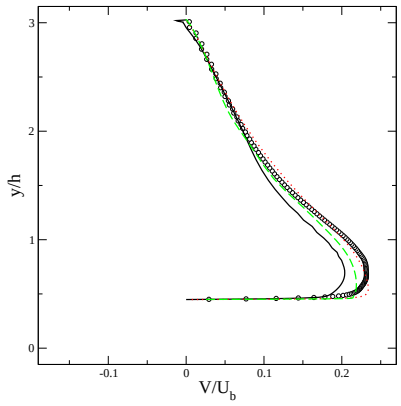

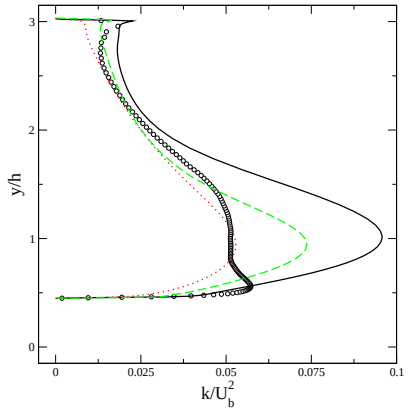

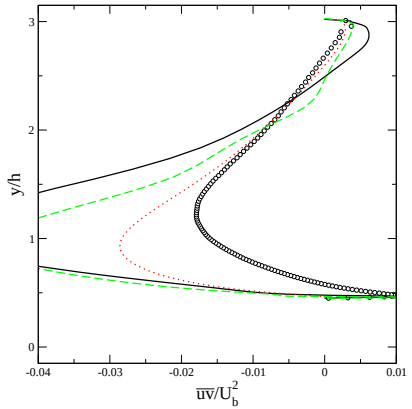

Figure 3.4.5.3

Flow over a 2–D hill: PROFILES

Nonlinear k–ε models

Location: 010 ($x/h = 8.00$)

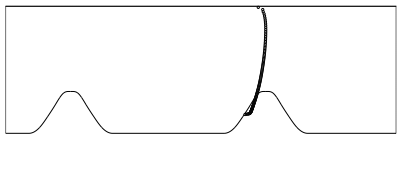

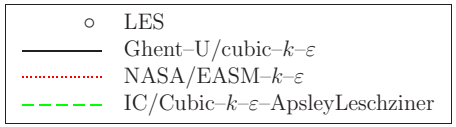

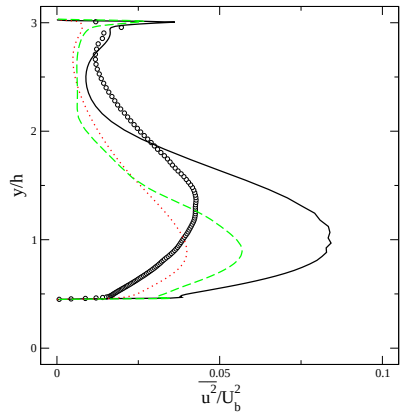

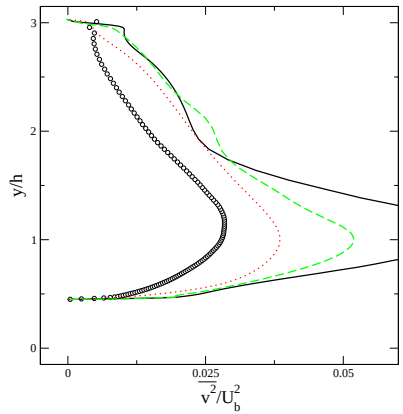

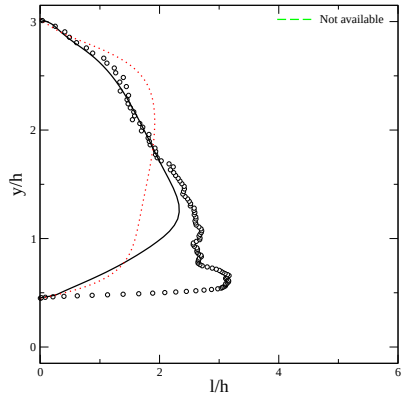

Flow over a 2–D hill: PROFILES

Nonlinear k–ω models

Location: 010 ($x/h = 8.00$)

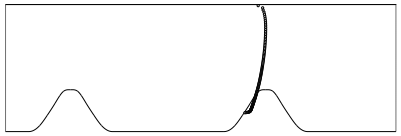

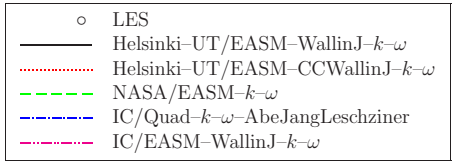

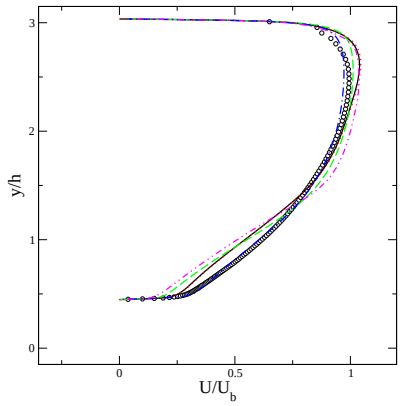

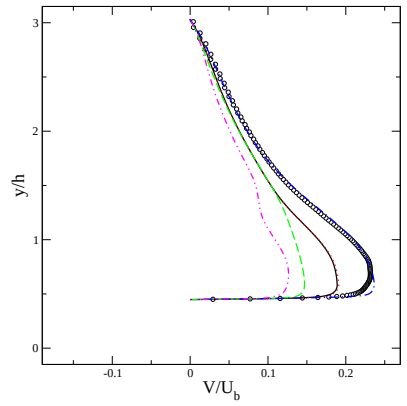

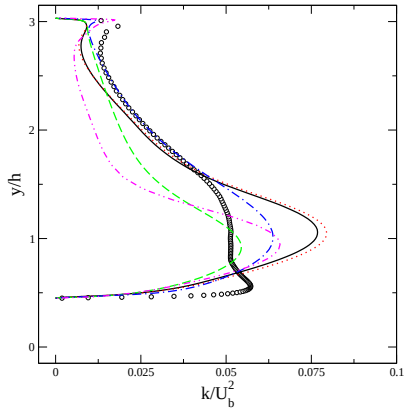

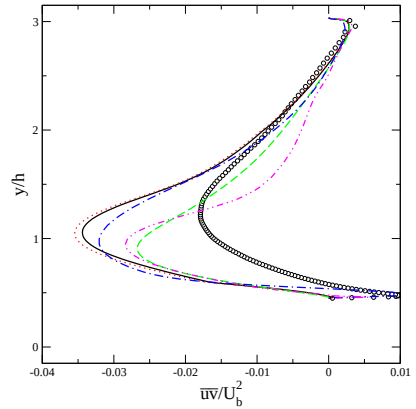

Flow over a 2–D hill: PROFILES

Nonlinear k–ω models

Location: 010 ($x/h = 8.00$)

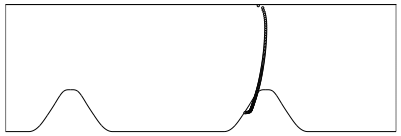

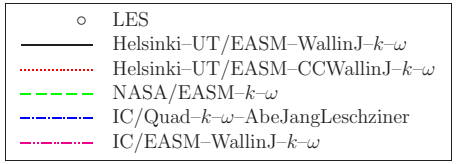

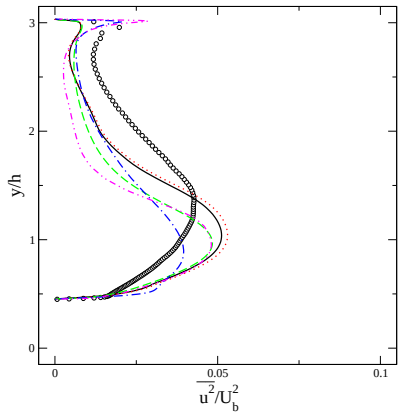

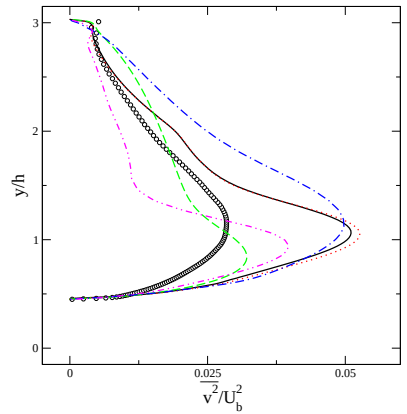

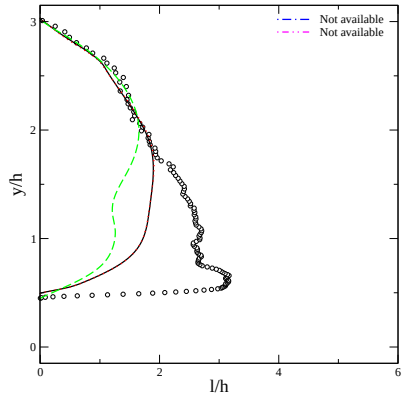

Figure 3.4.5.4

Other eddy-viscosity models:
Spalart-Allmaras model
$\overline{v^2}$–f model

Location: 010 ($x/h = 8.00$)

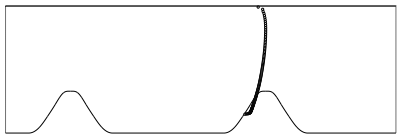

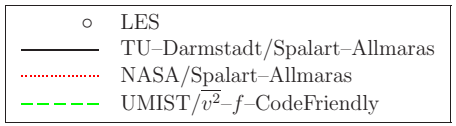

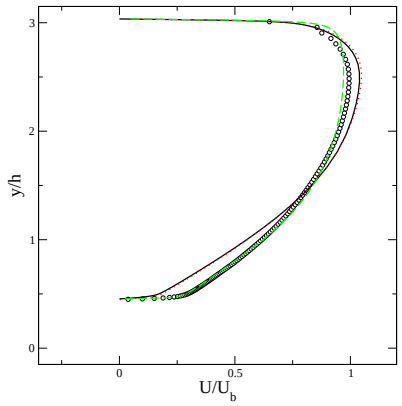

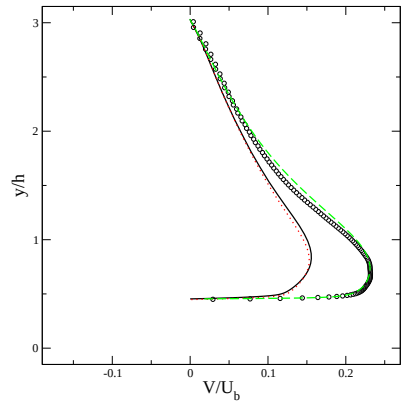

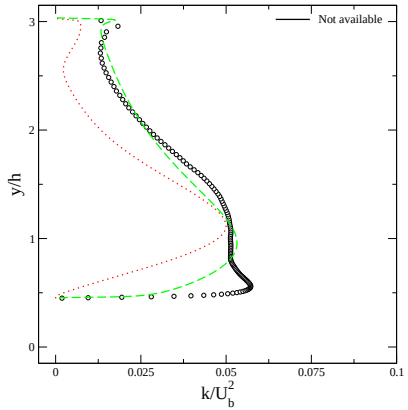

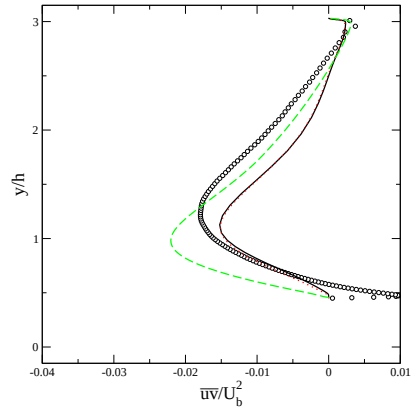

Figure 3.4.5.5

Other eddy-viscosity models:
Spalart-Allmaras model
$\overline{v^2}$–f model

Location: 010 ($x/h = 8.00$)

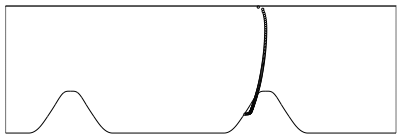

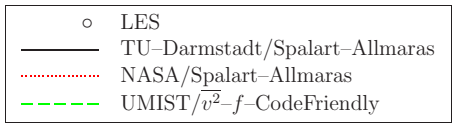

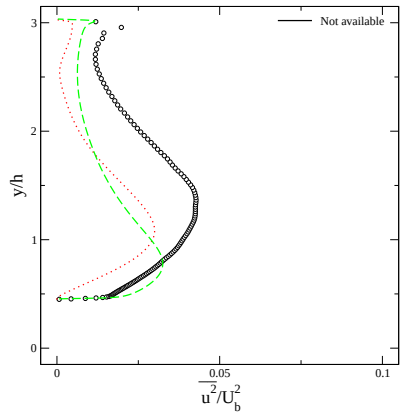

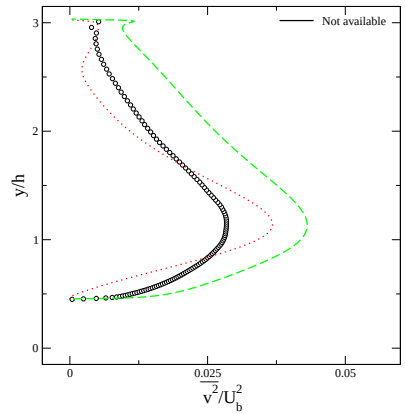

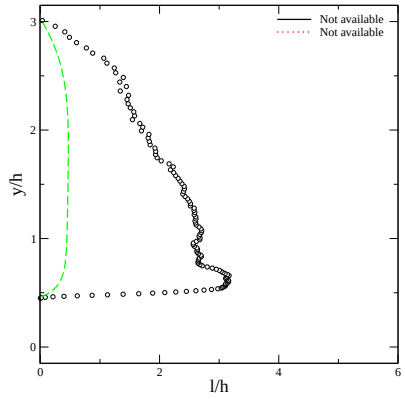

Flow over a 2–D hill: PROFILES

Reynolds stress models

Location: 010 ($x/h = 8.00$)

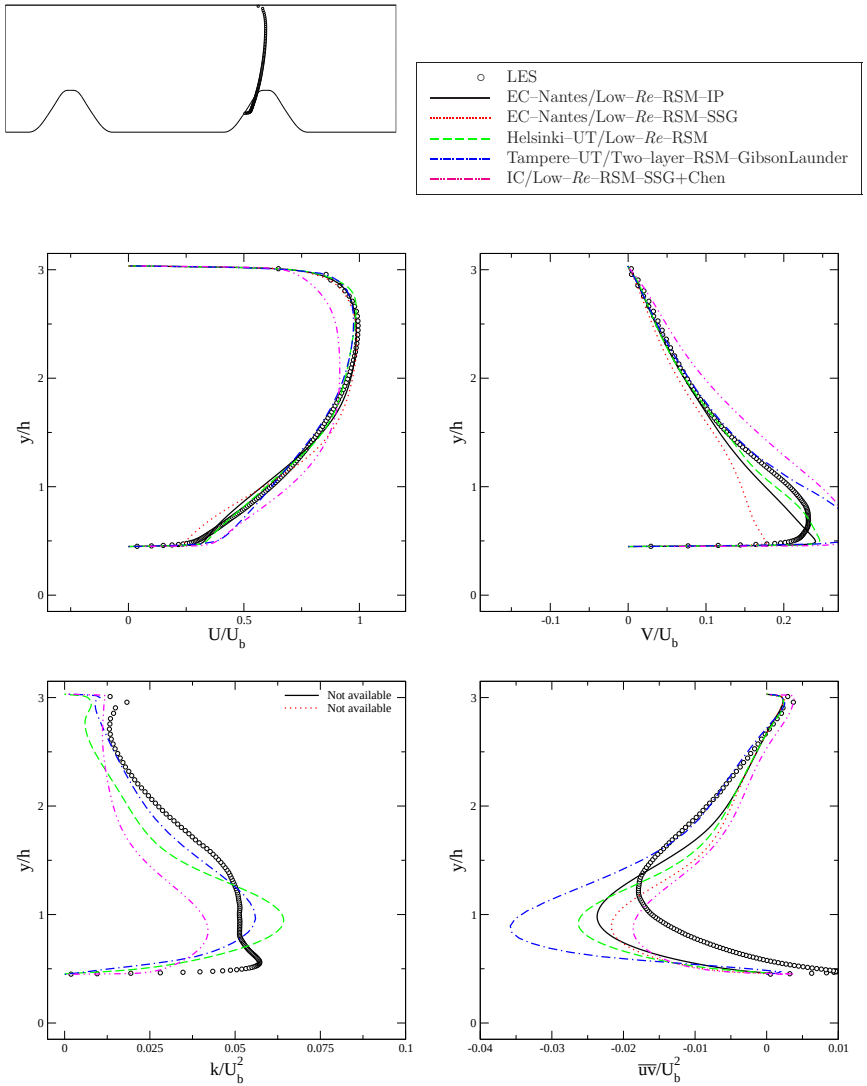

Figure 3.4.5.6

Flow over a 2–D hill: PROFILES

Reynolds stress models

Location: 010 ($x/h = 8.00$)

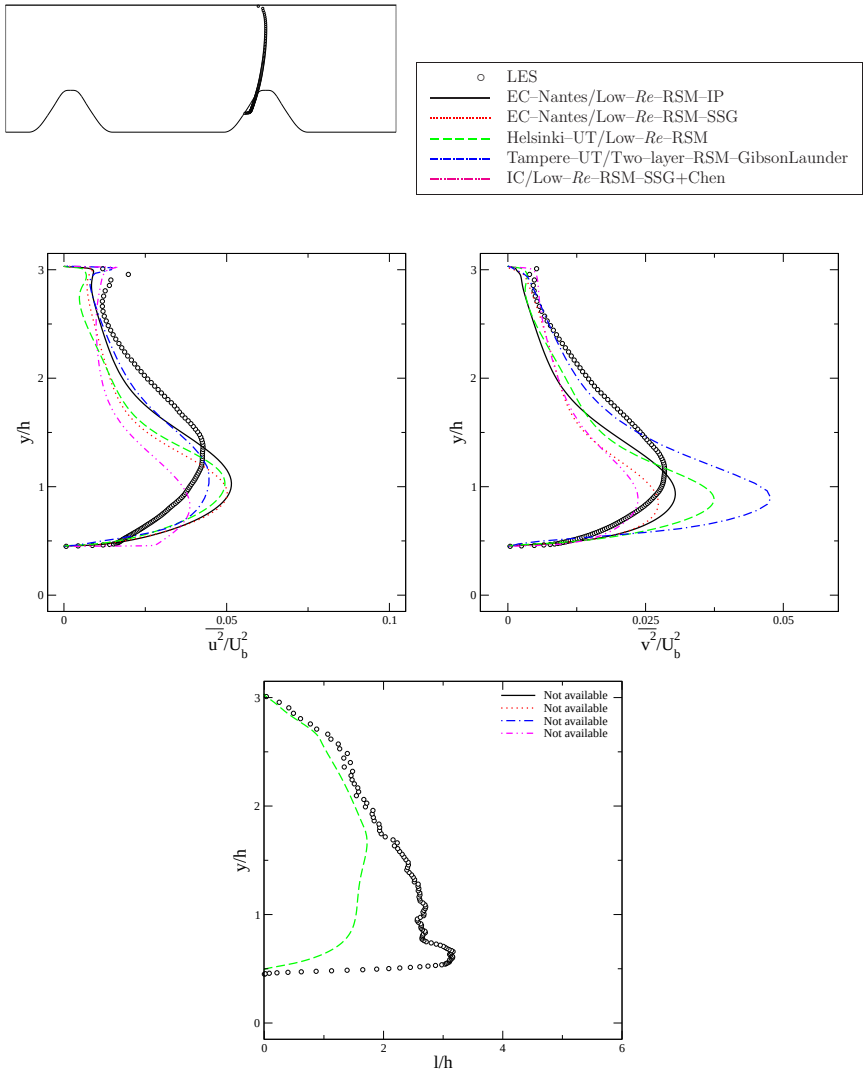

Flow over a 2–D hill: PROFILES

Comparison between EASM and its underlying RSM (Helsinki UT)

Location: 004 ($x/h = 2.00$)

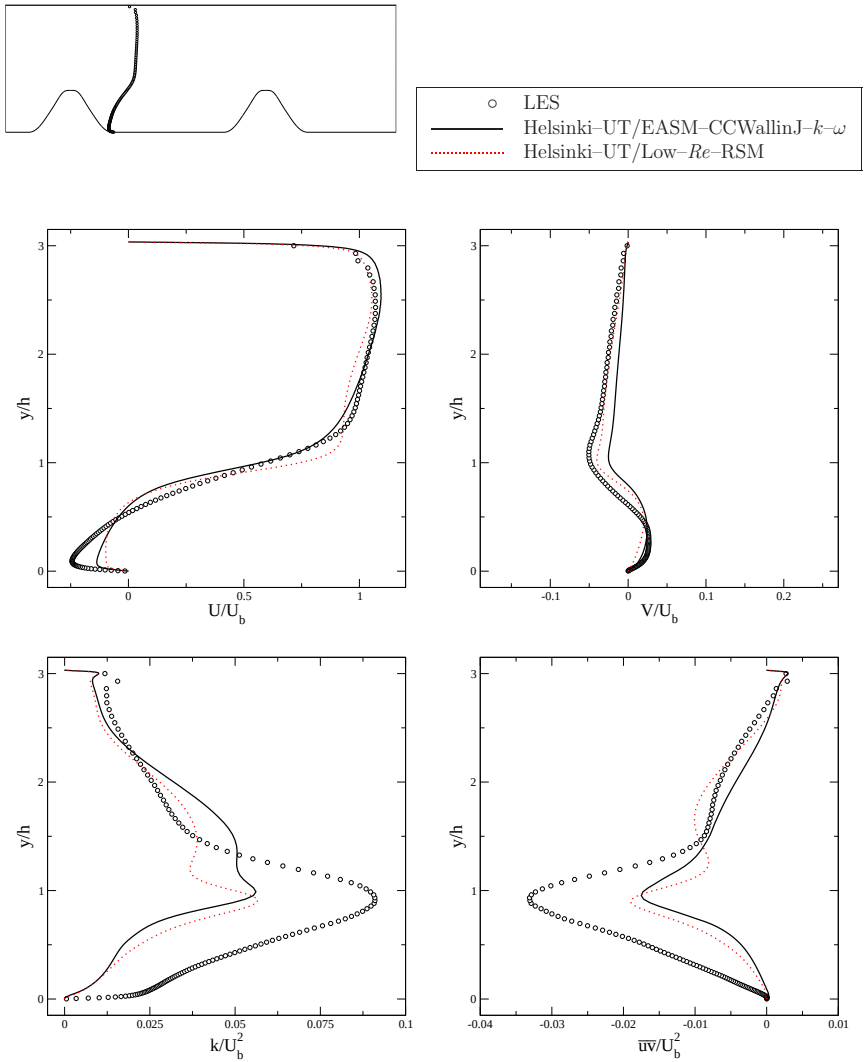

Figure 3.5.1

Flow over a 2–D hill: PROFILES

Comparison between EASM and its underlying RSM (Helsinki UT)

Location: 004 ($x/h = 2.00$)

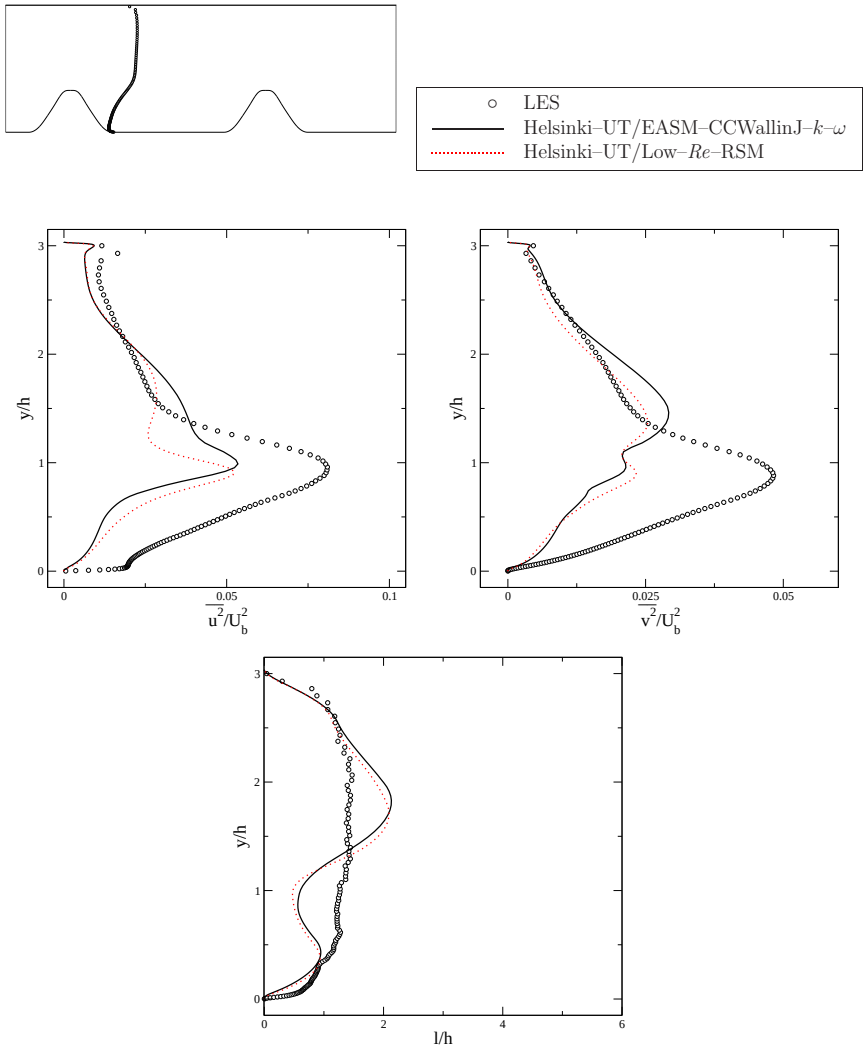

Comparison between EASM and its underlying RSM (Helsinki UT)

Location: 010 ($x/h = 8.00$)

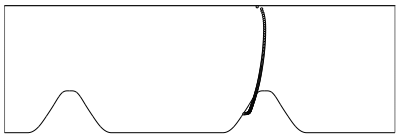

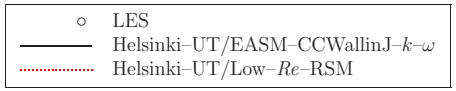

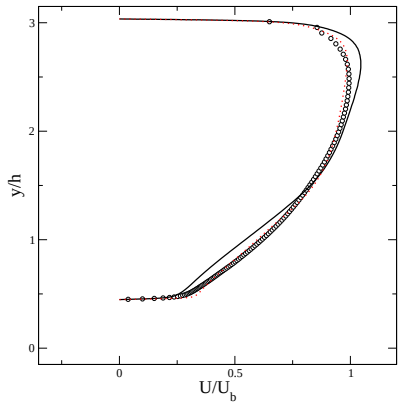

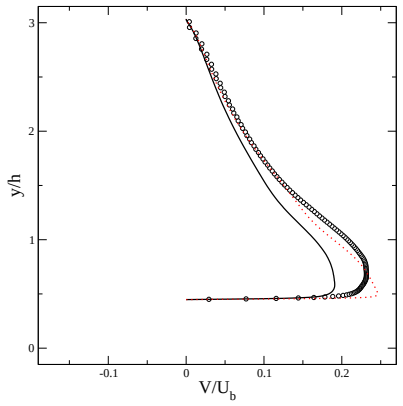

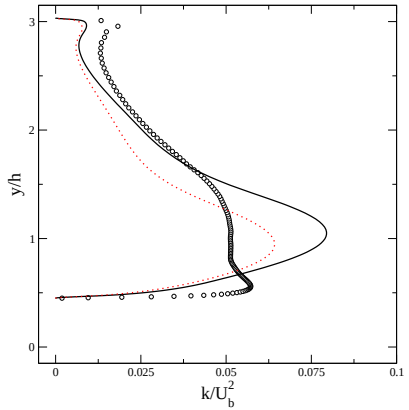

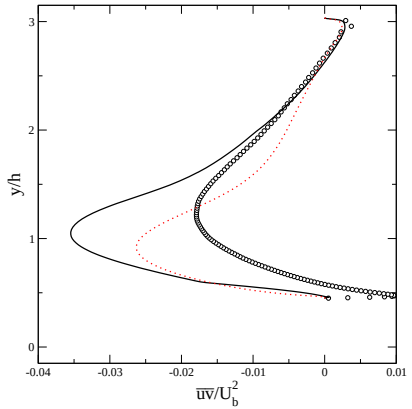

Figure 3.5.2

Comparison between EASM and its underlying RSM (Helsinki UT)

Location: 010 ($x/h = 8.00$)

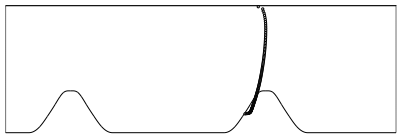

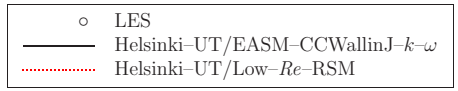

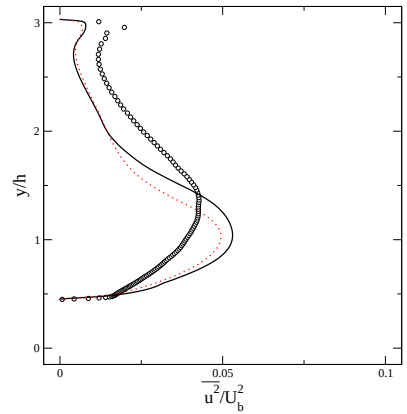

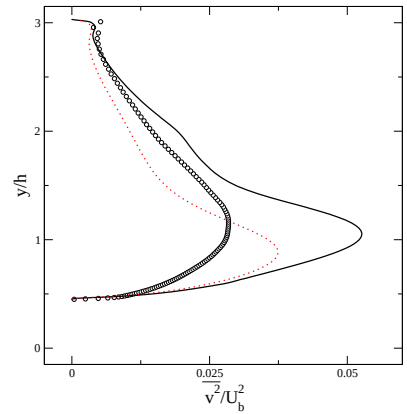

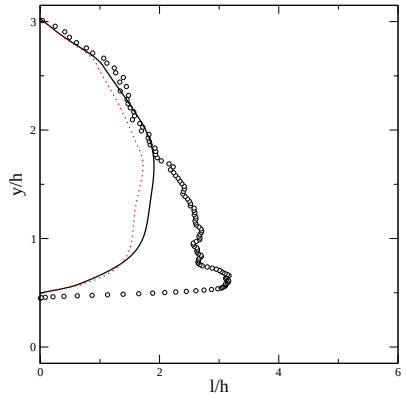

Location: 004 ($x/h = 2.00$)

Comparison of the different classes of models

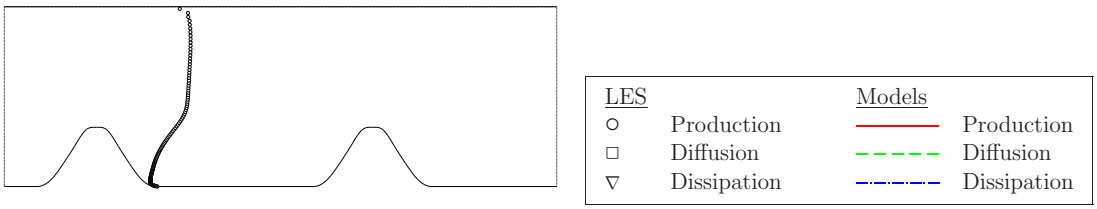

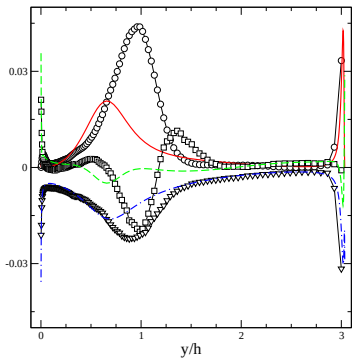

UMIST/$\overline{v^2}$–f–CodeFriendly

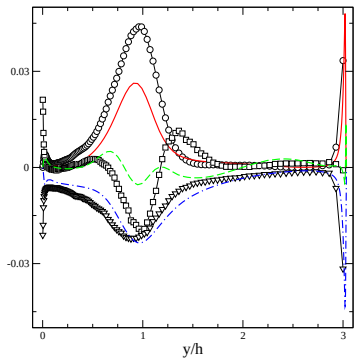

EC–Nantes/k–ω–BSL

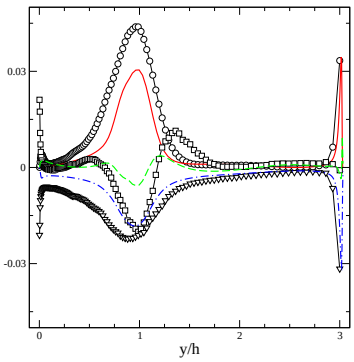

NASA/k–ω–SST

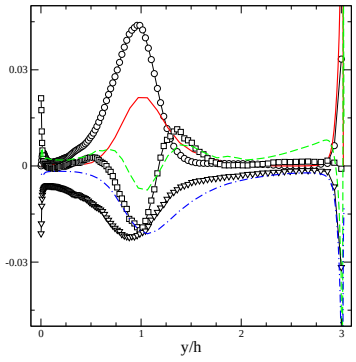

Ghent–U/cubic–k–ε

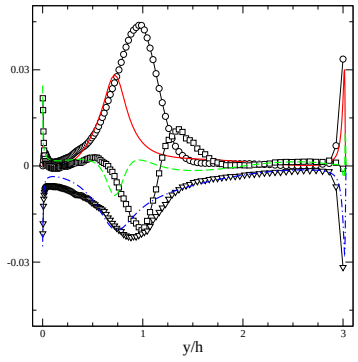

NASA/EASM–k–ε

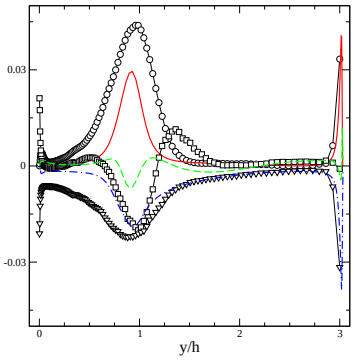

NASA/EASM–k–ω

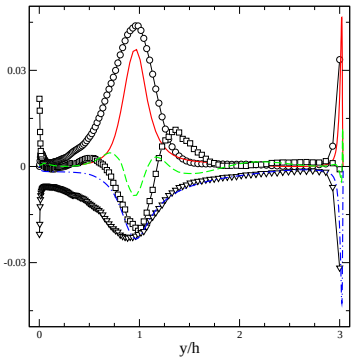

Helsinki–UT/EASM–CCWallinJ–k–ω

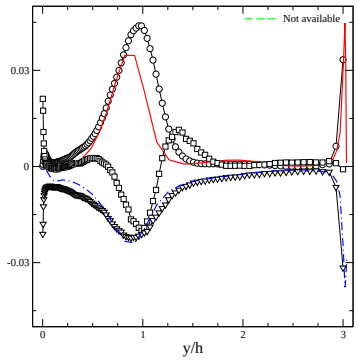

Tampere–UT/Two–layer–RSM–GibsonLaunder

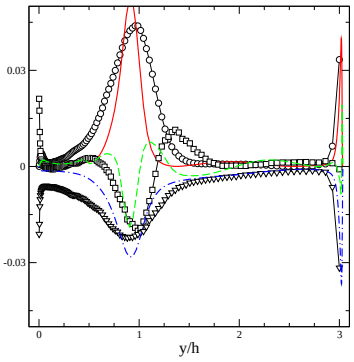

Helsinki–UT/Low–Re–RSM

Figure 3.6.1

Flow over a 2–D hill: BUDGETS

Location: 008 ($x/h = 6.00$)

Comparison of the different classes of models

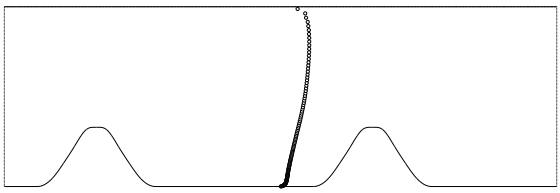

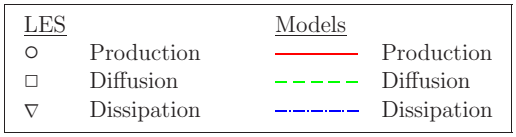

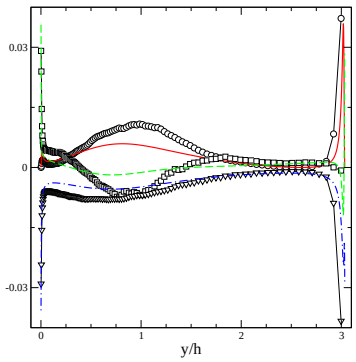

UMIST/$\overline{v^2}$–f–CodeFriendly

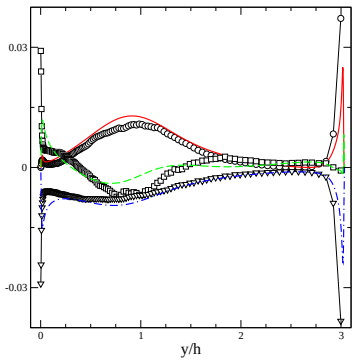

EC–Nantes/k–ω–BSL

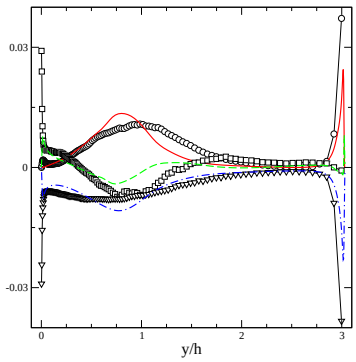

NASA/k–ω–SST

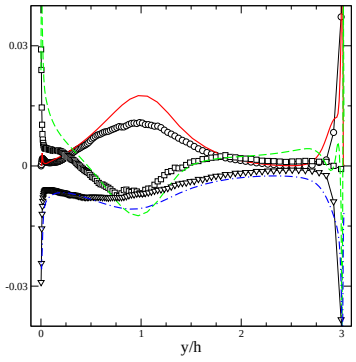

Ghent–U/cubic–k–ε

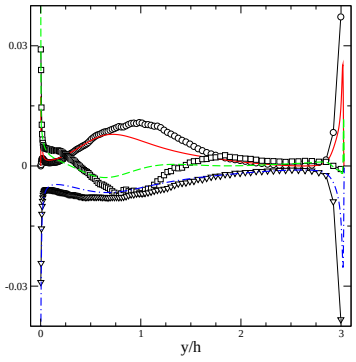

NASA/EASM–k–ε

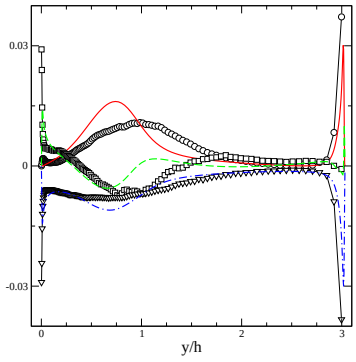

NASA/EASM–k–ω

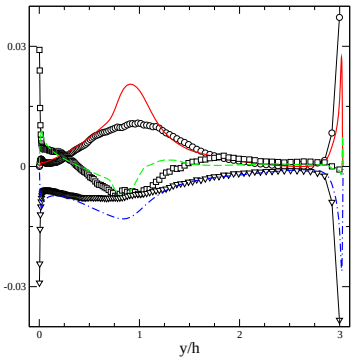

Helsinki–UT/EASM–CCWallinJ–k–ω

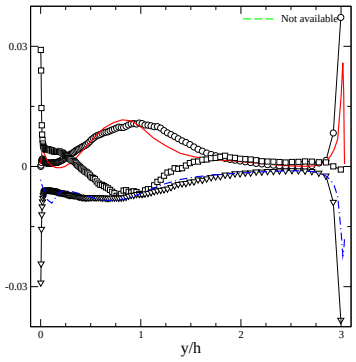

Tampere–UT/Two–layer–RSM–GibsonLaunder

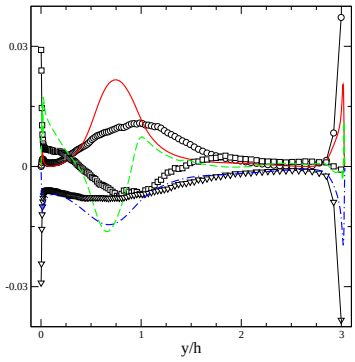

Helsinki–UT/Low–Re–RSM

Figure 3.6.2

Location: 010 ($x/h = 8.00$)

Comparison of the different classes of models

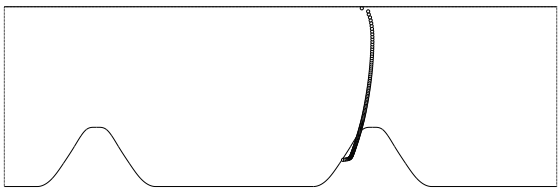

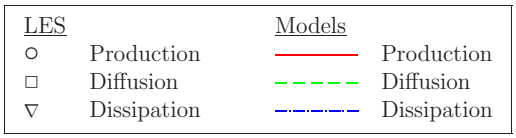

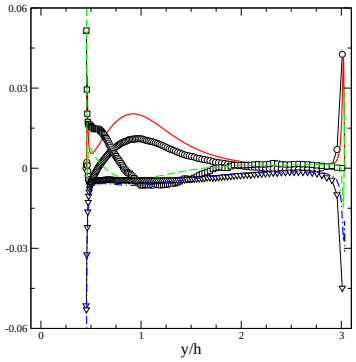

UMIST/$\overline{v^2}$–f–CodeFriendly

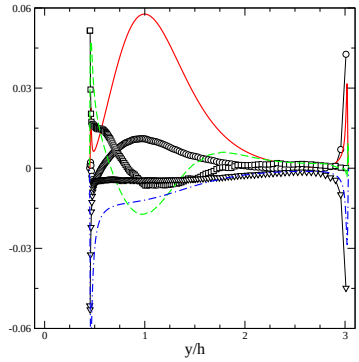

EC–Nantes/k–ω–BSL

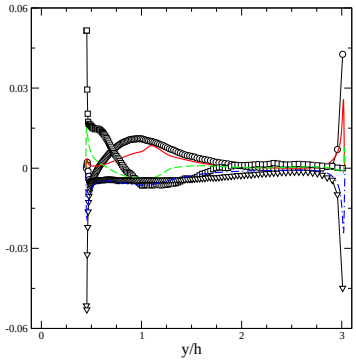

NASA/k–ω–SST

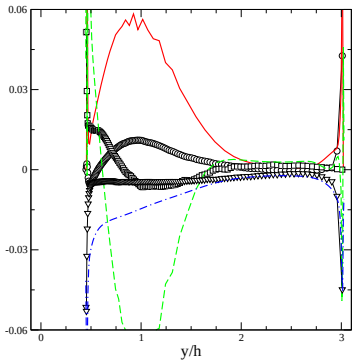

Ghent–U/cubic–k–ε

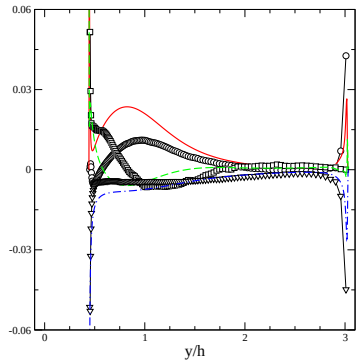

NASA/EASM–k–ε

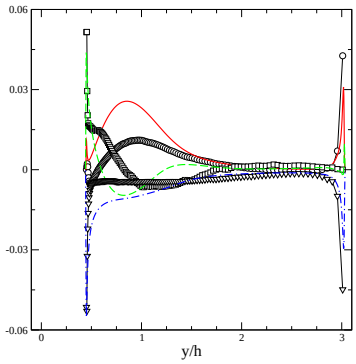

NASA/EASM–k–ω

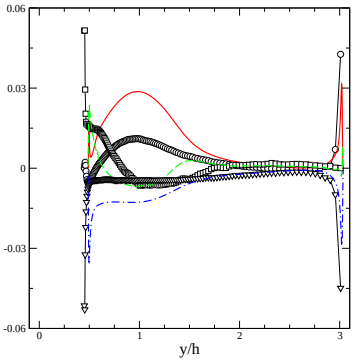

Helsinki–UT/EASM–CCWallinJ–k–ω

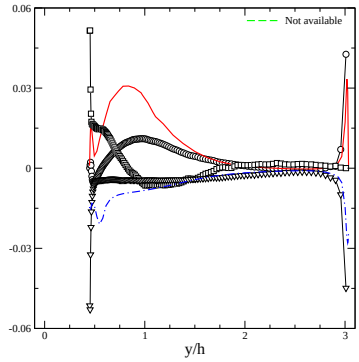

Tampere–UT/Two–layer–RSM–GibsonLaunder

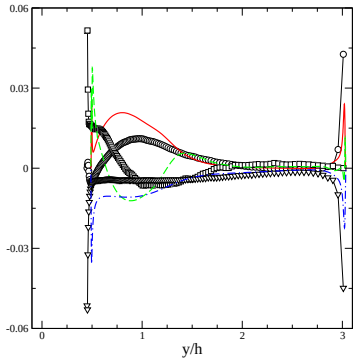

Helsinki–UT/Low–Re–RSM

Figure 3.6.3

Case 9.2

Articles written by the participants

-

10th ERCOFTAC-IAHR-QNET/CFD Workshop on **Refined Turbulence Modelling**,
University of Poitiers, France, October 10-11, 2002

CASE 9.2: FLOW OVER A 2-D HILL[1] DESCRIPTION OF THE COMPUTATIONAL METHOD

S. Šarić, A. Djugum and S. Jakirlić

Fachgebiet Strömungslehre und Aerodynamics, Darmstadt University of Technology
Petersenstr. 30, 64287 Darmstadt, Germany

Computational method

The computational results presented were obtained by using four computer codes, all based on a finite-volume numerical method for solving the Reynolds Averaged Navier-Stokes equations. Beside two commercial CFD packages FLUENT and SWIFT (AVL List GmbH), the two in-house codes denoted by FAN-2D and FAN-3D were also applied.

The computations performed with the FAN-2D (Hadžić, 1999) and FAN-3D (Lilek, 1997) codes used a finite volume method for block-structured, body-fitted, non-orthogonal meshes. Cell centered (collocated) variable arrangement and cartesian vector and tensor components are used in both codes. The equations are linearised and solved sequentially using an iterative ILU method. The velocity-pressure coupling is ensured by the pressure-correction method based on the SIMPLE algorithm. A special, selective interpolation procedure, involving the interpolation of equations, i.e. their terms, instead of the variables themselves, was applied for velocity-stress coupling. Diffusion fluxes are approximated by central differences. Whereas a blended, first-order upwind (UDS)/central differencing scheme (CDS) and first-order upwind/second-order upwind (LUDS), implemented in the so-called deferred-correction manner, were used for computations with the FAN-2D and FAN-3D codes (portions of CDS and LUDS schemes were 100 % for all variables) for the discretisation of convective terms in all transport equations, the commercial codes FLUENT and SWIFT applied the linear upwind scheme (LUDS) and the MINMOD version of the total variation diminishing scheme, respectively.

The solution domain ($length = 18h$ and $height = 3.035h$, h being the hill height) meshed by a body-fitted, non-orthogonal grid is shown in Fig. 1. Standard wall functions were used for high-Reynolds number model computations. The numerical grid used for high-Reynolds number model computations employed 364x60 cv's. The grid was uniformly distributed in the radial direction, providing the dimensionless wall distance y^+ of the numerical node closest to the wall being ≈ 20 on the top of the hill, ≈ 7 at the leeward side of the hill and ≈ 11 at the position $x/h = 2$, when computing with the FAN-3D code and the Standard $k-\varepsilon$ model. The numerical grid used by the SWIFT code (not shown here) comprized 500x60 cv's. The grid in the radial direction was squeezed in the shear layer and in the wall region. The results obtained were in a very good agreement (Fig. 4 and Table 1).

Two numerical grids were used for low-Reynolds number model computations. They employed 364x66 cv's (both FAN-2D and FLUENT used this grid) and 518x95 cv's (FLUENT), Fig. 2. The grids, squeezed in the shear layer and near-wall regions providing the dimensionless wall distance y^+ of the node closest to the wall being ≤ 0.5, were organized in a very different manner. However, very close agreement between results is achieved, Fig. 3.

[1]Mellen, C.P., Fröhlich, J., and Rodi, W. (2000): Large Eddy Simulation of the flow over periodic hills. *16th IMACS World Congress*, Lausanne

[1]Temmerman, L., and Leschziner, M.A. (2001): Large Eddy Simulation of separated flow in a streamwise periodic channel construction. *2nd Int. Symp. on Turbulence and Shear Flow Phenomena*, Stockholm, June 27-29

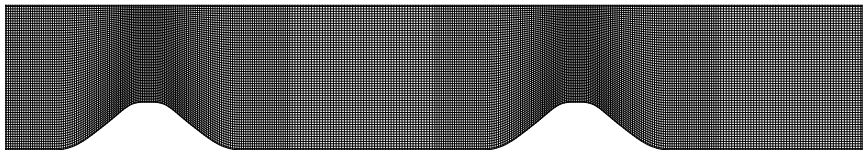

Fig. 1 Numerical mesh ($364x60$ cv's) used for the computations with high-Reynolds number models

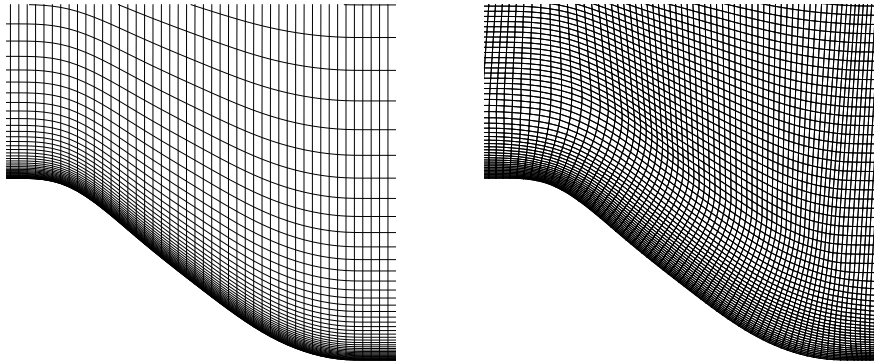

Fig. 2 Blow up of the numerical meshes: $364x66$ (left) and $518x95$ cv's (right) used for the computations with low-Reynolds number models

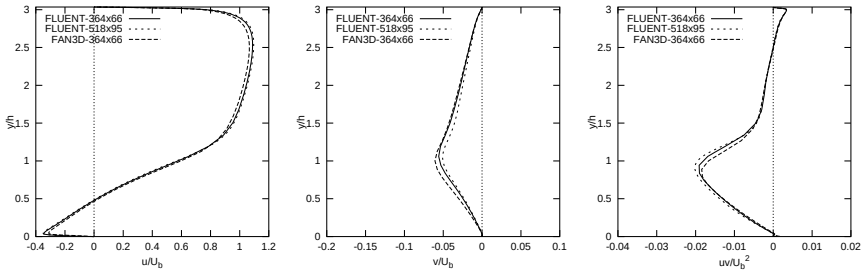

Fig. 3 Grid independence study and code independence study performed by using the Spalart-Allmaras one-equation model ($x/h = 3$)

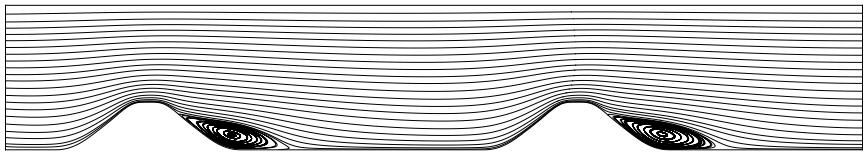

a) FAN-3D

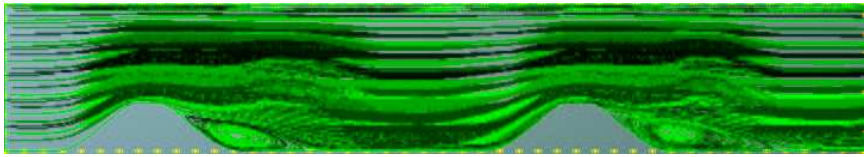

b) SWIFT

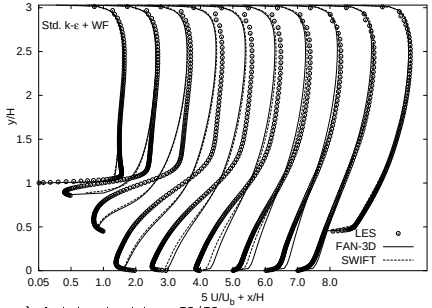

c) Axial velocities: U/Uo

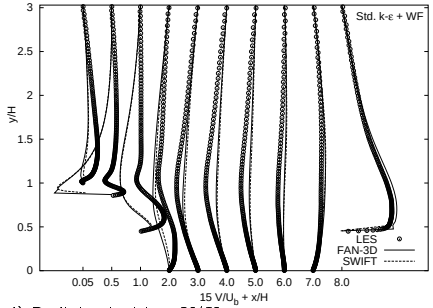

d) Radial velocities: V/Uo

Fig. 4 Code independence study performed by using the Standard $k-\varepsilon$ model + wall functions

Turbulence models

Computations were performed with:

- the standard high-Reynolds number $k-\varepsilon$ model,
- its low-Reynolds number extension due to Launder and Sharma (1974),
- two-layer version of the standard $k-\varepsilon$ model; a one-equation model (transport equation for the kinetic energy of turbulence k and algebraic definition of its dissipation rate) was applied in the near-wall layer, whose velocity scale is represented by the square root of the normal-to-the-wall Reynolds stress component (Rodi et al., 1993) and
- one-equation model based on the transport equation of the eddy viscosity ν_t (Spalart and Allmaras, 1994).

Results

Table 1 and Figs. 5 display the separation and reattachment lengths and streamline patterns obtained by all models applied.

Model	$(x/h)_{separat}$	$(x/h)_{reattach}$
Std. $k-\varepsilon$ + WF	0.61	3.16
Std. $k-\varepsilon$ + WF (SWIFT)	0.60	3.18
LS low-Re $k-\varepsilon$	0.54	3.05
$k-\varepsilon$ TLV	0.31	4.68
S-A	0.25	-
S-A (FLUENT)	0.25	-
LES	0.22	4.72

Table 1: Separation and reattachment lengths

Acknowledgements

The contributions of Dr. B. Basara (AVL List GmbH) and Mr. M. Oswald (Fluent Germany) are gratefully acknowledged.

References

AVL SWIFT Programme Manual, AVL List GmbH, Graz, Austria. CFD Solver v3.1.1, Document No. 15.0213.0606

FLUENT News (Winter 2001): Newsletter, Vol. 10, Issue 2

Hadžić I. (1999): Second-Moment Closure Modelling of Transitional and Unsteady Turbulent Flows. Ph.D. Thesis, Delft Univeristy, The Netherlands

Launder, B.E. and Sharma (1974): Application of the Energy-Dissipation Model of Turbulence to the Calculation of Flow Near a Spinning Disc. Letters in *Heat and Mass Transfer*, Vol 1., p 131

Lilek, Ž. (1997): User manual for the FAN-3D.

Rodi, W., Mansour, N.N., Michelassi (1993): One-Equation Near-Wall Turbulence Modelling With the Aid of Direct Simulation Data. *ASME J. of Fluids Engineering*, Vol. 115, pp 196-205

Spalart, P.R., and Allmaras, S.R. (1994): A one-equation turbulence model for aerodynamic flows. *La Recherche Aérospatiale*, No. 1, pp 5-21

Speziale, C.G., Sarkar, S., and Gatski, T.B. (1991): Modelling the Pressure-Strain Correlation of Turbulence: an Invariant Dynamical Systems Approach, *J. Fluid Mech.*, Vol. 227, pp. 245-272

a) Low-Re $k-\varepsilon$ model (Launder and Sharma, 1974)

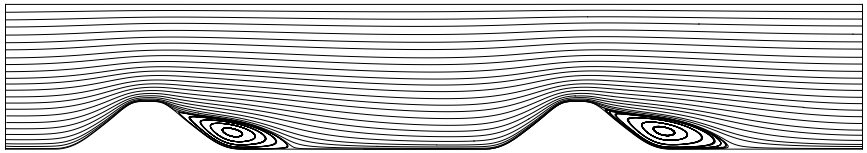

b) Two-layer $k-\varepsilon$ model (Rodi et al., 1993)

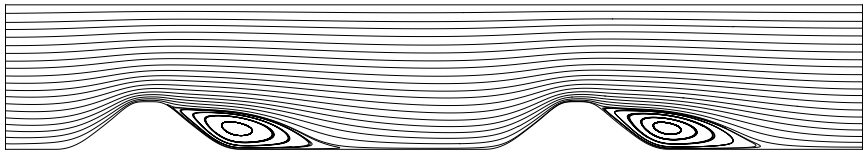

c) Spalart-Allmaras one-equation model (1994)

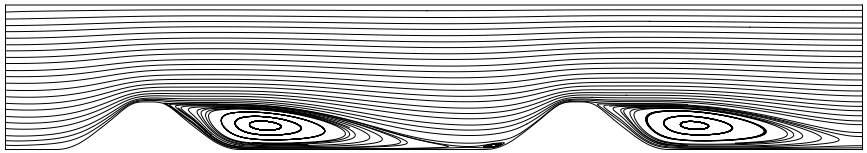

Fig. 5 Streamline patterns obtained with selected near-wall models

Prediction of separated flow with k-ω models and wall function

G.B. Deng & M. Visonneau
Laboratoire de Mécanique des Fluides, Ecole Centrale de Nantes
1 Rue de la Noë, B.P. 92101, 44321 Nantes Cedex 3, France
E-Mail: Ganbo.Deng@ec-nantes.fr

Introduction

Flow separation and reattachment around bodies is a phenomenon frequently encountered in engineering applications. Its accurate prediction is a challenging task in turbulence modeling. A successful prediction of such phenomena depends both on turbulence modelization and a careful near-wall treatment. The 2d hill configuration chosen for the present workshop is a good testcase for the assessment of turbulence model. Jang & al. [1] have presented an excellent paper showing the predictive ability of different turbulence models for this configuration. They have shown that the role of the length-scale governing equation is much more important than the contribution of the normal stresses. The K-ω model gives much better result than the k-ϵ model. Low Reynolds number models were used in their study. However, in most of the engineering applications, a wall function approach is employed. It is interesting to verify whether the advantage of the k-ω model for such application is preserved when using wall function. While the employment of the wall function approach with a k-ϵ model is common, few information is available for the k-ω model which is designed initially to be used without wall function. Recently, we have implemented the k-ω model with wall function in an industrial code (N3S-NATUR). The present paper is devoted to the validation of this implementation. Results will be presented for the Wilcox's k-ω model [2] and Menter's k-ω SST and BSL model [3]. Comparison will be performed with the k-ϵ model and corresponding models without wall function.

Turbulence models and Wall function approach in k-ω formulation

The k-ω models selected for the present study [2] [3] are well known models and, consequently, the details of model formulation will not be given here. Current implementation of Menter's k-ω model contains revision designed for swirling flow which will be briefly outlined below. Our implementation of the k-ω model in the N3S-NATUR code aims at swirling flow computation. The rotation and curvature revision of Menter's SST model proposed by Hellsten [4] is retuned by the authors for swirling flow [5]. It is based on the Richardson number defined by

$$R_i = max\left[max\left(2, \frac{|\Omega_{ij}|}{|S_{ij}|}\right)\left(max(2, \frac{|\Omega_{ij}|}{|S_{ij}|}) - 1\right), -\frac{0.8}{C_{sr}}\right]$$

The destruction term in the ω equation $\beta\rho\omega^2$ is multiplied by the swirling correction function computed by

$$F_{sr} = \frac{1}{1 + C_{sr}R_i}$$

Where $C_{sr} = 2.75$, $|S_{ij}| = \sqrt{2S_{ij}S_{ij}}$, and $|\Omega_{ij}| = \sqrt{2\Omega_{ij}\Omega_{ij}}$, S_{ij} and Ω_{ij} being the strain-rate and the vorticity tensor. The second revision concerns the eddy-viscosity limiter in the SST model. Hellsten [4] discovered that the limiter in the SST model is not rotational invariant, hence unsuitable for rotating flow computation. The revision proposed by Hellsten has been found to be unable to give satisfactory prediction for swirling flow by the authors [6]. In our implementation, we adapt the following eddy-viscosity limiter.

$$\nu_t = min\left(\frac{k}{\omega}, \frac{0.31k}{max(2|S_{12}|, 2|S_{13}|, 2|S_{23}|)}\right)$$

$$\nu_t = min\left(\nu_t, \frac{\frac{2}{3}k}{2S_{ii}}\right)$$

if $S_{ii} > 0$ (with no summation on i). The second limiter that does not exist in the original SST model ensures the positivity of the normal stress. The first eddy-viscosity limiter should be activated only on wall boundary layer. No mechanism has been designed in the present implementation to prevent the activation of the eddy-viscosity limiter in the free shear layer. It should be employed with caution.

The wall function approach is usually implemented with k-ϵ formulation. One of the advantage of Wilcox's k-ω model is that the high Reynolds number model can be integrated directly to the wall without using any damping function. For this reason, k-ω based models are usually implemented without wall function. However, in order to save the computational resources, it is desirable to also have a wall function approach implemented in the k-ω model. Few information is available in the literature concerning such implementation. By computing a fully developed turbulent channel flow, we found that the conventional wall function approach implemented in a k-ϵ model can be applied directly to a k-ω model. It is only necessary to replace the wall boundary condition applied to ϵ

$$\epsilon_p = \frac{C_\mu^{3/4} k_p^{3/2}}{\kappa y_p}$$

by a equivalent wall boundary condition applied to ω

$$\omega_p = \frac{\sqrt{k_p}}{\kappa y_p C_\mu^{1/4}}$$

Wilcox's k-ω and Menter's k-ω SST and BSL model are implemented in the N3S-NATUR code with the above wall boundary condition for ω. All other aspects of the wall function implementation in the N3S-NATUR code remain unchanged. The main purpose of this paper is to compare the same wall function implementation in k-ϵ formulation and in k-ω formulation rather than to assess the wall function itself. Details of the wall function implementation in the N3S-NATUR code can be found in [7]. Results obtained with Menter's k-ω SST and BSL model with the swirling revision mentioned above will be referred as SRSST and SRBSL model in the following.

Results and discussions

Geometry and flow characteristics are described in the testcase instruction for the workshop (http://labo.univ-poitiers.fr/informations-lea/Workshop-Ercoftac-2002) and will not be repeated here. Results obtained with wall function for the standard k-ϵ model, the Wilcox's k-ω model, the k-ω SRSST model and k-ω SRBSL model will be compared to the corresponding models without wall function. The computations with wall function are performed with the N3S-NATUR code. Those without wall function are done with the ISIS code developed by our team. The standard k-ϵ model will be compared with the Launder-Sharma low Reynolds number model [8]. Computations are performed on a 221*121 grid. Validations performed on a 331*181 grid shows that the solution is grid independant.

The reattachment position is a important parameter for the present configuration. The LES results of Temmerman & Leschziner [9] give a value of 4.72h. The low Reynolds number computation predict the reattachment positions of 3.35h, 5.35h, 5.35h and 4.75h respectively for the Launder-Sharma model, the k-ω Wilcox model, the k-ω SRSST model, and the the k-ω SRBSL model. Special attention must be made when using wall function. In the N3S-NATUR code, grid is fitted to the wall. The wall used in the wall function is shifted from the grid at a distance that remains constant through the whole domain specified by the user. Several computations were performed to check the grid independant solution and the influence of this user prescribed wall distance. We first held the wall distance at 0.0001m and change the grid spacing in the vertical direction. Three different grids are generated with the first grid space next to the wall of $0.05h_a$, $0.1h_a$ and $0.2h_a$ respectively where h_a is the averaged grid space in the vertical direction. With the k-ϵ model, the reattachment positions are located at 4.38h, 4.37h and 4.39h respectively. Little difference is observed on the U velocity profiles at x=2h shown in the figure 1 for the three grids. These results indicate that grid stretching independent solution is obtained. In the later computation, the second grid with $0.1h_a$ is employed. The first grid space is about $y^+ = 1$, which is fine enough to capture the near wall variation.

Then, we vary the distance from the wall. The reattachment positions for four different wall distances (0.0001m, 0.0002m, 0.0004m and 0.0006m) are shown in the figure 2 both for the k-ϵ model and for the k-ω model. Compared with the k-ϵ model, the recirlulation length is always longer when using the k-ω model. Thus, the distinct characteristic of the k-ω model for this flow is well preserved with wall function. Unfortunately, the user specified wall distance is found to have a substantial influence on the computational result, especially for the k-ω model. Comparison of the U velocity profiles at X=2h shown in the figures 3 and 4 confirms this observation.

To better understand this behaviour, the solutions are examined in more detail. Below 0.0002m, wall function approach gives a longer recirculation length for both models compared with the result obtained without wall function. Detailed inspection of the predicted velocity filed reveals that the velocity components at the first grid point away from the wall are erroneous. It results from the fact that at such a small distance, the wall is located below $y^+ = 5$ which is the limit at which $u^+ = y^+$ is imposed in the N3S-NATUR code. The erroneous result suggests that it is prefered not to locate the wall from the first grid point below $y^+ = 5$ with the present implementation.

In order to understand why the computational result is so sensitive to the wall distance for this configuration, we examine the result obtained with low Reynolds number model in more detail. The figure 5 shows the turbulence dissipation obtained with the Launder-Sharma model. It can be observed that the turbulent dissipation inside the separation zone is strongly influenced by the historical effect upstream. The maximum value of the turbulent dissipation is found in a position located at the windward side of the hill near the crest at about $y^+ = 10$ away from the wall. It is evident that an accurate resolution of the dissipation equation in this region is crucial for this configuration. Wall function approach is unlikely capable to resolve this maximum-dissipation-production region with accuracy. One can only try to minimize the error by locating the grid point as close to the wall as possible. Based on this observation, 0.0004m is the appropriate wall distance to be used in the present configuration.

Now that the grid and the wall distance have been chosen, we will compare the results obtained with and without wall function. The figure 6 compares the streamlines for four different turbulence models. Results obtained with and without wall function agree fairly well. More detailed comparison of U velocity profiles is presented on the figure 7. Discrepancies observed between the results obtained with and without wall function are similar for all turbulence models, which indicates the success of the wall function implementation in k-ω formulation. For all turbulence models, results obtained with low Reynolds number model agree better with the LES data as expected. The boundary layer on the upper wall which is quite simple is better predicted with low Reynolds number models. We believe that this is due to the fact that the boundary layer in the windward side is poorly resolved with wall function, resulting in an underestimation of the U velocity on the crest of the hill near the wall. The U velocity is increased near the upper wall to maintain the mass conservation, which results in an overestimation of the U velocity near the upper wall downstream due to the historical effect when using wall function.

It is interesting to note that the SRBSL model gives better prediction than the SRSST model for the present configuration. In our implementation, the eddy viscosity limiter in the SRSST model is applied everywhere. The resulting poor result suggests that it should not be applied to the free shear layer. Indeed, the eddy viscosity limiter is designed only for wall boundary layer under adverse pressure gradient. In the original SST model, attention was made such that the limiter is deactivated for free shear layer for external airfoil flow. For the present internal flow, due to the present of the two wall, the limiter is activated everywhere even for the original SST model, giving the location of the reattachment point at 6.45h. The swirling revision brings the reattachment point at 6.08h. But the recirculation length is still too long compared with LES result. The present computation suggests that the SST model must be employed with care for internal flow involving separation.

Results obtained by the SRBSL model are surprisingly good except for the developpment of the boundary layer on the windward side of the hill. The success of the SRBSL model is due to the original BSL model as well as the swirling revision. The comparison between the BSL model and the SRBSL model on the U velocity profiles shown in the figure 8 indicate that swirling revision improves the prediction mainly in the recovering region. It is worthwhile to mention that the swirling revision is calibrated by the authors using four different swirling flows without referencing to the present configuration. The good performance of the SRBSL model indicates that the contribution of normal stress anisotropy is not so important in the present configuration.

Without losing the main finding, only the results obtained with the SRBSL model with and without wall function are submitted to the workshop.

Conclusions

Computations with and without wall function have been performed for four different models both with k-ϵ and k-ω formulations. It is shown that the same wall function approach designed for the k-ϵ mode can be applied as well for the k-ω model although the influence of the wall distance seems to be a little bit more important. Better performances frequently observed for the k-ω based models compared with the k-ϵ based models for the prediction of separated flow are preserved when using wall function. In the present configuration, it is crucial to capture the maximum-dissipation-production region which is located in the windward side of the hill very close to the wall. It is unlikely possible for a wall function approach to obtain accurate solution unless it allows to

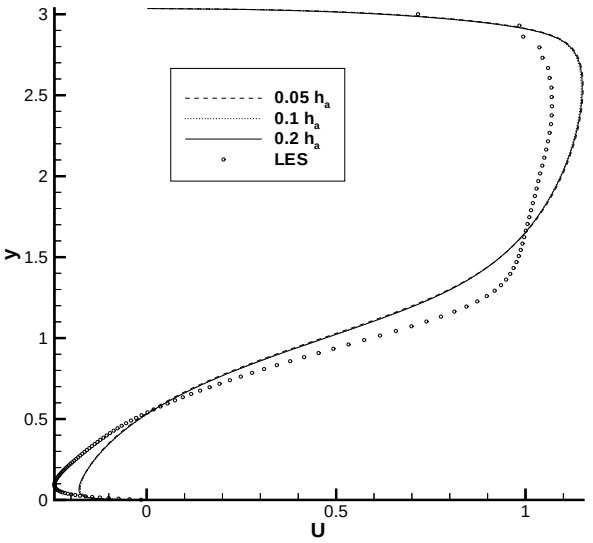

Figure 1: The grid stretching effect on the U velocity profiles at X=2h.

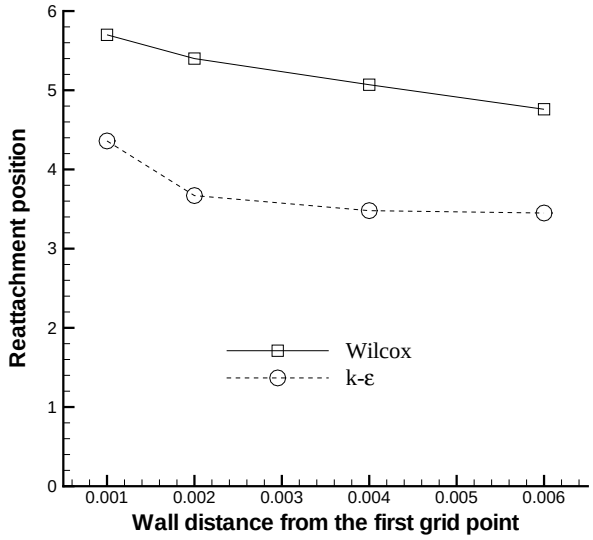

Figure 2: The wall distance effect on the reattachment position.

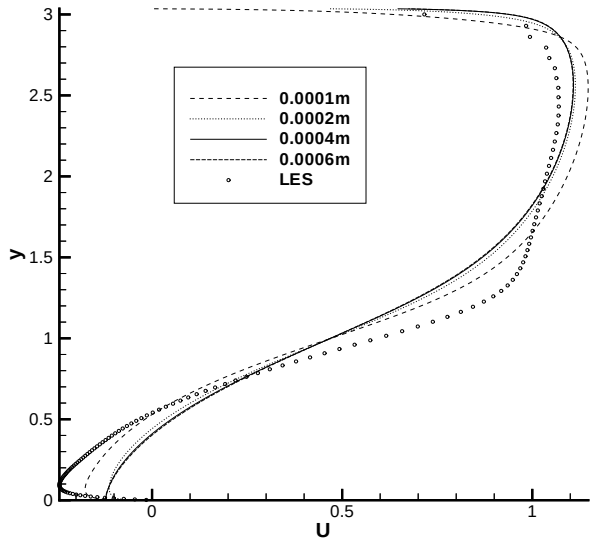

Figure 3: U velocity profiles at X=2h predicted by k-ϵ model with different wall distance.

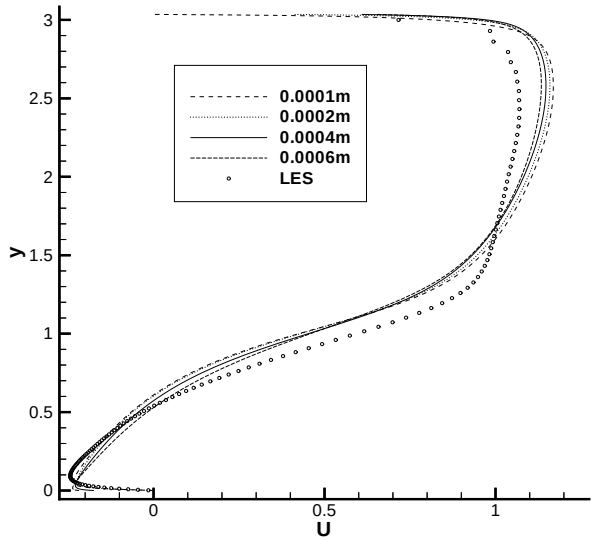

Figure 4: U velocity profiles at X=2h predicted by k-ω model with different wall distance.

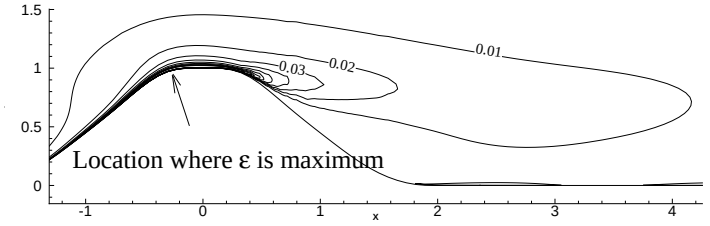

Figure 5: The turbulent dissipation predicted with the Launder-Sharma model.

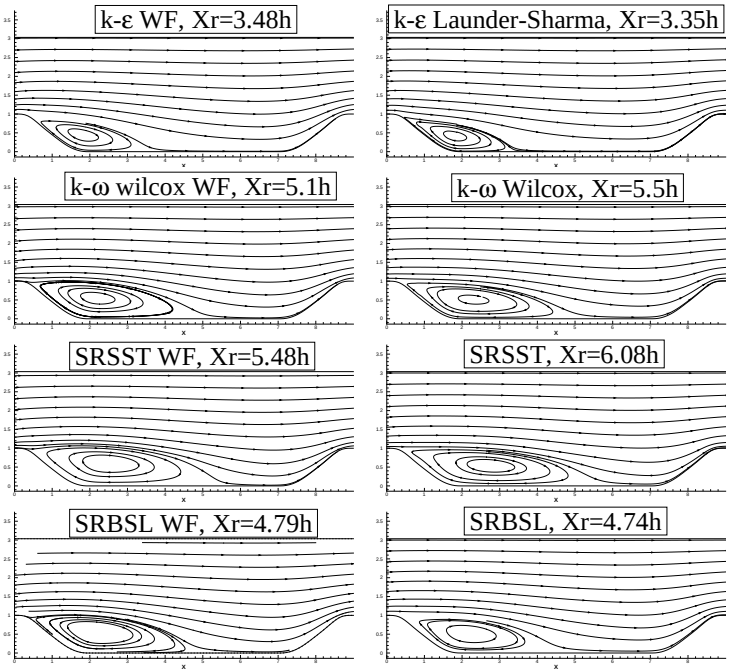

Figure 6: Comparison of streamlines predicted with and without wall function.

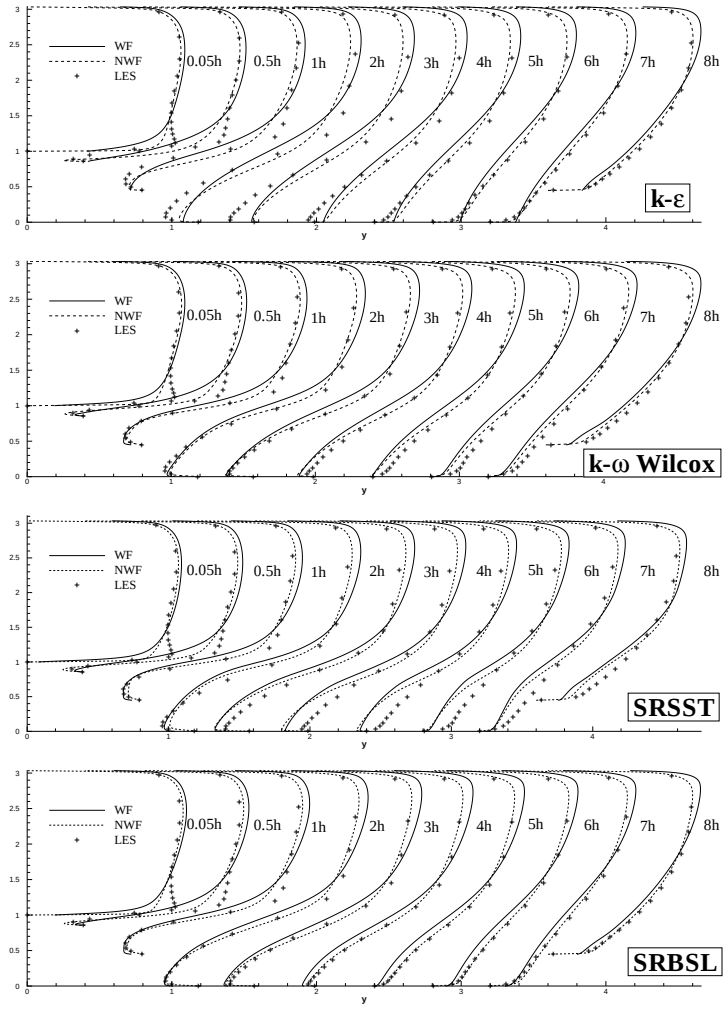

Figure 7: Comparision of U velocity profiles obtained with and without wall function. NWF in the legend stands for computation without wall function.

locate the first grid point much close to the wall in the critical region.

The BSL model with swirling revision is found to be fairly successful for the present configuration. Further investigation on other configurations is required to confirm its performance. On the other hand, the SRSST model tends to overestimate the recirculation length. The design of the eddy viscosity limiter for internal flow for the SST model has to be revised.

Annexe

Results obtained with two Reynolds stress models are also submitted to the workshop. One uses the IP pressure-strain model [10], and the other uses the SSG model [11]. Both have a low Reynolds number version proposed by the authors [12]. The streamlines and the U velocity profiles are shown in the figures 9 and 10 respectively. Both models overestimate the recirculation length. They give a correct prediction on the windward side where all other models fail, but give a poor prediction elsewhere, especially the separation zone. The good prediction at the crest of the hill leads to a better prediction of the velocity field near the upper wall for the reason mentioned above. We believe that the global poor performance of the Reynolds stress model for such a frequently encountered flow is the main reason for which it is not widely used in industrial applications even if it can provide a better prediction than the linear eddy-viscosity model in some flow region.

Acknowledgements

The authors gratefully acknowledge the SNECMA-Moteur Department for their financial support through the contract PEA-Titan for the implementation of the k-ω models into the N3S-NATUR code.

References

[1] Y. Jang, L. Temmerman, and M. Leschziner, "Investigation of anisotropy-resolving turbulence models by reference to highly resolved les data for separated flow," in *Procceding of ECCOMAS Computational Fluid Dynamics Conferenc*, (Swansea), 2001.

[2] D. Wilcox, "Reassessment of the scale-determining equation for advanced turbulence models.," *AIAA Journal*, vol. 26, pp. 1299–1310, 1988.

[3] F. Menter, "Zonal two-equations $k-\omega$ turbulence models for aerodynamic flows.," *AIAA Paper*, vol. 93-2906, 1993.

[4] A. Hellsten, "Some improvements in Menter's k-ω SST turbulence model," in *29th AIAA Fluid Dynamics Conference*, AIAA-98-2554, 1998.

[5] G. Deng and M. Visonneau, "Implantation et validation du modèlek-ω dans n3s-natur," tech. rep., Rapport de Contrat ECN, 2002.

[6] G. Deng and M. Visonneau, "Amélioration de la modélisation de la turbulence pour des écoulements internes en rotation," tech. rep., Rapport de Contrat ECN, 2001.

[7] SIMULOG, "Manuel théorique N3S-NATUR v1.4," tech. rep., Documentation N3S-NATUR, 2001.

[8] B. Launder and B. Sharma, "Application of the energy-dissipation model of turbulence to the calculation of flow near a spinning disc," *Letter in Heat and Mass Transfer*, vol. 1, pp. 131–138, 1974.

[9] L. Temmerman and M. Leschziner, "Large eddy simulation of separated flow in a streamwise periodic channel construction," in *Int. Symp. on Turbulence and Shear Flow Phenomena*, (Stockholm), 2001.

[10] M. Gibson and B. Launder, "Ground effects on pressure fluctuations in the atmospheric boundary layer," *J. Fluid Mech.*, vol. 86, pp. 491–511, 1978.

[11] C. Speziale, S. Sarkar, and T. Gatski, "Modeling the pressure-strain correlation of turbulence: An invariant dynamical systems approach," *Journal of Fluid Mechanics*, vol. 227, pp. 245–272, 1991.

[12] G. Deng and M. Visonneau, "Comparison of explicit algebraic stress models and second-order turbulence closures for steady flows around ships," in *Proc. 7th Int. Conf. on Numerical Ship Hydrodynamics*, 1999.

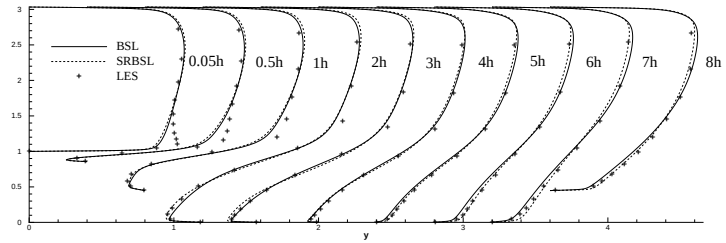

Figure 8: Comparision of U velocity profiles obtained with the BSL model and the SRBSL model.

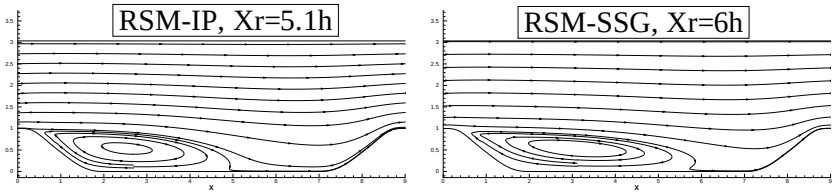

Figure 9: Streamlines predicted the RSM-IP and the RSM-SSG model.

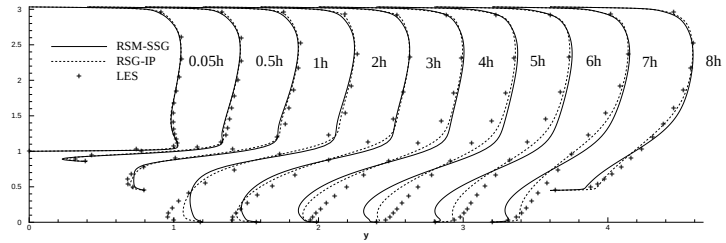

Figure 10: U velocity profiles obtained with the RSM-IP model and the RSM-SSG model.

Case 9.2: Description of the Cubic Low-Reynolds $k-\varepsilon$ Model, the Grid and the Method

B. Merci[1], C. De Langhe, K. Lodefier and E. Dick

Ghent University - Dept. of Flow, Heat and Combustion Mechs.
Tel.: +/32/9/264.33.14, Fax: +/32/9/264.35.86, E-mail: Bart.Merci@rug.ac.be
[1] Postdoctoral Fellow of the Fund for Scientific Research - Flanders (Belgium) (FWO-Vlaanderen).

1 Model Description

The model, which is completely described in [1], consists of a new constitutive law for the Reynolds stresses and an improved ε transport equation.

1.1 Constitutive Law

The anisotropy tensor $\overline{\mathbf{a}}$, defined as

$$\overline{a}_{ij} = \frac{\overline{v_i' v_j'}}{\overline{k}} - \frac{2}{3}\delta_{ij} \quad , \tag{1}$$

with δ_{ij} the Kronecker delta, is expressed in terms of the dimensionless strain rate tensor ($\mathbf{S}\tau_t$) and vorticity tensor ($\mathbf{\Omega}\tau_t$), where τ_t is the turbulence time scale (defined in eq. (4)).

The tensors $\mathbf{S}$ and $\mathbf{\Omega}$ are:

$$S_{ij} = \frac{1}{2}(\frac{\partial v_i}{\partial x_j} + \frac{\partial v_j}{\partial x_i}) - \frac{1}{3}\delta_{ij}\frac{\partial v_k}{\partial x_k} \tag{2}$$

and

$$\Omega_{ij} = \frac{1}{2}(\frac{\partial v_i}{\partial x_j} - \frac{\partial v_j}{\partial x_i}) \; . \tag{3}$$

The turbulence time scale τ_t is defined as:

$$\tau_t = \frac{k}{\varepsilon} + \sqrt{\frac{\mu}{\rho\varepsilon}} \; . \tag{4}$$

Two following tensor invariants are used:

$$S = \sqrt{2 S_{ij} S_{ij}} \; , \; \Omega = \sqrt{2\Omega_{ij}\Omega_{ij}} \; , \; \eta = \tau_t (S^2 + \Omega^2)^{1/2} \; . \tag{5}$$

The constitutive law is given by:

$$\begin{aligned} a_{ij} = & - 2 c_\mu f_\mu \tau_t S_{ij} \\ & + q_1 \tau_t^2 (S_{ik}S_{kj} - \frac{1}{3}\delta_{ij} S_{lm} S_{ml}) \\ & + (q_2 + q_1/6)\tau_t^2 (\Omega_{ik} S_{kj} - S_{ik}\Omega_{kj}) \\ & + \tau_t^3 (c_1 S_{mn} S_{nm} + c_2 \Omega_{mn}\Omega_{nm}) S_{ij} \\ & + c_3 \tau_t^3 (\Omega_{ik} S_{kl} S_{lj} - S_{ik} S_{kl} \Omega_{lj}) \; . \end{aligned} \tag{6}$$

The expression for c_μ is:

$$c_\mu = \frac{1}{A_1 + A_s \eta} \quad , \tag{7}$$

with

$$A_1 = 4 \quad , \quad A_s = \sqrt{3} cos\phi \tag{8}$$

$$\phi = \frac{1}{3} arccos(\sqrt{6} W) \quad , \quad W = 2^{1.5} \frac{S_{ij} S_{jk} S_{ki}}{S^3} \quad . \tag{9}$$

The damping function f_μ is defined as:

$$f_\mu = 1. - exp(-6\ 10^{-2}\sqrt{R_y} - 2\ 10^{-4} R_y^{1.5} - 2\ 10^{-8} R_y^4) \; , \tag{10}$$

with $R_y = \frac{\rho\sqrt{k}y}{\mu}$, y being the normal distance from the nearest solid boundary.

The coefficients q_1 and q_2 are:

$$\begin{cases} q_1 = (7 + 2.1\eta + 4.2\ 10^{-3}\eta^3)^{-1} \\ q_2 = (10 + 3.6\eta + 1\ 10^{-2}\eta^3)^{-1} \end{cases} \tag{11}$$

The coefficients c_i are:

$$\begin{cases} S \geq \Omega : c_1 = c_2 = -min(40 c_\mu^4 ; 0.15) \\ S < \Omega : c_1 = c_2 = -min(min(600 c_\mu^4 ; 0.15); 4 f_\mu c_\mu / (\Omega^2 \tau_t^2 - S^2 \tau_t^2)) \end{cases} \tag{12}$$

and

$$c_3 = -2 c_1 \; . \tag{13}$$

Note that for the present 2D case, the term with c_3 in (6) is identically equal to zero.

1.2 Dissipation rate equation

The transport equation for k is standard:

$$\frac{\partial}{\partial t}(\rho k) + \frac{\partial}{\partial x_j}(\rho k v_j) = \tau_{ij}^T \frac{\partial v_j}{\partial x_i} - \rho\varepsilon + \frac{\partial}{\partial x_j}[(\mu + \frac{\mu_t}{\sigma_k})\frac{\partial k}{\partial x_j}] \; , \tag{14}$$

with the eddy viscosity $\mu_t = \rho c_\mu f_\mu k \tau_t$. The transport equation for the dissipation rate is original[1]. It is a combination of the equation in [2] and the one in [3]:

$$\frac{\partial}{\partial t}(\rho\varepsilon) + \frac{\partial}{\partial x_j}(\rho\varepsilon v_j) = (1 - f_{R_y}) c_{\varepsilon 1} \frac{\tau_{ij}^T \frac{\partial v_j}{\partial x_i}}{\tau_t} + f_{R_y} C_1 S \rho\varepsilon - c_{\varepsilon 2} f_2 \rho\varepsilon \frac{1}{\tau_t} + \frac{\partial}{\partial x_j}[(\mu + \frac{\mu_t}{\sigma_\varepsilon})\frac{\partial\varepsilon}{\partial x_j}] + E \; . \tag{15}$$

The blending function f_{R_y} goes from zero to one as R_y goes from 1000 to 2000:

$$f_{R_y} = \frac{1}{2} + \frac{1}{2} sin(\frac{\pi}{2} min[max(\frac{R_y}{500} - 3; -1); 1]) \; . \tag{16}$$

Due to the blending, good results are obtained for free shear flows (in particular, the plane jet - round jet anomaly is resolved), as well as for wall-dominated flows. The model parameters are as follows:

$$c_{\varepsilon 1} = 1.44 \; , \; C_1 = max(0.43; \frac{Sk/\varepsilon}{5 + Sk/\varepsilon}) \; , \tag{17}$$

$$c_{\varepsilon 2} = max(1.83 + \frac{0.075\Omega\tau_t}{1 + S^2\tau_t^2}; C_2 f_{R_y}) \; ; C_2 = 1.9 \tag{18}$$

$$f_2 = 1 - 0.22 exp(-\frac{Re_T^2}{36}) \; , \; Re_t = \frac{\rho k \tau_t}{\mu} \; , \; \sigma_\varepsilon = 1.2 \; . \tag{19}$$

The source term E has been determined from the standard $k-\omega$ model:

$$E = -1.8(1 - f_\mu)(\mu + \frac{\mu_t}{\sigma_\varepsilon})\frac{\partial k}{\partial x_i}\frac{\partial \tau_t^{-1}}{\partial x_i} \; . \tag{20}$$

2 Grid Description

The structured computational grid consists of 181×73 grid nodes. At the upper boundary, the grid points are equidistant. At the lower boundary, the cells are refined in the neighbourhood of the top of the hill. The grid lines are orthogonal to the solid boundaries. The cells are refined in the vertical direction in the neighbourhood of solid boundaries, so that y^+ is lower than 1 everywhere. A part of the mesh is seen in fig. 1.

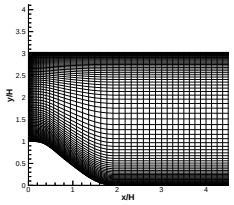

Figure 1: Picture of the computational grid.

3 Method Description

A finite volume method is used. The scheme is a second-order AUSM-like discretization, with a dissipation term in the mass equation for stability reasons, as described in [4] and [5]. The method contains preconditioning and multistage (pseudo-)time stepping towards the steady state solution, with four stages.

The boundary conditions are as follows. At the inlet boundary, all quantities are imposed as prescribed, except for static pressure, which is extrapolated from the flow field. The dissipation rate has been determined from the given length scale. At the solid boundaries, zero derivatives are imposed for the static pressure. The velocity components are set to zero. The boundary conditions for the turbulence quantities are turbulence quantities are $k_w = 0$ and $\varepsilon_w = 2\nu(\frac{\partial\sqrt{k}}{\partial y})^2$, where ν is the kinematic viscosity and y is the direction normal to the solid boundary. At the outlet boundary, static pressure is imposed and zero axial derivatives are used for all other quantities.

References

[1] Merci, B. and Dick, E., 'Predictive Capabilities of an Improved Cubic $k-\varepsilon$ Model for Inert Steady Flows', *Flow, Turbulence and Combustion* (in press).

[2] Merci, B., De Langhe, C., Vierendeels, J. and Dick, E., 'A Quasi-Realizable Cubic Low-Reynolds Eddy-Viscosity Turbulence Model with a New Dissipation Rate Equation', *Flow, Turbulence and Combustion*, 66(2):133–157, 2001.

[3] Shih, T.H., Liou, W.W., Shabbir, A., Yang, Z. and Zhu, J., 'A New $k-\varepsilon$ Eddy Viscosity Model for High Reynolds Number Turbulent Flows', *Computers and Fluids*, 24(3):227–238, 1995.

[4] Vierendeels, J., Merci, B. and Dick, E., 'A Blended AUSM+ Method for All Speeds and All Grid Aspect Ratios', *AIAA Journal*, 39(12):2278–2282, 2001.

[5] Merci, B., Steelant, J., Vierendeels, J., Riemslagh, K. and Dick, E., 'Computational Treatment of Source Terms in Two-Equation Turbulence Models', *AIAA Journal*, 38(11):2085–2093, 2000.

Description of the Computations for the Test Case 10.1

Katariina Salo and Antti Hellsten

Helsinki University of Technology
P.O.Box 4400
FIN-02015 HUT, FINLAND
E-mail Antti.Hellsten@hut.fi

General Description

A hierarchy of three turbulence models with different level of sophistication is applied in this case. This model hierachy consists of a full differential Reynolds stress model (RSM), an explicit algebraic Reynolds stress model (EARSM) with a modification included to approximate the advection of the anisotropy tensor caused by curvature effects, and finally an ordinary EARSM. The eddy viscosity models are left out of this comparison because the 9th workshop (2001) provided a plenty of results obtained using various eddy-viscosity models. Both EARSM versions are coupled with the same scale-determining two-equation model (Menter's $k-\omega$ BSL model), and also in the RSM-level, the dissipation is modelled using the same ω model, for the sake of consistency.

The Flow Solver

For the mean-flow prediction, a Navier-Stokes solver called FINFLO [1, 2] is utilized. The FINFLO code is developed at the Helsinki University of Technology in the Laboratory of Aerodynamics. It is based on the finite-volume method and utilizes structured multi-block grids. The solution method is an implicit time integration and a multigrid method is used to accelerate convergence. The inviscid fluxes are evaluated using Roe's method with MUSCL-type discretization, while the central-differencing scheme is used in the calculation of the viscous fluxes. No simplifications, such as the thin-layer approximation, are subjected to the diffusive fluxes.

Computational Grid

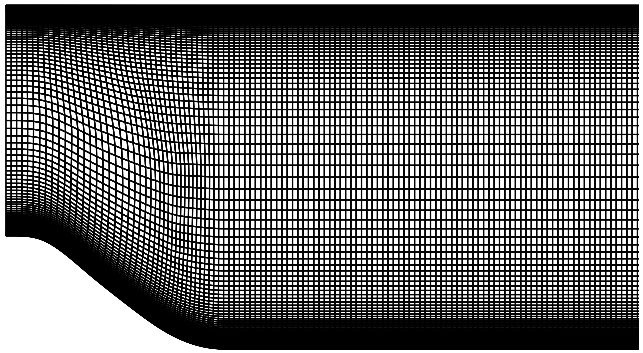

Figure 1: Part of the coarser (384×128) grid from $x/h = 0$ to $x/h = 4.5$. The whole domain starts from $x/h = -3$ and extends up to $x/h = 15$.

The submitted results are computed utilizing a structured single-block grid of very high-resolution. This grid consists of 768×256 control volumes in streamwise and transverse directions, respectively. The thickness of the first cell is kept well below 1 in y^+ everywhere, typically, it is around 0.2. All computations were performed also using a coarser (but still quite fine) 384×128 grid, which is obtained from the fine grid by omitting every other grid line in both directions. These results are practically identical, except that there are some minor differences in the leeward side of the hill where the separation occurs. This is owing to somewhat too coarse streamwise spacing in the 384×128 grid in this particular region.

Turbulence Modelling

Results obtained with three turbulence models are presented:

- EARSM WJ: The explicit algebraic Reynolds-stress model of Wallin and Johansson [3] (without the near-wall modifications) combined with Menter's $k-\omega$ BSL model [4].
- EARSM CCWJ: The EARSM of Wallin and Johansson derived for curved flows using a novel strain-rate based approach [5, 6], and combined with Menter's $k-\omega$ BSL model

- RSM: Full differential RSM where the EARSM CCWJ model is derived from [5, 6]. Dissipation is modelled using the ω-model adopted from Menter's $k-\omega$ BSL model.

Explicit Algebraic Reynolds-Stress Models

A general quasilinear Reynolds stress model written for the anisotropy tensor $\boldsymbol{a} = a_{ij} \equiv \overline{u_i u_j}/k - (2/3)\delta_{ij}$, where the turbulent kinetic energy $k \equiv \overline{u_i u_i}/2$, reads

$$\tau\left(\frac{\mathrm{D}\boldsymbol{a}}{\mathrm{D}t} - \boldsymbol{\mathcal{D}}^{(a)}\right) = A_0\left[\left(A_3 + A_4\frac{P}{\varepsilon}\right)\boldsymbol{a} + A_1\boldsymbol{S} - (\boldsymbol{a\Omega} - \boldsymbol{\Omega a}) + A_2\left(\boldsymbol{aS} + \boldsymbol{Sa} - \frac{2}{3}\mathrm{tr}\{\boldsymbol{aS}\}\boldsymbol{I}\right)\right] \tag{1}$$

On the right-hand side, the different physical terms (production, dissipation, and redistribution) are added together and the resulting terms are sorted according to their tensorial form. $\boldsymbol{S}$ and $\boldsymbol{\Omega}$ are the strain-rate and vorticity tensors normalized by the turbulent time scale $\tau = k/\varepsilon$ and $A_0, \ldots, A_4$ include the Reynolds stress model-coefficients.

The corresponding ARSM is obtained in the weak equilibrium limit where the left hand side of (1) is ignored, *i.e.* ignoring the advection and diffusion of $\boldsymbol{a}$. This assumption, when invoked in Cartesian coordinate system, may be strongly violated in curved flows — even in cases where the flow is changing slowly in the streamwise direction. One must keep in mind, however, that in this flow extremely rapid streamwise changes take place. Thus, the weak-equilibrium assumption is likely to be strongly violated in any coordinate system. Nevertheless, it is generally thought that the best ARSM for curved flows is obtained by ignoring the anisotropy advection in a suitable curvilinear coordinate system that follows the flow in some sense. The advection term can be expressed as

$$\frac{\mathrm{D}\boldsymbol{a}}{\mathrm{D}t} = \boldsymbol{T}^t\left[\frac{\mathrm{D}}{\mathrm{D}t}(\boldsymbol{TaT}^t)\right]\boldsymbol{T} - \left(\boldsymbol{a\Omega}^{(r)} - \boldsymbol{\Omega}^{(r)}\boldsymbol{a}\right) \tag{2}$$

where $\boldsymbol{T}$ is the transformation matrix from the inertial Cartesian background frame to the curvilinear system and

$$\boldsymbol{\Omega}^{(r)} = \frac{\mathrm{D}\boldsymbol{T}^t}{\mathrm{D}t}\boldsymbol{T} = -\boldsymbol{T}^t\frac{\mathrm{D}\boldsymbol{T}}{\mathrm{D}t} \tag{3}$$

The first term on the right-hand side is the material derivative in the curvilinear system transformed back to the Cartesian system while the last term arises purely from the curvature of the flow path. In principle, the optimal ARSM can be obtained by dropping only the first (differential) term in Eq. (2). The latter term

in (2) can be included in the ARSM, in fact, by only modifying the vorticity tensor, since $\boldsymbol{\Omega}^{(r)}$ is of similar tensorial form as $\boldsymbol{\Omega}$ (skew-symmetry). Redefining the vorticity tensor as

$$\boldsymbol{\Omega}^* = \boldsymbol{\Omega} - \frac{\tau}{A_0}\boldsymbol{\Omega}^{(r)} \tag{4}$$

corresponds to assuming the weak equilibrium in the given curvilinear system.

Now, the problem is reduced to finding a suitable curvilinear coordinate system. The most straightforward choice would be to attach the local basis to the velocity vector. This choice, however, violates Galilean invariance and is thus not generally acceptable. Galilean invariance could be achieved by using the acceleration coordinates but this method has been recently shown to be singular [7, 6]. In this study we use the strain-rate based method recently proposed by Wallin and Johansson [5] which is also Galilean invariant. The rationale behind this method is to assume that the best approximation for the neglected transport term of $\boldsymbol{a}$ is obtained in a system where also the transport effect of the strain rate tensor $\boldsymbol{S}$ has a minimum. In two-dimensional mean flows, like the present case, this leads to the formula already earlier suggested by Spalart & Shur [8]

$$\Omega_{12}^{(r)} = -\Omega_{21}^{(r)} = -\frac{S_{11}\dot{S}_{12} - S_{12}\dot{S}_{11}}{2(S_{11}^2 + S_{12}^2)} \tag{5}$$

The novelty of the Wallin & Johansson method is that, unlike the Spalart & Shur method, it provides a general formula also for three-dimensional mean flows, see Refs. [5, 6]. In practice, the singularity of Eq. (5) in non-strained regions must be removed by introducing a lower limit for the denominator. When the strain-rate tensor is normalized using the turbulent time scale, 10^{-2} is observed to be a suitable value for such a lower limit.

The resulting implicit algebraic relation for the Reynolds stress anisotropy $\boldsymbol{a}$, including the redefinition (4) of the vorticity tensor may be formally solved, resulting in an EARSM. The set of model coefficients, A_1–A_4, is given according to the Wallin & Johansson model [3]. The A_0 coefficient enters only in case of any contribution from the *l.h.s* of Eq. (1), which is the case for the curvature corrected version, and affects the effective vorticity tensor through Eq. (4). A_0 is derived by considering the point of neutral stability for the growth rate in rotating homogeneous shear flows (see Wallin and Johansson [5]). The coefficients are given in Table 1.

Table 1: The values of the A-coefficients.

A_0	A_1	A_2	A_3	A_4
-0.72	1.20	0	1.80	2.25

The explicit solution of the Reynolds stress anisotropy for two-dimensional mean flows consists of three tensor groups in terms of the strain- and modified rotation rate tensors, $\boldsymbol{S}$ and $\boldsymbol{\Omega}^*$

$$\boldsymbol{a} = \beta_1 \boldsymbol{S} + \beta_2 \left(\boldsymbol{S}^2 - \tfrac{1}{3} II_S \mathbf{I} \right) + \beta_4 \left(\boldsymbol{S}\boldsymbol{\Omega}^* - \boldsymbol{\Omega}^* \boldsymbol{S} \right) \tag{6}$$

Furthermore, β_2 is identically zero with the present choice of the model coefficients. The coefficients β_1 and β_4 are functions of the invariants $II_S = \mathrm{tr}\{\boldsymbol{S}^2\}$, $II_\Omega = \mathrm{tr}\{\boldsymbol{\Omega}^{*2}\}$ and are given by Wallin and Johansson [3].

Here, EARSM CCWJ stands for Wallin-Johansson EARSM with the approximation for the ignored advection term of $\boldsymbol{a}$ through Eqs. (4) and (5) as described above. EARSM WJ means the baseline Wallin-Johansson EARSM. Note, that the near-wall modifications proposed in Ref. [3] are not employed in this study.

The Background $k - \omega$ Model

The zonal high Reynolds-number $k - \omega$ BSL model developed by Menter has been utilized as a background model. This model is thoroughly described in the Ref. [4], thus its description is not repeated here.

Differential Reynolds-Stress Model

A full differential Reynolds stress model corresponding to EARSM CCWJ is also tested in order to assess the effect of the ignored transport terms on the EARSM. In the following, the Reynolds stress model is written directly for the stress components unlike Eq. (1), although these formulations are mathematically equivalent. The Reynolds stress model reads

$$\frac{\mathrm{D}\overline{u_i' u_j'}}{\mathrm{D}t} - \frac{\partial}{\partial x_k} \left(T_{ijk} + \nu \frac{\partial \overline{u_i' u_j'}}{\partial x_k} \right) = P_{ij} + \Phi_{ij} - \varepsilon_{ij} \tag{7}$$

where P_{ij} is the production term which needs no modelling. Dissipation of each stress component ε_{ij} is split into the deviator and isotropic parts as

$$\varepsilon_{ij} = \varepsilon e_{ij} + \frac{2}{3} \varepsilon \delta_{ij} \tag{8}$$

with $\varepsilon \equiv \varepsilon_{ii}/2$ being the dissipation rate of the turbulent kinetic energy. It is modeled using Menter's ω-model equation with $\varepsilon = 0.09 k\omega$. The deviator of $\varepsilon_{ij}$is lumped together with the redistribution term Φ_{ij}. The general quasilinear model

is adopted for this term

$$\begin{aligned} \frac{\Phi_{ij}}{\varepsilon} - e_{ij} = & -\frac{1}{2} \left(C_1^0 + C_1^1 \frac{P}{\varepsilon} \right) a_{ij} + C_2 S_{ij} \\ & + \frac{C_3}{2} \left(a_{ik} S_{kj} + S_{ik} a_{kj} - \frac{2}{3} a_{lk} S_{kl} \delta_{ij} \right) - \frac{C_4}{2} \left(a_{ik} \Omega_{kj} - \Omega_{ik} a_{kj} \right) \end{aligned} \tag{9}$$

The model coefficients are set to the values recalibrated by Wallin and Johansson [5], and given in Table 2. These values lead to the A-coefficients given in Table 1, when Eq. (1) is derived from Eq. (7). Although not submitted, a set of coefficients that is very close to the traditional LRR-model was also tested, and very similar results were obtained.

Table 2: The values of the redistribution model coefficients.

C_1^0	C_1^1	C_2	C_3	C_4
4.6	1.24	0.47	2.0	0.56

The turbulent flux of each stress component is modeled using a very simple gradient diffusion model

$$T_{ijk} \approx \sigma_k \beta^* k \tau \frac{\partial \overline{u_i' u_j'}}{\partial x_k} \tag{10}$$

with σ_k adopted from Menter's $k - \omega$ model [4], and $\beta^* = 0.09$.

Discussion on the Results

At least four major conclusions can be made from the results computed at HUT:

1. Only RSM is able to correctly predict the "very far from equilibrium turbulence" around the hill tops while EARSM WJ and even EARSM CCWJ failed in this region. This is because rapid streamwise changes are dominant over curvature effects on the advection term.

2. EARSM CCWJ introduced no improvement over the ordinary EARSM in this case unlike in some other cases maybe not this far away from the local equilibrium, e.g. the U-duct flow of Monson & Seegmiller, see Ref. [6].

3. The underlying scale-determining model predicts too slowly thickening shear layer above the recirculation leading to a delayed reattachment. Judging from the budgets, this seems to be connected with the underestimated turbulent diffusion. An improved $k - \omega$ model to be used with the EARSM is currently under development at HUT, and this fault is kept in mind in the development work.

4. RSM shows qualitatively incorrect flow structure in the reattachement region. In contrast to the LES-data, the dividing streamline makes a kink upstream. This seems to be the case also with many of the RSM-results seen in the 9th workshop. Further work is needed to discover the reason for this anomaly.

References

[1] T. Siikonen. An application of Roe's flux-difference splitting for the $k-\epsilon$ turbulence model. *International Journal for Numerical Methods in Fluids*, 21(11):1017–1039, 1995.

[2] P. Kaurinkoski and A. Hellsten. FINFLO: the Parallel Multi-Block Flow Solver. Report A-17, Helsinki University of Technology, Laboratory of Aerodynamics, 1998. ISBN 951–22–3940–X.

[3] S. Wallin and A. Johansson. A complete explicit algebraic Reynolds stress model for incompressible and compressible turbulent flows. *Journal of Fluid Mechanics*, 403:89–132, 2000.

[4] F.R. Menter. Two-Equation Eddy-Viscosity Turbulence Models for Engineering Applications. *AIAA Journal*, 32(8):1598–1605, 1994.

[5] S. Wallin and A.V. Johansson. Modelling streamline curvature effects in explicit algebraic Reynolds stress turbulence models. *International Journal of Heat and Fluid Flow*, 23(5):721–730, 2002.

[6] A. Hellsten, S. Wallin, and S. Laine. Scrutinizing Curvature Corrections for Algebraic Reynolds Stress Models. In *32nd AIAA Fluid Dynamics Conference*, St. Louis, Missouri, USA, June 2002. AIAA paper 2002–2963.

[7] A. Hellsten. Curvature Corrections for Algebraic Reynolds Stress Modeling: A discussion. *AIAA Journal*, 40(9):1909–1911, 2002.

[8] Spalart, P. and Shur, M., "On the Sensitization of Turbulence Models to Rotation and Curvature," *Aerospace Science and Technology*, No. 5, 1997, pp. 297–302.

Application of CFL3D to Case 9.2 (2-D Hill)

Christopher L. Rumsey*
NASA Langley Research Center
Hampton, Virginia 23681-2199

1 Description of the Code

The computer code CFL3D [1] solves the three-dimensional, time-dependent, Reynolds averaged compressible Navier-Stokes equations with an upwind finite-volume formulation. It can solve flows over multiple-zone grids that are connected in a one-to-one, patched, or overset manner, and can employ grid sequencing, multigrid, and local time stepping when accelerating convergence to steady state. Upwind-biased spatial differencing is used for the inviscid terms, and flux limiting is used to obtain smooth solutions in the vicinity of shock waves, when present. Viscous terms are centrally differenced, and cross-diffusion terms are neglected. For very low Mach number flows, preconditioning [2] is used to insure convergence and accuracy of the solutions.

The CFL3D code is advanced in time with an implicit approximate factorization method. The implicit derivatives are written as spatially first-order accurate, which results in block tridiagonal inversions for each sweep. However, for solutions that utilize Roe flux-difference splitting [3], the block tridiagonal inversions are further simplified using a diagonal algorithm with a spectral radius scaling of the viscous terms.

The turbulence models are solved uncoupled from the mean flow equations using implicit approximate factorization. Their advective terms are solved using first-order upwind differencing. Many turbulence models are available in CFL3D, but only those used in the current study are mentioned here. Descriptions of the one-equation Spalart-Allmaras (SA) and the two-equation Menter k-ω shear-stress transport (SST) turbulence models can be found in their respective references [4, 5], while a more detailed description of the EASM is given in the next section.

2 Algebraic Stress Models

The turbulent stress tensor for EASM is given by

$$\begin{aligned}\tau_{ij} = \quad & \frac{2}{3}K\delta_{ij} - 2\nu_t^*\Big(S_{ij} \\ & +\big[a_2 a_4 (S_{ik}W_{kj} - W_{ik}S_{kj}) \\ & -2a_3 a_4 \big(S_{ik}S_{kj} - \frac{1}{3}S_{kl}S_{lk}\delta_{ij}\big)\big]\Big),\end{aligned} \tag{1}$$

where $S_{ij} = [(\partial u_i/\partial x_j) + (\partial u_j/\partial x_i)]/2$ and $W_{ij} = [(\partial u_i/\partial x_j) - (\partial u_j/\partial x_i)]/2$. The nonlinear terms are within the brackets [ ]. The component τ_{ij} terms are used to close the Reynolds-averaged Navier-Stokes equations (see, e.g., Ref. [6]). The kinematic eddy viscosity ν_t^* is given by

$$\nu_t^* \equiv C_\mu^* K\tau = -K\alpha_1, \tag{2}$$

*Senior Research Scientist; Aerodynamics, Aerothermodynamics, and Acoustics Competency.

with $\tau \equiv 1/\omega$. Thus, α_1/τ is equivalent to $-C_\mu^*$. The value of α_1/τ is obtained from the solution to the following cubic equation at each point in the flow field:

$$\left(\frac{\alpha_1}{\tau}\right)^3 + p\left(\frac{\alpha_1}{\tau}\right)^2 + q\left(\frac{\alpha_1}{\tau}\right) + r = 0, \tag{3}$$

where

$$p = -\frac{\gamma_1^*}{\eta^2\tau^2\gamma_0^*} \tag{4}$$

$$\begin{aligned}q = \frac{1}{(2\eta^2\tau^2\gamma_0^*)^2}\Big(&\gamma_1^{*2} - 2\eta^2\tau^2\gamma_0^* a_1 \\ &-\frac{2}{3}\eta^2\tau^2 a_3^2 + 2\mathcal{R}^2\eta^2\tau^2 a_2^2\Big)\end{aligned} \tag{5}$$

$$r = \frac{\gamma_1^* a_1}{(2\eta^2\tau^2\gamma_0^*)^2}. \tag{6}$$

The correct root to choose from this equation is the root with the lowest real part [7]. Also, the degenerate case when $\eta^2 \to 0$ must be avoided. See Rumsey and Gatski [8] for further details. In the current implementation, the resulting $C_\mu^* = -(\alpha_1/\tau)$ is limited by $C_\mu^* = \max(C_\mu^*, 0.0005)$. The nominal level for C_μ^* in a zero-pressure-gradient log layer is approximately 0.09. Other parameters are given by

$$\eta^2 \equiv \{\mathbf{S}^2\} = S_{ij}S_{ji} = S_{ij}S_{ij} \tag{7}$$

$$\{\mathbf{W}^2\} = W_{ij}W_{ji} = -W_{ij}W_{ij} \tag{8}$$

$$\mathcal{R}^2 = -\frac{\{\mathbf{W}^2\}}{\{\mathbf{S}^2\}} \tag{9}$$

$$a_1 = \frac{1}{2}\left(\frac{4}{3} - C_2\right) \tag{10}$$

$$a_2 = \frac{1}{2}(2 - C_4) \tag{11}$$

$$a_3 = \frac{1}{2}(2 - C_3) \tag{12}$$

$$a_4 = \left[\gamma_1^* - 2\gamma_0^*\left(\frac{\alpha_1}{\tau}\right)\eta^2\tau^2\right]^{-1}\tau. \tag{13}$$

Also,

$$\gamma_0^* = C_1^1/2 \tag{14}$$

$$\gamma_1^* = \frac{1}{2}C_1^0 + \left(\frac{C_{\varepsilon 2} - C_{\varepsilon 1}}{C_{\varepsilon 1} - 1}\right) \tag{15}$$

and $C_{\varepsilon 1} = 1.44$, $C_{\varepsilon 2} = 1.83$, $C_1^0 = 3.4$, $C_1^1 = 1.8$, $C_2 = 0.36$, $C_3 = 1.25$, and $C_4 = 0.4$.

The preceding implementation is exactly the same for the EASM-ko (using K-ω equations) or EASM-ke (using K-ε equations), except that $\tau \equiv K/\varepsilon$ for EASM-ke. For EASM-ko, the explicit tensor representation for τ_{ij} is coupled with the following K-ω two-equation model:

$$\frac{DK}{Dt} = \mathcal{P} - f_{\beta^*}K\omega + \frac{\partial}{\partial x_k}\left[\left(\nu + \frac{\nu_t^*}{\sigma_K}\right)\frac{\partial K}{\partial x_k}\right] \tag{16}$$

$$\frac{D\omega}{Dt} = \gamma \frac{\omega}{K}\mathcal{P} - \beta\omega^2 + \frac{\partial}{\partial x_k}\left[\left(\nu + \frac{\nu_t^*}{\sigma_\omega}\right)\frac{\partial \omega}{\partial x_k}\right], \tag{17}$$

where

$$\mathcal{P} = -\tau_{ij}\frac{\partial u_i}{\partial x_j} \approx 2\nu_t^*\eta^2 \tag{18}$$

and $\sigma_K = 1$, $\sigma_\omega = \kappa^2/[\sqrt{C_\mu}(\beta-\gamma)]$, $\kappa = 0.41$, $\gamma = 0.53$, $\beta = 0.83$, and $C_\mu = 0.0895$. Note that for 2-D incompressible flows, $\mathcal{P} = 2\nu_t^*\eta^2$ is exact. Also, it should be noted that the values of σ_K and γ are different than reported in Rumsey and Gatski [8]. They were changed recently to improve the model's capability for jet-type flows (see Georgiadis et al. [9]). The change was found to have relatively small impact for wall-bounded flows in general. In the current implementation, $\mathcal{P}$ in the K-equation is limited to be less than 20 times the destruction term $f_{\beta^*}K\omega$. The function f_{β^*}, taken from from Wilcox [10], is given by

$$f_{\beta^*} = 1 \quad \text{when} \quad \chi_k \le 0 \tag{19}$$

$$f_{\beta^*} = \frac{1+680\chi_k^2}{1+400\chi_k^2} \quad \text{when} \quad \chi_k > 0 \tag{20}$$

$$\chi_k = \frac{C_\mu^2}{\omega^3}\frac{\partial K}{\partial x_j}\frac{\partial \omega}{\partial x_j}, \tag{21}$$

where the C_μ^2 term in the formula for χ_k is necessary because ω in the current model does not "absorb" C_μ as in Wilcox's model.

For the EASM-ke two-equation model:

$$\frac{DK}{Dt} = \mathcal{P} - \varepsilon + \frac{\partial}{\partial x_k}\left[\left(\nu + \frac{\nu_t^*}{\sigma_K}\right)\frac{\partial K}{\partial x_k}\right] \tag{22}$$

$$\frac{D\varepsilon}{Dt} = C_{\varepsilon 1}\frac{\varepsilon}{K}\mathcal{P} - f_\varepsilon C_{\varepsilon 2}\frac{\varepsilon^2}{K} + \frac{\partial}{\partial x_k}\left[\left(\nu + \frac{\nu_t^*}{\sigma_\varepsilon}\right)\frac{\partial \varepsilon}{\partial x_k}\right], \tag{23}$$

where $f_\varepsilon = [1-\exp(-Re_K/10.8)]$, $Re_K = K^{1/2}d/\nu$, $\sigma_K = 1.0$, $\sigma_\varepsilon = \kappa^2/[\sqrt{C_\mu}(C_{\varepsilon 2} - C_{\varepsilon 1})]$, $C_{\varepsilon 1} = 1.44$, $C_{\varepsilon 2} = 1.83$, $C_\mu = 0.0885$, and d is the distance to the nearest wall. Additional wall damping functions (such as f_μ, to achieve expected asymptotic behavior of the turbulence quantities very near the wall) are not employed in the current model.

The turbulent boundary conditions applied at solid walls are $K_w = 0$, $\varepsilon_w = 2\nu_w(\partial\sqrt{K}/\partial n)_w^2$, and $\omega_w = 10(6\nu_w)/[\beta(\Delta n)^2]$, where Δn is the distance to the first cell center away from the wall. The boundary condition for ω_w is from Menter [5]. This boundary condition simulates the analytical behavior of ω near solid walls without the need for specifying the solution at interior points.

3 Specifics of this Case

To simulate incompressible flow, the Mach number for the 2-D hill case was set very low (M=0.001), and preconditioning was employed. Reynolds number was 10595 per hill height H. For boundary conditions, the lower and upper walls were solid (viscous, adiabatic). Turbulence equations were integrated all the way to the walls. The minumum normal spacing at the lower wall ensured an average minimum y+ of approximately 0.25 for the finest grid, 0.5 on the medium grid, and 1.1 on the coarse grid. The outflow boundary condition set $p/p_{\text{ref}} = 1.0$ and extrapolated density and velocity from the interior. The subsonic inflow boundary specified density, velocity profiles, and turbulence quantity profiles (appropriate to each particular turbulence model) from the LES data, and extrapolated pressure from the interior.

The grid extended from x/H=−3 upstream to x/H=15 downstream, with some opening-up of the grid in the streamwise direction near the outflow boundary. The finest-level grid employed 737 streamwise points and 193 normal points. There was grid stretching in the normal direction in order to give appropriate minimum spacings near each wall (the minimum spacing near the upper wall was larger than that at the lower wall: on the fine grid, average minimum y+ for the upper wall was 1.7 while on the lower wall it was 0.25).

From the grid density study using the EASM-ke model, the separation location (at x/H=0.343 on the finest grid) converges in a second-order fashion as the grid is refined, consistent with second-order global spatial accuracy of CFL3D. Using extrapolation, the separation point on an infinitely-refined grid would be approximately x/H=0.340. However, the reattachment location (at x/H=3.704 on the finest grid) appears to be converging in only a first-order fashion as the grid is refined. Using extrapolation, the reattachment point on an infinitely-refined grid would be approximately x/H=3.9 for EASM-ke.

SA, SST and EASM-ko each did the best job predicting the onset of separation (between x/H=0.20 - 0.24), in good agreement with experiment, but then did a poor job predicting the separation length (it was greatly overpredicted). EASM-ke predicted the separation onset too late (near x/H=0.34), but it then predicted a more reasonable reattachment location and velocity profiles in the reattachment region. (Note that it was shown in Rumsey and Gatski [8] that EASM-ke is ill-suited to predict wall-bounded adverse pressure gradient flows, so it is not surprising that it predicted separation too late.) For this case, there is obviously some question as to whether the simulation of 3-D structures is necessary to predict the physics of this massively-separated flow field, once it has separated.

References

[1] Krist, S. L., Biedron, R. T., and Rumsey, C. L., "CFL3D User's Manual (Version 5.0)," NASA TM-1998-208444, June 1998.

[2] Weiss, J. M., and Smith, W. A., "Preconditioning Applied to Variable and Constant Density Flows," *AIAA Journal*, Vol. 33, No. 11, 1995, pp. 2050–2057.

[3] Roe, P. L., "Approximate Riemann Solvers, Parameter Vectors, and Difference Schemes," *J. Computational Physics*, Vol. 43, 1981, pp. 357–372.

[4] Spalart, P. R., and Allmaras, S. R., "A One-Equation Turbulence Model for Aerodynamic Flows," *La Recherche Aerospatiale*, No. 1, 1994, pp. 5–21.

[5] Menter, F. R., "Two-Equation Eddy-Viscosity Turbulence Models for Engineering Applications," *AIAA Journal*, Vol. 32, No. 8, 1994, pp. 1598–1605.

[6] Gatski, T. B., "Turbulent Flows: Model Equations and Solution Methodology," *Handbook of Computational Fluid Mechanics*, edited by R. Peyret, Academic Press, London, 1996, pp. 339–415.

[7] Jongen, T., and Gatski, T. B., "A Unified Analysis of Planar Homogeneous Turbulence Using Single-Point Closure Equations," *Journal of Fluid Mechanics*, Vol. 399, 1999, pp. 117–150.

[8] Rumsey, C. L., and Gatski, T. B., "Recent Turbulence Model Advances Applied to Multielement Airfoil Computations," *J. Aircraft*, Vol. 38, No. 5, 2001, pp. 904–910.

[9] Georgiadis, N. J., Rumsey, C. L., Yoder, D. A., and Zaman, K. B. M. Q., "Effects of RANS Turbulence Modeling on Calculation of Lobed Nozzle Flowfields," AIAA Paper 2003-1271, January 2003.

[10] Wilcox, D. W., *Turbulence Modeling For CFD*, 2nd ed., DCW Industries, La Canada, 1998.

10th joint ERCOFTAC-IAHR-QNET/CFD Workshop on Refined Turbulence Modelling
October 10-11, 2002

CASE 9.2

MODELLING OF PERIODIC FLOW OVER A 2-D HILL

Jonna Kolkka and Hannu Ahlstedt
Tampere University of Technology
Institute of Energy and Process Engineering
P.O. BOX 589
FIN-33101 Tampere, Finland
e-mail: jonna.kolkka@tut.fi

Modelling has been done with the commercial CFD software Fluent 6.0. Standard k-ε model, realizable k-ε model, Reynolds stress model and SST k-ω model have been used with structured and unstructured grid.

1. TURBULENCE MODELS

In the standard k-ε model (Launder & Spalding 1972) the following values of the model constants have been used

$$C_\mu = 0.09,\ C_{1\varepsilon} = 1.44,\ C_{2\varepsilon} = 1.92,\ \sigma_k = 1.0,\ \sigma_\varepsilon = 1.3 \tag{1}$$

In the realizable k-ε model (Shih et al. 1995) the equation for the turbulence kinetic energy is the same as in the standard k-ε model, but the equation for turbulent dissipation is

$$\rho\frac{D\varepsilon}{Dt} = \frac{\partial}{\partial x_j}\left[\left(\mu + \frac{\mu_t}{\sigma_\varepsilon}\right)\frac{\partial\varepsilon}{\partial x_j}\right] + \rho C_1 S\varepsilon - \rho C_2\frac{\varepsilon^2}{k+\sqrt{\nu\varepsilon}} \tag{2}$$

where $C_1 = max\left[0.43, \frac{\eta}{\eta+5}\right]$, $\eta = \frac{Sk}{\varepsilon}$ and $C_2 = 1.9,\ \sigma_k = 1.0,\ \sigma_\varepsilon = 1.2$. In this model C_μ is no longer constant, but it is computed from equation

$$C_\mu = \frac{1}{A_0 + A_S\frac{U^* k}{\varepsilon}} \tag{3}$$

where $A_0 = 4.04$, $A_S = \sqrt{6}\cos\left[\frac{1}{3}arc\cos\left(\sqrt{6}\frac{S_{ij}S_{jk}S_{ki}}{\sqrt{S_{ij}S_{ij}}}\right)\right]$, $U^* = \sqrt{S_{ij}S_{ij} + \tilde{\Omega}_{ij}\tilde{\Omega}_{ij}}$ and $\tilde{\Omega}_{ij} = \bar{\Omega}_{ij} - 3\varepsilon_{ijk}\omega_k$.

The Reynolds stress model proposed by Launder, Reece and Rodi (1975) has been used. Turbulent diffusive transport has been modelled using a scalar turbulent diffusivity as follows

$$D_{ij}^T = \frac{\partial}{\partial x_k}\left(\frac{\mu_t}{\sigma_k}\frac{\partial\overline{u_i u_j}}{\partial x_k}\right) \tag{4}$$

where $\sigma_k = 0.82$. Pressure-strain term has been modelled using the following decomposition

$$\phi_{ij} = \phi_{ij,1} + \phi_{ij,2} + \phi_{ij}^w \tag{5}$$

The slow pressure-strain term, $\phi_{ij,1}$, has been modelled using Rotta's (1951) linear return to isotropy model and the rapid pressure-strain term, $\phi_{ij,2}$, using the isotropization of production model (Naot et al. 1970). The wall-reflection term has been determined from the equation

$$\phi_{ij}^w \equiv C'_1\frac{\varepsilon}{k}\left(\overline{u_k u_m}n_k n_m\delta_{ij} - \frac{3}{2}\overline{u_i u_k}n_j n_k - \frac{3}{2}\overline{u_j u_k}n_i n_k\right)\frac{k^{3/2}}{C_l\varepsilon d} + C'_2\left(\phi_{km,2}n_k n_m\delta_{ij} - \frac{3}{2}\phi_{ik,2}n_j n_k - \frac{3}{2}\phi_{jk,2}n_i n_k\right)\frac{k^{3/2}}{C_l\varepsilon d} \tag{6}$$

where C'_1=0.5, C'_2=0.3, $C_l = C_\mu^{3/4}/\kappa$, $C_\mu = 0.09$ and $\kappa = 0.41$. The dissipation rate, ε, has been computed similarly as in the standard k-ε model, except the production has been evaluated directly from the Reynolds stresses

$$\rho\frac{D\varepsilon}{Dt} = \frac{\partial}{\partial x_j}\left[\left(\mu + \frac{\mu_t}{\sigma_\varepsilon}\right)\frac{\partial\varepsilon}{\partial x_j}\right] + C_{1\varepsilon}\frac{1}{2}P_{ii}\frac{\varepsilon}{k} - C_{2\varepsilon}\rho\frac{\varepsilon^2}{k} \tag{7}$$

where $\sigma_\varepsilon = 1.0$, $C_{\varepsilon 1} = 1.44$ and $C_{\varepsilon 2} = 1.92$.

SST k-ω model (Menter 1994) blends effectively the robust and accurate formulation of the standard k-ω model (Wilcox 1998) in the near-wall region with the free-stream independence of the standard k-ε model in the far field. In the model the equations for the turbulence kinetic energy and the specific dissipation rate are

$$\rho\frac{Dk}{Dt} = \frac{\partial}{\partial x_i}\left[\left(\mu + \frac{\mu_t}{\sigma_k}\right)\frac{\partial k}{\partial x_i}\right] + G_k - Y_k \tag{8}$$

$$\rho\frac{D\omega}{Dt} = \frac{\partial}{\partial x_i}\left[\left(\mu + \frac{\mu_t}{\sigma_\omega}\right)\frac{\partial\omega}{\partial x_i}\right] + G_\omega - Y_\omega + D_\omega \tag{9}$$

The turbulent viscosity is computed

$$\mu_t = \frac{\rho k}{\omega}\frac{1}{max\left[\frac{1}{\alpha^*}, \frac{\Omega F_2}{a_1\omega}\right]} \tag{10}$$

where $\alpha^* = \alpha_\infty^*\left(\frac{\alpha_0^* + Re_t/R_k}{1 + Re_t/R_k}\right)$, $Re_t = \frac{\rho k}{\mu\omega}$, $\Omega \equiv \sqrt{2\Omega_{ij}\Omega_{ij}}$, $\sigma_k = \frac{1}{\frac{F_1}{\sigma_{k,1}} + \frac{1-F_1}{\sigma_{k,2}}}$ and $\sigma_\omega = \frac{1}{\frac{F_1}{\sigma_{k,1}} + \frac{1-F_1}{\sigma_{k,2}}}$.

The blending functions, F_1 and F_2, are given by

$$F_1 = \tanh(\Phi_1^4) \tag{11}$$

$$\Phi_1 = min\left[max\left(\frac{\sqrt{k}}{0.09\omega y}, \frac{500\mu}{\rho y^2\omega}\right), \frac{4\rho k}{\sigma_{\omega,2}D_\omega^+ y^2}\right] \tag{12}$$

$$D_\omega^+ = max\left(2\rho\frac{1}{\sigma_{\omega,2}}\frac{1}{\omega}\frac{\partial k}{\partial x_j}\frac{\partial \omega}{\partial x_j}, 10^{-20}\right) \quad (13)$$

$$F_2 = \tanh(\Phi_2^2) \quad (14)$$

$$\Phi_2 = max\left(2\frac{\sqrt{k}}{0.009\omega y}, \frac{500\mu}{\rho y^2 \omega}\right) \quad (15)$$

The production of turbulence kinetic energy is defined in the same manner as in the standard k-ε model and the production of specific dissipation rate is

$$G_\omega = \alpha\frac{\omega}{k}G_k \quad (16)$$

where $\alpha = \frac{\alpha_\infty}{\alpha^*}\left(\frac{\alpha_0 + Re_t/R_\omega}{1 + Re_t/R_\omega}\right)$, $\alpha_\infty = F_1\alpha_{\infty,1} + (1-F_1)\alpha_{\infty,2}$, $\alpha_{\infty,1} = \frac{\beta_{i,1}}{\beta_\infty^*} - \frac{\kappa^2}{\sigma_{\omega,1}\sqrt{\beta_\infty^*}}$

and $\alpha_{\infty,2} = \frac{\beta_{i,2}}{\beta_\infty^*} - \frac{\kappa^2}{\sigma_{\omega,2}\sqrt{\beta_\infty^*}}$.

The dissipation of turbulence kinetic energy is

$$Y_k = \rho\beta^* k\omega \quad (17)$$

where $\beta^* = \beta_\infty^*\left(\frac{4/15 + (Re_t/R_\beta)^4}{1 + (Re_t/R_\beta)^4}\right)$

and the dissipation of specific dissipation rate is

$$Y_\omega = \rho\beta_i\omega^2 \quad (18)$$

where $\beta_i = F_1\beta_{i,1} + (1-F_1)\beta_{i,2}$.

To blend the standard k-ω model and the standard k-ε model together, the standard k-ε model has been transformed into equations based on k and ω, which leads to the introduction of a cross-diffusion term

$$D_\omega = 2(1-F_1)\rho\sigma_{\omega,2}\frac{1}{\omega}\frac{\partial k}{\partial x_j}\frac{\partial \omega}{\partial x_j} \quad (19)$$

Model constants are

$$\alpha_0^* = 0.024,\ \alpha_\infty^* = 1,\ \alpha_0 = \frac{1}{9},\ R_k = 6,\ R_\omega = 2.95,\ R_\beta = 8 \quad (20)$$

$$\beta_\infty^* = 0.09,\ \sigma_k = \sigma_\omega = 2.\dot{0},\ \kappa = 0.41,\ \beta_{i,1} = 0,075,\ \beta_{i,2} = 0,0828$$

$$\sigma_{k,1} = 1.176,\ \sigma_{\omega,1} = 2.0,\ \sigma_{k,2} = 1.0,\ \sigma_{\omega,2} = 1.168,\ a_1 = 0.31$$

2. BOUNDARY CONDITIONS

Specified inlet conditions have been entered at X/h=-3.

Enhanced wall treatment have been used with standard k-ε model, realizable k-ε model, Reynolds stress model. It is a near-wall modelling method that combines a two-layer model with enhanced wall functions. The demarcation of two regions, where different approaches are used, is determined by a wall-distance-based, turbulent Reynolds number, Re_y, defined as

$$Re_y \equiv \frac{\rho y\sqrt{k}}{\mu} \quad (21)$$

where y is interpreted as the distance to the nearest wall

$$y \equiv \min_{\vec{r}_w \in \Gamma_w}\left\|\vec{r} - \vec{r}_w\right\| \quad (22)$$

In the fully turbulent region, $Re_y > Re_y^*$, Re_y^*=200, the k-ε models or the RSM are employed.

In the viscosity-affected near-wall region, $Re_y < Re_y^*$, the one-equation model of Wolfshtein (1969) is employed. The turbulent viscosity is computed from

$$\mu_{t,2layer} = \rho C_\mu l_\mu\sqrt{k} \quad (23)$$

where the length scale is computed from

$$l_\mu = yc_l(1 - e^{-Re_y/A_\mu}) \quad (24)$$

The two-layer formulation for turbulent viscosity is used as a part of the enhanced wall treatment in which the two-layer definition is smoothly blended with the high-Reynolds-number μ_t definition from outer region (Jongen 1992)

$$\mu_{t,enh} = \lambda_\varepsilon\mu_t + (1-\lambda_\varepsilon)\mu_{t,2layer} \quad (25)$$

A blending function λ_ε is defined in such a way that it is equal to unity far from walls and zero very near to walls

$$\lambda_\varepsilon = \frac{1}{2}\left[1 + \tanh\left(\frac{Re_y - Re_y^*}{A}\right)\right] \quad (26)$$

The constant A determines the width of the blending function

$$A = \frac{|\Delta Re_y|}{\tanh(0.98)} \quad (27)$$

If the whole flow domain is inside the viscosity-affected region, the ε field is computed from

$$\varepsilon = \frac{k^{3/2}}{l_\varepsilon} \quad (28)$$

The length scales are computed from Chen and Patel (1988)

$$l_\varepsilon = yc_l(1 - e^{-Re_y/A_\varepsilon}) \quad (29)$$

A procedure for the ε specification that is similar to the μ_t bending has been used in order to ensure a smooth transition between algebraically-specified ε in the inner region and the ε obtained from solution of the transport equation in the outer region.

The constants in the length scale formulas are taken from Chen and Patel (1988)

$$c_l = \kappa C_\mu^{-3/4},\ A_\mu = 70,\ A_\varepsilon = 2c_l \tag{30}$$

The enhanced wall functions have been derived by blending linear and logarithmic laws of the wall using a function (Kader 1993)

$$u^+ = e^{\Gamma} u^+_{lam} + e^{1/\Gamma} u^+_{turb} \tag{31}$$

where the blending function is given by

$$\Gamma = -\frac{a(y^+)^4}{1 + by^+} \tag{32}$$

and $c = e^{(E/E" - 1.0)}$, $a = 0.01c$, $b = 5/c$.

3. NUMERICAL METHOD

Fluent solvers are based on the finite volume method. Calculations have been made with double-precision, segregated solver. Discretization of convection terms have been done using second order upwind scheme. The diffusion terms are discretized using second order central-differenzing. The basis for pressure-velocity coupling has been the SIMPLE algorithm.

The convergence criterion was the fall of the norm of residuals 5...9 orders of magnitude. In order to obtain a converged solution typically from 15 000 to 60 000 iterations were required.

4. GRIDS

The calculations have been done using both structured and unstructured grid. The basic grids have been designed at the beginning of the calculation and then they have been refined near the walls during the computation so that $y^+ \leq 1$. The structured grid contains 73532 cells and the unstructured grid 86371 cells. The grids near the hill are shown in Figure 1. The effect of the grid-spacing on the solution was tested using structured grid and RSM with 299408 cells. Only near the reattachment point minor differences have been found.

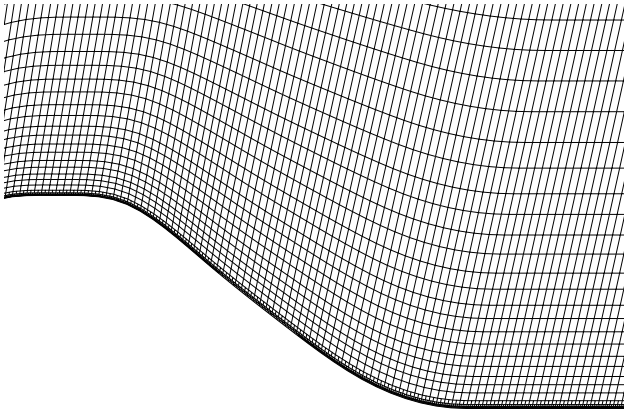

(a)

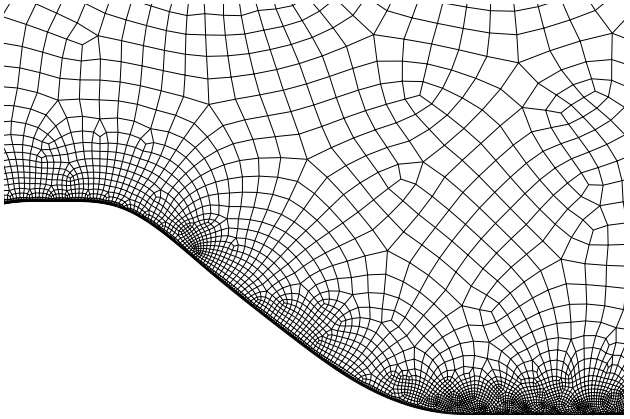

(b)

Figure 1. Calculation grid between X/h=-0.2...2.6 (a) structured grid, (b) unstructured grid.

5. DISCUSSION

The pathlines for the four turbulence models and two grids are shown in Figure 2. All cases give the separation at the same point. The reattachment length of the RSM is the closest value to the LES results. Some kind of bulge can be found in the streamline of the RSM near the reattachment. The realizable k-ε model has longer separation area than the standard k-ε model and the SST k-ω model.

The differences between the results of the standard and realizable k-ε model are very little. The two equation models produce u-velocity values better inside the separation area than the RSM. After the separation area the u-values near the lower wall calculated using the RSM are too high. The SST k-ω model and the RSM gives v-velocities better than the k-ε models. The maximum values of the normal stresses are underestimated by the RSM. At the lower wall dissipation values obtained by LES are increasing towards the wall while all used models produce decreasing values. The k-ε models produce small negative u-velocity values at one or two cells near the lower wall also outside the separation area.

The results of structured and unstructured grids are near each other, but some differences can be noticed. The use of unstructured grid yielded at few points saw tooth profiles for v-velocity. The SST k-ω model with the structured grid could not model the shape of the turbulence kinetic energy profiles especially the peak near the upper wall.

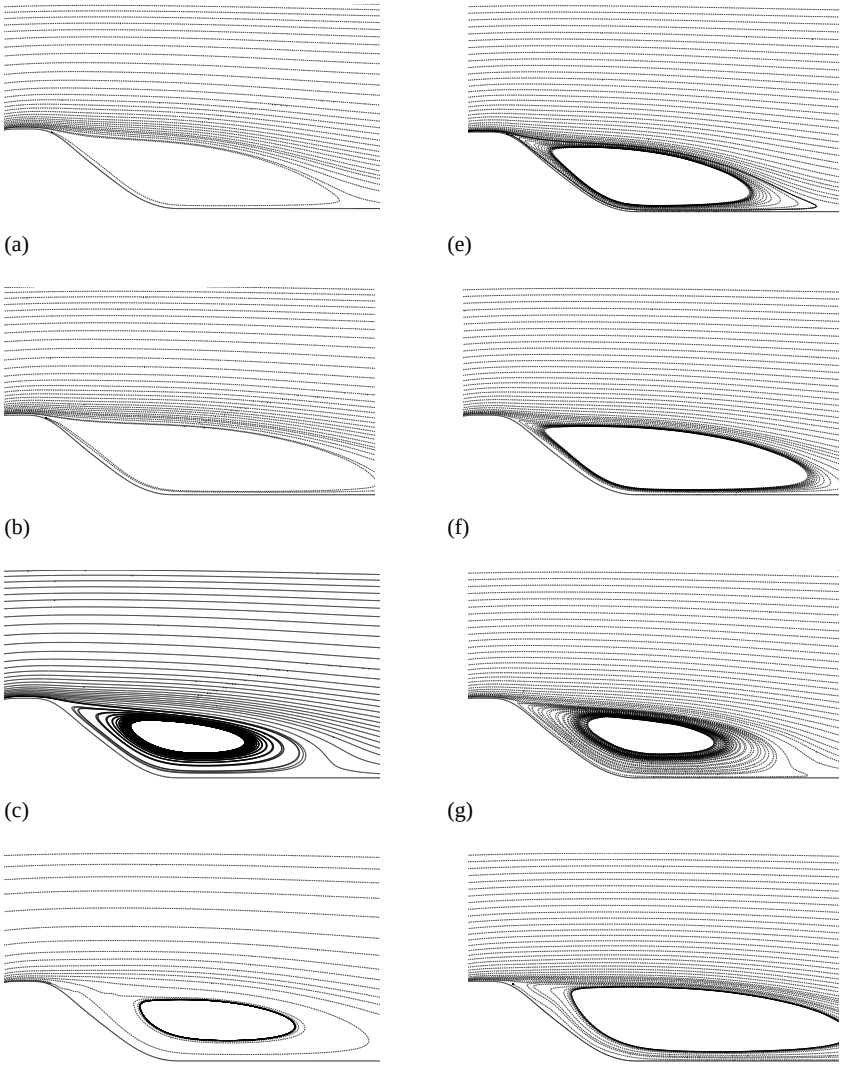

Figure 2. Pathlines after hill (a) standard k-ε model with structured grid, (b) realizable k-ε model with structured grid, (c) Reynolds stress model with structured grid, (d) SST k-ω model with structured grid (e) standard k-ε model with unstructured grid, (f) realizable k-ε model with unstructured grid, (g) Reynolds stress model with unstructured grid and (h) SST k-ω model with unstructured grid.

REFERENCES

Chen, H. C. and Patel, V. C., Near-Wall Turbulence Models for Complex Flows Including Separation, *AIAA Journal*, 26(6):641-648, 1988.

Jongen, T., Simulation and Modelling of Turbulent Incompressible Flows. PhD thesis, EPF Lausanne, Switzerland, 1992.

Kader B., Temperature and Concentration Profiles in Fully Turbulent Boundary Layers, *Int. J. Heat Mass Transfer*, 24(9):1541-1544, 1993.

Launder, B. E., Reece, G. J. and Rodi, W., Progress in the Development of a Reynolds-Stress Turbulence Closure, *J. Fluid Mech.*, 68(3):537-566, 1975.

Launder, B. E. and Spalding, D. B., Lectures in Mathematical Models of Turbulence. Academic Press, London, England, 1972.

Menter, F. R., Two-Equation Eddy-Viscosity Turbulence Models for Engineering Applications, *AIAA Journal*, 32(8):1598-1605, 1994.

Naot, D., Shavit, A. and Wolfshtein, M., Interactions Between Components of the Turbulent Velocity Correlation Tensor Due to Pressure Fluctuations, *Israel J. Technol*, 8:259-269, 1970.

Rotta, J. C., Statistische Theorie nichthomogener Turbulenz, *Z. Phys*, 129:547-572, 1951.

Shih, T. H., Liou, W. W., Shabbir, A. and Zhu, J., A New k-ε Eddy-Viscosity Model for High Reynolds Number Turbulent Flows - Model Development and Validation, *Computers Fluids*, 24(3):227-238, 1995.

Wilcox, D. C., Turbulence Modeling for CFD. DCW Industries, Inc., La Canada, California, 1998.

Wolfshtein, M., The Velocity and Temperature Distribution of One-Dimensional Flow with Turbulence Augmentation and Pressure Gradient, *Int. J. Heat Mass Transfer*, 12:301-318, 1969.

10th Ercoftac/IAHR Workshop on Refined Turbulence Modelling. Case 9.2

J.C. Uribe[1], D. Laurence[1,2]

[1]UMIST - Turbulence Mechanics and CFD Research group.

PO Box 88 Manchester M60 1QD UK. email: J.uribe@umist.ac.uk

[2] EDF- Electricite de France, Mecanique des Fluides et Transfets Thermiques Department, Chateau, France

1 Introduction

The case 9.2 was computed using the *Code Saturne,* developed at EDF and modified at UMIST to implement the V2F model. The code uses finite volume discretization and can handle both structured or unstructured grids. Spatial discretization is based on collocated cell centered storage and the time advancement uses a Rhie and Chow filter on the projection step of the pressure [1]

2 Model

The "code friendly" version of the V2f model [2] was used in the computations.

This particular variation of the model was chosen because it does not require a coupling in the boundary conditions between $\overline{v^2}$ and f. This is achieved by making a change of variables from the original form which allows one to take a simple boundary condition at the wall. The function is thus expressed as :

$$f = \overline{f} - 5\varepsilon\frac{\overline{v^2}}{k^2} \tag{1}$$

And the elliptic equation is solved for $\overline{f}$, which takes a value of zero at the wall. The model equations are:

$$\frac{Dk}{Dt} = P_k - \varepsilon + \frac{\partial}{\partial x_j}\left(\left(\nu + \frac{\nu_t}{\sigma_k}\right)\frac{\partial k}{\partial x_j}\right) \tag{2}$$

$$\frac{D\varepsilon}{Dt} = \frac{(C_{\varepsilon 1}P_k - C_{\varepsilon 2}\varepsilon)}{T} + \frac{\partial}{\partial x_j}\left(\left(\nu + \frac{\nu_t}{\sigma_\varepsilon}\right)\frac{\partial \varepsilon}{\partial x_j}\right) \tag{3}$$

$$\frac{D\overline{v^2}}{Dt} = k\overline{f} - 6\overline{v^2}\frac{\varepsilon}{k} + \frac{\partial}{\partial x_j}\left(\nu + \frac{\nu_t}{\sigma_k}\right)\frac{\partial \overline{v^2}}{\partial x_j} \tag{4}$$

$$L^2\frac{\partial^2\overline{f}}{\partial x_i^2} - \overline{f} = \frac{1}{T}(C_1 - 1)\left[\frac{\overline{v^2}}{k} - \frac{2}{3}\right] - C_2\frac{P_k}{k} - 5\varepsilon\frac{\overline{v^2}}{k^2} \tag{5}$$

where

$$T = \max\left(\frac{k}{\varepsilon}, C_t\sqrt{\frac{\nu}{\varepsilon}}\right) \tag{6}$$

$$L = C_L \max\left(\frac{k^{3/2}}{\varepsilon}, C_\eta\left(\frac{\nu^3}{\varepsilon}\right)^{1/4}\right) \tag{7}$$

$$C_{\varepsilon 1} = 1.4\left(1 + 0.05\sqrt{\frac{k}{\overline{v^2}}}\right) \tag{8}$$

The turbulent viscosity is calculated from

$$\nu_t = C_\mu\overline{v^2}\frac{k}{\varepsilon} \tag{9}$$

The constants used for this model are described in table 1:

$C_{\varepsilon 1}$	$C_{\varepsilon 2}$	C_μ	σ_ε	σ_κ	$C1$	$C2$	C_L	C_η
Eq(8)	1.9	0.22	1.6	1	1.4	0.3	0.23	70

Table 1. Coefficients used in $\overline{v^2} - f$ model, code friendly version

3 Mesh

The results presented were obtained after a grid dependence study, with a final block structured mesh with 42300 (150x282x1) control volumes being employed. The expansion ratio in the vertical direction was 1.05 and the maximum nondimensional distance of the first cell centre from the wall was $y^+ = 0.27$. No wall functions were used as the model is designed to resolve the viscous affected near wall layer.

The computational domain is presented in Figure 1.

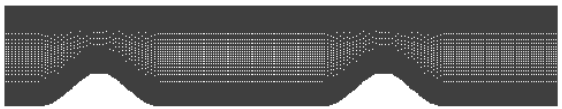

Figure 1: Grid using 150x282 elements

and a close up of the mesh can be seen in Figure 2.

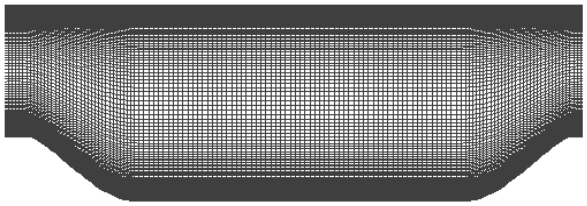

Figure 2: Zoom showing the distribution of the elements.

4 Boundary conditions

For the inlet and outlet, two approaches have been used. In the first, the inlet profiles obtained from the LES data available [3] were used for U, V, k, ε, $\overline{v^2}$ and for f, the condition $\frac{\partial f}{\partial n} = 0$ was used. The outlet boundary was treated with zero gradient conditions. In the second approach (Case 9.2, 9th ERCOFTAC/ IAHR/ COST Workshop. Darmstad, Germany) fully periodic conditions were applied between the inlet and the outlet boundaries.

The wall boundary conditions involved imposing all variables as zero for all the variables except for ε, where the standard value of $\varepsilon_w = 2\nu\frac{k}{y^2}$ was used.

5 Numerical Method

All the variables are stored in the centre of gravity of the cells, and the momentum equations are solved by considering an explicit mass flux. Velocity and pressure are coupled by a prediction/correction method with a SIMPLEC algorithm [4]. The conjugated gradient method is used to solve the Poisson equation for the pressure and the scalar f. An upwind first order scheme is used for the discretization of all the turbulent variables and a second order centered scheme is used for the velocity components

6 Results

The streamlines for the non-periodic calculation are presented in Figure 3. After the first hill the flow separates at 0.39h and it reattaches at 3.71h giving a smaller recirculation zone compared with the LES data. After the second hill, the flow separates at 0.38h after the top of the hill and it reattaches at 3.65h.

Streamlines for the period case are shown in Figure 4. The separation point is 0.35h and the reattachment point is 4.34h which gives a longer recirculation zone compared to the double hill case, but still smaller than the LES calculation.

The velocity profiles are shown in Figure 5 and are compared with the LES data

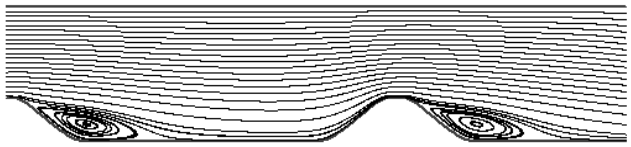

Figure 3: Streamlines for the code friendly v2f model

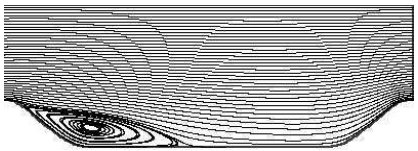

Figure 4: Streamlines for the periodic hills case.

and the results obtained of the calculation for the periodic hills case. It is important to note that the non-periodic treatment results in an earlier reattachment (Figure 10). On the top of the hill, the non-periodic predictions seem to be closer to the LES data (Figure 9) but of course, this is partly a reflection of the inlet conditions being applied to match the LES in this case.

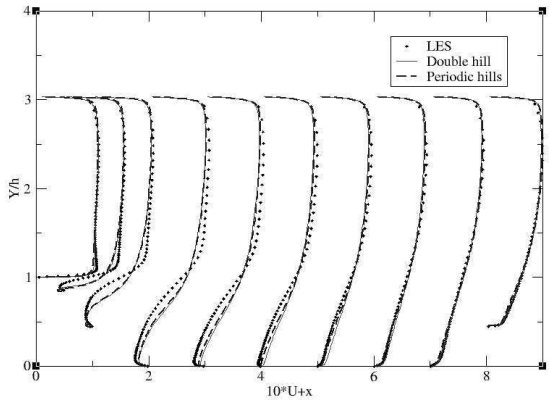

Figure 5: Velocity profiles

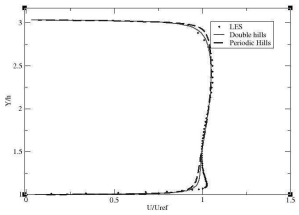

Figure 6. Velocity profiles at $x/h = 0.05$

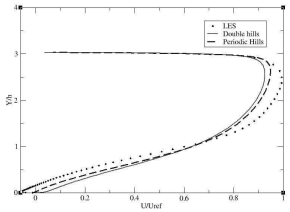

Figure 7. Velocity profiles at $x/h = 4$

Another important comparison is the turbulent kinetic energy, as it is shown in Figure 8.

As can be seen from the figure, the peak in the kinetic energy is under predicted in both cases, but on top of the hill the periodic case gives a lower level of kinetic energy, compared to the non-periodic case. The lower level of turbulent energy (and hence viscosity) result in recirculation zone of the periodic case being larger than the non-periodic one.

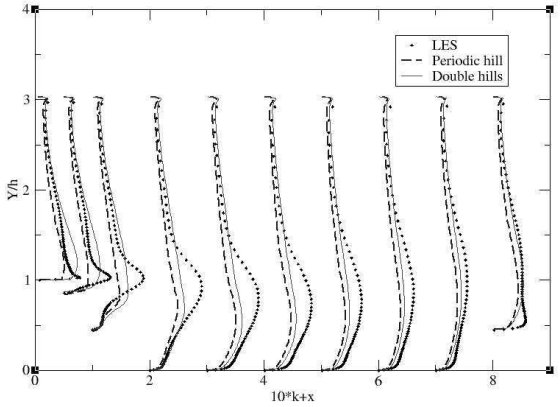

Figure 8: Kinetic energy profiles.

In Figures 9 and 10 the profiles of the shear stress $\overline{uv}$ are shown for two sections, $x/h = 0.05$ and $x/h = 8$. This comparison shows how the high level of shear stress before the hill produces a wrong profile on the top of the hill, resulting in the difference on the velocity profile at the top of the hill (For the periodic case). This is consistent with the results presented on [3] with other ε -based models.

Since in the non-periodic case, the inlet profile is given by the LES data, agreement with the data is expected to be better than in the periodic case, specially at

the top of the hill where the velocity profile is in better agreement due to a better level of turbulent energy. In the periodic case, the turbulence levels at the top of the hill are not constrained by inlet values, because of the periodicity, and this leads to lower levels and a worse velocity profile at the top of the hill.

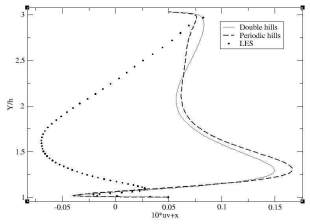

Figure 9: Profile for uv at $x/h = 0.05$

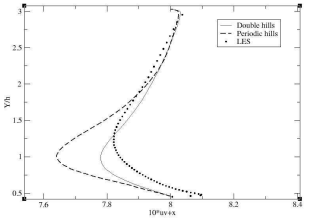

Figure 10: Profile for uv at $x/h = 8$

References

[1] Rhie C.M., Chow W.L., Numerical study of the turbulent flow past an airfoil with trailing edge separation, AIAA Journal, Vol 21-11, pp.1525-1532 (1983).

[2] Lien F. S., Durbin P. A. Non linear $k - \varepsilon - \overline{v^2}$ modeling with application to high lift. Center For Turbulent Research, Proceedings of the Summer Program pp.5-26 (1996).

[3] Jang Y.J., Temmerman L., Leschziner M.A., Investigation of anisotropy-resolving turbulence models by reference to highly-resolved LES data for separated flow, ECCOMAS conference (2001).

[4] Ferziger J.H. and Peric M, Computational Methods for Fluid Dynamics. Springer, second edition, 1999.

10th IAHR/ERCOFTAC Workshop on Refined Turbulence Modelling
October, 2002, University of Poitier

Contribution of Imperial College to Test Case 9.2: Periodic flow over 2D hill

C. Wang, Y.J. Jang and M. Leschziner
Department of Aeronautics, Imperial College London,
London, UK. Email: mike.leschziner@imperial.ac.uk

1. Numerical Methodology

The computations contributed to the workshop have been performed with the code STREAM, developed by Lien & Leschziner (1994) and extended by Apsley & Leschziner (2000). The major features of the code are as follows:

- general non-orthogonal 2d/3d finite-volume formation;
- cartesian velocity components;
- fully collocated storage;
- multiblock capability;
- pressure-correction strategy;
- TVD form (Lien and Leschziner (1994))of the quadratic QUICK scheme (Leonard (1979)) for convection; central differencing for diffusion;
- wide range of non-linear EVMs and second-moment closure models (high-Re and low-Re) incorporated;
- incompressible- and compressible-flow capability.

2. Turbulence Models

Results are presented for 5 turbulence models:

- the linear low-Re k-ε EVM model of Launder and Sharma (1974);
- the cubic low-Re k-ε EVM of Apsley and Leschziner (1998);
- the quadratic low-Re k-ω EVM of Abe, Jang and Leschziner (2003) (see also Jang et al (2003));
- the quadratic low-Re k-ω EARSM of Wallin and Johansson (2000);
- the second-moment closure of Sarkar, Speziale and Gatski (1991), extended to low-Re conditions by Chen et al (2000), with modified coefficients.

Most of the above models are well know and require no elaboration. However the model by Abe et al is know. This quadratic low-Re model differs in two important respects from others. First, it augments the basic quadratic constitutive EVM form by two additive fragments intended to account, respectively, for high normal straining and strong near-wall anisotropy. Second, it uses a form of the ω-equation that is much closer than Wilcox's form to the ε-equation. Specifically, it includes product of k and ω gradients and coefficients for the production and destruction terms which are directly equivalent to $C_{\varepsilon 1}$ and $C_{\varepsilon 2}$ normally used in the ε-equation.

An influential addition for strong near-wall anisotropy is that accounting for specifically the correct decay towards two-component turbulence that is observed in reality through DNS. This decay cannot be represented solely by use of terms combining strain and vorticity, and there is a need to introduce a tensorially correct term that takes into account the wall orientation. In the present model, the wall-direction indicator is

$$d_i = \frac{N_i}{\sqrt{N_k N_k}} \qquad N_i = \frac{\partial l_d}{\partial x_i} \qquad l_d = n \text{ (=wall distance)}$$

which is then used in the wall-anisotropy correction

$${}^{w}a_{ij} = -f_w\left(d_i d_j - \frac{\delta_{ij}}{3} d_k d_k \right)$$

with f_w being a viscosity-related damping function. In the above, a composite time scale is used, which combines the macro-scale k/ε with the Kolmogorov scale $\sqrt{\nu/\varepsilon}$. The damping function f_w then provides a smooth transition between the two scales across the near-wall layer.

3. Computational details

The computational domain is shown in Fig. 1. As seen, we have opted to compute a sequence of **3 rather than 2 hills**. This was motivated by the desire to minimise the influence of the synthetic exit conditions on the flow behind the second hill and by the wish to identify the rate at which the solution 'converges', towards the periodic state. This state was previously computed by Jang et al (2003) with the 8 models (a related contribution has also been made to the 9th IAHR/ERCOFTAC Workshop, Jakirlic et al (2001)). We are therefore able to compare the new 3-hill solution to the that in which periodicity was imposed.

The finite-volume mesh contains 221 × 91 grid lines per hill segment (crest-to-crest distance). The total number of grid lines is therefore 721x91, which has been in grid-independent. To provide adequate resolution of the viscous sublayer and buffer layer adjacent to a solid wall, the minimum grid spacing in the near-wall region is maintained at 10^{-3} of hill height, which corresponds to a wall coordinate y^+ of order of 0.5 for low-Re calculation. The conditions at the inlet, including that for dissipation rate, were taken from the LES solution. At the exit, zero-gradient boundary conditions were prescribed.

4. Results

Solutions for the streamfunction fields are contained in Fig. 2. The degree to which the flow is changing with hill number is indicated in Fig. 3: the solid dots identify the reattachment locations after hills 1,2 and 3; the solid horizontal line gives the periodic

solution obtained under the present grid, finally, the chained line indicates the periodic LES solution. As seen, the model by Abe et al return the closest agreement with the LES data. The Wallin-Johansson model substantially over-estimates the length of the separated zone, while the linear EVM of Launder and Sharma seriously under-estimates this length. The change in the solution from hill to hill is rather small with most models. One exception is the Wallin and Johansson model, the steep downward trend implying that the modelled periodic conditions at the inlet are especially far from the corresponding LES conditions.

Profiles of velocity and turbulence energy at x/h=2, 4 and 6 for one model (Abe, Jang and Leschziner) are shown in Fig. 4. These figures give a clearer picture of the changes from hill to hill, and closer examination reveals a progressive correspondence with the periodic solution as the flow moves downstream over sequential hills. Agreement between the three-hill and the periodic solution is fairly close, especially in the separated region.

References

K. **Abe**, Y-J. Jang and M.A. Leschziner, "An investigation of wall-anisotropy expressions and length-scale equations for non-linear eddy-viscosity models", *Int. J Heat and Fluid Flow*. **24**, 181-198, (2003)

D.D. **Apsley**, and M.A. Leschziner, M.A., Advanced turbulence modelling of separated flow in a diffuser, *Flow, Turbulence and Combustion*, **63**, 81-112. (2000)

D.D. **Apsley** and M.A. Leschziner, "A new low-Reynolds-number nonlinear two-equation turbulence model for complex flows", *Int. J. Heat and Fluid Flow*, **19**, 209-222 (1998).

H.C. **Chen**, Y.J. Jang and J.C. Han, "Computation of heat transfer in rotating two-pass square channels by a second-moment closure model", *Int. J. Heat and Mass Transfer*, **43**, 1603-1616 (2000).

T.B. **Gatski** and C.G. Speziale, "On explicit algebraic stress models for complex turbulent flows", *Journal of Fluid Mech.*, **254**, 59-78 (1993).

S. **Jakirlic**, R. Jester-Zuerker and C. Tropea (Eds.), Proc. 9th ERCOFTAC/IAHR/COST Workshop on Refined Turbulence Modelling, Darmstadt, October 2001

Y.J. **Jang**, M.A. Leschziner, K. Abe and L. Temmerman, Investigation of anisotropy-resolving turbulence models by reference to highly-resolved LES data for separated flow, Flow, Turbulence and Combustion (in press), 2003

B.E. **Launder** and B.I. Sharma, "Application of the energy-dissipation model of turbulence to the calculation of flow near a spinning disc", *Letters in Heat and Mass Transfer*, **1**,131-138 (1974).

B.P. **Leonard**, "A stable and accurate convective modeling procedure based on quadratic upstream interpolation", *Comp. Meth. Appl. Mech. Eng.*, **19**, 59-98 (1979).

F.S. **Lien** and M.A. Leschziner, "A general non-orthogonal collocated finite volume algorithm for turbulent flow at all speeds incorporating second-moment turbulence-transport closure, Part I: Computational implementation", *Comp. Meth. Appl. Mech. Eng.*, **114**,123-148 (1994).

F.S. **Lien** and M.A. Leschziner, "Upstream monotonic interpolation for scalar transport with application to complex turbulent flows", *Int. J. Num. Meth. In Fluids*, **19**, 527-548 (1994).

C.G. **Speziale**, S. Sarkar and T.B. Gatski, " Modeling the pressure-strain correlation of turbulence: an invariant dynamical systems approach", *Journal of Fluid Mech.*, **227**, 245-272 (1991).

S. **Wallin** and A.V. Johansson, "An explicit algebraic Reynolds stress model for incompressible and compressible turbulent flows", *Journal of Fluid Mech.*, **403**, 89-132 (2000).

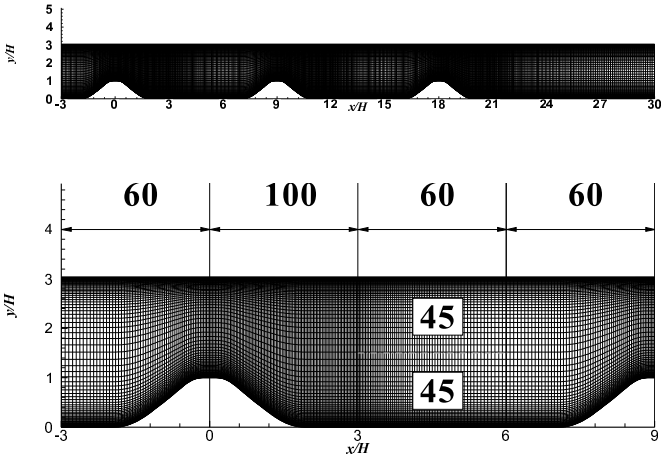

Fig. 1: Computational domain and grid

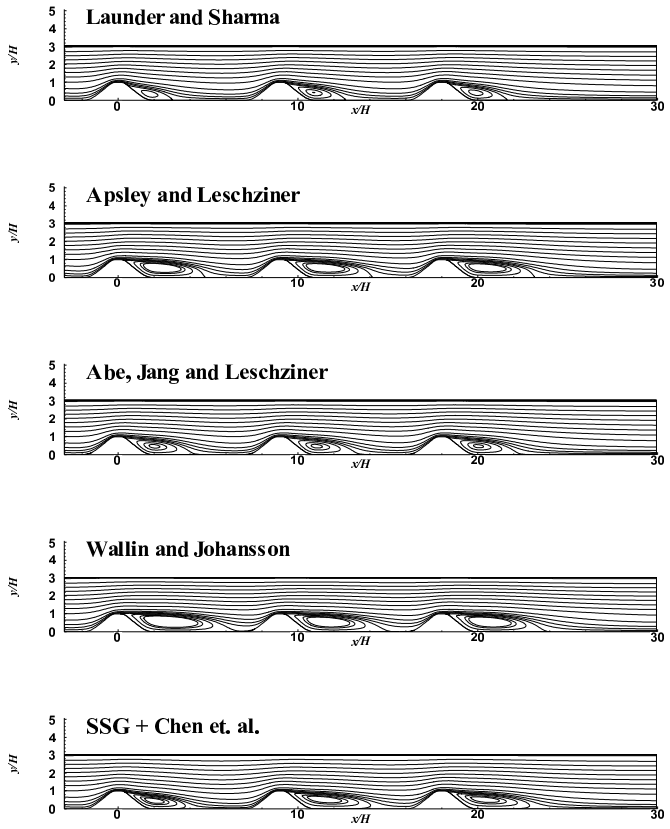

Fig. 2: streamfunction fields

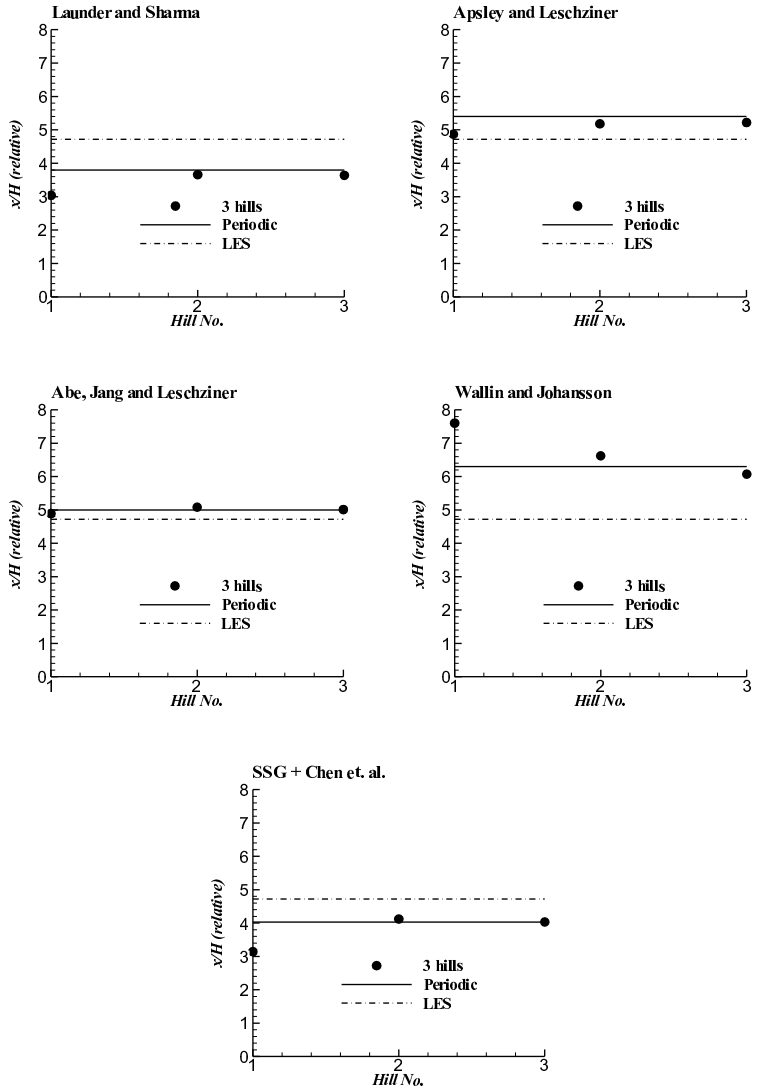

Fig.3: The degree to which the reattachment location is changing with hill number

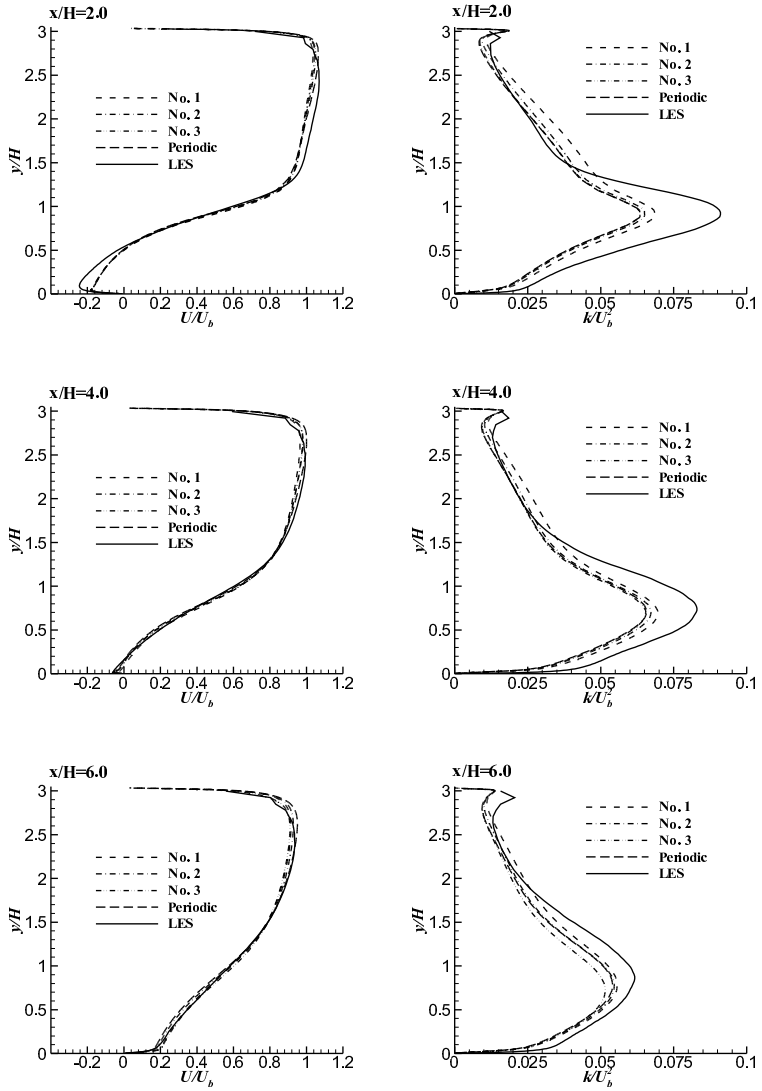

Fig. 4: Profiles of velocity and turbulence energy at x/h=2, 4 and 6 for Abe, Jang and Leschziner model

-

Case 9.4

Results and comments

-

Test Case 9.4: Flow around a simplified car body (Ahmed body)

Florian Menter, ANSYS-CFX, Germany

1. Test case Description

The Ahmed body is a generic car geometry with a slanted back. Different slant angles have been studied in the experiments in order to investigate the changes in the flow structure and the global forces due to this variation in the geometry. Figure 1 and |Figure 2 show the geometry of the Ahmed body and the main dimensions in millimeters, as well as the definition of the slant angle.

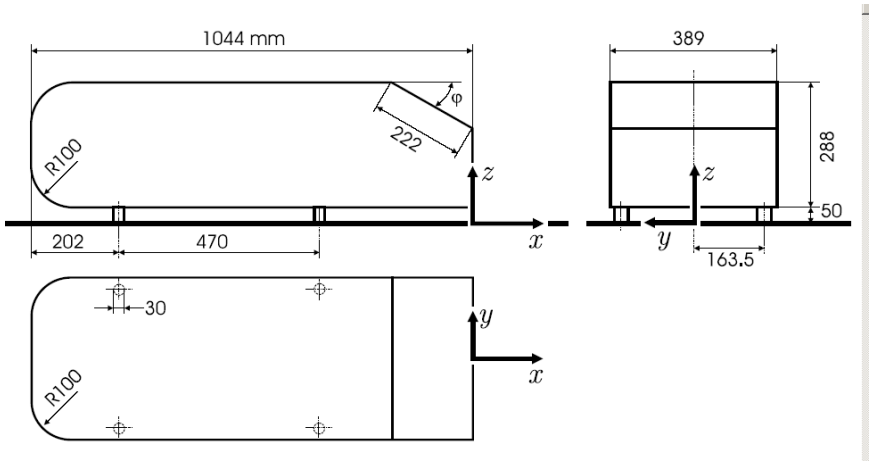

Figure 1: Ahmed car geometry (taken from Hinterberger et al. 2003)

Figure 2: Definition of slant angle

The first experimental studies on this shape were carried out by Ahmed (1984). The present comparison is based on the data of Lienhart et al. (2000) and Lienhart and Becker (2003) at the LSTM (low speed wind tunnel) of Erlangen.. The slant angle was varied between α=0° and 40°. The emphasis of the experimental investigations was on the flow structure in the slant region and downstream of the body.

The body was mounted on 4 stilts (diameter 30[mm]), so that it is located 50[mm] above of the ground. The cross-section of the tunnel was 1.87x1.4[m^2]. The studies were conducted in a ¾ open test section (i.e. floor but no sides or ceiling) with a blockage ratio of 4%. The velocity and air temperature were controlled by a computer-feedback system. The inlet velocity was 40[m/s], the kinematic viscosity of air is $15x10^{-6}$[m^2/s], which gives a length-based Reynolds number of $2.784x10^6$. It should be noted that in most simulations, the drag of the stilts is not included. As it is included in the overall drag of the experimental body, corrections have to be applied, see Durand et al. (2002).

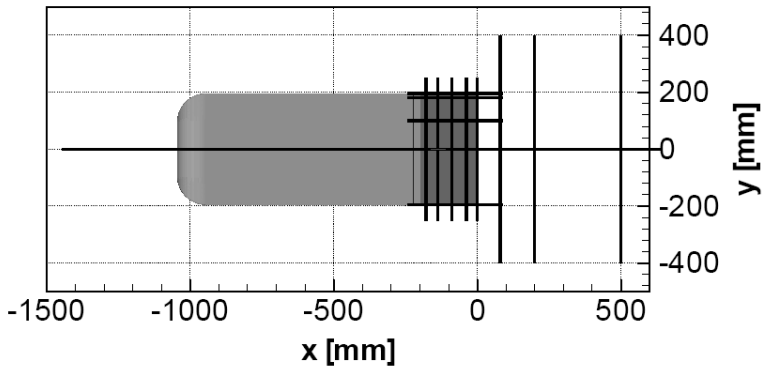

Figure 3: LDA measurement positions (taken from Lienhard et al. 2000)

Flow visualizations were made on the slant with oil/soot streaks. Velocity-profile measurements were performed by a 2-component hot wire system in the plane placed 400[mm] upstream of the Ahmed body.

For the other measurements, a 2-component laser-Doppler anemometer (LDA) was used and moved by a 3-dimensional computer controlled traversing system. Three components of velocity were obtained in the symmetry plane and for several planes in the wake. The LDA provided mean flow velocity components, as well as Reynolds stresses. Measurement positions are shown in Figure 3.

2 Flow Topology

An important aspect of this flow is that the geometric and therefore also the flow topology are identical for a slant angle of α=0° and α=90°, as shown in Figure 4.

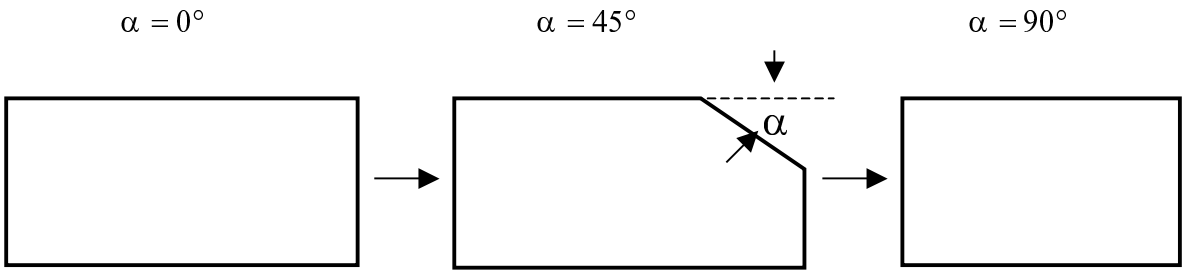

Figure 4: Change in geometric topology with slant angle

As the lift and drag depend essentially on the flow topology in the aft part of the body, this implies that both values have to be close to identical for α=0° and α=90°. Figure 5 shows the drag coefficients as a function of the slant angle (c_S-slant, c_B-base, c_K-front body, c_R-wall shear, c_W-combined).

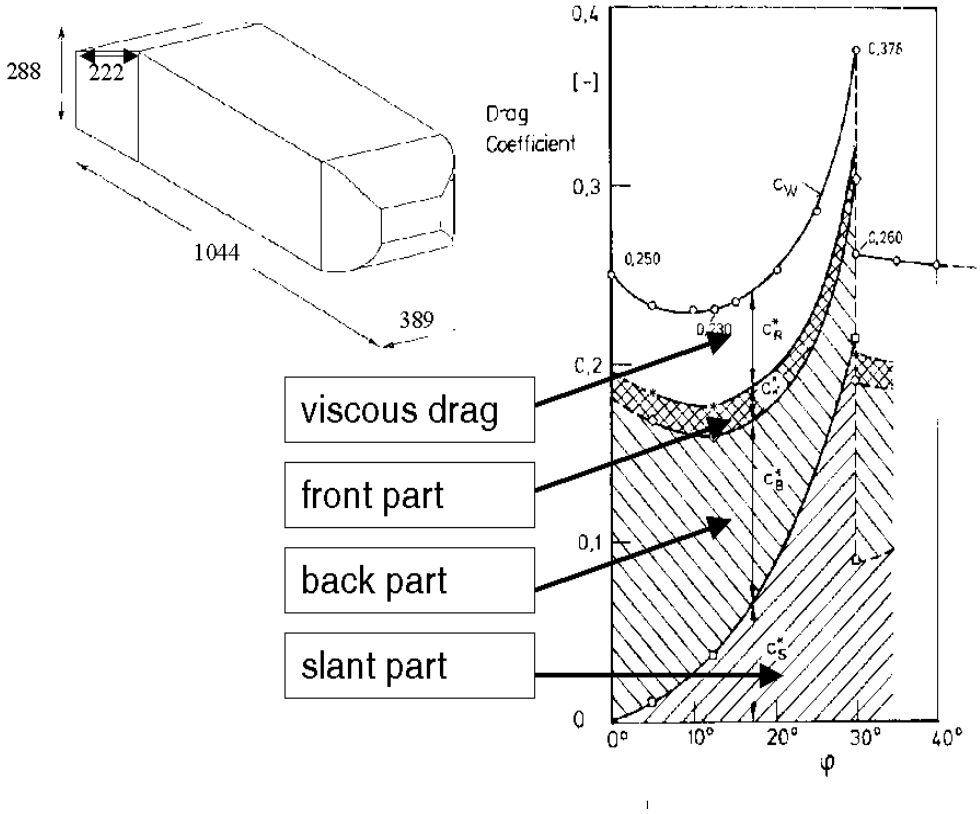

Figure 5: Drag for Ahmed car body as function of slant angle a. c_w=combined drag, c_R-friction drag c_B-base drag, c_s-slant drag, c_K-drag of front part.

Starting from α=0º, the flow in the rear is a fully separated base flow. For this configuration, the body has a very low lift coefficient, as there is little turning of the external flow. The drag is mainly base-drag (c_B) caused by the low pressure on the vertical rear part of the body. With increasing slant angle, the outer flow follows the slant of the body and experiences an ever-increasing lift due to the turning of the external flow – similar to a finite-span wing with a flap of increasing angle of attack, see Figure 6. As a result, a pair of side vortices (trailing vorteces) develops at both sides of the slant, as shown in Figure 7. The drag of the body increases due to the increasing strength of these vortices (induced drag). Below the critical slant angle α_c=30º, the flow essentially follows the turning of the slant, although a closed separation bubble develops in the central part of the slant, as shown in Figure 7. From the argument made around Figure 4, it is clear that the lift of the body must eventually decrease again with a further increase of α, as the flow at α=90º is topologically identical to that for α=0º. The change in flow topology takes place abruptly at the critical angle of α_c~30º, as can be inferred from the drag coefficients shown in Figure 5. At α_c the flow can no longer follow the turning of the slant and a massive separation over the entire slant is observed (similar to the stall over the flap of an airfoil). At this point, the lift breaks down and the strength of the side vortices decreases substantially. With further increase in slant angle the flow returns back to the original base flow.

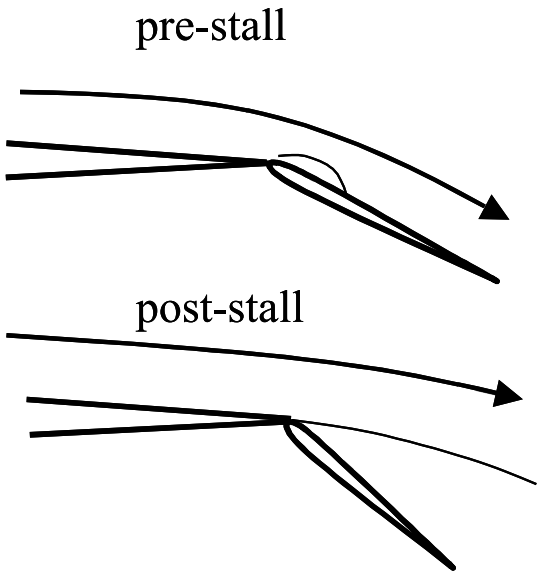

Figure 6: Flow topology for airfoil with flap for different flap angles

For the workshop, two slant angles of α=25° and α=25° have been computed. The lower angle is below and the higher angle above the critical value α_c, meaning that two different flow topologies had to be predicted.

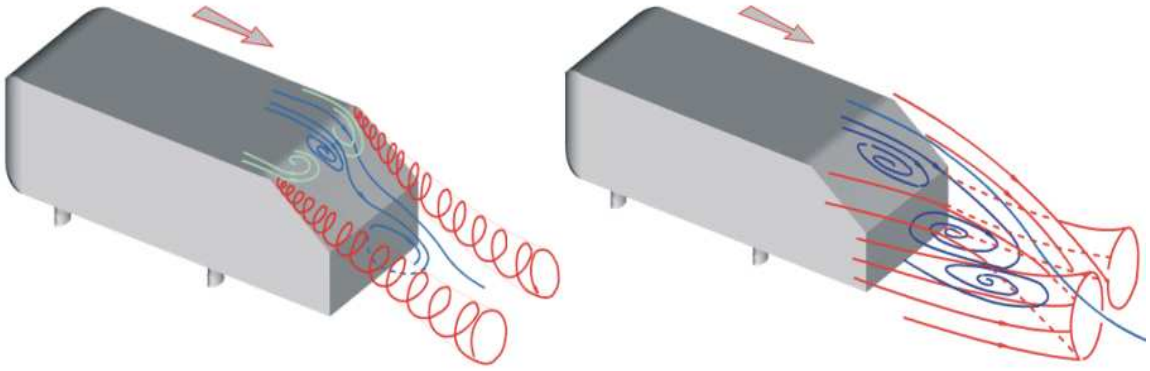

Figure 7: Flow topology for α=25° (left) and α=35° (right). Courtesy Lienhart, LSTM Erlangen

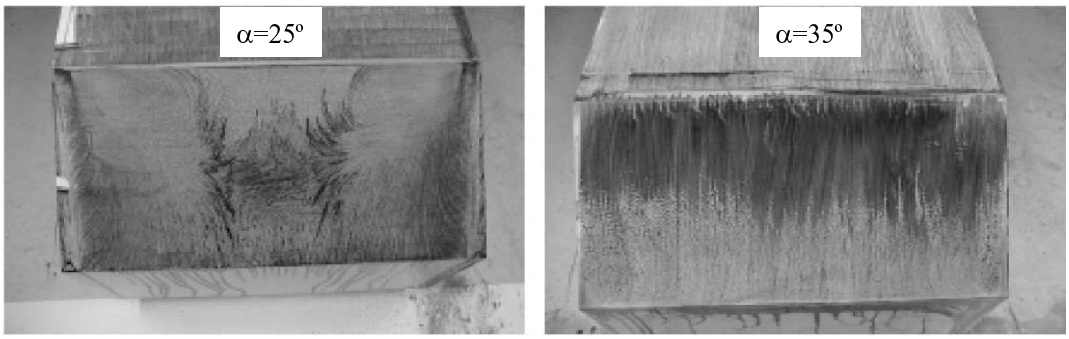

Figure 8: Surface streamlines on slant for two different slant angles. Left – pre-stall toplogy with closed separation bubble. Right – post-stall topology with fully separated flow (taken from Lienhard et al. (2000)).

For α=25°, the flow is essentially following the slant contour, resulting in high lift and strong side vortices (pre-stall). In the middle of the slant, a closed separation bubble appears, which requires that flow separation and subsequent reattachment must be predicted by the turbulence models in the central part of the slant. This flow topology will then automatically result in a

correspondingly strong lift and strong side vortex prediction. For $\alpha=35^o$, the flow is fully separated over the entire slant (post-stall). The challenge to the turbulence model is essentially to predict the separation at the onset of the slant. The separation in turn determines again the rest of the flow topology. The flow topologies for the two different slant angles are shown in Figure 7and Figure 8.

One of the confusing issues concerning this test case is that the combined experimental drag for $\alpha=25^o$ ($c_W=0.285$) and $\alpha=35^o$ ($c_W=0.260$) is not very different, although the flow undergoes a dramatic change in topology. When only comparing total drag with the experimental data, one can easily arrive at the wrong conclusion, as the drag might be predicted well, although the flow topology is missed. Sometimes the flow for $\alpha<\alpha_c$ the flow is called "high-drag" and for $\alpha>\alpha_c$ the flow "low-drag". This is confusing, as the drag for both cases can be very similar. In the following, the two flow topologies will be called pre-stall and post-stall topology.

3. Steady versus Unsteady for the $\alpha=25^o$ case

3.1 *Small-scale instability*

An open question concerns an eventual unsteady behavior of the flow in the slant region for the $\alpha=25^o$ case. A LES solution (Krajnovic and Davidson, 2004) indicates that local Kelvin-Helmholtz vortices develop in the separating shear layer emanating from the slant. Figure 9 shows flow structures over the slant, as computed by an LES (albeit at a lower Reynolds number).

These vortices appear to lead to a significant increase in the turbulent stresses, an effect, which is not captured by RANS models, as shown in Figure 10, which shows a comparison of the turbulent kinetic energy from the experiment with that computed from the SST model. (A similar discrepancy was observed for all RANS models, which predicted a separation near the slant onset). It is not surprising that RANS models do not predict the extremely large peak

value of the turbulent kinetic energy in this separating shear layer, as it is much higher than for a self-similar mixing layer (Table 1) for which the model have been calibrated:

	Self-similar mixing layer	Slant mixing layer
$k_{\max}/U_{\infty}^2$	~0.035	~0.2

Table 1: Ratio of $k_{\max}/U_{\infty}^2$ for self-simlar mixing layer and slant-mixing layer for α=25º

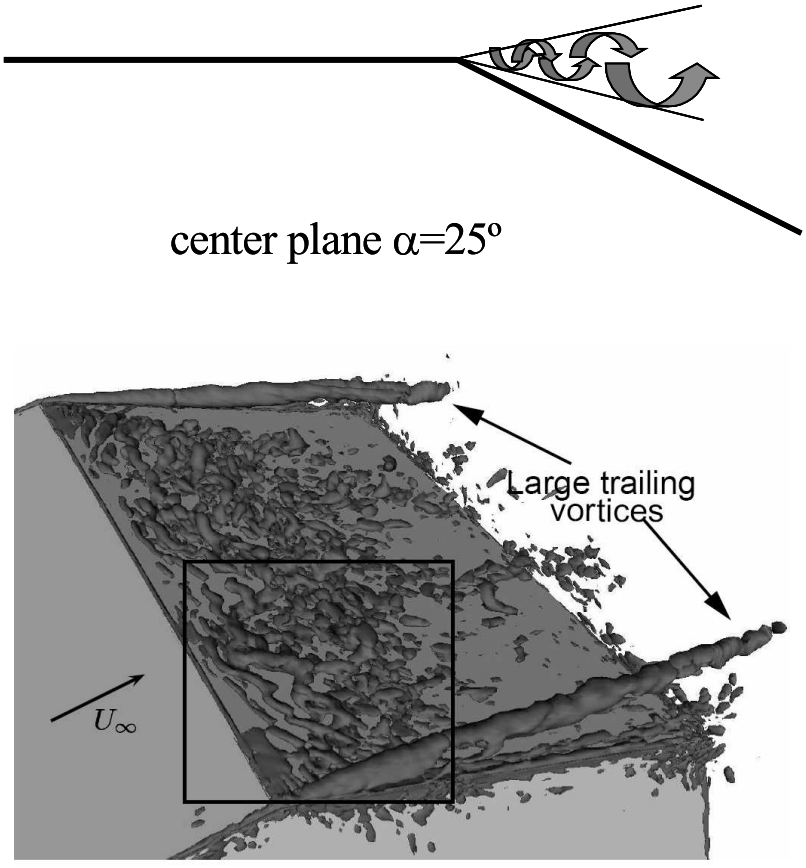

Figure 9: Kelvin-Helmholtz-type vortices in slant region for α=25º case (taken from Krajnovic and Davidson, 2004)

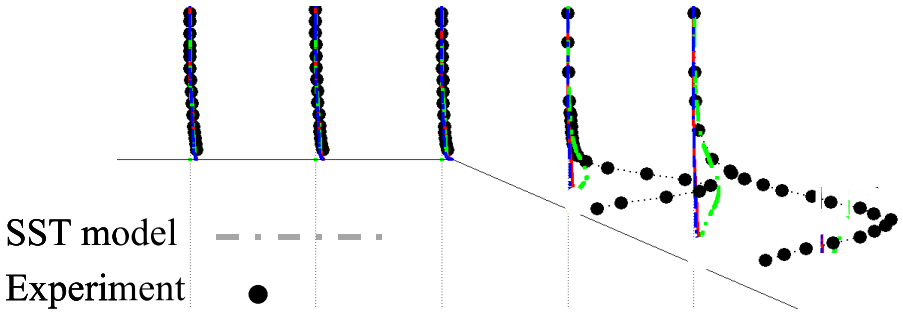

Figure 10: Turbulent kinetic energy in centre-plane of the slant-onset for the α=25º case

One of the possible explanations would be that the occurrence of the Kelvin-Helmholtz-type instability shown in Figure 9, leads to a significantly increased ratio of $k_{\max}/U_{\infty}^2$. It is however difficult to explain, why this instability, which is also present in the self-similar mixing layer (Lin et al., 2004), should have such a strong effect on the stresses. One possible difference could be the substantial adverse pressure gradient observed in the experiment in the region past the slant corner, which is not present in the self-similar mixing layer. The fact that the LES predicts the correct flow topology for the α=25º case would support that the structures shown in Figure 9 are the cause of the high value of the turbulent stresses. Unfortunately, no stress profiles are given in Krajnovic and Davidson, 2004. One should however keep in mind that the LES was carried out at a lower Re number than the experiment.

The LES of Hinterberger et al. (2004) does predict a peak a in the turbulent kinetic energy in this region which is about ~2/3 of the experimental data. This is much better than the RANS models, but still not sufficient to predict the flow reattachment on the slant. This is most likely a result of the grid resolution, as the experimental Reynolds number was simulated.

3.2 *Large-scale instability*

There is some indication that the flow might experience a more global instability at α=25º, as a result of the interaction of the separation bubble with the side vortices. Such a behavior was

observed in the DES simulation of Menter and Kuntz (2004). Figure 11 shows the side vortex computed from that simulation at a given instance in time. A flow visualization shows that at that instance, the separation bubble has moved towards the left and interferes with the left side vortex., leading to a temporary break-down of the vortex strength. At the same time, the right vortex is not affected and shows the tight structure typical of the high-lift flow topology. As time progresses, the bubble moves towards the right leading to the same effect on the right side of the slant.

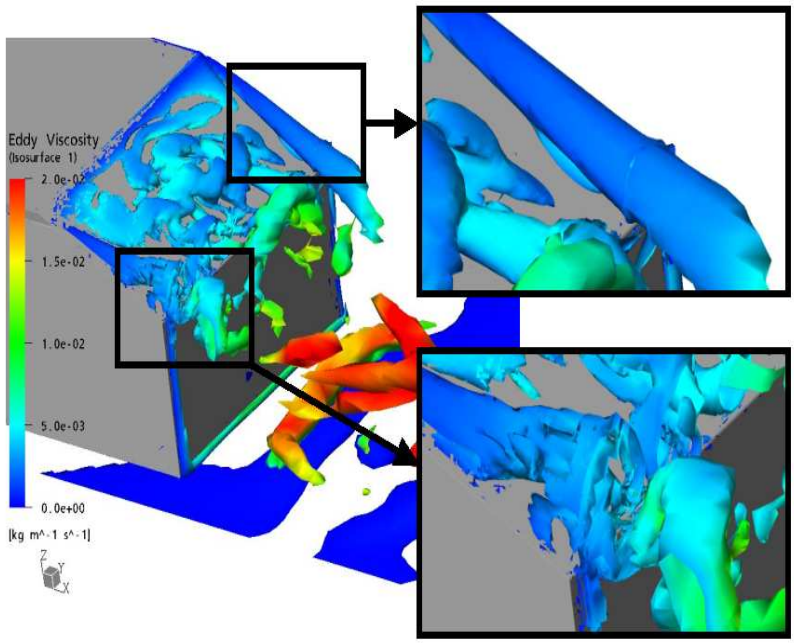

Figure 11: Global flow instability due to interactioin of separation bubble and side vortices (taken from Menter and Kuntz, 2004).

Such an instability would lead to a large scale unsteadiness near the slant onset, from attached to separated flow at different instances in time. The associated flipping of the velocity, when included in the time averaged turbulent kinetic energy, would results in a ratio of $k_{\max}/U_{\infty}^2 \sim 0.25$ close to the experimental value (Spalart – personal communication).

It was observed in the experiments at $\alpha=30^{o}$ that a change in flow topology could be achieved with a splitter plate mounted in the symmetry plane of the wake. Without the splitter plate the pre-stall behavior of $\alpha<\alpha_c$ was observed whereas with the splitter plate the post-stall condition

(low-lift) typical for $\alpha>\alpha_c$ was obtained. As the splitter plate mainly suppresses lateral ("spanwise") instabilities, this is also an indication that such an instability is instrumental in maintaining the pre-stall flow topology near but below $\alpha=\alpha_c$.

2. The Contributors and their Approaches

Six groups provided simulations for the 2002 ERCOFTAC workshop. The groups and the turbulence models used are listed in Table 2. The models ranged from standard k-ε model with wall functions over k-ω based models to EARSM and full RSM, as well as one LES. Different types of wall treatments have been applied. It was however found that the main difference between the results was not sensitive to the near wall treatment, but to the ability of the turbulence models to predict separation onset and reattachment.

Models adopted fall into the following groups::

- Variants of the linear eddy-viscosity (LEVM) *k*-ε model (Launder and Spalding, 1974):
  - standard wall functions
  - scalable wall functions (Esch et al. 2003)
  - UMIST A and N wall functions (Chieng and Launder, 1980, Craft et al. 2002)
  - low-Re form of Launder and Sharma (1974) and Yang Shih (1993)
  - Realizability (May, 1998)
- Variants of the linear EVM *k*-ω form, the major ones being the basic form of Wilcox (1988) and of Menter (1994).
- The V2F model Durbin (1991).
- Non-linear eddy-viscosity (NLEVM) and explicit algebraic Reynolds-stress (EARSM) models, including the models by Craft et al. (1996), Rumsey and Gatski, (2001), Apsley and Leschziner (1998), Abe et al. (2003)
- Reynolds-stress-transport models (RSM) of Speziale Sarkar and Gatski (1991).
- LES Hinterberger et al. (2004)

Authors	Institution	Identifier	25°	35°
Becker, Lienhart, Stoots	University of Erlangen	Experiments	×	×
Hinterberger, Garcia-Villaba, Rodi	University of Karlsruhe	Karlsruhe U./LES	×	
Leonard *et al.*	NUMECA Int.	NUMECA/Low *Re* k–ε Yang–Shih	×	
Hadžiabdić, Hanjalić, Khier, Liu, Oulhous	TU Delft	TU Delft/k–ε + WF		×
Hadžiabdić, Hanjalić, Khier, Liu, Oulhous	TU Delft	TU Delft/$\overline{v^2}$–f + WF		×
Hadžiabdić, Hanjalić, Khier, Liu, Oulhous	TU Delft	TU Delft/SSG + WF		×
Craft, Gant, Iacovides, Launder, Robinson	UMIST	UMIST/k–ε–Linear + SCL WF	×	×
Craft, Gant, Iacovides, Launder, Robinson	UMIST	UMIST/k–ε–Linear + UMIST–N WF	×	
Craft, Gant, Iacovides, Launder, Robinson	UMIST	UMIST/k–ε–Realiz. Linear + SCL WF	×	×
Craft, Gant, Iacovides, Launder, Robinson	UMIST	UMIST/k–ε–Realiz. Linear + UMIST–A WF	×	×
Craft, Gant, Iacovides, Launder, Robinson	UMIST	UMIST/k–ε–Nonlinear + SCL WF	×	×
Craft, Gant, Iacovides, Launder, Robinson	UMIST	UMIST/k–ε–Nonlinear + UMIST–A WF	×	×
Kuntz, Menter, Durand	CFX Germany	CFX/k–ε	×	×
Kuntz, Menter, Durand	CFX Germany	CFX/SST	×	×
Rumsey	NASA LaRC	NASA/EASM-k–ω	×	×
Rumsey	NASA LaRC	NASA/SST	×	×
Jang, Leschziner	Imperial College	IC/Low–*Re* Quad. k–ε Abe-Jang-Leschziner	×	
Jang, Leschziner	Imperial College	IC/Low–*Re* Quad. k–ω Abe-Jang-Leschziner	×	
Jang, Leschziner	Imperial College	IC/Low–*Re* Cubic k–ε Apsley-Leschziner	×	
Jang, Leschziner	Imperial College	IC/Low–*Re* Lin. k–ε Launder-Sharma	×	
Jang, Leschziner	Imperial College	IC/Low–*Re* RSM SSG-Chen	×	
Jang, Leschziner	Imperial College	IC/k–ω Wilcox	×	

Table 2: List of contributions to workshop

3. Contributed Results

3.1 General comments

Although numerous numerical methods, turbulence models and numerical grids have been used, it was possible to draw relatively consistent conclusions for the two testcases. The case α=25° proved difficult and none of the RANS models produced satisfactory results, albeit different models failed for different reasons. The LES showed improved results, but was still not in close agreement with the experiments. The α=35° case on the other hand could be handled by all models with surprising accuracy.

3.2 Grid-dependence tests

The LES simulation of the University of Karlsruhe has been carried out on 18,500,000 nodes. Due to the high costs of LES, no grid refinement study was performed for the workshop.

Most RANS contributors have carried out a grid sensitivity study. The grid resolution for the RANS simulations ranged from 330,00 to 2,500,000 nodes.

Contributor	Coarse	Medium	Fine
Karlsruhe			18.5×10^6
NUMECA (local ref.)	0.47×10^6	0.76×10^6	0.81×10^6
TU Delft	0.49×10^6		0.82×10^6
UMIST		0.34×10^6	
CFX	0.66×10^6	1.25×10^6	2.5×10^6
NASA		1.25×10^6	
Imperial College		1.8×10^6	

Table 3: Grids used by the different groups

It was found that the grid resolution was not the main factor for the model behaviour, although subtle differences between the coarsest and finest grids were observed. Additional sensitivity studies concerning the extent of the domain and the boundary conditions have been reported by Durand et al. (2002).

3.3 Discussion of Results

3.3.1 *The Case α=25°*(pre-stall)*

The RANS models can be grouped into two classes. The first group predicted the correct pre-stall flow topology with strong side-vortices and high lift. The models which fall into that category are:

Pre-stall topology:

- All k-ε models:
    - CFX (Launder Spalding)
    - NUMECA (Yang-Shih)
    - UMIST (linear + realizable)
    - Imperial College (Launder-Sharma)
    - LES

The second group of models predicted the incorrect post-stall flow topology:

- k-ω (IC)
- SST (CFX, NASA)
- EARSM:
    - NASA
    - Imperial College (quadratic and qubic)
    - UMIST
- RSM (IC) – convergence?

The decision on the flow-topology predicted by the models was based on the strength of the side vortices (see pressure plots in the Appendix). Strong side vortices (strong pressure minimum) were associated with the pre-stall topology and weak side vortices (weak pressure minimum) with the post-stall topology.

A number of models and most notably the least optimized k-ε model predicted the correct pre-stall flow topology. However all RANS model in that category did so for the wrong reasons, namely because they missed the flow separation at the onset of the slant and did therefore not predict a separation bubble on the slant. Missing the separation means that the difficult flow reattachment did not have to be captured.

The models which failed to predict the correct flow topology, where those which have been optimised to properly predict the onset of flow separation for other test cases. However, all these models failed to predict the reattachment of the flow on the slant. For this reason, the predicted flow topology was fully stalled flow (post-stall).

Figure 12 shows two low-Re solutions to illustrate the situation. On the left, the NUMECA Low-Re Yang-Shih model for a pre-stall example and on the right, the NASA EASM model for a post-stall topology (low-Re models were selected to avoid issues of wall functions). The k-ε model clearly misses the bubble separation and predicts a fully attached flow, whereas the EASM predicts a fully stalled flow over the slant.
The turbulent shear stresses (u'w') are shown in Figure 13 illustrating the problem observed with both models. Both models miss the peak in the shear stress near the slant edge. However,

the k-ε model misses it because it predicts an attached flow, which would never exhibit such high stress levels, whereas the EASM misses the stress level despite the correctly predicted flow separation there.

One could argue that there are two modelling problems. The first is that some models miss the separation. The other models, which have overcome this deficiency run into the second problem and miss the reattachment. It would therefore be an incorrect (in the present authors opinion) to conclude that the pre-stall type models are superior, because from a modelling standpoint, one would have to overcome two deficiencies, to optimize them.

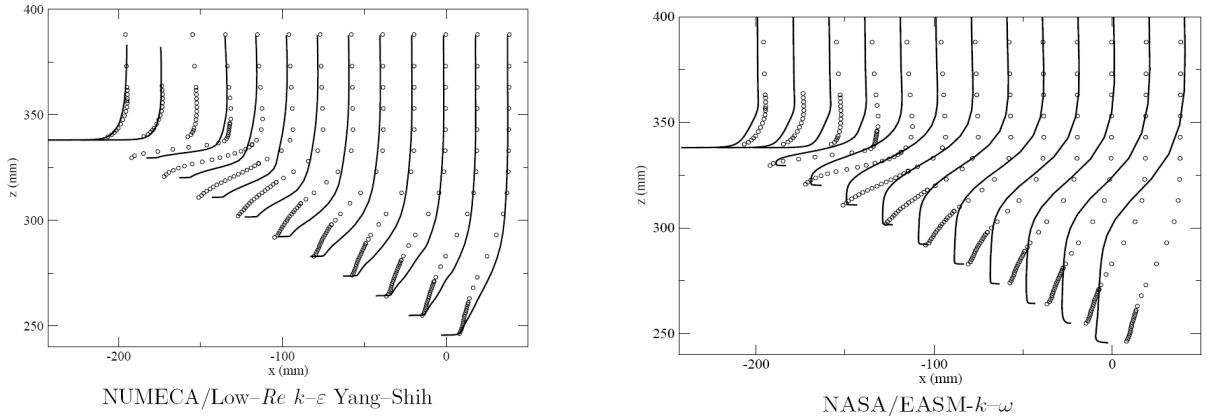

Figure 12: U-velocity in symmetry plane for α=25º case. Left: pre-stall topology. Right: post-stall topology.

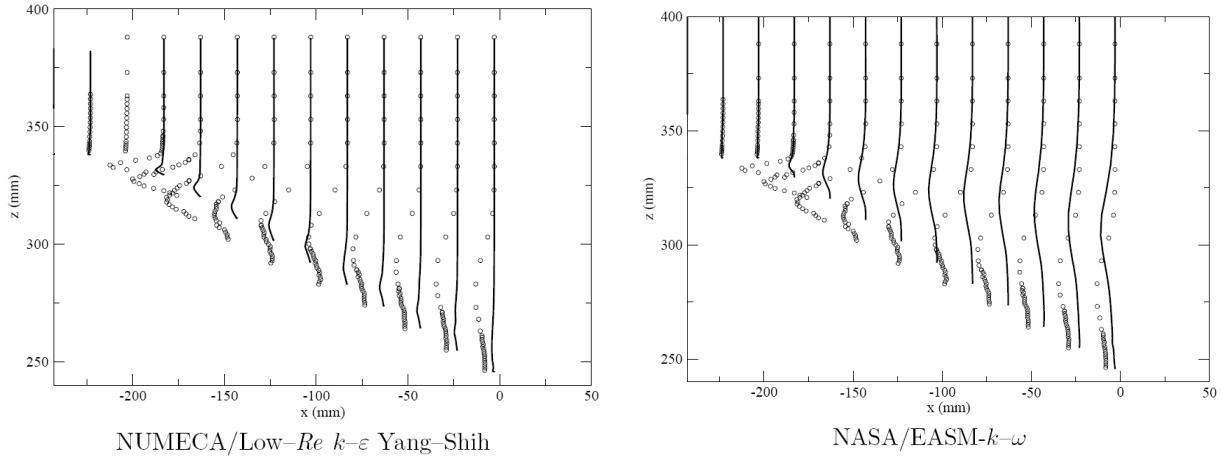

Figure 13: Principal Reynolds stress u'w' in symmetry plane for α=25º case. Left: pre-stall topology. Right: post-stall topology.

The LES simulation is also not perfect for this flow as shown in Figure 14. The LES fails to predict the closed separation bubble observed in the experiment. Nevertheless, the LES gives the correct pre-stall flow topology (as seen from the tip vortex pictures in the Appendix).

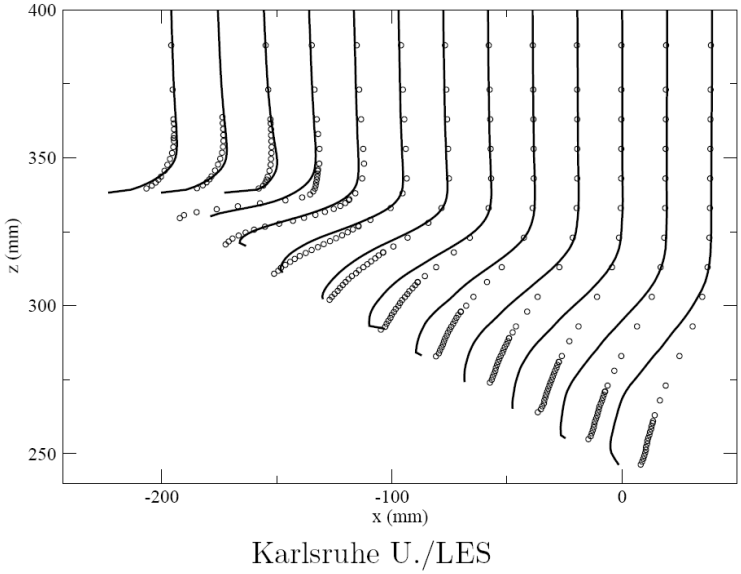

Figure 14: U velocity in symmetry plane for α=25º case for LES.

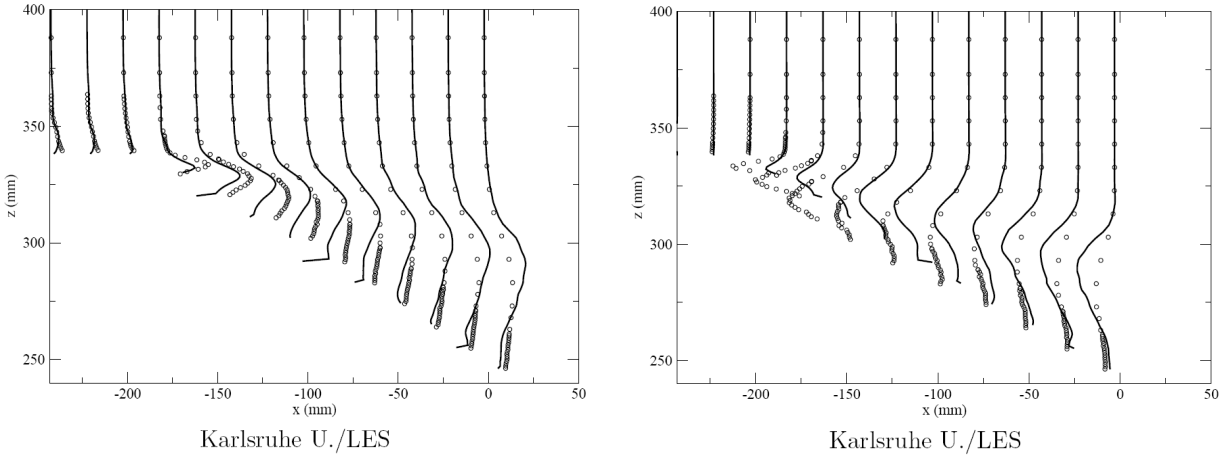

Figure 15: LES Reynolds stresses in symmetry plane for α=25º. Left: u'u' stresses. Right u'w' stresses

Figure 16 shows the Reynolds stresses u'u' and u'w' in the symmetry plane for the LES. Albeit significantly higher than those produced by the RANS models, they are still not in good agreement with the experiments. The under-prediction and the incorrect location of the peak

value of the principal shear stress u'w' seems to be the reason for the failure of the LES simulation to capture flow reattachment on the slant.

3.3.2 *The Case α=35°*(post-stall)*

This case is fully separated in the experiments and all RANS models were able to predict the correct flow topology.

Figure 17 shows the same two models (the low-Re model of NUMECA was not available for this case) compared for the previous case.

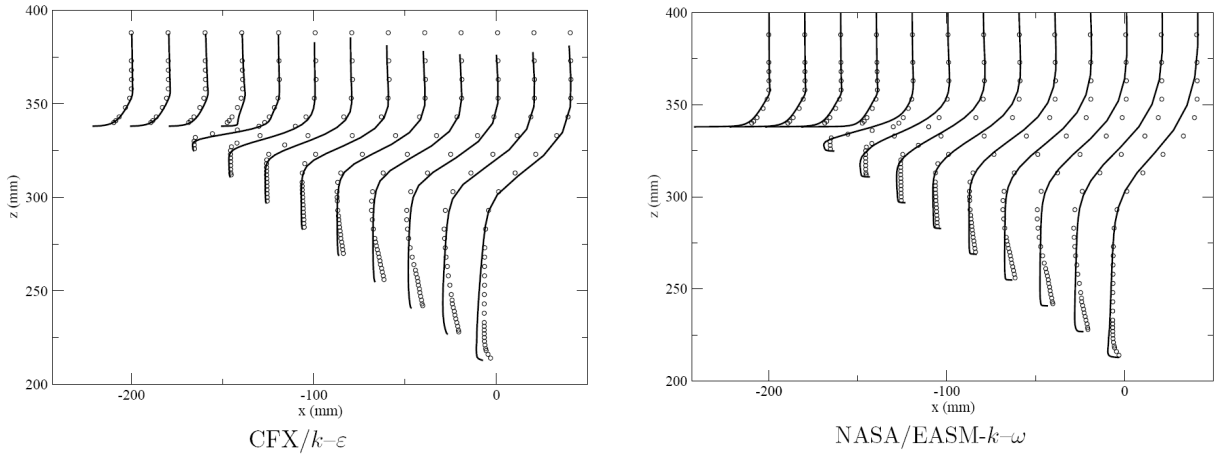

Figure 17: U-velocity in symmetry plane for α=35º case. Left: k-ε. Right EASM.

Clearly both models predict the velocity field very well. They also produce the correct flow topology.

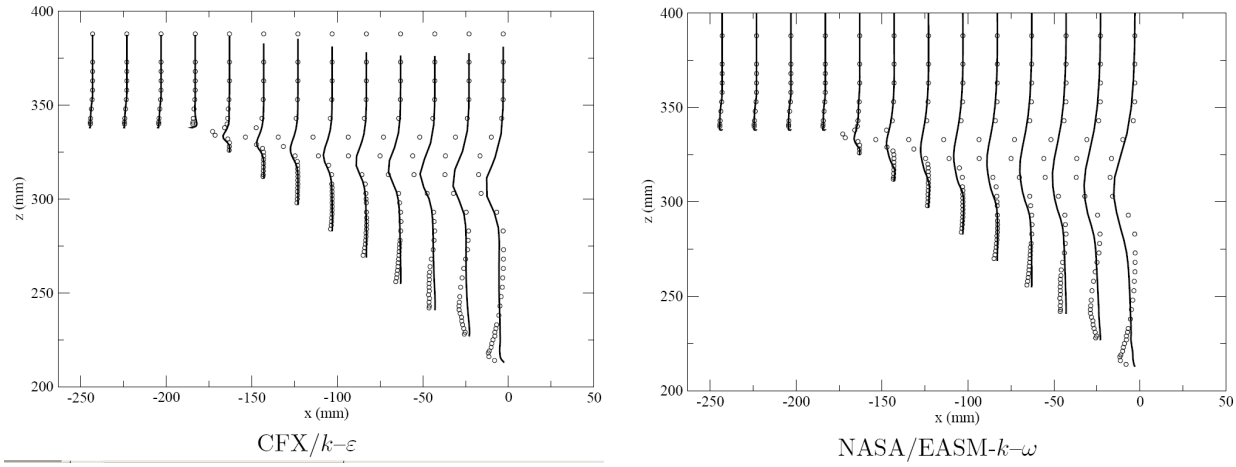

Figure 18: u'w' Reynolds stresse in symmetry plane for α=35º case. Left: k-ε. Right EASM.

Figure 18 shows two interesting aspects of the α=35º case. Firstly, the experimental Reynolds stresses are significantly reduced from the α=25º case. And secondly, both models still under-

predict the stress level by a factor of more than two. In this case the under-prediction of the stresses is however of little consequence, as the flow does not reattach.

References

Abe, K., Jang, Y.-J. and Leschziner, M.A.(2003), " An investigation of wall-anisotropy expressions and length-scale equations for non-linear eddy-viscosity models", *Int. J Heat and Fluid Flow* 24, 181-198

Ahmed S.R. & Ramm G.: (1984), "Some salient features of the time-averaged ground vehicle wake*"* SAE technical paper 840300; 1984.

Apsley, D.D. and Leschziner, M.A.(1998), "A new low-Reynolds-number nonlinear two-equation turbulence model for complex flows", Int. J. Heat and Fluid Flow 19, 209-222

Chieng, C. C. and Launder B.E., 1980, "On the calculation of turbulent heat transfer downstream from an abrupt pipe expansion", Numerical Heat Transfer, 3:189-207, 1980.

Craft, T. J. Gerasimov, A.V., Iacovides, H. and Launder, B.E., (2002), "Progress in the generalization of wall-function treatments", Int. J. Heat an Fluid Flow, 23:148-160.

Craft T.J., Launder, B.E. and Suga, K. (1996), Development and application of a cubic eddy-viscosity model of turbulence", Int. J. Heat and Fluid Flow, 17:108-115.

Durand, L, M. Kuntz and Menter F.R. (2002), ''Validation of CFX for the Ahmed Car Body'', CFX Validation report

Durbin, P.A. (1991), "Near-wall turbulenceclosure model without damping functions", Theoretical and Numerical Fluid Dynamics, 3,1.

Esch, T., Menter, F.R. and Vieser, W., (2003), "Heat transfer predictions based om two-equations turbulence models", 6th ASME-JSME Thermal Engineering Joint Conference, Paper TED-AJ03-542.

Gilliéron P. & Chometon F.: (1999) "Modeling of stationary three-dimensional separated air flows around an Ahmed reference model*"* ESAIM Symp.

C. Hinterberger, M. García-Villalba, W. Rodi, (2004), "Large Eddy Simulation of flow around the Ahmed body". In "Lecture Notes in Applied and Computational Mechanics / The Aerodynamics of Heavy Vehicles: Trucks, Buses, and Trains", R. McCallen, F. Browand, J. Ross (Eds.), Springer Verlag, ISBN 3-540-22088-7.

Krajonovic, S. and Davidson, L., (2004), "Large eddy simulation of the flow around a simplified car model", 2004 SAE World Congress, SAE paper No. 2004-01-0227, Detroit/USA.

Launder, B.E. and Sharma, B.I. (1974), "Application of the energy-dissipation model of turbulence to the calculation of flow near a spinning disc", Letters in Heat and Mass Transfer 1, 131-138.

Li, N., Balaras, E. and Wallace, J.M., (2004), "An experimental and numerical investigation of the scalar and momentum transport in mixing layers", Advances in Turbulence X, Proceeedings of the tenth European Conference, Eds. Anderson H.I, and Krogstad, P.-A., Barcelona.

Lienhart H., Stoots C., Becker S. (2000), "Flow and turbulence structures in the wake of a simplified car model (Ahmed model)" DGLR Fach Symp . der AG Stab, Stutgart University; Nov. 2000.

Lienhard h. and Becker, S., (2003), "Flow and turbulence structure in the wake of a simplified car model., SAE Paper 2003-01-0656.

May, N.E. (1998), "Efficient implementation of two-equation and differential stress turbulence models into a cell-vertex, explicit, time-marching, Navier-Stokes flow code", Technical report M345, Aircraft Research Assoc.

Menter F.R.: "Two-equation eddy-viscosity turbulence models for engineering applications", AIAA Journal, vol.32 No.8 pp.1598-1605; 1994a.

Menter, F.M, and Kuntz, M., (2004), Adaptation of eddy-viscosity turbulence models to unsteady sperated flow behind vehicles", In "Lecture Notes in Applied and Computational Mechanics / The Aerodynamics of Heavy Vehicles: Trucks, Buses, and Trains", R. McCallen, F. Browand, J. Ross (Eds.), Springer Verlag, ISBN 3-540-22088-7.

Rumsey, C.L. and Gatski, T.B., (2001), "Recent turbulence models advances applied to multielement airfoil computations", J. Aircraft, Vol. 38, No. 5.

Speziale C.G. & Sarkar S. & Gatski T.B.(1991) "Modeling the pressure-strain correlation of turbulence", Journal of fluid mechanics, vol.227, pp245-272; 1991.

Wilcox D.C.: "*Turbulence modeling for CFD*", DCW industries, Inc; 1998

Yang, Z. and Shih, T.H., (1993), "Galilean and tensorial invariant k-ε model for near wall turbulence", AIAA Paper 93-3105.

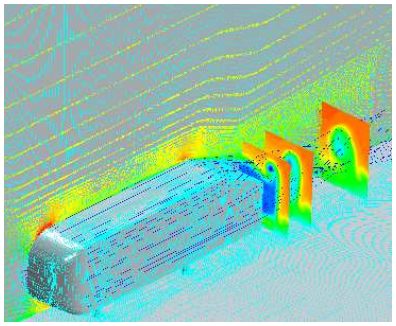

Plane: $x = -38$

Velocity vectors
Colorscale: norm

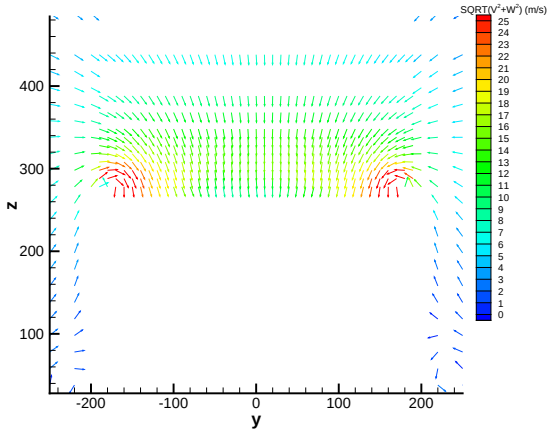

Experiments

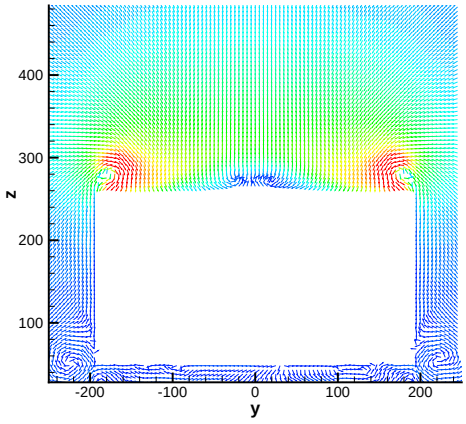

Karlsruhe U./LES

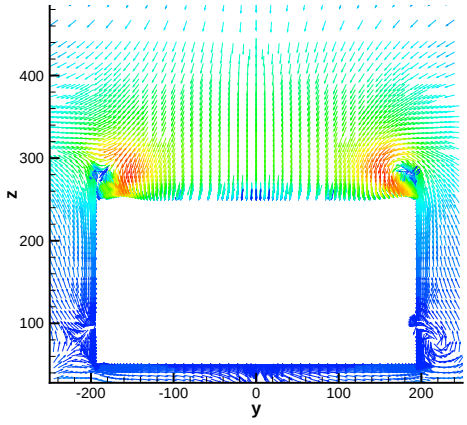

NUMECA/Low–*Re* k–ε Yang–Shih

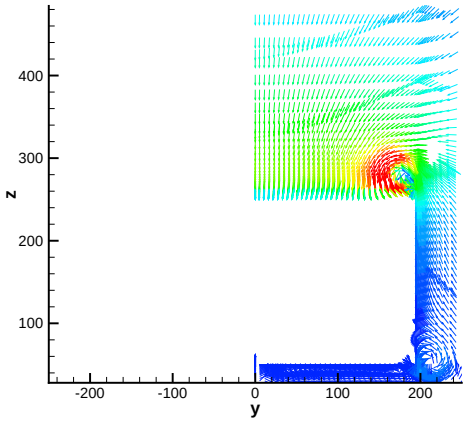

CFX/k–ε

Sample of plots available on the CD-Rom

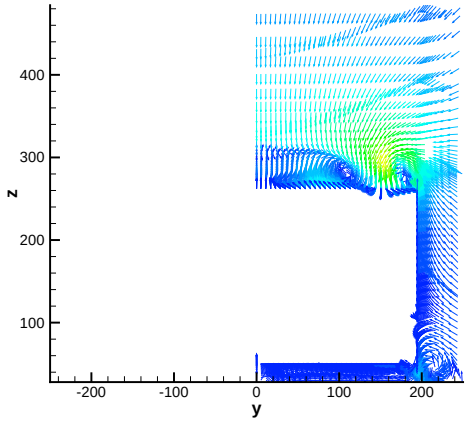

CFX/SST

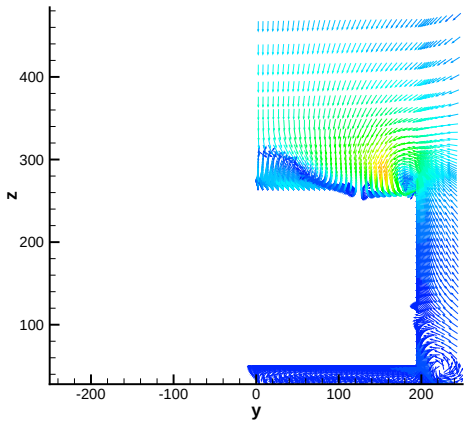

NASA/SST

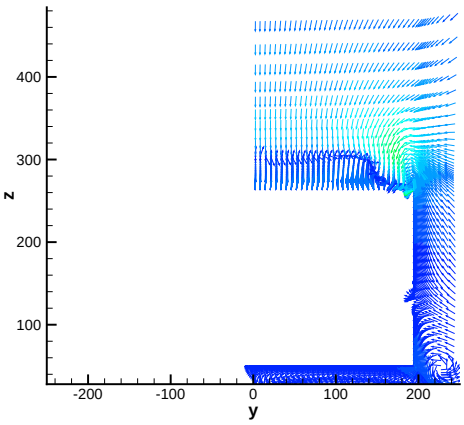

NASA/EASM-k–ω

Sample of plots available on the CD-Rom

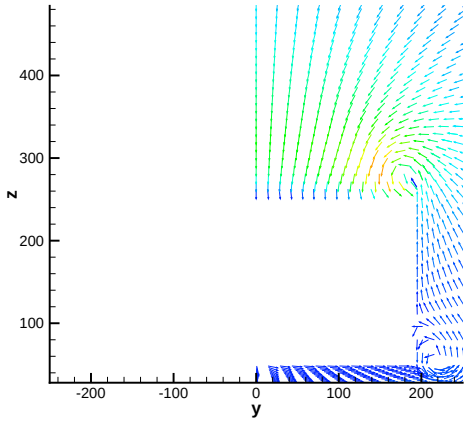

UMIST/k–ε–Linear + SCL WF

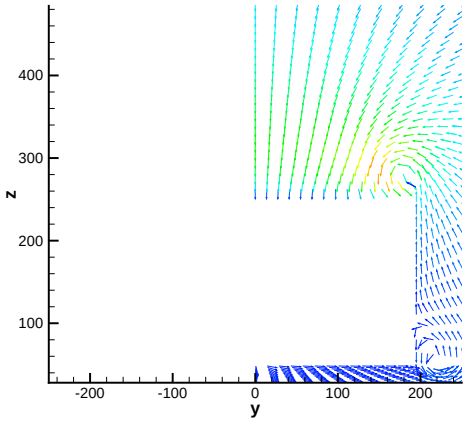

UMIST/k–ε–Linear + UMIST–N WF

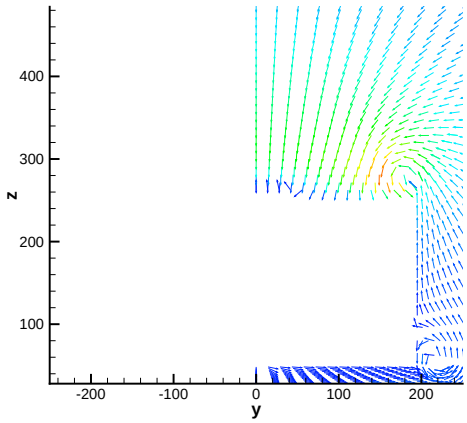

UMIST/k–ε–Realiz. Linear + SCL WF

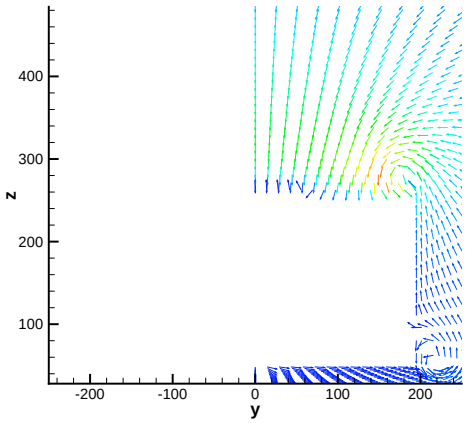

UMIST/k–ε–Realiz. Linear + UMIST–A WF

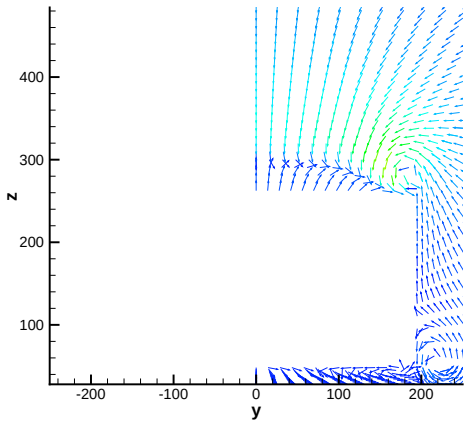

UMIST/k–ε–Nonlinear + SCL WF

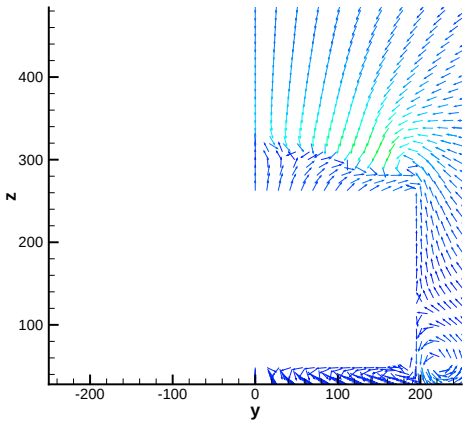

UMIST/k–ε–Nonlinear + UMIST–A WF

Sample of plots available on the CD-Rom

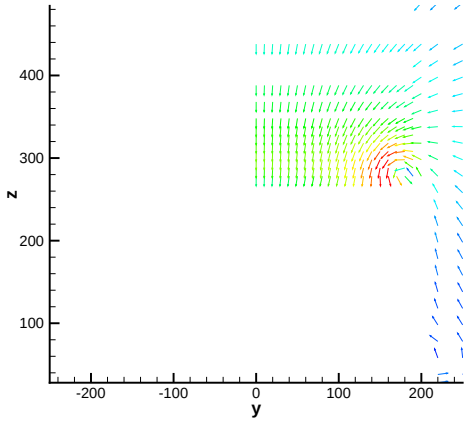

IC/Low–Re Lin. k–ε Launder-Sharma

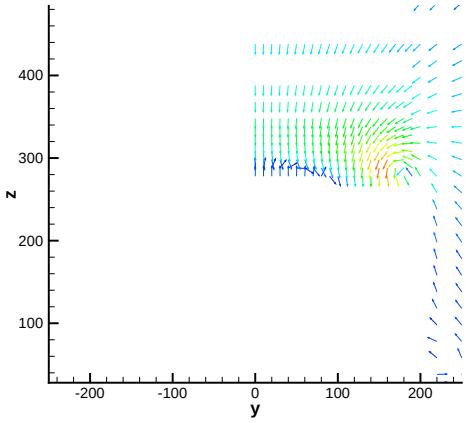

IC/k–ω Wilcox

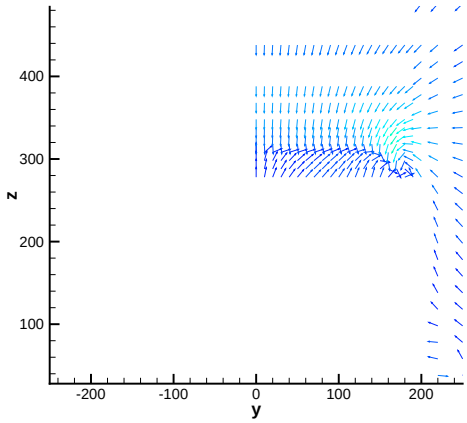

IC/Low–Re Quad. k–ε Abe-Jang-Leschziner

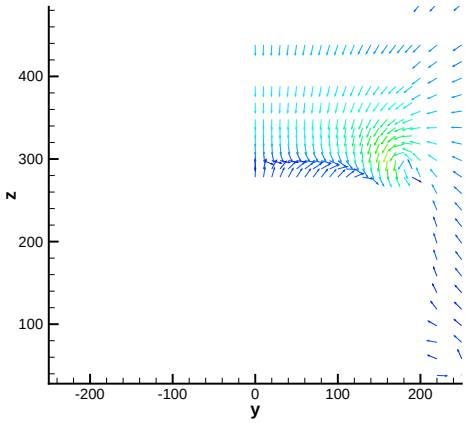

IC/Low–Re Quad. k–ω Abe-Jang-Leschziner

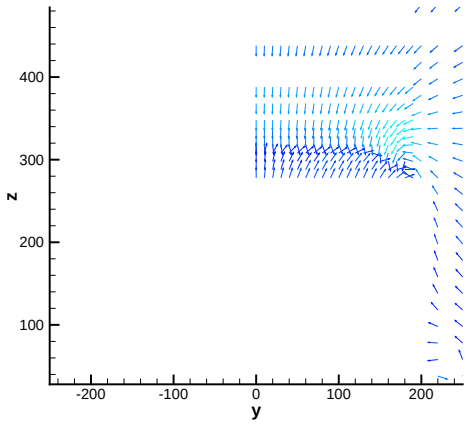

IC/Low–Re Cubic k–ε Apsley-Leschziner

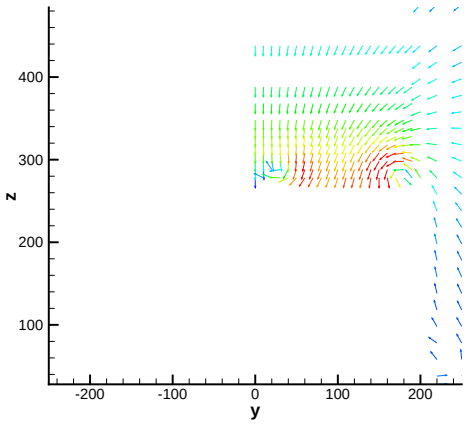

IC/Low–Re RSM SSG-Chen

Sample of plots available on the CD-Rom

Case 9.4

Articles written by the participants

Case 9.4: (Ahmed body)

Flow around a simplified car body LES with wall functions

C. Hinterberger, M. García-Villalba, W. Rodi
Institut für Hydromechanik, Universität Karlsruhe
Kaiserstraße 12, 76128, Germany
hinterberger@ifh.uni-karlsruhe.de

Method

- $LESOCC_2$–Code (Large Eddy Simulation on Curvilinear Coordinates)
- Finite-Volume, Hexaedra, structured, body fitted multi block grid
- Collocated arrangement, Rhie and Chow momentum interpolation
- SIMPLE method for velocity pressure coupling
- Pressure correction equation solved with SIP
- Runge-Kutta time stepping, pressure equation is solved only in last substep, second order
- Fluxes (convective and diffusive) discretized with second order central differences
- Parallelization by domain decomposition using MPI

Parameters

- Flow parameters:
  Experiment: $U_b = 40[m/s]$, $L = 1.044[m]$, $Re = U \cdot L/\nu = 2784000$
  Simulation: $U_b^* = 1$, $L^* = 1.044$, $1/\nu^* = Re/(U_b^* \cdot L^*)$
- Size of computational domain: $[-2.3, 5] \times [-0.935, 0.935] \times [0, 1.4]$
- Grid: 214 blocks, $18.5 \cdot 10^6$ cells
- Subgrid scale model: Smagorinsky model, $C_S = 0.13$
- Boundary conditions:
  Inflow boundary at $x = -2.3[m]$, constant inflow with $U_{in} = U_b = 40[m/s]$
  Convective outflow boundary at $x = 5[m]$
  Logarithmic law of the wall is applied at the walls of the ahmed body and at the bottom of the channel
  Slip boundaries at the top and the sides of the channel
- Adaptive time stepping with maximum Courant number = 0.6, $\Delta t^* \approx 1.3 \cdot 10^{-4}$ ($\Delta t \approx 3 \cdot 10^{-6}[s]$)
- Averaging time: $T^* \approx 4.5$ ($T \approx 0.11[s]$)
- Simulations were performed using 2*64 processors on the IBM SP-SMP (Power3) of the University Computing Center Karlsruhe. Each at a cost of approximatly 30 000 CPU hours.

Block structure and Grid

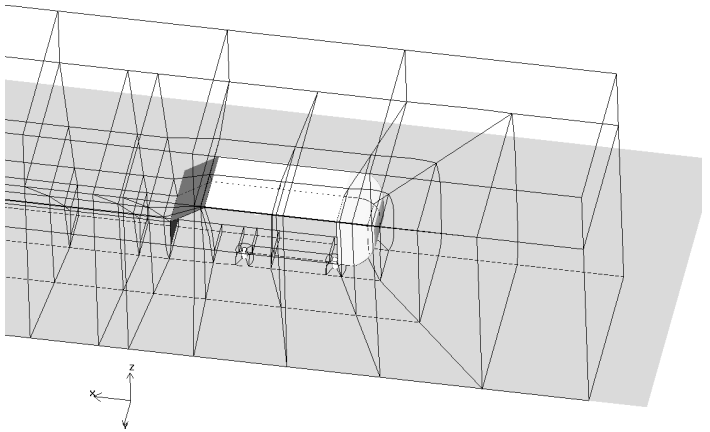

Figure 1: block structure (blocks plotted only in one half of the domain)

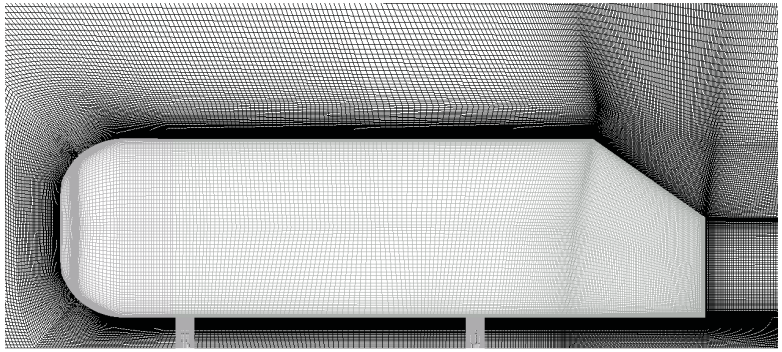

Figure 2: Cut in $x - z$ direction through the grid. (35° slant angle)

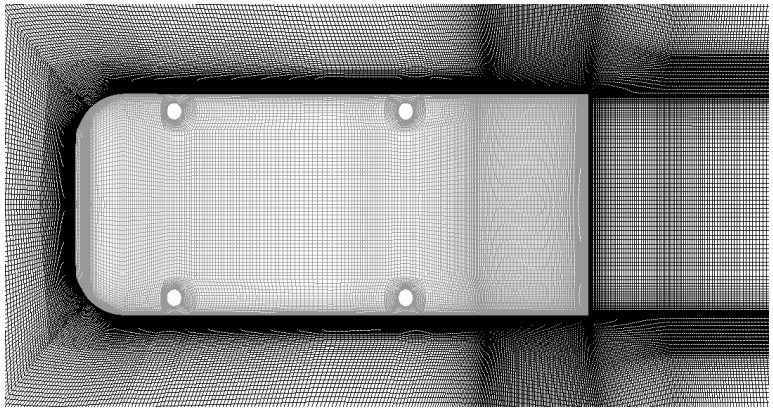

Figure 3: Cut in $x - y$ direction through the grid.

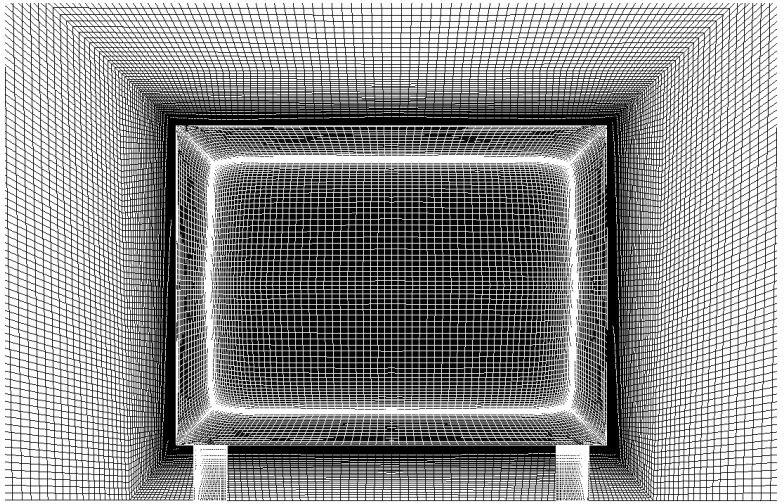

Figure 4: Cut in $y - z$ direction through the grid.

Results

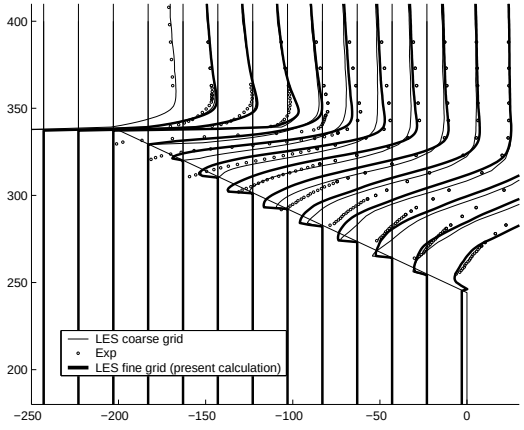

Figure 5: u-velocity at symmetry plane (25° slant angle)

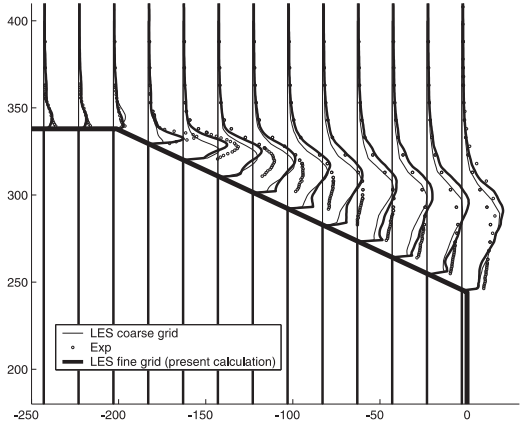

Figure 6: u'_{rms} at symmetry plane (25° slant angle)

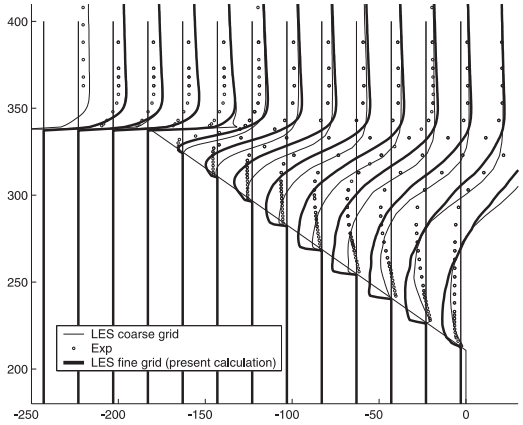

Figure 7: u-velocity at symmetry plane (35° slant angle)

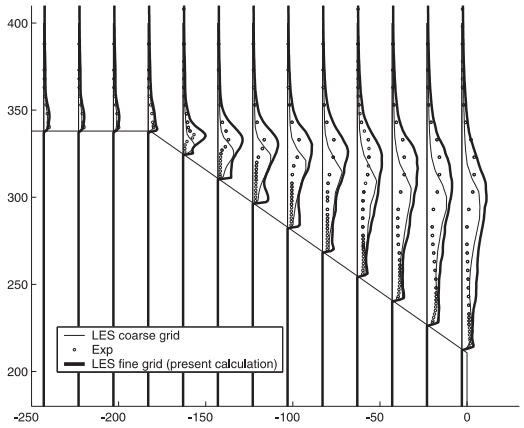

Figure 8: u'_{rms} at symmetry plane (35° slant angle)

10th joint ERCOFTAC-IAHR-QNET/CFD Workshop on Refined Turbulence Modelling

CASE 10.3: Flow around a simplified car body

(Ahmed body)

Description of the Model and Computational Method

B. Leonard, Ch. Hirsch and K. Kovalev
Fluid Mechanics Department
Vrije Universiteit Brussels, Brussels, Belgium

M. Elsden, K. Hillewaert and A. Patel
NUMECA Int., Av. F. Roosevelt, 5, 1050 Brussels, Belgium

1 Introduction

In terms of fluid dynamics, road vehicles are bluff bodies in very close proximity to the ground. Their external geometry is very complex. The flow over a vehicle is fully three-dimensional and boundary layers are turbulent. Flow separation is common, and may be followed by reattachment. Large turbulent wakes are formed at the rear, and in many cases they interact with longitudinal vortices shed from the aftbody. As is typical for bluff bodies, drag is primarily pressure drag. Accordingly, the avoidance of separation or, if this is not possible, its control is among the main objectives of vehicles aerodynamics.
To understand these flow phenomena and to study their interaction in detail, simplified car shapes of reduced geometrical complexity have been studied experimentally by Ahmed et al. (1984) and more recently by Lienhart et al. (2000). These experiments provide detailed experimental data that may be very useful in validating CFD codes and turbulence models for vehicle external aerodynamics.

2 Numerical Methods

The flow around the Ahmed body was studied using the HEXANS CFD code developed by NUMECA and VUB (Vrije Universiteit Brussel). HEXANS is a new unstructured hexahedral adaptive flow solver, Delanaye *et al.* (2002).
The spatial discretization method is based on cell centered finite volume approach. The advective fluxes across a face are computed by flux averaging with added artificial dissipation, Jameson (1995). The latter results in a blend of second and fourth order dissipation terms. A pressure switch triggers the second order dissipation factor in discontinuities or in regions of high flow gradients to avoid large amplitude oscillations.
The viscous fluxes require the computation of temperature and velocity gradients on the cell faces. For this purpose, a diamond control volume is created around each face and consists of two pyramidal elements. Each of which is formed by the face itself, and the left and right cell center as opposite summit respectively. For this purpose, the solution at the vertices is interpolated from the values stored in the cell.
An explicit Runge-Kutta scheme integrates the discretized set of equations in time to reach the steady state. Convergence acceleration is obtained through local time stepping and multigrid acceleration. In the multigrid approach, the creation of coarse grid levels is tightly coupled with mesh geometry and flow adaptation.
To deal with low Mach number flow or incompressible flow, the preconditioning methodology developed by Hakimi (1997) is used. It is derived from the artificial compressibility method introduced for incompressible flows by Chorin.

3 Flow adaptation

In the unstructured adaptive solver, mesh adaptation is performed automatically. The basic structure of an adaptive solution procedure consists of:

- Calculation of the solution on the coarse grid
- Identification of the cells to be refined and the cells to be removed
- Refinement or removal of the flagged cells

Anisotropic refinement allows cells to be split in 2,4 or 8 subcells. To ensure mesh quality, refinement flags are propagated so to permit only one hanging node per edge. Furthermore, "islands and voids" in the mesh are prevented. A hierarchical mesh coarsening technique has also been integrated.
Mesh adaptation is governed by criteria based on flow physics, geometry particularities or a simple error estimator. The first type are flow feature sensors aimed at the detection of regions where significant flow variations exist. The choice of appropriate feature detection parameters is guided by the physical nature of the flow. Various criteria based on flow physics are used. Undivided and divided differences of the velocity magnitude as well as vorticity are used to capture viscous effects.

4 Turbulence Modelling

The low-Reynolds k-ε turbulence model of Yang-Shih (1992), (1993) has been used to simulate the flow around the 25° Ahmed body.
Two additional equations are solved for the turbulent kinetic energy k and the turbulent dissipation rate ε.

$$\frac{\partial \rho k}{\partial t} + \vec{\nabla} \bullet \left(\rho \vec{v} k - \left(\mu + \frac{\mu_t}{\sigma_k} \right) \vec{\nabla} k \right) = P - \rho \varepsilon \tag{1}$$

$$\frac{\partial \rho \varepsilon}{\partial t} + \vec{\nabla} \bullet \left(\rho \vec{v} \varepsilon - \left(\mu + \frac{\mu_t}{\sigma_\varepsilon} \right) \vec{\nabla} \varepsilon \right) = \frac{1}{T} (C_{\varepsilon 1} P - C_{\varepsilon 2} \rho \varepsilon) + E \tag{2}$$

where P is the turbulence production, T is the turbulent time scale and E, is a term specific to the Yang-Shih model. Denoting the trace of a matrix product by Tr, the production term is defined by:

$$P = Tr\left(-\left(\overline{\rho \vec{v}'' f \vec{v}''} \right) \bar{\bar{S}} \right) \tag{3}$$

where $-\left(\overline{\rho \vec{v}'' f \vec{v}''} \right)$ is the turbulent Reynolds stress tensor and $\bar{\bar{S}}$ is the mean flow strain tensor. The Reynolds stresses and the velocity gradients are related through the Boussinesq hypothesis:

$$-\left(\overline{\rho \vec{v}'' f \vec{v}''} \right) = 2\mu_t \bar{\bar{S}} - \frac{2}{3} \rho k \bar{\bar{I}} \tag{4}$$

$\bar{\bar{I}}$ being the identity matrix. The turbulent time scale T and the term E are defined according to Yang and Shih:

$$\begin{cases} T = \dfrac{k}{\varepsilon} + \left(\dfrac{\nu}{\varepsilon} \right)^{0,5} \\ E = \nu \mu_t \left(\vec{\nabla}^2 \bar{\bar{S}} \right)^2 \end{cases} \tag{5}$$

The turbulent constants are those given as follows:

$$C_\mu = 0{,}09,\ C_{\varepsilon 1} = 1{,}44,\ C_{\varepsilon 2} = 1{,}92,\ \sigma_k = 1{,}0 \text{ and } \sigma_\varepsilon = 1{,}3 \tag{6}$$

The turbulent eddy viscosity μ_t is defined by a Kolmogorov-Prandtl type formula:

$$\mu_t = \rho C_\mu f_\mu k T \tag{7}$$

In the original version of this model, used here, the damping function f_μ was defined by Yang and Shih as a function of the Reynolds number based upon the distance to the wall, y:

$$f_\mu = \sqrt{1 - \exp\left(-c_1 Re_y - c_2 Re_y^3 - c_3 Re_y^5 \right)} \text{ with } Re_y = \frac{\rho \sqrt{k} y}{\mu} \tag{8}$$

where the constants are given by:

$$c_1 = 1{,}5 \times 10^{-4},\ _2 = 5{,}0 \times 10^{-7},\ c_3 = 1{,}0 \times 10^{-10} \tag{9}$$

5 Computational domain and boundary conditions

For the current simulation, only half of the body is considered. A symmetry plane is used at y=0[mm]. This results in a cross section of 935*1400[mm]. The recommendation of ERCOFTAC for the extension behind the car has been followed, to define the length of the domain. Therefore the grid ends five body length behind the rear of the body. The domain starts 2100[mm] in front of the body in order to match the experimental profiles at 400[mm] upstream. The stilts, on which the model is supported in the wind tunnel experiments, were not included in the computational grid.
At the inlet, the x-component of the velocity is constant and equals to 40m/s. The turbulent quantities are initialised based on the assumption that the fractional intensity Tu is 1% and the viscosity ratio is 1.
Smooth wall boundary conditions were used for the ground and the Ahmed body. Since a low-Reynolds turbulence model was used in the present simulation, the first mesh point has to be characterised by a y^+ of ~1.

The initial grid has been generated using the unstructured mesh generator HEXPRESS^{TM}, Delanaye *et al.* (2002). It consists of 470770 cells and is illustrated in figure 1.

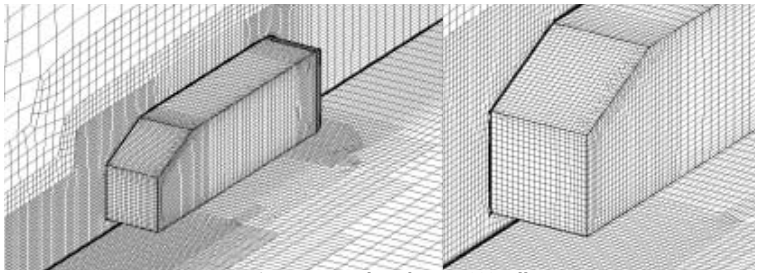

Figure 1. Initial mesh: ~471000 cells

Using the adaptation module available in HEXANS, two anisotropic refinements have been performed, based on the flow solution obtained on the initial grid. A first adaptation is performed in the slant region as well as in the wake. After one adaptation, the mesh consists of 756190 cells, as illustrated in fig.2.

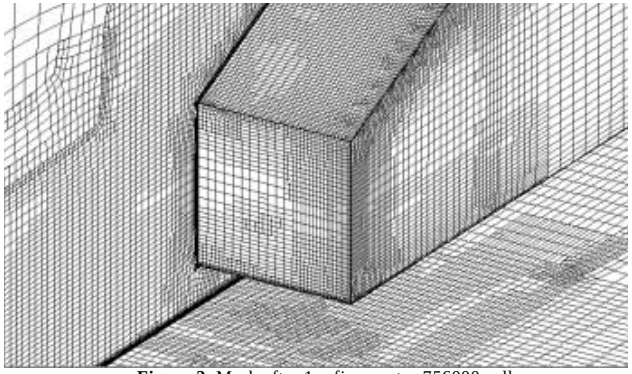

Figure 2. Mesh after 1 refinement: ~756000 cells

Once the steady solution is obtained, a second adaptation is performed in the slant region. After these two adaptations, the mesh consists of 814528 cells and is illustrated in fig. 3. During the workshop, only the results obtained on this final mesh will be presented.

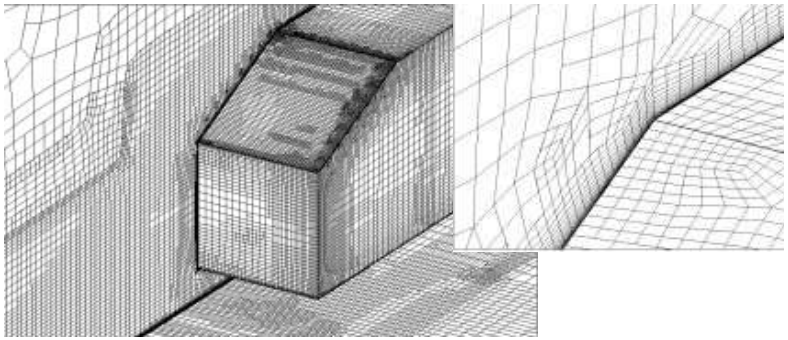

Figure 3. Final mesh: ~815000 cells

6 Results

Since between each local adaptation a steady state solution is obtained, these solutions can be compared in order to evaluate the accuracy gain brought by the adaptation and in order to check the grid independency of the final solution. Figure 4 presents the velocity evolution at different positions along the slant.

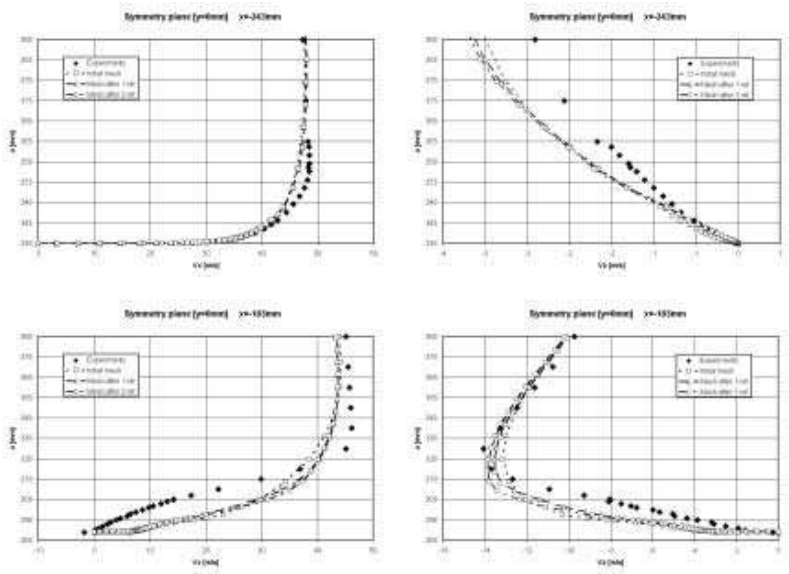

Figure 4. Velocity profiles [Slant x=-243, -103(mm)]

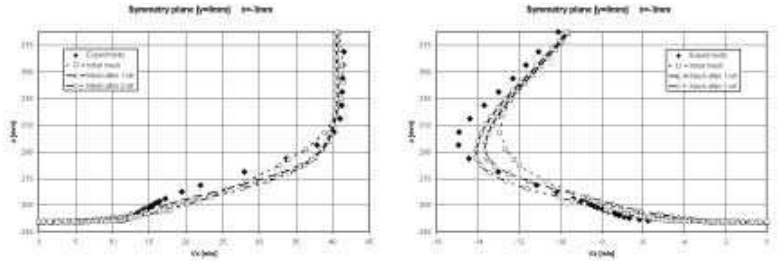

Figure 5. Velocity profiles [Slant x=-3mm]

From figure 4 and 5, we see that for the x-component of velocity, the solution obtained after one or two adaptation is equivalent. For the z-component of velocity, the solution is improved by grid adaptation, especially at the rear end of the slant.
In figure 6, the same comparison is shown for the velocity profiles in the wake region, x=38mm.

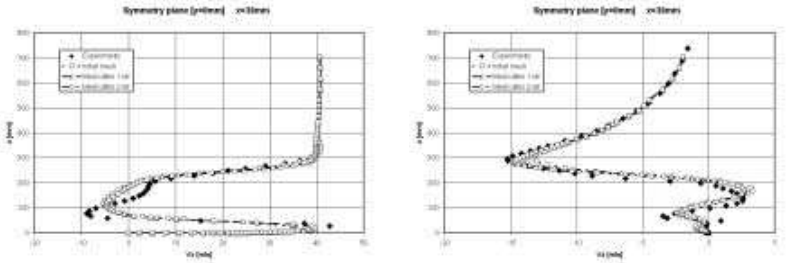

Figure 6. Velocity profiles [x=38mm]

7 Conclusions

The results presented are preliminary results. We can notice that the simulation with the low-Reynolds k-ε turbulence does not predict the recirculation on a level with the slant. The streamwise distribution of nodes near the slant edges has to be increased in order to capture velocity and pressure gradients accurately.
Some additional adaptations will have to performed in order to check the grid independency of the solution. Some other turbulence models, as Spalart-Allmaras will be tested and the results will be compared to the present ones.

References

Ahmed, S., Ramm, G. and Faltin, G., "*Some salient features of the time-averaged ground vehicle wake*", SAE Paper 840300, 1984.

Delanaye, M., Patel, A., Kovalev, K., Leonard B. and Hirsch, Ch., "*From CAD to Flow Solution with Adaptive Unstructured Hexahedral Meshing*", WCCM V, Fifth World Congress on Computational Mechanics, Vienna, Austria, July 7-12, 2002.

Hakimi, N., "*Preconditioning methods for time dependent Navier-Stokes equations / Application to environmental and low speed flows*", PhD, Vrije Universiteit Brussel, 1997.

Jameson, A. "*Analysis and design of numerical schemes for gas dynamics*", Int. J. Comp. Fluid Dyn., 4, No 3-4, 171-217, 1995.

Lienhart Becker and Stoots, "*Flow and turbulence structures in the wake of a simplified car model (Ahmed model)*", DLGR Fach Symposium der AG STAB Stuttgart University, 15-17. November, 2000.

Yang, Z. and Shih, T.H., "*A k-ε calculation of transitional boundary layers*", NASA Technical Memorandum 105604 ICOMP-92-08. CMOTT-92-05, 1992.

Yang, Z. and Shih, T.H., "*A Galilean and tensorial invariant k-e model for near wall turbulence*", AIAA Paper 93-3105, 1993.

10^{th} ERCOFTAC/IAHR Workshop on Refined Turbulence Modelling

Test-case 9.4
Flow around a simplified car body (Ahmed car model)

Authors:
M. Hadžiabdić, K. Hanjalić, W. Khier, YunLong Liu and O. Oohlous,

Faculty of Applied Sciences, Delft University of Technology
Lorentzweg 1, 2628 CJ Delft, The Netherlands

October 10-11, 2002,University of Poitiers, France

1 Numerical methods

The computations of all cases have been performed using the in-house version of the X-STREAM CFD code, developed jointly by the TNO-TPD and the Thermofluids section of TU Delft. The code has a finite-volume solver for structured, multi-block non-orthogonal, curvilinear grid, with collocated data arrangement.

The convection was discretised by a hybrid scheme with a high (over 60%) of central differencing. The diffusion is approximated using full central differencing scheme. The overall solution procedure is iterative and is based on the SIMPLE-like segregated algorithm which ensures coupling between velocity and pressure fields. The X-STREAM is written in Fortran 90 and is fully parallelized.

2 Turbulence models

The computations of the flow over the Ahmed car model were performed by three turbulence models: the standard linear $k-\varepsilon$ model, $k-\varepsilon-\overline{v^2}$ combined with wall functions (hence denoted as $k-\varepsilon-\overline{v^2}+WF$ and the Reynolds stress model + WF, with the Speziale, Sarkar and Gatski (1991) pressure-strain model and the modification of the ε equation (S_l term of Hanjalić and Jakirlić, 1998).

2.1 The k-ε-v^2-f elliptic relaxation model

Durbin's k-ε-v^2-f elliptic relaxation model retains the standard linear stress-strain relation

$$\overline{u_i u_j} = \frac{2}{3}k\delta_{ij} - \nu_t S_{ij} \tag{1}$$

where $S_{ij} = \frac{1}{2}\left(\frac{\partial U_i}{\partial x_j} + \frac{\partial U_j}{\partial x_i}\right)$ is the mean rate of strain. The eddy viscosity is defined as:

$$\nu_t = C_\mu \overline{v^2} T \tag{2}$$

where T is the characteristic turbulent time scale defied for high Re-number flows as $T = k/\varepsilon$. Hence, ν_t is defined in terms of *three* turbulence properties, k, v^2 and ε, which are provided from solutions of separate transport equations:

$$\frac{Dk}{Dt} = P - \varepsilon + \nabla\cdot((\nu+\nu_T)\nabla k) \tag{3}$$

$$\frac{D\varepsilon}{Dt} = \frac{C'_{\varepsilon_1}P - C_{\varepsilon_2}\varepsilon}{T} + \nabla\cdot\left((\nu+\frac{\nu_T}{\sigma_\varepsilon})\nabla\varepsilon\right) \tag{4}$$

$$\frac{D\overline{v^2}}{Dt} = kf - \frac{\overline{v^2}}{k}\varepsilon + \nabla\cdot\left((\nu+\nu_T)\nabla\overline{v^2}\right) \tag{5}$$

where $P = 2\nu_T S_{ij}S_{ij}$ is the production of turbulence kinetic energy, v^2 is another scalar which can be identified with the wall-normal turbulent stress in close vicinity of a solid wall, and f is the elliptic relaxation function. The latter is obtained from the solution of the elliptic relaxation equation in the form

$$\mathcal{L}(f) = (C_1 - 1)\frac{(2/3 - \overline{v^2}/k)}{T} + C_2\frac{P}{k} \tag{6}$$

The operator $\mathcal{L}(f)$ takes different forms depending on the model variant. The original and the simplest form is:

$$\mathcal{L}(f) = f - L^2\nabla^2 f \tag{7}$$

The turbulent time and length scales appearing in the above equations take the conventional definitions away from a wall, but lower bounds are imposed by Kolmogorov scales - becoming effective very close to a wall. These bounds are supposed to account for viscosity effects and prevent numerical singularities at the wall:

$$T = \max\left(\frac{k}{\varepsilon}; C_T\left(\frac{\nu}{\varepsilon}\right)^{\frac{1}{4}}\right); \qquad L = C_L \max\left(\frac{k^{\frac{3}{2}}}{\varepsilon}; C_\eta\left(\frac{\nu^3}{\varepsilon}\right)^{\frac{1}{4}}\right);$$

$$C_\mu = 0.22; \quad C_{\varepsilon_1} = 1.4; \quad C_{\varepsilon_2} = 1.9; \quad \sigma_\varepsilon = 1.3$$

$$C'_{\varepsilon_1} = C_{\varepsilon_1}\left(1 + \alpha\left(\frac{k}{\overline{v^2}}\right)^{\frac{1}{2}}\right)$$

$$C_1 = 1.4; C_2 = 0.3; C_L = 0.22$$

$$C_\eta = 85.0; C_T = 6.0; \alpha = 0.045$$

The wall boundary conditions are: $U_i = 0$; $k = 0$; $v^2 = 0$; $\varepsilon = \frac{2\nu k}{y^2}$; $f = -\frac{20\nu^2\overline{v^2}}{\varepsilon\, y^4}$ Note that the wall boundary conditions for f originates from the exact balance of terms in v^2 equation at the wall for the specific formulation of the pressure-strain term of Durbin. Its form can cause numerical instability if the first grid point is too close to a wall. Different, more robust alternatives have been proposed, e.g. Lien and Durbin [3] reformulated the source term in the v^2 equation that leads to $f = 0$ at the wall, but the quality of predictions were generally inferior to the original formulation.

2.2 The $k-\varepsilon-v^2-f$ model in conjunction with Wall Functions

While the k-ε-v^2 model returns good predictions of different generic flows, its application to complex high Reynolds flows may still not be feasible. Either the integration to the wall - requiring still a fine mesh in the near-wall region - may be too expensive and time consuming, or it may be difficult to assure that the nearest grid point is sufficiently close to the wall (e.g. $y^+ \leq 6$) over all bounding surfaces. In such cases, the use of wall functions may be unavoidable. Notwithstanding the fact that the optimum and universal wall functions are still not available, the idea of using wall functions with improved turbulence models is appealing. For that reason we considered the possibility of combining the k-ε-v^2-f model with the standard WF.

This hybrid approach implies that both options should be available in the CFD code and each model will become active depending on the wall distance of the first grid point. The criterion for switching from one to another model can be expressed in terms of $y+$ of turbulence Reynolds number. The first prerequisite for such a hybrid approach is to derive wall functions for the k-ε-v^2 model, and this is outlined below.

We adopted here the standard wall-function treatment of velocity, k and ε and derived analogue wall functions for the new variables v^2 and f. For the first we simply assume that $v^2/k = 0.25$. For f we solve *a priori* analytically the one-dimensional elliptic relaxation equation for f (6) by inserting the variables in the right hand side from the near-wall constant-stress equilibrium constraints used in formulating the standard wall functions, i.e. $k(y) = U_\tau^2/C_\mu^{1/2}$, $\varepsilon = U_\tau^3/\kappa y$, $\mu_t = \rho\kappa U_\tau y$, $\tau = k/\varepsilon$ and $L = C_L k^{3/2}/\varepsilon$. This yields the expression for the normalised f ($f^+ = f\nu/U_\tau^2$) in terms of y^+, which can serve as a wall function for f:

$$f^+ = 0.697\frac{1}{y^+} + C_{b1}y^{+(-1.56)} + C_{b2}y^{+(2.564)} \tag{8}$$

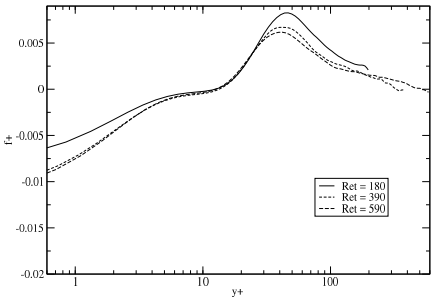

Figure 1: f derived from DNS data for different Re numbers (DNS data Kim, Moin and Moser (1987))

The last term in Eq.8 influences only the slope of the curve in the region $y^+ > 200$ and hence it can be neglected.

The coefficients Cb_1 and Cb_2 should be evaluated from reference DNS or experimental data. It is uncertain at present whether equation (8) would have a universal character. Evaluation from DNS data for a fully developed plane channel flow (Moser, Kim and Moin [4]) show some Re-number dependence, as shown in Fig 1), though this dependence seem to diminish with an increase in Re number, hopefully leading to a unique solution, at least for channel flows. For $Re_\tau = 595$ the DNS data yield the following coefficients: $C_{b1} = 0.7$ and $C_{b2} = 4.4$.

2.3 Differential Second-moment Closures (DSM)

In the Differential Second-Moment closure (DSM) (Re-stress models), the turbulent stress tensor $\overline{u_i u_j}$ is obtained directly from the the modelled differential transport equation, which is solved together with the transport equation for turbulence energy dissipation ε or an other scale-providing equation. For incompressible flow, the $\overline{u_i u_j}$ equation can be written as

$$\frac{D\overline{u_i u_j}}{Dt} = -\left(\overline{u_i u_k}\frac{\partial U_j}{\partial x_k} + \overline{u_j u_k}\frac{\partial U_i}{\partial x_k}\right) + \frac{\partial}{\partial x_k}\left(\nu\frac{\partial \overline{u_i u_j}}{\partial x_k}\right) + \mathcal{D}^t_{ij} + \Pi_{ij} - \varepsilon_{ij} \tag{9}$$

where

$$\mathcal{D}^t_{ij} = \frac{\partial}{\partial x_k}(-\overline{u_i u_j u_k}) \qquad \Pi_{ij} = -\frac{1}{\rho}\left(\overline{u_i\frac{\partial p}{\partial x_j}} + \overline{u_j\frac{\partial p}{\partial x_i}}\right) \qquad \varepsilon_{ij} = 2\nu\overline{\frac{\partial u_i}{\partial x_k}\frac{\partial u_j}{\partial x_k}}$$

representing respectively the turbulent velocity diffusion, velocity-pressure correlation and viscous stress dissipation, remain to be modelled.

We used a high-Re-numberDSM with wall functions, in which Π_{ij} is defined as a quasi-linear expression in term of stress anisotropy a_{ij} and mean flow strain-rate and vorticity, S_{ij} and Ω_{ij}, proposed by Speziale, Sarkar and Gatski [5], hence denoted as DNS-SSG. In this model, the velocity - pressure-gradient correlation Π_{ij} is first decomposed in the conventional way into pressure - strain Φ_{ij} and pressure diffusion $\mathcal{D}^p_{ij}$, i.e $\Pi_{ij} = \Phi_{ij} + \mathcal{D}^p_{ij}$. The latter is presumed to be lumped with $\mathcal{D}^t_{ij}$, while Φ_{ij} is modelled according to Speziale *at al.*

$$\Phi_{ij} = -C_1\varepsilon a_{ij} - C'_1\varepsilon(a_{ik}a_{jk} - \frac{1}{3}A_2\delta_{ij}) - C'_2 P a_{ij} + C_3 k S_{ij} +$$
$$C_4 k(a_{ik}S_{jk} + a_{jk}S_{ik} - \frac{2}{3}a_{kl}S_{kl}\delta_{ij}) + C_5 k(a_{ik}\Omega_{jk} + a_{jk}\Omega_{ik}) \tag{10}$$

where $C_1 = 1.7$, $C_1' = -1.05$, $C_2 = 0.9$, $C_4 = 0.625$, $C_5 = 0.2$, $C_3 = 0.8 - 0.625 A_2^{1/2}$, and $A_2 = a_{mn} a_{mn}$.

The stress dissipation tensor is modelled in the conventional manner as

$$\varepsilon_{ij} = \frac{2}{3} \varepsilon \delta_{ij} \tag{11}$$

The dissipation rate ε is obtained from the high-Re-number ε equation, modified with an extra term S_l to control the length-scale growth (Hanjalić and Jakirlić 1998).

$$\frac{D\varepsilon}{Dt} = \frac{\partial}{\partial x_k} \left(C_\varepsilon \frac{k}{\varepsilon} \overline{u_k u_l} \frac{\partial \varepsilon}{\partial x_l} \right) + (C_{\varepsilon_1} P - C_{\varepsilon_2} \varepsilon) \frac{\varepsilon}{k} + S_l \tag{12}$$

where

$$S_l = max \left\{ \left[\left(\frac{1}{C_l} \frac{\partial l}{\partial x_n} \right)^2 - 1 \right] \left(\frac{1}{C_l} \frac{\partial l}{\partial x_n} \right)^2 ; 0 \right\} \frac{\varepsilon \varepsilon}{k} A \tag{13}$$

and $l = k^{3/2}/\varepsilon$ is the turbulence length scale and $C_l = 2.5$.

3 Computation grids

Two meshes were used for the computation of the flow around the Ahmed car model: the coarse mesh with 490k cells consists of 33 blocks, and the fine mesh with 820k cells consisting of of 73 blocks. Both grids are clustered in the vicinity of the body surface. The fine mesh was used only for the computations with the standard $k - \varepsilon$ model, whereas the other two models (the Reynolds Stress (SSG) and $k - \varepsilon - \overline{v'^2} + WF$) were solved only on the coarse mesh. The wall-nearest grid point for coarse mesh was $y^+ = 17$, for fine mesh $y^+ = 11$.

References

[1] Durbin (1991), P. A. Near-wall turbulence closure model without damping functions. *Theoretical and Computational Fluid Dynamics*, **3**, 1.

[2] Hanjalić, K. and Jakirlić, S. (1998) Contribution towards the second-moment closure modelling of separating turbulent flows Computers and Fluids, **27**, 2,: 137-156.

[3] Lien, F.S. and P.A. Durbin (1996) Non-linear k-ε- v^2 modelling with application to high lift. *Proc. Summer Program*, Center for Turbulence Research, NASA Ames/Stanford Univ., 5-22.

[4] R. D.Moser, J. Kim, P. Moin (1999). Direct numerical simulation of turbulent channel flow up to $Re_\tau = 590$. *Phys. Fluids*, Vol. 11, No 4, pp 943-945.

[5] Speziale, S. C., Sarkar, S. and Gatski, T.B. (1991). Modelling a pressure-strain correlation of turbulence: an invariant dynamical systems approach. *J.Fluid Mech.* 227, 245-272

Computational Methods Applied to the Study of Flow Around a Simplified "Ahmed" Car Body (Case 9.4)

T. J. Craft, S. E. Gant, H. Iacovides, B. E. Launder and C. M. E. Robinson

UMIST, Manchester, UK

A number of RANS simulations of flow around the "Ahmed" body have been undertaken for the 10th Joint ERCOFTAC(SIG-15)-IAHR-QNET/CFD Workshop on Refined Turbulence Modelling. These calculations form part of a detailed study of vehicle aerodynamics supported by the European Union BRITE/EURAM Models for Vehicle Aerodynamics (MOVA) project (BE-97-4043). The simulations have involved three different turbulence models: a linear $k-\varepsilon$ model, a linear $k-\varepsilon$ model with realizability constraint and a non-linear $k-\varepsilon$ model with three different wall functions.

1 Numerical Methods

The flow around the Ahmed body was studied using the STREAM CFD code of Lien of Leschziner [1] (Simulation of Turbulent Reynolds-averaged Equations for All Mach numbers). STREAM is a three-dimensional, fully-elliptic, finite-volume solver which uses a structured, non-orthogonal, curvilinear, multi-block grid and a fully-collocated arrangement for data storage. The code uses the SIMPLE pressure-correction algorithm [2] and a Rhie & Chow interpolation [3] to prevent unrealistic pressure fluctuations due to the non-staggered grid arrangement. Convection is discretized using either an upwind scheme or UMIST (Upstream Monotonic Interpolation for Scalar Transport) a TVD scheme based on the third-order accurate QUICK [4]. In the majority of the Ahmed body computations, the UMIST scheme was used for convection of both momentum and turbulence scalars, but in some cases it was necessary to use the less accurate but more stable upwind scheme (see Table 1). This was due, firstly, to the analytical wall function (UMIST-A) which could not be implemented as robustly as the standard log-law-based Simplified Chieng & Launder (SCL) wall function and, secondly, to the grid which contained some highly-skewed cells with corner angles of approximately 45^o. Calculations were converged until velocity, mass and turbulence residuals were below 10^{-4}. A number of tests were undertaken in order to ensure that the results obtained were fully converged, including running some time-dependent calculations, for details see Robinson [5].

2 Computational Grids

Separate computational grids were defined for the 25^o and 35^o Ahmed bodies which principally differed over the rear slant, although there were minor differences in the grid structure over the upstream portion of the body (see Figures 1, 2 and 3). Both grids used 22 blocks and approximately

Rear Slant	Model	Wall Function	Mean Velocities	Turb. Variables	Inlet
25^o	Linear	SCL	UMIST	UMIST	
		UMIST-N	UMIST	UMIST	
	Realiz. Linear	SCL	UMIST	UMIST	*
		UMIST-A	UMIST	UMIST	*
	Non-Linear	SCL	UMIST	UMIST	*
		UMIST-A	UMIST	Upwind	*
35^o	Linear	SCL	UMIST	UMIST	
	Realiz. Linear	SCL	UMIST	UMIST	*
		UMIST-A	UMIST	Upwind	*
	Non-Linear	SCL	UMIST	Upwind	*
		UMIST-A	UMIST	Upwind	*

Table 1: Convection schemes and inlet conditions used in calculations of Ahmed body flow. The earlier calculations marked with an asterisk (*) in the final column used $\nu_t/\nu = 60$ to determine inlet values for ε whilst the more recent calculations (shown without an asterisk) used $\nu_t/\nu = 10$.

300,000 cells, as shown in Table 2. The legs, or stilts, on which the model was supported in the wind tunnel experiments, were not included in the computational grid. Grids were adjusted to maintain y^* values of as many as possible near-wall cells around the body to within the limits $55 < y^* < 550$, but these limits were exceeded in some regions of stagnation and boundary-layer separation or reattachment. The y^* values of the near-wall cells adjacent to the ground plane were not controlled, since to maintain $y^* < 550$ would have required high-aspect ratio cells which would have compromised the stability of the calculation. Due to the large number of nodes required to model the Ahmed body, it was not possible to refine the grids and establish grid independence. However, a coarser grid was generated for the 25^o Ahmed body to investigate the effect of grid coarsening and provided some information regarding grid independence (see [5]).

Slant Angle	No. Blocks	No. Cells
25^o	22	331,000
35^o	22	355,000

Table 2: Ahmed body grids with the number of cells to the nearest thousand

3 Boundary Conditions

The floor of the domain and the Ahmed body itself were treated as wall boundary conditions, using either the Simplified Chieng & Launder (SCL) wall function, the analytical wall function (UMIST-A) or the numerical wall function (UMIST-N) (see Figure 4). The domain boundary along the centreline of the body (at $y = 0$) and opposite boundary at the outside limit of the domain ($y = 1.044$m) and the upper domain boundary ($z = 1.044$m) were all treated as symmetry planes. Ideally the upper domain boundary and the domain boundary opposite the centre-plane would be treated as entrainment boundaries. However, symmetry planes were used instead to provide a more stable calculation and were justifiable as there is little deflection of the flow at these boundaries. The downstream outlet was set with zero-gradient for all variables. Flat profiles

(i.e. constant values) of velocity and turbulence parameters were set at the inlet plane, one body-length upstream of the Ahmed body. Values of the inlet streamwise velocity and turbulent kinetic energy were calculated by integrating the measured U- and k-profiles across the flow domain at $x = -1.444$m. This resulted in an inlet bulk U-velocity which was lower (38.51ms^{-1}) than the stated experimental bulk U-velocity of 40ms^{-1}. The lower inlet bulk velocity corresponded to an inlet Reynolds number of $Re = 7.57 \times 10^5$ (based on the body's height) which compares to the original Ahmed experimental value of $Re = 1.18 \times 10^6$. The Reynolds number is sufficiently high that this minor adjustment should not have significantly influenced the results. The inlet turbulent kinetic energy was calculated as $k_{in} = 6.58 \times 10^{-3}\text{m}^2\text{s}^{-2}$. Early simulations of the Ahmed body flow, marked with an asterisk ($*$) in Table 1, calculated ε_{in} from an assumed ratio of the turbulent to the molecular viscosity of $\nu_t/\nu = 60$. At a later date, LSTM provided a more accurate estimate of the experimental inlet dissipation rate ($\nu_t/\nu \approx 10$). Tests showed that switching to the new value had no impact on the calculated flow around the body and the more recent calculations using the linear $k-\varepsilon$ model have used the inlet condition $\nu_t/\nu = 10$.

4 Turbulence Models

Three turbulence models were used to calculate the flow around the Ahmed body: the linear $k-\varepsilon$ model of Launder & Spalding [6], the same linear model with the realizability condition of May [7], and the non-linear $k-\varepsilon$ model of Craft *et al.* [8].

Linear $k-\varepsilon$ Model

In the high-Reynolds-number form of the $k-\varepsilon$ model by Launder & Spalding [6], the Reynolds stress, $\overline{u_i u_j}$ is a linear function of the strain-rate, and the eddy-viscosity is calculated from the turbulent kinetic energy, k, and dissipation rate, ε, as follows:

$$\nu_t = c_\mu \frac{k^2}{\varepsilon} \tag{1}$$

Transport equations are solved for k and ε, which for a steady flow can be expressed in Cartesian tensors as follows:

$$\frac{\partial\left(\rho U_j k\right)}{\partial x_j} = \frac{\partial}{\partial x_j}\left[\left(\mu + \frac{\mu_t}{\sigma_k}\right)\frac{\partial k}{\partial x_j}\right] + P_k - \rho\varepsilon \tag{2}$$

$$\frac{\partial\left(\rho U_j \varepsilon\right)}{\partial x_j} = \frac{\partial}{\partial x_j}\left[\left(\mu + \frac{\mu_t}{\sigma_\varepsilon}\right)\frac{\partial \varepsilon}{\partial x_j}\right] + c_{\varepsilon 1} f_1 P_k \frac{\varepsilon}{k} - c_{\varepsilon 2} f_2 \rho \frac{\varepsilon^2}{k} + \rho Y_c \tag{3}$$

where the so-called "Yap correction", Y_c, is included as a source term in the ε-equation to reduce the turbulent length scale in regions of flow impingement and reattachment. The standard Yap correction is based on the ratio of the length scale, $k^{3/2}/\varepsilon$, to the equilibrium length scale, defined by $l_e = 2.55y$, where y is the wall-normal distance:

$$Y_c = max\left[0.83\left(\frac{k^{3/2}/\varepsilon}{2.55y} - 1\right)\left(\frac{k^{3/2}/\varepsilon}{2.55y}\right)^2, 0\right] \tag{4}$$

Realizability Condition

The realizability constraint, derived by May [7], which was used in conjunction with the linear $k-\varepsilon$ model, was coded into STREAM as follows:

$$\mu_t = \min\left[c_\mu \rho \frac{k^2}{\varepsilon}, \frac{\rho k}{\max\left(TINY, \alpha_1, \alpha_2, \alpha_3\right)}\right] \tag{5}$$

where $TINY$ is an arbitrarily small value and α_1, α_2 and α_3 are given by:

$$\alpha_1 = \frac{3}{2}\left\{\frac{\partial U}{\partial x} + \frac{\partial V}{\partial y} + \left[\left(\frac{\partial V}{\partial y} - \frac{\partial U}{\partial x}\right)^2 + \left(\frac{\partial U}{\partial y} - \frac{\partial V}{\partial x}\right)^2\right]^{1/2}\right\} \tag{6}$$

$$\alpha_2 = \frac{3}{2}\left\{\frac{\partial V}{\partial y} + \frac{\partial W}{\partial z} + \left[\left(\frac{\partial W}{\partial z} - \frac{\partial V}{\partial y}\right)^2 + \left(\frac{\partial V}{\partial z} - \frac{\partial W}{\partial y}\right)^2\right]^{1/2}\right\} \tag{7}$$

$$\alpha_1 = \frac{3}{2}\left\{\frac{\partial W}{\partial z} + \frac{\partial U}{\partial x} + \left[\left(\frac{\partial U}{\partial x} - \frac{\partial W}{\partial z}\right)^2 + \left(\frac{\partial W}{\partial x} - \frac{\partial U}{\partial z}\right)^2\right]^{1/2}\right\} \tag{8}$$

In a simple shear flow the latter part of the minimum function in Equation (5) can be rearranged and shown to be equivalent to taking c_μ as a function of the strain invariant, S:

$$c_\mu = \frac{2}{3S} \tag{9}$$

Non-Linear $k-\varepsilon$ Model

In the non-linear $k-\varepsilon$ model of Craft *et al.* [8], additional quadratic and cubic functions of strain and vorticity are introduced into the equation for the Reynolds stress, as follows:

$$\begin{aligned}
-\overline{u_i u_j} + \frac{2}{3}\delta_{ij}k = \quad & \nu_t S_{ij} \\
+ \quad & c_1 \frac{\nu_t k}{\varepsilon}\left(S_{ik}S_{kj} - \frac{1}{3}S_{kl}S_{kl}\delta_{ij}\right) \\
+ \quad & c_2 \frac{\nu_t k}{\varepsilon}\left(\Omega_{ik}S_{kj} + \Omega_{jk}S_{ki}\right) \\
+ \quad & c_3 \frac{\nu_t k}{\varepsilon}\left(\Omega_{ik}\Omega_{kj} - \frac{1}{3}\Omega_{lk}\Omega_{lk}\delta_{ij}\right) \\
+ \quad & c_4 \frac{\nu_t k^2}{\varepsilon^2}\left(S_{ki}\Omega_{lj} + S_{kj}\Omega_{li}\right)S_{kl} \\
+ \quad & c_5 \frac{\nu_t k^2}{\varepsilon^2}\left(\Omega_{il}\Omega_{lm}S_{mj} + S_{il}\Omega_{lm}\Omega_{mj} - \frac{2}{3}S_{lm}\Omega_{mn}\Omega_{nl}\delta_{ij}\right) \\
+ \quad & c_6 \frac{\nu_t k^2}{\varepsilon^2}S_{ij}S_{kl}S_{kl} \\
+ \quad & c_7 \frac{\nu_t k^2}{\varepsilon^2}S_{ij}\Omega_{kl}\Omega_{kl}
\end{aligned} \tag{10}$$

This model also takes c_μ to be a function of the invariants of the strain and vorticity tensors:

$$c_\mu = \frac{0.3}{1+0.35\left[\max\left(S,\Omega\right)\right]^{1.5}}\left(1-\exp\left\{-0.36\exp\left[0.75\max\left(S,\Omega\right)\right]\right\}\right) \tag{11}$$

5 Wall Functions

Three wall functions were used in the Ahmed body calculations: the log-law-based Simplified Chieng & Launder (SCL) wall function and two recently developed treatments which involve the solution of simplified boundary-layer-type transport equations across the near-wall cell. The two new wall functions are denoted UMIST-A and UMIST-N for Unified Modelling through Integrated Sublayer Treatment, using respectively an Analytical or Numerical approach. All of the wall functions are similar in terms of implementation: a no-slip condition is employed at the wall surface ($U_i = 0$), the velocity variation within the near-wall cell is accounted for by setting to zero the momentum flux to the wall and including in its place an expression for the wall shear stress, τ_{wall}. Likewise, the production and dissipation source terms (P_k and ε) in the discretized k-equation within the near-wall cells are replaced with cell-averaged production and dissipation source terms ($\overline{P_k}$ and $\overline{\varepsilon}$). In the SCL and UMIST-A wall functions, the ε-equation is not solved in the near-wall cell and instead its value at the near-wall node is prescribed from assuming an equilibrium turbulence length scale variation, $k^{3/2}/\varepsilon = c_l y$. The UMIST-$N$ wall function, however, solves both the k- and ε-equations in the near-wall cell using cell-averaged source terms.

Simplified Chieng & Launder (SCL)

The wall function proposed by Chieng & Launder [9] divided the near-wall cell into two layers: the viscous sublayer (defined as $y^* = yk^{1/2}/\nu < 20$) and the fully turbulent region. In the viscous sublayer the velocity was assumed to increase linearly, the turbulent shear stress to be zero and the turbulent kinetic energy to vary quadratically, whilst in the fully turbulent region the velocity was assumed to follow the "universal" log-law profile and both $\rho\overline{uv}$ and k were assumed to vary linearly with wall distance. Since at the wall the dissipation rate is given by $\varepsilon = 2\nu\left(\partial k^{1/2}/\partial y\right)^2$ and k varies quadratically, ε was assumed to take a constant value in the viscous sublayer. In the fully turbulent region, ε was obtained from assuming an equilibrium turbulence length scale variation, $k^{3/2}/\varepsilon = c_l y$ (where $c_l = 2.55$). The simplified version of the wall function employed in the Ahmed body calculations assumed a constant turbulent kinetic energy and shear stress in the fully turbulent region. This gave the following expressions for the wall shear stress, τ_{wall}, average production, $\overline{P_k}$ and average dissipation $\overline{\varepsilon}$:

$$\tau_{wall} = \frac{\rho\kappa c_\mu^{1/4}k_p^{1/2}U_p}{\ln\left(Ec_\mu^{1/4}k_p^{1/2}y_p/\nu\right)}$$

$$\overline{P_k} = \frac{1}{y_n}\int_{y_v}^{y_n}\tau_{wall}.\frac{\tau_{wall}}{\kappa c_\mu^{1/4}\rho k_p^{1/2}y}\mathrm{d}y = \frac{\tau_{wall}^2}{\kappa c_\mu^{1/4}\rho k_p^{1/2}y_n}\ln\left(\frac{y_n}{y_v}\right)$$

$$\overline{\varepsilon} = \frac{1}{y_n}\left(y_v\frac{2\nu k_p}{y_v^2} + \int_{y_v}^{y_n}\frac{c_\mu^{3/4}k_p^{3/2}}{\kappa y}\mathrm{d}y\right) = \frac{1}{y_n}\left(\frac{2\nu k_p^{3/2}}{k_p^{1/2}y_v/\nu} + \frac{c_\mu^{3/4}k_p^{3/2}}{\kappa}\ln\left(\frac{y_n}{y_v}\right)\right)$$

where subscript p denotes the value at the wall-adjacent node, U is the wall-parallel velocity and y_p the distance from the wall to the near-wall node and the sublayer thickness, y_v, is calculated from $y_v k_p^{1/2}/\nu = 20$.

Analytical Wall Function (UMIST-A)

In the UMIST-A wall function neither the log-law velocity profile nor the constant or linear variation in shear stress is assumed. Instead, a simplified momentum equation is specified in the near-wall cell:

$$\frac{\partial\left(\rho UU\right)}{\partial x} + \frac{\partial\left(\rho UV\right)}{\partial y} = -\frac{\partial P}{\partial x} + \frac{\partial}{\partial y}\left[\left(\mu+\mu_t\right)\frac{\partial U}{\partial y}\right] \tag{12}$$

and integrated analytically across the near-wall cell using a prescribed turbulent viscosity profile:

$$\begin{aligned}\mu_t &= 0 && \text{for} \quad y < y_v\\ &= \rho c_\mu c_l k_p^{1/2}\left(y-y_v\right) && \text{for} \quad y \geq y_v\end{aligned} \tag{13}$$

where $c_l = 2.55$. A detailed derivation of the analytical wall function can be found in Robinson [5] or in a similar approach for buoyancy-affected flows by Craft *et al.* [10]. Expressions for the wall shear stress and average production of turbulent kinetic energy for the near-wall cell are provided below:

$$\tau_w = -\frac{\rho k_p^{1/2}}{\mu_v}A_1$$

$$\overline{P_k} = \frac{\rho\alpha k_p^{1/2}}{y_n\mu_v}\int_{y_v^*}^{y_n^*}\mu_v(y^*-y_v^*)\left[\frac{A_1 + C_1y_v^* + C_2(y^*-y_v^*)}{\mu_v\left[1+\alpha(y^*-y_v^*)\right]}\right]^2 dy^*$$

$$\overline{\varepsilon} = \frac{1}{y_n}\left[\frac{2k_p^{3/2}}{y_\varepsilon^*} + \frac{k_p^{3/2}}{c_l}\ln\left(\frac{y_n^*}{y_\varepsilon^*}\right)\right]$$

where A_1, C_1 and C_2 are given by:

$$A_1 = \frac{\alpha\mu_v U_n - C_2(y_n^*-y_v^*) + \left[C_1y_v^* - \frac{C_2}{\alpha}\right]\ln\left[1+\alpha(y_n^*-y_v^*)\right] + \frac{\alpha C_1 y_v^{*2}}{2}}{\alpha y_v^* + \ln\left[1+\alpha(y_n^*-y_v^*)\right]}$$

$$C_1 = \frac{\mu_v^2}{\rho^2 k_p}\left[\frac{\partial p}{\partial x} + \gamma\rho U\frac{\partial U}{\partial x} + \gamma\rho V\frac{\partial U}{\partial y}\right]$$

$$C_2 = \frac{\mu_v^2}{\rho^2 k_p}\left[\frac{\partial p}{\partial x} + \rho U\frac{\partial U}{\partial x} + \rho V\frac{\partial U}{\partial y}\right]$$

γ is an empirical constant (taken as 1.0) which is used to control the influence of convection inside the laminar sub-layer, and $\alpha = c_\mu c_l$. The turbulence and dissipation viscous sublayer thicknesses y_v^* and y_ε^* are 10.8 and 5.1 respectively.

Numerical Wall Function (UMIST-N)

The UMIST-N wall function does not use any assumed profiles of velocity and length scale. Instead, profiles of the mean flow and turbulence parameters near the wall are obtained by solving simplified boundary-layer-type transport equations using a fine "subgrid" spanning the wall-

adjacent control volume (see Figure 5). The wall function differs from standard low-Re treatments in that it decouples the numerical solution of the near-wall region from that of the main region of the flow domain and also because it does not involve the solution of the pressure correction equation over the subgrid. The new wall function therefore does not suffer from the slow convergence problems of a low-Re calculation. Previous tests of UMIST-N in impinging-jet and spinning-disc flows have indicated that computing times are approximately twice those of standard log-law wall function calculations but an order-of-magnitude less than full low-Re model calculations.

The transport equations solved by the wall function across the subgrid account for convection both parallel and normal to the wall, pressure gradient, diffusion normal to the wall and source terms. In the present study, a linear $k-\varepsilon$ model has been used and so simplified k- and ε-equations have been solved across the subgrid in addition to equations for the wall-parallel velocity components. Since two independent wall-parallel velocity components are solved (in a three-dimensional geometry) the UMIST-N wall function is able to account for skewing of the velocity vector close to the wall. The wall function is also not restricted to using a linear $k-\varepsilon$ model and can, in principle, be applied with any level of turbulence closure.

The subgrid transport equations are discretized in a similar manner to that used for simple one-dimensional diffusion problems and solved using a Tri-Diagonal Matrix Algorithm (TDMA). The wall-normal W-velocity profile across the near-wall cell is calculated from continuity within each of the subgrid cells and is scaled to ensure that the subgrid W-velocity at the outer edge of the subgrid (position t in Figure 5) is consistent with the main-grid wall-normal velocity at that location. One subgrid iteration is performed for each main-grid iteration so the subgrid solution converges as the main-grid solution converges. After each subgrid iteration, the wall shear stress, τ_{wall}, and average values of the source terms across the subgrid are calculated (e.g. $\overline{P_k}$, $\bar{\varepsilon}$). Low-Reynolds-number damping terms are included in the main-grid transport equations to enable unlimited refinement of the grid near the wall.

The subgrid transport equations are relatively straight-forward to derive for a Cartesian grid arrangement and are provided in Craft *et al.* [11]. For a non-orthogonal curvilinear grid arrangement, used in the present study, the subgrid transport equations are obtained using velocity components parallel to the grid-lines (i.e. using covariant base vectors). Subgrid transport equations for momentum, turbulent kinetic energy and dissipation rate in non-orthogonal curvilinear coordinates have the generic form:

$$\frac{\rho U}{\sqrt{g_{11}}}\left(\frac{\partial\phi}{\partial\xi}\right)^{*}+\frac{\rho V}{\sqrt{g_{22}}}\left(\frac{\partial\phi}{\partial\eta}\right)^{*}+\frac{\rho W}{\sqrt{g_{33}}}\left(\frac{\partial\phi}{\partial\zeta}\right)^{*}=\frac{1}{J}\frac{\partial}{\partial\zeta}\left(Jg^{33}\Gamma\frac{\partial\phi}{\partial\zeta}\right)+C \qquad (14)$$

where ϕ denotes one of the subgrid parameters: U, V, k or $\bar{\varepsilon}$, Γ the diffusivity and the source term, C, includes geometry-related source terms, the pressure gradient in the momentum equations and production and dissipation sources in the k- and $\bar{\varepsilon}$-equations. The non-orthogonal subgrid coordinate system has directional components (ξ,η,ζ) where it is assumed that the ξ- and η-components are aligned to grid lines which are parallel to the wall whilst the ζ-axis is usually, but not necessarily, wall-normal. The velocity components U, V and W act in the ξ, η and ζ directions respectively and are "physical" velocities, i.e. they have units of (length/time). Gradient terms appearing in the convection are discretized using upwind differencing. The asterisk (*) denotes the fact that upstream values of ϕ appearing in the discretized convection terms need to be transformed

from the coordinate system used in the upstream cell into the current cell coordinate system. This transformation only affects convection of momentum where the direction of the velocity vectors in the upstream cell may differ from those in the current cell. Since scalar parameters (k and $\bar{\varepsilon}$) are invariant of the reference frame, their upstream values do not require transformation. The $\sqrt{g_{11}}$, $\sqrt{g_{22}}$ and $\sqrt{g_{33}}$ terms (square-roots of the covariant metric tensor components) are equivalent to the physical widths of the cells in the ξ, η and ζ directions respectively. The Jacobian, J, is equivalent to the cell volume when the cell dimensions are unity, $\Delta\xi=\Delta\eta=\Delta\zeta=1$.

Since convective terms are evaluated using neighbouring subgrid values, the velocity components, k and ε are stored in computer memory for each subgrid node along the length of the wall. Storing the subgrid velocity components is also necessary in order to calculate the wall-normal W-velocity from continuity, using mass fluxes through the subgrid cell faces. In order to accommodate the block-structured grid arrangement used around the Ahmed car body, a multiblock formulation of the UMIST-N wall function has been used with subgrid blocks mirroring the main-grid block structure. The subgrid was generated around the Ahmed body using 45 nodes within each of the main-grid near-wall cells. Subgrid nodes were clustered towards the wall using an expansion ratio of 1.09. Increasing the number of subgrid nodes to 60 had no effect on the results of the simulation.

References

[1] F. S. Lien and M. A. Leschziner. A general non-orthogonal finite-volume algorithm for turbulent flow at all speeds incorporating second-moment turbulence-transport closure. *Comp. Meth. Appl. Mech. Eng.*, 114:123–167, 1994.

[2] S. V. Patankar and D. B. Spalding. A calculation procedure for heat, mass and momentum transfer in three-dimensional parabolic flows. *Int. J. Heat Mass Transfer*, 15:1787, 1972.

[3] C. M. Rhie and W. L. Chow. Numerical study of the turbulent flow past an airfoil with trailing edge separation. *AIAA J.*, 21:1525–1532, 1983.

[4] F. S. Lien and M. A. Leschziner. Upstream monotonic interpolation for scalar transport with application to complex turbulent flows. *Int. J. Num. Meth. Fluids*, 19:527–548, 1994.

[5] C. M. E. Robinson. *Advanced CFD modelling of road-vehicle aerodynamics*. PhD thesis, Dept. of Mechanical Engineering, UMIST, 2001.

[6] B. E. Launder and D. B. Spalding. The numerical computation of turbulent flows. *Computer Methods in Applied Mechanics and Engineering*, 3:269–289, 1974.

[7] N. E. May. Efficient implementation of two-equation and differential Reynolds stress turbulence models into a cell-vertex, explicit, time-marching, Navier-Stokes flow code. Technical Report M345/1, Aircraft Research Assoc., 1998.

[8] T. J. Craft, B. E. Launder, and K. Suga. Development and application of a cubic eddy-viscosity model of turbulence. *Int. J. Heat and Fluid Flow*, 17:108–115, 1996.

[9] C. C. Chieng and B. E. Launder. On the calculation of turbulent heat transport downstream from an abrupt pipe expansion. *Numerical Heat Transfer*, 3:189–207, 1980.

[10] T. J. Craft, A. V. Gerasimov, H. Iacovides, and Launder B. E. Progress in the generalization of wall-function treatments. *Int. J. Heat and Fluid Flow*, 23:148–160, 2002.

[11] T. J. Craft, S. E. Gant, H. Iacovides, and B. E. Launder. Development and application of a new wall function for complex turbulent flows. In *ECCOMAS CFD 2001*, 2001.

Figures

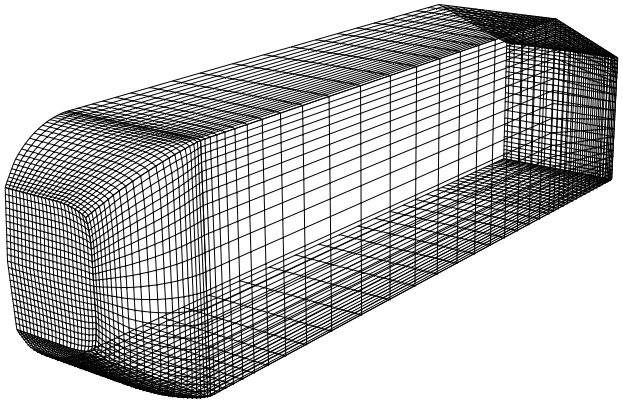

Figure 1: Grid on nose cone and front portion of Ahmed body

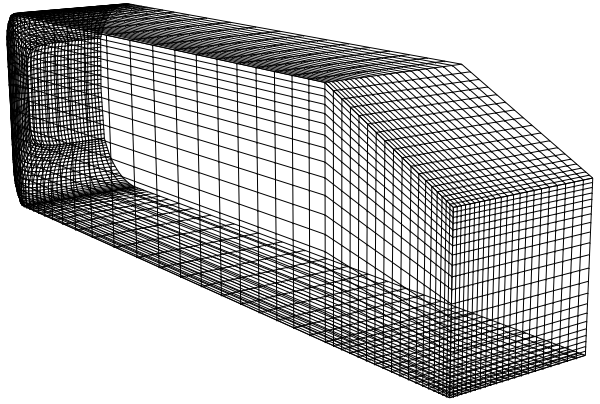

Figure 2: Grid used on rear section and slant of 25^o Ahmed body

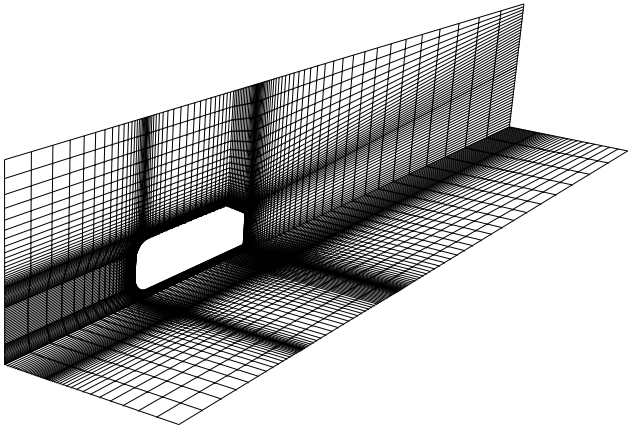

Figure 3: Grid on symmetry plane and floor showing some refinement propagated at block boundaries

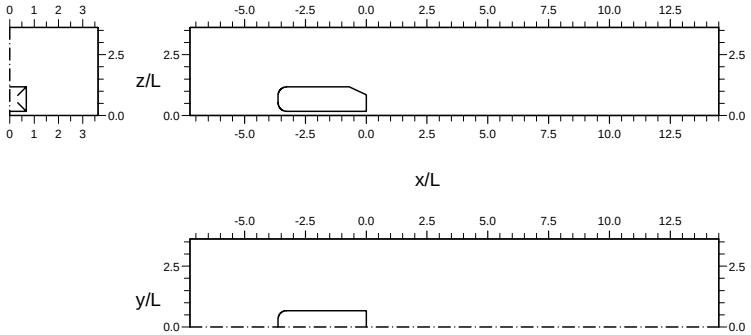

Figure 4: Sketch of domain in third angle projection used for Ahmed body calculations

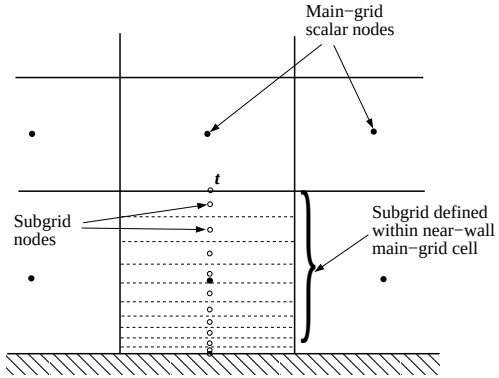

Figure 5: Subgrid arrangement within near-wall main-grid control volume

Validation of CFX-5 for the Ahmed Car Body (Synopsis)

Ludovic Durand[1], Martin Kuntz[2], Florian Menter[2]
[1]Ecole Centrale de Nantes
[2]CFX-Germany

1 Introduction

Simulations have been carried out for the generic car body (Ahmed body) for 25° and 35° slant angle. At a previous workshop in Darmstadt, the results of the different groups showed significant variations, even when the same turbulence models were used. This indicates that either the grids used in the investigations were too coarse to reduce the numerical errors below an acceptable limit, or that other factors, like boundary conditions, model implementation etc. had a significant effect on the simulations. In any case, the results of the simulations were inconclusive, leading to a revaluation of this test case.

In order to eliminate some of the uncertainties of previous simulations, best practice procedures [1] have been applied in the current report. This includes a systematic grid refinement study, a sensitivity study concerning the treatment of the far field boundaries and an investigation of the influence of different turbulence models.

A series of grids has been generated and the solutions for these grids have been compared in order to determine the grid resolution requirements for this flow. In a second step, different turbulence models have been applied and the influence of the models has been investigated in detail, including a comparison with the experimental data.

Part of the work was carried out within the EU funded project FLOMANIA: Physical Flow Modeling – An Integrated Approach. Due to the limited space only a general description of the methods and some major results can be presented. A full validation report [2] is available from one of the authors (florian.menter@cfx-germany.com).

2 Numerical Method

All simulations have been computed with CFX-5 of AEA Technology. The main characteristics of the solver are:

- Fully conservative, vertex based finite volume method.
- Unstructured hybrid meshes.
- Co-located variables.
- Second-order accuracy in space and time.
- Different advection schemes – first and second order upwind, TVD.
- Coupled implicit solver (mass and momentum).
- Rhie and Chow velocity pressure coupling.
- Algebraic multi-grid solver.
- Large range of turbulence models.
- Advanced near wall treatment.

3 Turbulence models used in the study

3.1.1 *k*-ε model with scalable wall function

Two extra-equations are needed for the system-closure with this standard model. These values are obtained from their transport equations:

$$\frac{\partial \rho k}{\partial t} + \frac{\partial}{\partial x_i}(\rho U_i k) = P_k - \rho\varepsilon + \frac{\partial}{\partial x_i}\left(\frac{\mu_{eff}}{\sigma_k}\frac{\partial k}{\partial x_i}\right)$$

$$\frac{\partial \rho \varepsilon}{\partial t} + \frac{\partial}{\partial x_i}(\rho U_i \varepsilon) = \frac{\varepsilon}{k}(C_{\varepsilon 1}P_k - C_{\varepsilon 2}\rho\varepsilon) + \frac{\partial}{\partial x_i}\left(\frac{\mu_{eff}}{\sigma_\varepsilon}\frac{\partial \varepsilon}{\partial x_i}\right)$$

In these equations, P_k is the turbulence production defined by (incompressible):

$$P_k = \mu_t \frac{\partial U_j}{\partial x_i}\left(\frac{\partial U_i}{\partial x_j} + \frac{\partial U_j}{\partial x_i}\right)$$

The momentum equation becomes:

$$\frac{\partial \rho U_l}{\partial t} + \frac{\partial}{\partial x_i}(\rho U_i U_l) = -\nabla p' + \frac{\partial}{\partial x_i}\left(\mu_{eff}\frac{\partial U_l}{\partial x_i}\right)$$

Where $p' = p + \frac{2}{3}\rho k$ is the modified pressure and $\mu_{eff} = \mu + \mu_t = \mu + C_\mu \rho \frac{k^2}{\varepsilon}$ is the effective viscosity.

The constants are: C_μ=0.09, $C_{\varepsilon 1}$=1.44, $C_{\varepsilon 2}$=1.92, σ_k=1, σ_ε=1.3

Whereas simulations with a standard wall function are sensitive to the near-wall meshing (as a consequence of their dependency on the location of the first point of meshing), simulations with scalable wall functions overcome this by assuming that the wall coincides with the edge of the viscous sub-layer for fine grids (defined to be at $y^+=11$) and by preventing the computed y^+ values from falling below this value. Therefore, all grid points are outside the viscous sub-layer and all fine grid inconsistencies are avoided.

3.1.2 SST model with automatic wall treatment

The SST version of the *k*-ω model also requires two transport equations for the two extra variables: *k* the turbulence kinetic energy and ω, the turbulence frequency. In order to take advantage of the accurate prediction of turbulent flow separation by the *k*-ω model and to avoid its free-stream sensitivity, a blending between the Wilcox model and a transformed *k*-ε model is used. The equations employed are:

$$\frac{\partial(\rho k)}{\partial t}+\frac{\partial}{\partial x_i}(\rho U_i k)=P_k-\beta'\rho k\omega+\frac{\partial}{\partial x_i}\left[\left(\mu+\frac{\mu_t}{\sigma_k}\right)\frac{\partial k}{\partial x_i}\right]$$

$$\frac{\partial(\rho\omega)}{\partial t}+\frac{\partial}{\partial x_i}[\rho U_i\omega]=\alpha\frac{\omega}{k}P_k-\beta\rho\omega^2+\frac{\partial}{\partial x_i}\left[\left(\mu+\frac{\mu}{\sigma_{\omega t}}\right)\frac{\partial\omega}{\partial x_i}\right]+2(1-F_1)\rho\sigma_{w2}\frac{1}{\omega}\frac{\partial k}{\partial x_i}\frac{\partial\omega}{\partial x_i}$$

Where the blending function F_1 is defined by:

$$F_1=\tanh\left\{\left\{\min\left[\max\left(\frac{\sqrt{k}}{\beta'\omega y},\frac{500\nu}{y^2\omega}\right),\frac{4\rho\sigma_{\omega2}k}{CD_{k\omega}y^2}\right]\right\}^4\right\}$$

Where $CD_{kw}=\max\left(2\rho\sigma_{\omega2}\frac{1}{\omega}\frac{\partial k}{\partial x_i}\frac{\partial\omega}{\partial x_i},\ 10^{-10}\right)$ and y is the distance to the nearest wall.

F_1 is equal to zero away from the surface (*k*-ε model), and switches over to one inside the boundary layer (*k*-ω model).

The equations are available for both the SST and the BSL model. The difference between these two models is made by the introduction of a limiter in the SST model. This modification is used to avoid the over-prediction of the eddy-viscosity in adverse pressure gradient regions by taking into account the transport of the shear stress. Practically:

$$\nu_t=\frac{a_1k}{\max(a_1\omega,SF_2)}$$

Where $\boldsymbol{S}$ is an invariant measure of the strain rate and F_2 is a blending function defined by:

$$F_2=\tanh\left[\left[\max\left(\frac{2\sqrt{k}}{\beta'\omega y},\frac{500\nu}{y^2\omega}\right)\right]^2\right]$$

All constants are computed by a blend from the corresponding constants of the *k*-ε and the *k*-ω model by $\alpha=\alpha_1F+\alpha_2(1-F)$ etc. The constants for this model are: β'=0.09, α_1=5/9, β_1=3/40, σ_{k1}=2, $\sigma_{\omega1}$=2, α_2=0.44, β_2=0.0828, σ_{k2}=1, $\sigma_{\omega2}$=0.856.

A production limiter is used in the model to avoid stagnation flow problems:

$$\tilde{P}_k=\min(P_k;10\varepsilon)$$

Turbulence models based on the ω-equation provide an analytic expression of ω in the viscous sub-layer. This allows for a near-wall formulation, which gradually and automatically switches from wall-functions to a low-Re near wall formulations, as the grid is refined. In the current simulations, low-Re grids are used.

3.1.3 SSG Reynolds stress model

There are some changes in the momentum equations for the mean velocity compared to two-equations models:

$$\frac{\partial\rho U_l}{\partial t}+\frac{\partial}{\partial x_i}(\rho U_iU_l)-\frac{\partial}{\partial x_i}\left(\mu\frac{\partial U_l}{\partial x_i}\right)=-\nabla p''-\frac{\partial}{\partial x_i}\left(\rho\overline{u_iu_l}\right)+B_l$$

Where $p''=p+\frac{\partial U_l}{\partial x_i}\left(\frac{2}{3}\mu-\zeta\right)$ is the modified pressure and ζ the bulk viscosity.

The six equations for the transport of the Reynolds stress are solved in the following form:

$$\frac{\partial}{\partial t}\left(\rho\overline{u_iu_j}\right)+\frac{\partial}{\partial x_k}\left(U_k\rho\overline{u_iu_j}\right)=P_{ij}+\Phi_{ij}+\frac{\partial}{\partial x_k}\left[\left(\mu+\frac{2}{3}c_s\rho\frac{k^2}{\varepsilon}\right)\frac{\partial\rho\overline{u_iu_j}}{\partial x_k}\right]-\frac{2}{3}\delta_{ij}\varepsilon\rho$$

with a simplified isotropic diffusion term and with:

$$\Phi_{ij} = \left\{ -\rho\varepsilon\left[C_{s1}a_{ij} + C_{s2}\left(a_{ik}a_{kj} - \frac{1}{3}a_{ij}a_{ij}\delta_{ij} \right) \right] \right\} +$$

$$\left\{ -C_{r1}P_k a_{ij} + C_{r2}\rho k S_{ij} - C_{r3}\rho k S_{ij}\sqrt{a_{kj}a_{jk}} + C_{r4}\rho k\left(a_{ik}S_{jk} + S_{ik}a_{jk} - \frac{2}{3}a_{ij}S_{ij}\delta_{ij} \right) + C_{r5}\rho k\left(a_{ik}W_{jk} + W_{ik}a_{jk} \right) \right\}$$

With $P_k = 0.5P_{ii}$, $a_{ij} = \frac{\overline{u_i u_j}}{k} - \frac{2}{3}\delta_{ij}$, $S_{ij} = \frac{1}{2}\left(\frac{\partial U_i}{\partial x_j} + \frac{\partial U_j}{\partial x_i} \right)$, $W_{ij} = \frac{1}{2}\left(\frac{\partial U_i}{\partial x_j} - \frac{\partial U_j}{\partial x_i} \right)$

Where Φ is the pressure-strain correlation, $\boldsymbol{a}$ the anisotropy tensor, $\boldsymbol{S}$ the strain rate and $\boldsymbol{W}$ the vorticity tensor. $\boldsymbol{P}$ is the exact production term:

$$P_{ij} = -\rho\left(\overline{u_i u_k}\frac{\partial U_k}{\partial x_j} + \frac{\partial U_k}{\partial x_i}\overline{u_k u_j} \right)$$

As the turbulence dissipation ε appears in the transport equations, one equation is required to solve it:

$$\frac{\partial \rho\varepsilon}{\partial t} + \frac{\partial}{\partial x_i}(\rho U_i \varepsilon) = \frac{\varepsilon}{k}(c_{\varepsilon 1}P - c_{\varepsilon 2}\rho\varepsilon) + \frac{\partial}{\partial x_i}\left[\frac{1}{\sigma_{\varepsilon RS}}\left(\mu + \rho C_{\mu RS}\frac{k^2}{\varepsilon} \right)\frac{\partial \varepsilon}{\partial x_i} \right]$$

The constants are: C_s=0.22, $C_{\varepsilon 1}$=1.45, $C_{\varepsilon 2}$=1.83, $C_{\mu RS}$=0.1, $\sigma_{\varepsilon RS}$=1.36, C_{s1}=1.7, C_{s2}=-1.05, C_{r1}=0.9, C_{r2}=0.8, C_{r3}=0.65, C_{r4}=0.625, C_{r5}=0.2

4 Best Practice

It is frequently found in validation studies, that a wide spread of numerical results is presented by different groups, even with similar turbulence models and flow solvers. It is therefore essential to apply Best Practice techniques to reduce the influence of:

- Grid resolution (grid refinement study).
- Solver convergence (convergence study).
- Boundary conditions (sensitivity study).
- Arbitrary assumptions (sensitivity study).

As recommended, the simulations have been performed without the stilts used in the experiment to support the model. The influence of the stilts was analytically estimated.

4.1 Grid refinement

For both cases (25 and 35 deg), grid refinement studies have been performed. Table 1 shows the information on the 35 deg case grids used in the study. Similar grids have been used for the 25 deg case. It was found that even the smallest grid gave acceptable results for the drag coefficient as can be seen in Table 2. However, a more detailed comparison of the results showed that the medium grid was more suitable for the prediction of the local velocity profiles. It was therefore used in the model comparison. It was also found that a fully second order numerical scheme was essential to achieve quality results.

35° slant angle		Coarse	Medium	Fine
Nodes		665 091	1 256 010	2 538 030
Elements (on the body)		8476	12956	20229
Average y+ (body)		0.79	0.76	0.75
Average y+ (ground)		1.06	1.06	1.06
Max y+ (body)		3.6	3.7	3.6
Max y+ (ground)		3.1	3.1	3.1
Min grid angle	Min	28.5	28.5	28.5
	Average	74.3	76.1	76.1
Max grid angle	Max	151.5	151.5	151.5
	Average	105.8	104.2	102.7
Edge length ratio	Average	252	170	120
	Max	20747	18269	15024
	Average (body)	1828	1421	1122
	Max (body)	10256	4059	2774
Element volume ratio	Average	2.1	1.71	1.43
	Max	126.3	116	90
	Average (body)	1.5	1.3	1.2
	Max (body)	6.9	7.2	7.2

Table 1: Grid refinement for 35 deg case

Grids	Coarse	Medium	Fine	Expe.	"Expe. without stilts"
C_d value	0.246	0.240	0.238	0.260	0.234
Relative error(%) (Ref. "Expe. without stilts")	5,1	2.5	1.7	/	/

Iterations	200	165	200	/	/
Run time (H)	10	16	40	/	/

Table 2: Drag coefficient as a function of the grid resolution

4.2 Convergence study

Detailed convergence studies have been carried out to eliminate arbitrary convergence criteria. Details can be found in [2].

4.3 Sensitivity studies

In order to eliminate the influence of arbitrary assumptions made in the simulation, the following aspects of the simulations have been investigated by sensitivity studies:

- Location of inlet boundary condition.
- Formulation of outer boundary conditions (opening vs. slip wall).
- Advection scheme.

5 Turbulence model evaluation

5.1 35°- case

For the 35°- case, the two-equation models showed a good agreement with the experimental data, as can be seen from Table 3. Only the SSG model gives a drag coefficient, which is significantly lower than for the other two models.

Turbulence model	*k*-ε	SST	SSG	Expe.	"Expe. without stilts"
C_d value	0.228	0.240	0.199	0.260	0.234
Relative error(%) (Ref. "Expe. without stilts")	-2.6	2.5	-15	/	/
Iterations	250	165	450	/	/

Table 3: Model comparison for the 35 deg case

Figure 1 shows the velocity profiles in the symmetry plane for the different models. The differences between the models are small and most pronounced for the SSG model. The k-e model also gives some differences at the onset of the slant. More details can be found in [2].

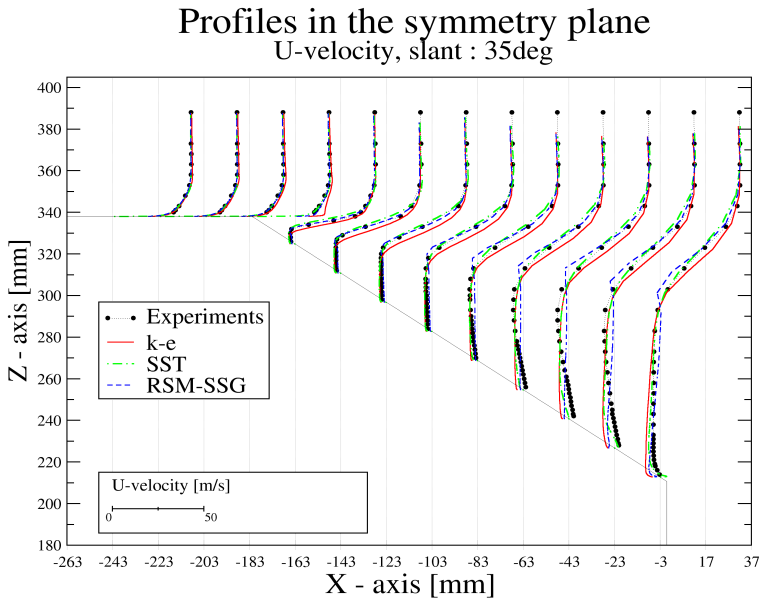

Figure 1: Velocity profiles for 35 deg case in the symmetry plane

5.2 35°- case

For the 25°- case, the models again showed a good agreement with the experimental drag data, as can be seen from Table 4. This is surprising considering the large differences in the velocity profiles shown in Figure 2. Clearly none of the models is able to predict the separated and re-attaching flow in the slant region correctly.

Turbulence model	*k*-ε	SST	SSG	Expe.	"Expe. without stilts"
C_d value	0.256	0.258	0.245	0.285	0.257
Relative error(%) (Ref. "Expe. Without stilts")	-0.4	0.4	-4.7	/	/
Iterations	160	200	240-340	/	/

Table 4: Model comparison for 25 deg case

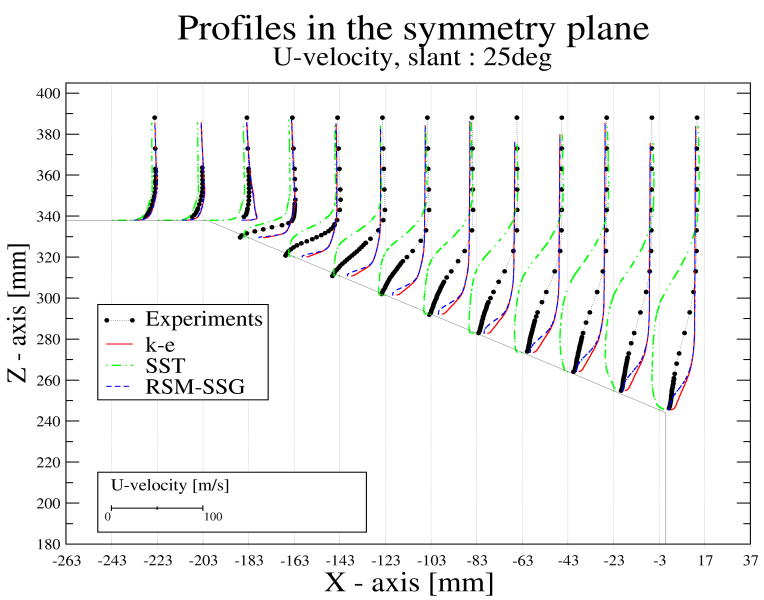

Figure 2: Velocity profiles for 25 deg case in the symmetry plane

6 Conclusions

CFD simulations have been carried out for two slant angles of *25°* and *35°*. Best practice procedures were applied to reduce the different sources of errors, which can be present in numerical CFD simulations.

Three different grids have been tested for the *35°*-case. It was shown that the medium and the fine grid produce results very close to each other, whereas the coarse grid was sufficiently accurate for quick screening and optimization purposes. For all remaining simulations, the medium grid was employed. In order to ensure that the differences in the flow structure observed for the *25°*-case are not results of grid sensitivities, the simulation has also been performed with a fine grid and the SST model. It was shown that the flow structure did not change as a function of the resolution.

A study of the influence of the discretisation scheme showed that a fully second order discretisation gave superior results, both in terms of convergence and accuracy.

CFX

Three models were used in the study (*k*-ε, SST and SSG). It was found that for the *35°* case, the two-equation models were in good agreement with the mean flow experimental data. The SST model gave an overall more realistic agreement with the data than the other two models.

For the *25°*-case, the differences between the solutions were much stronger. While the *k*-ε and the SSG model failed to predict flow separation on the slant, the SST model gave a massive separation over the entire slant region. This results in different flow topologies in the off-symmetry planes.

The results for the *25°*-case illustrate the dilemma of turbulence modeling for flows with massive flow separation. Most models would underestimate or miss the separation entirely and return too optimistic flow predictions. Other models, which have been optimized to accurately predict the separation onset, fail in the massively separated region. The problem is also visible from the experimental data, where the turbulence levels in the separated zones differ by almost one order of magnitude between the two slant angles. None of the models is able to reproduce this effect.

Surprisingly, the values for the drag coefficient have not shown a strong sensitivity to the flow details. Part of the good agreement for this value might therefore be the result of a cancellation of errors.

The next step of the current study will be to apply the SST-DES model developed by Strelets to the *25°*-case in order to test if the resolution of the large turbulent structures in the separated region will overcome the deficiencies of the SST model in that area.

7 Referencess

[1] ERCOFTAC Special Interest Group on ‘‘Quality and trust in industrial CFD’’ Casey M., Wintergerste T.: “*best practice guidelines”;* Jan. 2000.

[2] Durand, L, M. Kuntz and Menter F.R. ‘‘Validation of CFX for the Ahmed Car Body’’, CFX Validation report (florian.menter@cfx-germany.com)

Application of CFL3D to Case 9.4 (Ahmed Body)

Christopher L. Rumsey*
NASA Langley Research Center
Hampton, Virginia 23681-2199

1 Description of the Code

The computer code CFL3D [1] solves the three-dimensional, time-dependent, Reynolds averaged compressible Navier-Stokes equations with an upwind finite-volume formulation. It can solve flows over multiple-zone grids that are connected in a one-to-one, patched, or overset manner, and can employ grid sequencing, multigrid, and local time stepping when accelerating convergence to steady state. Upwind-biased spatial differencing is used for the inviscid terms, and flux limiting is used to obtain smooth solutions in the vicinity of shock waves, when present. Viscous terms are centrally differenced, and cross-diffusion terms are neglected. For very low Mach number flows, preconditioning [2] is used to insure convergence and accuracy of the solutions.

The CFL3D code is advanced in time with an implicit approximate factorization method. The implicit derivatives are written as spatially first-order accurate, which results in block tridiagonal inversions for each sweep. However, for solutions that utilize Roe flux-difference splitting [3], the block tridiagonal inversions are further simplified using a diagonal algorithm with a spectral radius scaling of the viscous terms.

The turbulence models are solved uncoupled from the mean flow equations using implicit approximate factorization. Their advective terms are solved using first-order upwind differencing. Many turbulence models are available in CFL3D, but only two were applied to the Ahmed body case: SST (Menter's shear stress transport [4]), and EASM-ko (a k-ω version of the explicit algebraic stress model [5, 6]). A description of EASM-ko is given in the CFL3D write-up on Case 9.2 (2-D Hill).

2 Specifics of this Case

The Mach number for the Ahmed body cases was M=0.117, and the Reynolds number per mm was Re=2667. For boundary conditions, the body and floor were solid (viscous, adiabatic). Turbulence equations were integrated all the way to these surfaces. The average minumum y+ at all solid walls was approximately 1.5. Only one half of the body was simulated (a symmetry plane was employed along the centerline of the body). A farfield (Riemann-invariant) boundary condition was employed in the far field. This "open" type of far field conditions was found by Durand et al. [7] to yield improved inlet velocity profiles over "closed" boundary conditions (for which the farfield boundaries above and to the side of the body are modeled as solid slip walls).

The grids were obtained from CFX, a supplier of computational fluid dynamics software and service (Durand et al. [7]). Only two slant angles were considered: 25° and 35°. In both cases the stilts beneath the body were ignored. For the 25° slant angle case, the grid contained 1.3×10^6 gridpoints. For the 35° slant angle case, the grid contained 1.25×10^6 gridpoints. Each grid was a multi-zone grid (29 zones) with 1-to-1 connectivity between the zones.

In the grids, the distance from the leading edge of the car to the inflow plane of the grid was 2100 mm, and the distance from the back of the car to the outflow plane of the grid was 5220 mm (the length of the car was 1044 mm). The body height was 288 mm. Its bottom was 50 mm above the floor, and the total grid height from the floor was 1206 mm (1062 mm from the top of the car). The car half-width was 194.5 mm, and the total grid width from the center plane was 935 mm (740.5 mm from the side of the car).

*Senior Research Scientist; Aerodynamics, Aerothermodynamics, and Acoustics Competency.

References

[1] Krist, S. L., Biedron, R. T., and Rumsey, C. L., "CFL3D User's Manual (Version 5.0)," NASA TM-1998-208444, June 1998.

[2] Weiss, J. M., and Smith, W. A., "Preconditioning Applied to Variable and Constant Density Flows," *AIAA Journal*, Vol. 33, No. 11, 1995, pp. 2050–2057.

[3] Roe, P. L., "Approximate Riemann Solvers, Parameter Vectors, and Difference Schemes," *J. Computational Physics*, Vol. 43, 1981, pp. 357–372.

[4] Menter, F. R., "Two-Equation Eddy-Viscosity Turbulence Models for Engineering Applications," *AIAA Journal*, Vol. 32, No. 8, 1994, pp. 1598–1605.

[5] Rumsey, C. L., and Gatski, T. B., "Recent Turbulence Model Advances Applied to Multielement Airfoil Computations," *J. Aircraft*, Vol. 38, No. 5, 2001, pp. 904–910.

[6] Georgiadis, N. J., Rumsey, C. L., Yoder, D. A., and Zaman, K. B. M. Q., "Effects of RANS Turbulence Modeling on Calculation of Lobed Nozzle Flowfields," AIAA Paper 2003-1271, January 2003.

[7] Durand, L., Kuntz, M., and Menter, F., "Validation of CFX-5 for the Ahmed Car Body," CFX validation report, CFX-VAL13/1002, 2002.

10th IAHR/ERCOFTAC Workshop on Refined Turbulence Modelling
October, 2002, University of Poitier

Contribution of Imperial College to Test Case 9.4: Flow around a simplified car body

Y.J. Jang and M. Leschziner
Department of Aeronautics, Imperial College London,
London, UK. Email: mike.leschziner@imperial.ac.uk

1. Numerical Methodology

The computations contributed to the workshop have been performed with the code STREAM, developed by Lien & Leschziner (1994) and extended by Apsley & Leschziner (2000). The major features of the code are as follows:

- general non-orthogonal 2d/3d finite-volume formation;
- cartesian velocity components;
- fully collocated storage;
- multiblock capability;
- pressure-correction strategy;
- TVD form (Lien and Leschziner (1994))of the quadratic QUICK scheme (Leonard (1979)) for convection; central differencing for diffusion;
- wide range of non-linear EVMs and second-moment closure models (high-Re and low-Re) incorporated;
- incompressible- and compressible-flow capability.

2. Turbulence Models

Results are presented for 5 turbulence models:

- the linear low-Re k-ε EVM of Launder and Sharma (1974);
- the linear low-Re k-ω EVM of Wilcox (1994)
- the cubic low-Re k-ε EVM of Apsley and Leschziner (1998);
- the quadratic low-Re k-ω EVM of Abe, Jang and Leschziner (2003) (see also Jang et al (2002));
- the second-moment closure of Sarkar, Speziale and Gatski (1991), extended to low-Re conditions by Chen et al (2000).

Most of the above models are well known and require no elaboration. However the model by Abe et al is less well known. This quadratic low-Re model differs in two important respects from others. First, it augments the basic quadratic constitutive EVM form by two additive fragments intended to account, respectively, for high normal straining and strong near-wall anisotropy. Second, it uses a form of the ω-equation that is much closer than Wilcox's form to the ε-equation. Specifically, it includes product of k and ω gradients and coefficients for the production and destruction terms which are directly equivalent to $C_{\varepsilon 1}$ and $C_{\varepsilon 2}$ normally used in the ε-equation.

An influential addition for strong near-wall anisotropy is that accounting for specifically the correct decay towards two-component turbulence that is observed in reality through DNS. This decay cannot be represented solely by use of terms combining strain and vorticity, and there is a need to introduce a tensorially correct term that takes into account the wall orientation. In the present model, the wall-direction indicator is

$$d_i = \frac{N_i}{\sqrt{N_k N_k}} \qquad N_i = \frac{\partial l_d}{\partial x_i} \qquad l_d = n \text{ (=wall distance)}$$

which is then used in the wall-anisotropy correction

$${}^{w}a_{ij} = -f_w\left(d_i d_j - \frac{\delta_{ij}}{3} d_k d_k \right)$$

with f_w being a viscosity-related damping function. In the above, a composite time scale is used, which combines the macro-scale k/ε with the Kolmogorov scale $\sqrt{\nu/\varepsilon}$. The damping function f_w then provides a smooth transition between the two scales across the near-wall layer.

3. Computational details

The computational grid is shown in Fig. 1.

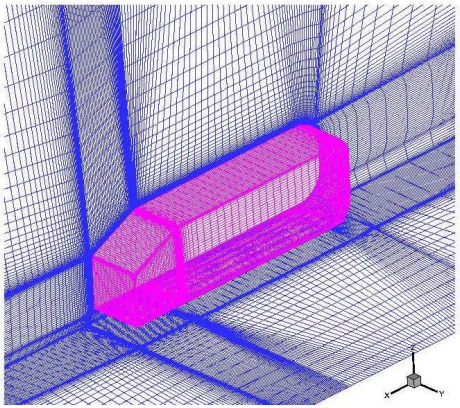

Fig. 1: 44-block, 1.8 M node mesh used for the computations

This mesh, intended for use with low-Re models, was provided to the writers by CFX. The original block topology was modified, however. Specifically, some blocks were subdivided and others agglomerated. However, nodal positions were not changed. The wall-normal distance (y^+) of the nodes in the wall-closest layer was less than 1 over most of the surface. The stilts were not included in the calculation.

The calculation was undertaken with an iterative scheme on the assumption that the solution would be steady. Thus, the domain extended over one half of the car body, from its symmetry plane to the spanwise box boundary at which symmetry conditions were prescribed. The same treatment was applied at the upper boundary of the solution domain.

4. Results

Results are included for the 25° only. For this case, the Launder-Sharma k-ε EVM returns a fully attached solution on the inclined roof. In contrast, the Wilcox k-ω EVM gives a fully detached flow, indicating too little mixing in the separated shear layer. Experience shows the non-linear EVMs to return mixing levels which are considerably lower than those providede by linear k-ε models. Hence, it is not surprising to observe that these models provoke massive separation on the leeward side, indicating far too little mixing. This behaviour was also expected to be produced by the SSG second-moment closure. However, as seen from the results, the predicted flow is much closer to the measured one. In particular, marginal separation followed by reattachment on the slanted roof is predicted. Whether this result is correct needs to be ascertain by further investigations and by comparisons with solutions by other contributors for this same model.

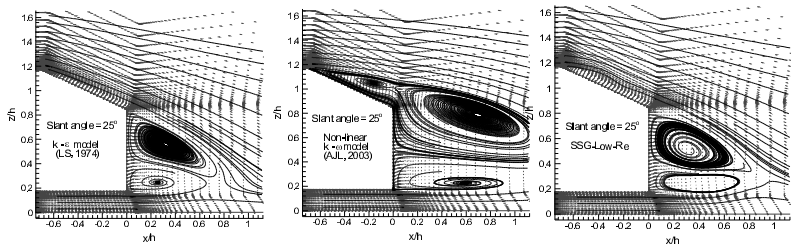

Fig. 2: Velocity-field solutions over the car-symmetry plane with linear EVM, non-linear EVM and Reynolds-stress model

References

K. **Abe**, Y-J. Jang and M.A. Leschziner, "An investigation of wall-anisotropy expressions and length-scale equations for non-linear eddy-viscosity models", *Int. J Heat and Fluid Flow*. **24**, 181-198, (2003)

D.D. **Apsley**, and M.A. Leschziner, M.A., Advanced turbulence modelling of separated flow in a diffuser, *Flow, Turbulence and Combustion*, **63**, 81-112. (2000)

D.D. **Apsley** and M.A. Leschziner, "A new low-Reynolds-number nonlinear two-equation turbulence model for complex flows", *Int. J. Heat and Fluid Flow*, **19**, 209-222 (1998).

H.C. **Chen**, Y.J. Jang and J.C. Han, "Computation of heat transfer in rotating two-pass square channels by a second-moment closure model", *Int. J. Heat and Mass Transfer*, **43**, 1603-1616 (2000).

Y-J. **Jang**, M.A. Leschziner, K. Abe, and L. Temmerman, Investigation of anisotropy-resolving turbulence models by reference to highly-resolved LES data for separated flow, *Flow, Turbulence and Combustion*, **69**, pp. 161-203 (2002).

B.E. **Launder** and B.I. Sharma, "Application of the energy-dissipation model of turbulence to the calculation of flow near a spinning disc", *Letters in Heat and Mass Transfer*, **1**,131-138 (1974).

B.P. **Leonard**, "A stable and accurate convective modeling procedure based on quadratic upstream interpolation", *Comp. Meth. Appl. Mech. Eng.*, **19**, 59-98 (1979).

F.S. **Lien** and M.A. Leschziner, "A general non-orthogonal collocated finite volume algorithm for turbulent flow at all speeds incorporating second-moment turbulence-transport closure, Part I: Computational implementation", *Comp. Meth. Appl. Mech. Eng.*, **114**,123-148 (1994).

F.S. **Lien** and M.A. Leschziner, "Upstream monotonic interpolation for scalar transport with application to complex turbulent flows", *Int. J. Num. Meth. In Fluids*, **19**, 527-548 (1994).

C.G. **Speziale**, S. Sarkar and T.B. Gatski, " Modeling the pressure-strain correlation of turbulence: an invariant dynamical systems approach", *Journal of Fluid Mech.*, **227**, 245-272 (1991).

D.C. **Wilcox**, "Simulation transition with a two-equation turbulence model", *AIAA J.* **32,** 247-255 (1994).